

## INFORMATION TO USERS

This manuscript has been reproduced from the microfilm master. UMI films the text directly from the original or copy submitted. Thus, some thesis and dissertation copies are in typewriter face, while others may be from any type of computer printer.

**The quality of this reproduction is dependent upon the quality of the copy submitted.** Broken or indistinct print, colored or poor quality illustrations and photographs, print bleedthrough, substandard margins, and improper alignment can adversely affect reproduction.

In the unlikely event that the author did not send UMI a complete manuscript and there are missing pages, these will be noted. Also, if unauthorized copyright material had to be removed, a note will indicate the deletion.

Oversize materials (e.g., maps, drawings, charts) are reproduced by sectioning the original, beginning at the upper left-hand corner and continuing from left to right in equal sections with small overlaps. Each original is also photographed in one exposure and is included in reduced form at the back of the book.

Photographs included in the original manuscript have been reproduced xerographically in this copy. Higher quality 6" x 9" black and white photographic prints are available for any photographs or illustrations appearing in this copy for an additional charge. Contact UMI directly to order.

# UMI

A Bell & Howell Information Company  
300 North Zeeb Road, Ann Arbor MI 48106-1346 USA  
313/761-4700 800/521-0600



**UNIVERSITY OF CALIFORNIA**  
**Santa Barbara**

**1.55 Micron In-plane Lasers Using Wafer Fused Cladding Layers**

**A Dissertation submitted in partial satisfaction of the requirements for the degree  
of**

**Doctor of Philosophy  
in  
Electrical and Computer Engineering  
by  
Archie Lee Holmes, Jr.**

**Committee in charge:**

**Professor Steven P. DenBaars, Chairperson  
Professor John E. Bowers, co-Chairperson  
Professor S. James Allen  
Professor Evelyn L. Hu**

**June 1997**

**UMI Number: 9800462**

---

**UMI Microform 9800462**  
**Copyright 1997, by UMI Company. All rights reserved.**

**This microform edition is protected against unauthorized  
copying under Title 17, United States Code.**

---


**UMI**  
**300 North Zeeb Road**  
**Ann Arbor, MI 48103**

The dissertation of Archie Lee Holmes, Jr  
is approved



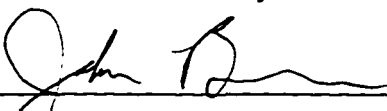
---

Professor S. James Allen



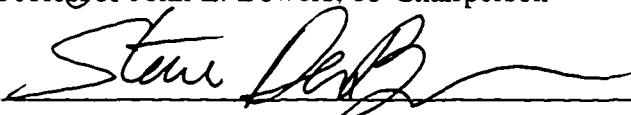
---

Professor Evelyn L. Hu



---

Professor John E. Bowers, co-Chairperson



---

Professor Steven P. DenBaars, Chairperson

## Acknowledgments

“It takes an entire village to raise a child...”

— Old African Proverb

I think that the above quote accurately summarizes my thoughts on my graduate experience at UCSB. Except that I have to admit that I was a child at the age of 23. But in terms of doing research, I was a babe; the last six years have allowed me to obtain a lot of knowledge, help, and encouragement from others. Thanks first of all goes out to my committee. With Steve DenBaaras and John Bowers, I got a lot of freedom to try many different things and to learn from the successes and mistakes without constant justification to them. Both of them were also there throughout to provide encouragement when things were not progressing as I would have like. I also would like to give special thanks to my other committee members -- Jim Allen and Evelyn Hu. Although I did not take the time out to utilize them as much as I would have like, their probing questions during my qualifier were extremely beneficial in my formulation of the problem being addressed and the ultimate limits that the approach would provide.

But learning in one's graduate school experience is only partly from the faculty. A lot of this comes from ones fellow students. I chose not to list them here because I fear leaving out someone. The ones who were important for the results contained within this document (Dr. Patrick Abraham, Yi-Jen Chiu, Dr. Scott Corzine, Greg Fish, and Dr. Richard Mirin) are thanked when their contribution is covered. The rest of you know who you are and your help was greatly appreciated.

The research done in experimental solid-state physics is not cheap to pursue. I was fortunate to have obtained funding from the Office of Naval Research via a National Defense Science and Engineering Graduate Fellowship. Other funding during my stay came from DARPA's Optoelectronics Technology Center, NSF's Center for Quantized Electronics Structures, DARPA contract with Dr. John Bowers for wafer fusion, and the UCSB Graduate Division.

But I cannot forget the important things I will miss in the Santa Barbara community as I leave it to head to Austin, Texas: the view from (and movies at) the Riviera Theater, iced blended mochas at Häva Java, lunches at the Greek and Italian Deli, book shopping at Chaucer's, CDs at MorningGlory, and last -- but certainly not least -- volleyball with the East Beach Nooners.

The reasonable man adapts himself to the world: the unreasonable one persists in trying to adapt the world to himself. Therefore all progress depends on the unreasonable man

— George Bernard Shaw

This dissertation is dedicated to all of the unreasonable ones who make the world go round.....

As well as family and friends. Without their support I would have never made it this far in life.



## Vita

- December 19, 1967:** Born in Chicago Heights, Ill.
- May 1991:** B.S., Electrical Engineering, University of Texas at Austin with highest honors
- December 1992:** M.S., Electrical Engineering, University of California at Santa Barbara
- May 1997:** Ph.D., Electrical Engineering, University of California at Santa Barbara

## Publications and Conference Talks

1. A.L. Holmes, Jr., M.E. Heimbuch, and S.P. DenBaars, "Strained GaInAsP Single Quantum Well Lasers Grown with Tertiarybutylarsine and Tertiarybutylphosphine" *Applied Physics Letters* **63** (25), pp. 3417-3419 (1993).
2. A.L. Holmes, Jr., M.E. Heimbuch, G. Fish, S.P. DenBaars, and L.A. Coldren, "InP-Based Multiple Quantum Well Structures Grown with Tertiarybutylarsine and Tertiarybutylphosphine: Effects of Growth Interruptions on Structural and Optical Properties", *Journal of Electronic Materials* **25**, 965.
3. M.E. Heimbuch, A.L. Holmes, Jr., M.P. Mack, S.P. DenBaars, L.A. Coldren, and J.E. Bowers, "Low Threshold 1.5  $\mu\text{m}$  Quantum Well Lasers Grown by Atmospheric Pressure MOCVD with Tertiarybutylarsine (TBA) and Tertiarybutylphosphine (TBP)", *Electronics Letters* **29** (4), pp. 340-341 (1993).
4. M.E. Heimbuch, A.L. Holmes, Jr., C.M. Reaves, M.P. Mack, S.P. DenBaars, and L.A. Coldren, "Tertiarybutylarsine (TBA) and Tertiarybutylphosphine (TBP) for the MOCVD Growth of Low Threshold 1.55  $\mu\text{m}$  In<sub>x</sub>Ga<sub>1-x</sub>As/InP Quantum Well Lasers", *Journal of Electronic Materials* **23** (2), pp. 87-91 (1994).
5. M.E. Heimbuch, A.L. Holmes, Jr., M.P. Mack, S.P. DenBaars, L.A. Coldren, and J.E. Bowers, "High Quality Long Wavelength Lasers Grown by

Atmospheric Pressure MOCVD with Liquid Group V Sources", IEEE Proceedings of the 5th Intl. InP and Related Materials Conf., Paris, France, ISBN 0-7803-0993-6, IEEE Society, Piscataway, New Jersey, pp. 239-242 (1993).

6. S.P. DenBaars, A.L. Holmes, Jr., M.E. Heimbuch, and C.M. Reaves, "Low Threshold Strained  $\text{In}_x\text{Ga}_{1-x}\text{As}_y\text{P}_{1-y}/\text{InP}$  Quantum Well Lasers Grown with TBA and TBP", paper LE-19, *Extended Abstracts of European Workshop on MOVPE-V*, Malmo, Sweden (1993).

7. S.P. DenBaars, A.L. Holmes, Jr., and M.E. Heimbuch, "Compressively Strained  $1.55\ \mu\text{m}$   $\text{In}_x\text{Ga}_{1-x}\text{As}_y\text{P}_{1-y}/\text{InP}$  Quantum Well Laser Diodes Grown by MOCVD with Tertiarybutylarsine (TBA) and Tertiarybutylphosphine (TBP)", *Proceedings of SPIE Intl. Symposium on Optoelectronics for Information and Microwave Systems, Laser Diode Technology VI*, Los Angeles CA, pp. 179-188 (1994).

8. K. Itaya, A.L. Holmes, S. Keller, S.G. Hummel, L.A. Coldren, and S.P. DenBaars, "Lasing Characteristics of  $\text{InGaP}/\text{InGaAlP}$  Visible Lasers Grown by Metalorganic Chemical Vapor Deposition with Tertiarybutylphosphine (TBP)", *Japanese Journal of Applied Physics Part 2 - Letters* **34** (11B), L1540-1542 (1995).

9. S.P. DenBaars, A.L. Holmes, M.E. Heimbuch, V.J. Jayaraman, C.M. Reaves, J.B. Shealy, U. Mishra, L.A. Coldren, and J.E. Bowers, "Indium Phosphide (InP) Based Heterostructure Materials and Devices Grown by MOCVD using Tertiarybutylarsine (TBA) and Tertiarybutylphosphine (TBP)", *Journal of the Korean Physical Society* **28**, pp. S37 - S42 (1995).

10. Rangchen Yu, Radhakrishnan Nagarajan, T. Reynolds, A. Holmes, J.E. Bowers, S.P. DenBaars, and Chung-En Zah, "Ultra-high Speed Performance of a Quantum Well Laser at Cryogenic Temperatures", *Applied Physics Letters* **65** (5), 528-530 (1994).

11. B.P. Keller, J.C. Yen, A.L. Holmes, S.P. DenBaars, and U. Mishra "Flow Modulation Epitaxy of  $\text{Ga}_x\text{In}_{1-x}\text{As}/\text{AlAs}$  Heterostructures on InP for Resonant Tunneling Diodes", *Applied Surface Science* **82-83**, pp. 179-88 (1994).

12. I-Hsing Tan, C.M. Reaves, A.L. Holmes, Jr., E.L. Hu, J.E. Bowers, and S. DenBaars, "Low-Temperature Pd bonding of III-V semiconductors", *Electronics Letters* **31** (7), pp. 588-589 (1995).
  
13. Daniel A. Tauber, Ralph Spickermann, Radhakrishnan Nagarajan, Thomas Reynolds, Archie L. Holmes, Jr., and John E. Bowers, "Inherent Bandwidth Limits in Semiconductor Lasers due to Distributed Microwave Effects", *Applied Physics Letters* **64** (13), pp. 1610 - 1612 (1994)
  
14. Monique S. Gaffney, Roy S. Smith, Archie L. Holmes, Jr., Casper M. Reaves, and Steven P. DenBaars, "Improved Composition and Thickness Control of III-V Epitaxy in a Metalorganic Chemical Vapor Deposition Process", Proceedings of the 34th IEEE Conference on Decision and Control, New Orleans, LA, pp. 2490-2495 (1995)
  
15. D.G. Yu, B.P. Keller, A.L. Holmes, Jr., S.P. DenBaars, and E.L. Hu, "Analysis of InP Etched Surfaces using MOCVD Regrown Quantum Well Structures", *Journal of Vacuum Science and Technology B* **13** (6), 2381 - 2385 (1995).
  
16. Monique S. Gaffney, Casper M. Reaves, Roy S. Smith, Archie L. Holmes, Jr. and Steven P. DenBaars, "Control of III-V Epitaxy in a Metalorganic Chemical Vapor Deposition Process: Impact of Source Flow Control on Composition and Thickness", accepted to *Journal of Crystal Growth* (October 1995)
  
17. I-Hsing Tan, C.M. Reaves, James Dudley, Archie L. Holmes, Jr., Dubravco Babic, Evelyn Hu, John Bowers, and Steven P. DenBaars, "Low Temperature Pd Direct Bonding and Electrical Transport Across InP-Pd-GaAs Interfaces", IEEE Proceedings of the 6th Intl. InP and Related Materials Conf., Santa Barbara, California, USA , ISBN 0-7803-1476-X, IEEE Society, Piscataway, New Jersey, pp. 628-31 (1994).
  
18. R.K. Sink, S. Keller, B. Keller, D.I. Babic, A.L. Holmes, D. Kapolnek, S.P. DenBaars, J.E. Bowers, X.H. Wu, J.S. Speck, "Cleaved GaN facets by wafer fusion of GaN to InP", *Applied Physics Letters* **68**, 2147 (1996)

19. P. Abraham, A.L. Holmes, M.E. Heimbuch, G. Fish, S.P. DeBaars, and J.E. Bowers, "1.55  $\mu\text{m}$  Lasers using Separate Strain Compensation Structure", submitted Journal of Electronic Materials, March 1997.

### Conference Presentations

- A.L. Holmes, M.E. Heimbuch, , C.M. Reaves, S.P. DenBaars, and L.A. Coldren, "Strained and Unstrained  $\text{In}_x\text{Ga}_{1-x}\text{As}/\text{InP}$  and  $\text{In}_x\text{Ga}_{1-x}\text{As}_y\text{P}_{1-y}/\text{InP}$  Quantum Well grown by Non-Hydride MOCVD with TBA and TBP," oral presentation, Electronic Materials Conference, Santa Barbara CA, United States, June 1993.
2. S.P. DenBaars, A.L. Holmes, Jr., M.E. Heimbuch, , and C.M. Reaves, "Low Threshold Strained  $\text{In}_x\text{Ga}_{1-x}\text{As}_y\text{P}_{1-y}/\text{InP}$  Quantum Well Lasers Grown with TBA and TBP," oral presentation, Fifth European Workshop on MOVPE, Malmo, Sweden, June 1993.
3. M.E. Heimbuch, A.L. Holmes, Jr., C.M. Reaves, M.P. Mack, S.P. DenBaars, and L.A. Coldren, "Tertiarybutylarsine (TBA) and Tertiarybutylphosphine (TBP) for the MOCVD Growth of Low Threshold 1.55  $\mu\text{m}$   $\text{In}_x\text{Ga}_{1-x}\text{As}/\text{InP}$  Quantum Well Lasers," oral presentation, Organometallic Vapor Phase Epitaxy Workshop, Palm Springs, CA, United States, March 1993.
4. I-H. Tan, C. Reaves, J.J. Dudley, A.L. Holmes, D.I. Babic, E.L. Hu, J.E. Bowers, and S.P. DenBaars, "Low-Temperature Pd Direct Bonding and Electrical Transport Across  $\text{InP-Pd-GaAs}$  Interfaces," oral presentation, Sixth International Conference on Indium Phosphide and Related Materials, Santa Barbara CA, United States, March 27-31 (1994).
5. D.A. Tauber, R. Spickermann, R. Nagarajan, T. Reynolds, A.L. Holmes, Jr., and J.E. Bowers, "Distributed Microwave Effects in High Speed Semiconductor Lasers", oral presentation, IEEE MTT-S International Microwave Symposium Digest, paper TU1C-1, San Diego, CA, May 22-28 (1994).

6. R. Nagarajan, R. Yu, T. Reynolds, A. Holmes, J.E. Bowers, and Steve DenBaars, "Cryogenic Microwave Optical Sources", Invited Paper, Engineering Foundation Third Conference on High Speed Optoelectronic Devices for Communications and Interconnects, San Luis Obispo, CA, August 14-18 (1994).
  
7. D.A. Tauber, R. Spickermann, R. Nagarajan, T. Reynolds, A.L. Holmes, Jr., and J.E. Bowers, "Microwave Propagation Effects in Directly Modulated Semiconductor Lasers", oral presentation, GOMAC '94 (Government Microcircuits Applications Conference), San Diego, CA, November 7-10 (1994).
  
8. R. Yu, R. Nagarajan, T. Reynolds, A. Holmes, and J.E. Bowers, "An Ultrahigh Speed Cryogenic Optical Fiber Link", oral presentation, CLEO 1994, paper CThJ2, Anaheim, CA, May 8-13 (1994).
  
9. D.A. Tauber, R. Spickermann, R. Nagarajan, T. Reynolds, A.L. Holmes, Jr., and J.E. Bowers, "Inherent Bandwidth Limits in Semiconductor Lasers due to Distributed Microwave Effects", oral presentation, CLEO 1994, paper CThB3, Anaheim, CA, May 8-13 (1994).
  
10. Monique S. Gaffney, Roy S. Smith, Archie L. Holmes, Jr., Casper M. Reaves, and Steven P. DenBaars, "Improved Composition and Thickness Control of III-V Epitaxy in a Metalorganic Chemical Vapor Deposition Process", 34th IEEE Conference on Decision and Control (1995).
  
11. Monique S. Gaffney, Casper M. Reaves, Roy S. Smith, Archie L. Holmes, Jr., Steven P. DenBaars, "Composition Control in a Metalorganic Chemical Vapor Deposition Process", 13th World Congress IFAC (1996).
  
12. M.S. Gaffney, C.M. Reaves, R.S. Smith, A.L. Holmes, Jr., and S.P. DenBaars, "Real-time Composition Control Techniques in a Metalorganic Chemical Vapor Deposition Process", Materials Research Society Symposium Proceedings **406** (1995).
  
13. D.G. Yu, C.-H. Chen, A.L. Holmes, Jr., S.P. DenBaars, and E.L. Hu, "A Comparison of Ion Damage in GaAs and InP", accepted to Micro and NanoEngineering 1996.

14. D. Tauber, M. Horita, A.L. Holmes, Jr., B.I. Miller, J. Piprek, and J.E. Bowers, "InGaAsP Metal Fused Microstrip Laser", Engineering Foundation High Speed Optoelectronics Conference, Devices and Systems, Snowbird, Utah, August 1996.

15. M. Horita, D.A. Tauber, A.L. Holmes, Jr., B.I. Miller, and J.E. Bowers, "Metal Fused Microstrip InGaAsP/InP MQW Lasers", Technical Report of the Institute of Electronics, Information, and Communications Engineers, ED96-70, OPE96-36, LQE96-38, p. 19, July 1996

16. D. Tauber, M. Horita, A.L. Holmes, Jr., B.I. Miller, and J.E. Bowers, "The Microstrip Laser", Proceedings of the Integrated Photonics Research Conference, Boston, MA, April 1996.

## Abstract

### 1.55 Micron In-plane Lasers Using Wafer Fused Cladding Layers

by

Archie L. Holmes, Jr.

1.55  $\mu\text{m}$  lasers have received considerable research interest due to the low attenuation and dispersion characteristic of optical fibers at that wavelength. These optical fiber characteristics make 1.55  $\mu\text{m}$  lasers the choice for current and future long-haul optical communications. The use of these lasers in this capacity is hampered by their high sensitivity to temperature which results in an increase in temperature and a reduction in the slope efficiency above threshold.

In this work, 1.55  $\mu\text{m}$  lasers are studied theoretically and experimentally to devise a new method of reducing these temperature-dependent characteristics. A model was developed that uses realistic material parameters and gain curve characteristics to simulate the static properties of 1.55  $\mu\text{m}$  lasers. It is found through this modeling that the temperature performance of 1.55  $\mu\text{m}$  lasers can be improved with a reduction of *either* Auger recombination (which is inherent in these structures) *or* carrier overflow. Furthermore, it takes a reduction of *both* parameters to obtain the temperature performance characteristics of shorter wavelength InGaAs/GaAs lasers.

To obtain this reduction in carrier overflow, a novel approach for 1.55  $\mu\text{m}$  in-plane laser structures is developed. This approach involves the use of wafer fusion to define the cladding layers of the device. The main benefit of this approach is that it allows the device designer an additional degree of freedom in device design. Thus, electron confinement can be achieved without a severe

reduction in optical confinement that is seen in more conventional structures. Experimental results on these novel structure are presented. The results show that characteristic temperatures ( $T_c$ ) can be achieved that are comparable to conventional devices. Furthermore, improved slope efficiency properties are seen. The reasons for this are discussed along with area for further improvement.



## Table of Contents

<b>Acknowledgments</b>	<b>iv</b>
<b>Vita</b>	<b>vii</b>
<b>Abstract</b>	<b>xii</b>
<b>1. Introduction</b>	<b>1</b>
1.1. Introduction to (Semiconductor) Lasers	2
1.2. Development of Fiber Optic Communication Systems at 1.55 $\mu\text{m}$ : A Brief History	7
1.3. Performance of 1.55 $\mu\text{m}$ Lasers Versus Other Semiconductor Lasers	11
1.4. Dissertation Overview	16
1.5. References	18
<b>2. Modeling of In-Plane Semiconductor Lasers: Approach</b>	<b>27</b>
2.1. Introduction to 1.55 $\mu\text{m}$ Lasers: Design Aspects and General Features	27
2.1.1. Design Issues and Definitions	29
2.1.2. Auger Recombination and 1.55 $\mu\text{m}$ Lasers	31
2.1.3. Carrier Overflow and Device Performance	34
2.2. General Modeling Approach	38
2.2.1. Gain Curves of GaInAsP Quantum Wells for 1.55 $\mu\text{m}$ Emission	40
2.2.2. Determining the Operating Point of a In-plane Laser	44
2.2.3. Heating Effects in In-plane Laser Operation	46
2.3.4. Calculation of Threshold Current and Light vs. Current Curves	49
2.3. Measuring the Temperature Dependence of 1.55 $\mu\text{m}$ Lasers	51

2.3.1.	Characteristic Temperature ( $T_0$ ) Approach	51
2.3.2.	The Maximum Temperature ( $T_{max}$ ) Approach	54
2.3.3.	The Critical Temperature ( $T_c$ ) Approach	57
2.4.	Summary	60
2.5.	References	61
<b>3.</b>	<b>Modeling of In-Plane Semiconductor Lasers: Results</b>	<b>69</b>
3.1.	Effect of Structural Parameters	70
3.2.	Auger Recombination Effects	80
3.3.	Carrier Overflow Effects	85
3.4.	Summary	86
3.5.	References	89
<b>4.</b>	<b>Design of 1.55 <math>\mu\text{m}</math> Lasers with Reduced Carrier Overflow</b>	<b>91</b>
4.1.	Methods of Reducing Carrier Overflow in 1.55 $\mu\text{m}$ Lasers	91
4.1.1.	Raising the Barrier Height in GaInAsP-based Multiple Quantum Well Lasers	91
4.1.2.	Use of AlGaInAs as a Barrier Material in 1.55 $\mu\text{m}$ Lasers	93
4.1.3.	Other Approaches	96
4.2.	Wafer Fusion for 1.55 $\mu\text{m}$ Lasers with Reduced Carrier Overflow	98
4.2.1.	Introduction to Wafer Fusion	98
4.2.2.	Applications of Wafer Fusion	102
4.3.	Design of 1.55 $\mu\text{m}$ Lasers Using Wafer Fused Structures	103
4.3.1.	General Issues and Definitions	103
4.3.2.	Modeling Formulation	111
4.3.3.	Structures with GaInAsP ( $\lambda=1.1 \mu\text{m}$ ) waveguides	113
4.3.4.	Structures with InP waveguides	116
4.4.	Summary	117

4.5.	References	120
<b>5.</b>	<b>Materials Growth and Fabrication of 1.55 <math>\mu\text{m}</math> Wafer Fused Lasers</b>	<b>129</b>
5.1.	Materials Growth	129
5.1.1.	Active Region Growth by Metalorganic Chemical Vapor Deposition: An Introduction	130
5.1.2.	Active Region Structures for 1.55 $\mu\text{m}$ Wafer Fused Lasers	135
5.1.3.	Cladding Layer Growth by Molecular Beam Epitaxy	137
5.1.4.	Final Growth Structures	141
5.2.	Fusion Process for 1.55 $\mu\text{m}$ In-Plane Lasers	143
5.2.1.	Initial Sample Preparation	145
5.2.2.	First Fusion	146
5.2.3.	InP Substrate Removal	148
5.2.4.	Second Fusion and GaAs Substrate Removal	148
5.3.	Summary	149
5.4.	References	150
<b>6.</b>	<b>Theoretical Predictions and Theoretical Results</b>	<b>153</b>
6.1.	Theoretical Predictions	153
6.2.	Experimental Results	159
6.2.1.	Effects of the Fusion Temperature on 1.55 $\mu\text{m}$ Lasers: Structural, Optical, and Broad-Area Results	159
6.2.2.	Single-Fused Laser Results: Narrow Ridge Devices	170
6.2.3.	Double-Fused Laser Results	179
6.3.	Summary	180
6.4.	References	182
<b>7.</b>	<b>Recapitulation and Future Work</b>	<b>185</b>
7.1	Recapitulation of Dissertation	185
7.2	Future Work	188

<b>A.</b>	<b>Gain Curve Modeling of GaInAsP Quantum Wells</b>	<b>197</b>
A.1	General Gain Curve Calculation Procedure	197
A.2.	Modifications to Calculate GaInAsP Gain Curves	200
A.2.1.	GaInAsP Material Parameters	200
A.2.2.	Quantum Well Band Offsets	203
A.2.3.	Occupation of Barrier and SCH Regions	203
A.2.4.	Temperature Dependence	204
A.3.	Modeling of GaInAsP quantum wells with GaInAsP or InP barriers	205
A.4.	References	206
<b>B.</b>	<b>Device Processing of 1.55 <math>\mu\text{m}</math> Lasers with Wafer Fused Cladding Layers</b>	<b>217</b>
B.1.	Lithography for p-metal contact and p-metallization	217
B.2.	Ridge Etch of Laser Structure and p-metal anneal	219
B.3.	Bond Pad Lithography and Metallization	219
B.4.	Sample Thinning and n-metallization	220
B.5.	Summary	221
B.6.	References	222

---

# 1. Introduction

The ability to communicate has been one of the major driving forces in the development of modern society. Human ingenuity has allowed us to discover many important things throughout time: how to harness fire, how to make a wheel, how to study the stars and forces of nature, etc. However, alongside discovery, humans are communal creatures in the respect that they desire to share information they encounter with others (and in too many cases receive way more credit for it than they deserve). As we move to the end of the first millennium, the amount of information available for use keeps exponentially increasing. Scientists and engineers have been working to devise ways to send more information as quickly as possible. Fiber optic-based communications has emerged as one of the best ways to achieve this goal. This chapter will first introduce lasers in general and semiconductor lasers specifically. Next, I will give a brief overview of the development of semiconductor lasers leading to light sources for fiber optic communications at  $1.55\ \mu\text{m}$ . Following this, the performance of  $1.55\ \mu\text{m}$  lasers is compared to GaAs-based and AlGaInP-based quantum well lasers. Lastly, the organization of this dissertation will be discussed.

## 1.1 Introduction to (Semiconductor) Lasers

As suggested by the title of this dissertation, the focus of my research is experimentally improving the performance of semiconductor lasers that emit light at  $1.55\ \mu\text{m}$ . Thus, two natural questions emerge: how do semiconductor lasers work and why are lasers emitting at  $1.55\ \mu\text{m}$  important. In answering these two questions, I need to first define the term 'laser' which stands for Light Amplification by the Stimulated Emission of Radiation. Therefore, in order for there to be a laser, some type of amplification region is needed. Furthermore,

this amplification region must be finite and have some sort of feedback mechanism that sends the amplified light back through the amplification region to sustain the laser action. This is illustrated in Figure 1-1.



**Figure 1-1.** Basic Schematic of a Laser

The mirrors reflect some of the light back into the amplification region and allow the rest to escape the cavity in order for the light to be emitted from the device. If the reflection of these mirrors is known, then an energy conservation equation can be established so that the light “generated” by the amplification region is equal to the amount of energy lost through the mirrors. The expression for this reduces to

$$r_1 r_2 \exp[-i2\beta L] = 1 \quad (1-1)$$

where  $\beta$  is the complex propagation coefficient of the lasing mode given by

$$\beta = \frac{2\pi n}{\lambda_0} + i \frac{(g - \alpha)}{2} \quad (1-2)$$

and  $r_1$  and  $r_2$  are the field reflectivities of the mirrors,  $g$  and  $\alpha$  are the power-amplification and power-loss inside the cavity, and  $L$  is the length of the cavity. Looking at the real part of Equation ( 1-1) leads to the following expression

$$r_1 r_2 \exp[(g - \alpha)L] = 1 \quad (1-3)$$

from which  $g$  can be solved. Doing so yields

$$g = \alpha - \frac{1}{L} \ln(r_1 r_2) \quad (1-4)$$

Note that a typical representation of equation ( 1-4) replaces the field reflectivity with the power reflectivity ( $r = \sqrt{R}$ ) so that the equation becomes

$$g = \alpha + \frac{1}{2L} \ln \frac{1}{R_1 R_2} \quad (1-5)$$

What the above equation shows is that the amount of amplification needed in order to obtain laser action is inversely dependent on the length of this region and the reflectivity of the mirrors. The only requirement that is further imposed on the laser is that the light be coherent. In other words, all of the components of the light (i.e., photons) must have the same wavelength and phase. This is achieved by the process of stimulated emission which requires achieving a state (known as population inversion) such that the probability of light being generated is higher than that of light being absorbed in the amplification region. The idea of population inversion is illustrated in the case of a simple four-level

laser (see Reference [1]). Population inversion requires that the lasing state having a higher energy (marked as  $E_2$  in Figure 1-2) has a higher population density than the lower lasing state (marked as  $E_1$ ). To achieve this, some sort of external pumping must be supplied.

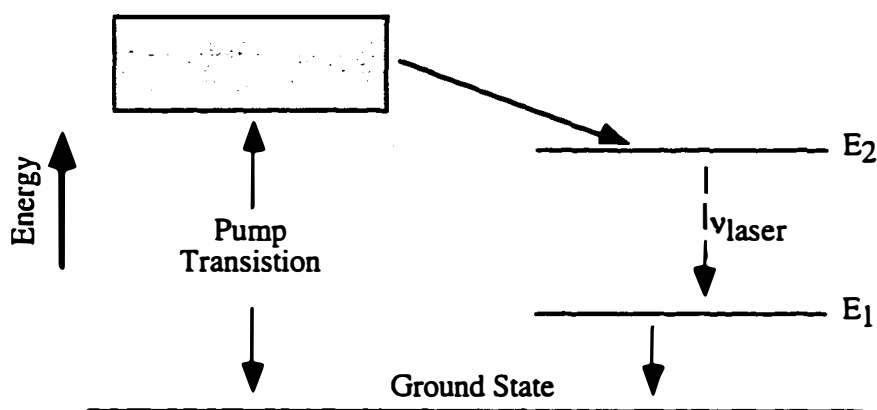


**Figure 1-2.** Energy Diagram of a Four-Level Laser

In the scientific community, many different laser systems have been developed and used for a variety of applications. Three main classes of lasers have resulted from this work: solid-state lasers (such as the ruby and Neodymium lasers), gas lasers (such as the Helium-Neon and carbon-dioxide), and semiconductor lasers. Each laser differs not only in the means by which population inversion is achieved, but also by the means by which amplification occurs and the resulting energy of emitted light<sup>i</sup>. Semiconductor lasers, however, enjoy a number of outstanding features when compared to other types of lasers. First, population inversion is fairly easy to achieve<sup>ii</sup>. In a semiconductor, population inversion is

<sup>i</sup> For more information, see Chapters 6 through 9 of Reference [2].

<sup>ii</sup> If the "right" semiconductor is chosen. See the next section for the history of the development of semiconductor lasers.



achieved by injecting carriers via an applied voltage (which produces a current) into the device as shown in Figure 1-3 below for a p-i-n diode. In this non-equilibrium condition, there exists an excess of electrons in the conduction band and an excess of holes (or empty electron states) in the valence band.

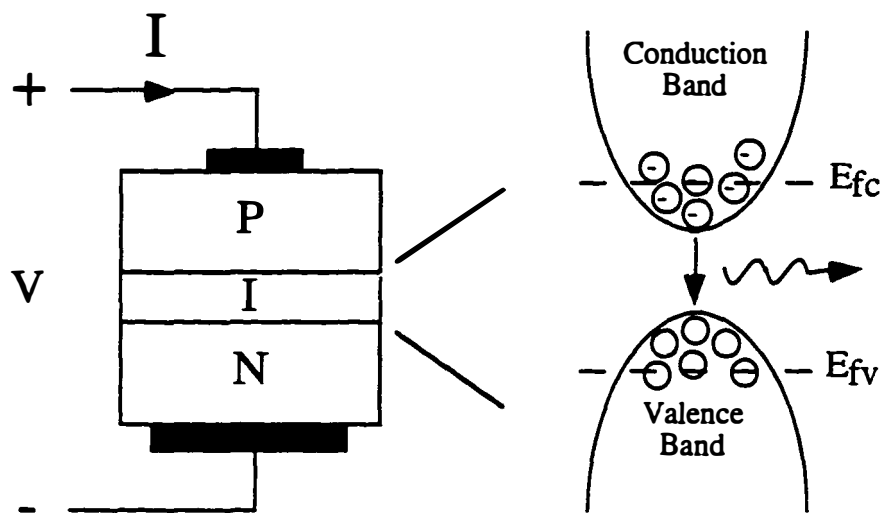


**Figure 1-3.** Example of Population Inversion in a P-I-N semiconductor diode. The quasi-Fermi levels for electrons ( $E_{fc}$ ) and holes ( $E_{fv}$ ) are also shown.

These conduction-band electrons see these empty states at lower energy and at some time (known as the spontaneous emission lifetime) will fall down to the valence band emitting a photon of light with the energy of the electron's transition. This process, known as spontaneous emission, does not result in coherent light. If one of these emitted photon now induces another electron transition, the result is an exact duplicate of the initial photon – a process known as stimulated emission. This process is continued and a large number of identical photons are generated in the laser cavity which leads to coherent light.

Second, these lasers use quantum wells so that the benefits of quantization can be used to improve performance (see Chapter 2 for more information). In-plane lasers have active region cross-section of  $5 \times 300 \mu\text{m}^2$  or less; with the emergence of vertical-cavity lasers (VCLs), this area can be reduced to  $< 50 \mu\text{m}^2$ . This smaller area for VCLs leads to a smaller active region (due to the quantum wells) volumes and threshold currents of less than 1 mA where in-plane lasers are in the milliamp regime[3-7]. Schematics of these lasers are shown in Figure 1-4 below.

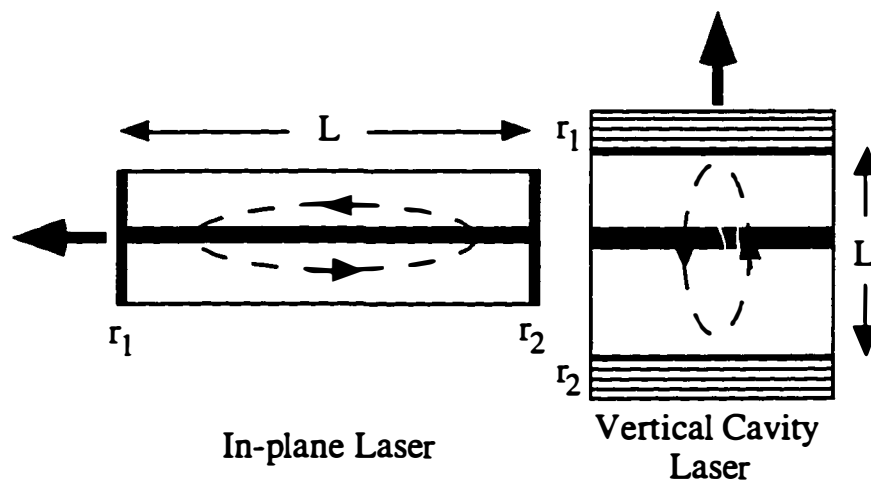


**Figure 1-4.** Simple schematics of an in-plane and a vertical cavity semiconductor laser. The path which the light travels around the cavity is denoted by the arrows.

Third, even though their size is very small, these lasers can emit milliwatts of power at wavelengths from the visible to the infra-red ( $0.6$  to  $\approx 2 \mu\text{m}$ ). And lastly, the conversion efficiency of the input pump power (which is typically in the form of electrical power) is very high. Semiconductor lasers can have 30 - 50% wall-plug efficiencies as compared to less than 1% for most other lasers.

## 1.2 Development of Fiber Optic Communication Systems at 1.55 $\mu\text{m}$ : A Brief History

The development of communication systems beyond smoke signals and letters carried from monarch to monarch via ship is an interesting story<sup>iii</sup>. The advent of telegraphy[9] in the 1830s can mark the start of the modern communication age. With the use of Morse code, approximately 10 bits of information per second (10 b/s) could be sent over distance of 1000 km with the use of intermediate relay stations. In fact, transatlantic telegraph communications occurred first in 1866. Another evolution occurred with the development of the telephone[10] in 1876. To give the reader an idea of the change that the telephone made in communications, I will use the product of the bit rate of information sent and the distance it was sent (the *bit-rate distance product* with units of (b/s)-km) as a figure of merit. For the telegraph in the 1860s, the bit-rate distance product was in the neighborhood of 10 (b/s)-km; the telephone around 1900 had a value of approximately 500 (b/s)-km (See Figure 1.1 of Reference [8]). Further advance with the use of coaxial cable and microwaves led to bit-rate bandwidth products of approximately 100 (Mb/s)-km due to fundamental limitations. It was realized in the middle of this century that the capacity of communication systems could be increased if light was used as a carrier. However, in those times (1950s), there was not a coherent compact optical source nor was there an adequate transmission medium for this light. (An interesting side note: It was suggested – before the creation of good optical fibers – that one use a sequence of gas lenses to confine light. [11] )

---

<sup>iii</sup> This account is paraphrased from the account given by Agrawal in Reference [8].

In the evolution of things it was the semiconductor laser that was developed first<sup>iv</sup>. The first documented discussion of the possibility of stimulated light from a semiconductor was made in an unpublished manuscript by John von Neumann[15] in 1953 (a year before the demonstration of the MASER [16]). The first discussion of obtaining coherent light from a semiconductor was made by Pierre Aigrain in June of 1958 (see Reference 8 in [14]). About the same time, researchers in the USSR had independently come up with a similar idea (see Reference 9 in [14]). The point here is that these discussions considered theoretical aspects of stimulated emission in a semiconductor. There were still major issues to decide: what semiconductor(s) to use and what type of transitions (either conduction band-to-valence band or conduction band-to-acceptor level) to investigate. Later, researchers at CNET [17,18] used the idea of “quasi-Fermi levels” to derive the equations for the onset of stimulated emission in a semiconductor although they believed this was possible in an indirect semiconductor such as Ge or Si.

The next big jump in the development of the semiconductor laser occurred in April of 1962 when researchers at the Joffe Physicotechnical Institute published a paper describing a slight narrowing of the “intrinsic recombination radiation” in GaAs p-n junctions. Even though it is now known this was not a laser, it strongly suggested how one could identify when stimulated emission was occurring. After this, the achievement of high efficiency electroluminescence from GaAs p-n junctions was reported by a number of researchers (see references 19-21 of Reference [14]) . This started an avalanche of work on achieving a semiconductor laser. Within one month, four different research

---

<sup>iv</sup> This is an absolutely fascinating story. There are several accounts of the development of the semiconductor laser [12-14] which differ slightly from each other. This account roughly follows Reference [14].

groups had written accounts of coherent emission of light from either GaAs [19-21] or  $\text{GaAs}_{1-x}\text{P}_x$ [22].

Now that the semiconductor laser had been developed, The quest to find a suitable transmission medium was now begun (With further work CW operation was first achieved [23,24] with the use of a double heterostructure laser structure; the addition of quantum wells [25-29] with biaxial strain [30-39] came later.). In 1966, it was suggested that silica-based optical fibers may be the best choice[40]. However, at the time, fiber losses were greater than 1000 dB/km. By 1970, fiber loss in silica was about 20 dB/km near the wavelength of 1  $\mu\text{m}$  [41] – approximately the emission wavelength of GaAs lasers. By 1976 with GaAs lasers and optical fibers, the system capacity of fiber optic communication systems was in the neighborhood of 500 (Mb/s)-km as compared to 100 (Mb/s)-km for coaxial cable. Later in the 1970s, it was realized that repeater stations (for boosting the amplitude of the light) could be spaced farther apart at 1.3  $\mu\text{m}$  due to reduced fiber loss (Figure 1-5) and minimal dispersion (Figure 1-6) . This led to efforts in obtaining devices made from GaInAsP that emit at this wavelength with success being achieved in 1977 [42]. Further advances were made by moving to 1.55  $\mu\text{m}$  where the loss in optical fibers is a minimum (approximately 0.2 dB/km) [43,44]. However, a price was paid because of the large dispersion at this wavelength. In order to reap the benefits of lower fiber loss, fibers were designed such that the fiber's dispersion characteristics were either flattened or the zero dispersion point was shifted out to 1.55  $\mu\text{m}$  (see Figure 1-6). In addition, lasers that operated in a single longitudinal mode were also pursued.

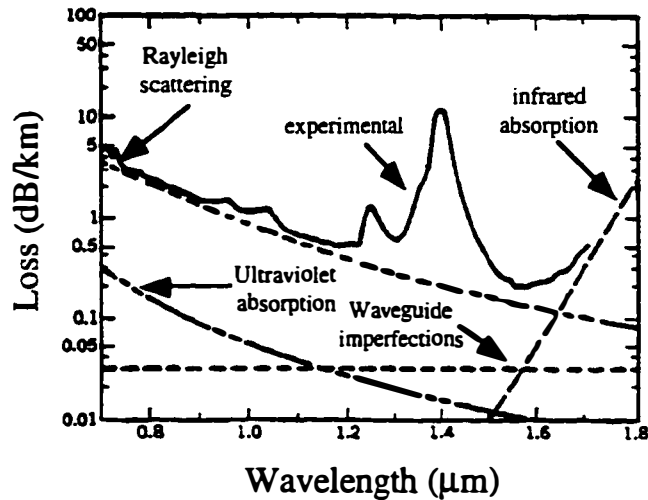


**Figure 1-5.** Loss (in dB/km) in a silica-based optical fiber as a function of wavelength. The dashed lines represent the processes that fundamentally limit the continued improvement of these fibers. Taken from Reference [8].

With the advent of optical amplifiers that could boost the signal without an expensive repeater station [45-47], 1.55  $\mu\text{m}$  has become the wavelength of choice for current and future optical communication systems. Now, system capacity can be as high as 10,000 (Gb/s)-km -- a 5 order of magnitude increase in capacity over coaxial cables. This increase in system capacity for semiconductor lasers over time is shown in Figure 1-7.

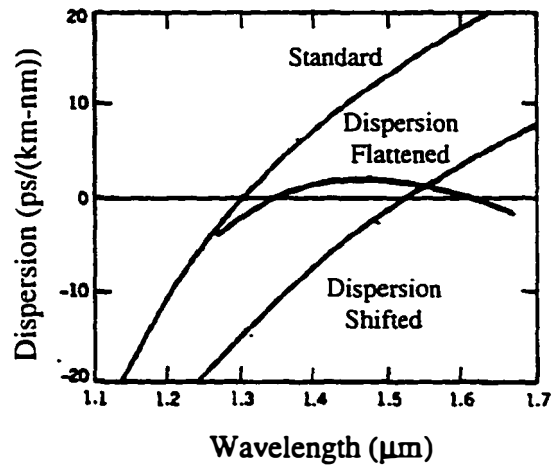


**Figure 1-6.** Dispersion versus wavelength for a standard, a dispersion-flattened, and a dispersion shifted optical fiber. Taken from Reference [8].

### 1.3 Performance of 1.55 μm Lasers Versus Other Semiconductor Lasers

The interest in 1.55 μm quantum well lasers revolves around their use in long-haul fiber optic communications. For these communication systems, it is expected that 1.55 μm quantum well lasers meet certain performance criteria in order to operate effectively in this capacity. This performance criteria (in bold) along with some device related characteristics (in italics) are listed below.

- **Low Input Power.** This is related to *the operating current and voltage* of the laser -- both of which are desired to be as low as possible.

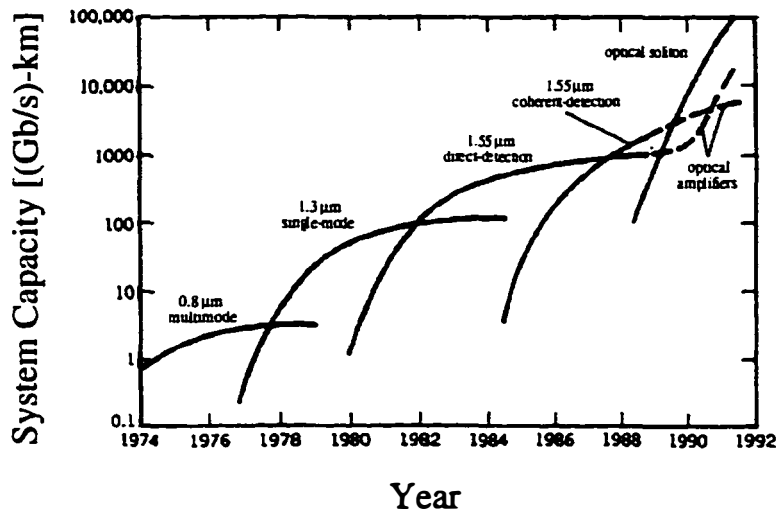


**Figure 1-7.** System capacity of fiber optic communication systems as a function of year since 1974. Taken from Reference [8].

- **High Output Power in a Single Mode.** For transmission down the fiber, this will minimize the number of repeater stations needed. This is further related to how hard the device can be pushed (i.e., how much input power it can take) and have it still operate without the adverse effects of *device heating*.
- **High Wall Plug Efficiency.** This is how well the laser converts electrical power (*operating voltage and current*) to light (output power). The higher this value, the less *device heating* occurs in the device.
- **Wide Operating Temperature Range.** This is important in that it is not desired to externally control the temperature at which the laser operates in order to have predictable device performance. Criteria that are important here are low *temperature sensitivity and device heating* effects, and *stable* (i.e., temperature independent) *slope efficiency*.



- **High Modulation Bandwidth.** This parameter is related to how fast information can be sent down an optical fiber. There are two controlling parameters here, the *output power* and the *differential gain*.
- **Low Chirp.** When the laser is modulated, the frequency of the emitted light usually changes due to coupling of the gain and refractive index with a change in the number of carriers injected. This is usually quantified in a parameter called *the linewidth enhancement factor*.

Current 1.55  $\mu\text{m}$  in-plane lasers are adequately operating in optical communication systems [48-57]. In many cases, however, the directly modulated laser is being replaced with more complicated structures which use multi-electrodes or integrated modulators [58-63] for improved performance. Even in the pursuit of more complicated structures to achieve better system performance, there is a lot of work being focused into improving directly modulated lasers due to their ease of fabrication. To give the reader an appreciation of the current state-of-the-art, Table 1-1 shows some of the typical device performance criteria for 1.55  $\mu\text{m}$  lasers as compared to GaAs-based 0.98  $\mu\text{m}$  lasers. Some important things are shown in Table 1-1. As compared to 0.98  $\mu\text{m}$  lasers, 1.55  $\mu\text{m}$  lasers are not performing as well. More specifically, 1.55  $\mu\text{m}$  lasers have higher threshold current densities, are more temperature sensitive (in terms of a smaller  $T_0$ ), cannot be modulated as quickly, and cannot emit as much single mode power. From Table 1-2, there are some important differences between the materials used for 1.55  $\mu\text{m}$  and 0.98  $\mu\text{m}$  lasers. Most importantly, there are two main factors<sup>v</sup> on which I would like to focus: Auger recombination and the conduction band barrier height. How these parameters affect device performance will be the subject of Sections 3.3 and 3.4.

---

<sup>v</sup> P-type absorption will not be considered as a major factor in the reduced performance of 1.55  $\mu\text{m}$  lasers as compared to 0.98  $\mu\text{m}$  and 0.67  $\mu\text{m}$  lasers. See Chapter 4 for an explanation.

**Table 1-1.** Typical Device Performance Values for 1.55  $\mu\text{m}$  (InP-Based) and 0.98  $\mu\text{m}$  (GaAs-Based) Edge-Emitting Lasers as Reported in the Literature.

Parameter	GaInAs(P) QWs	GaInAs QWs
	GaInAsP barriers	AlGaAs barriers
Typical Threshold Current Density per Well ( $\text{A}/\text{cm}^2$ )	80 - 100	40 - 60
Single Mode Output Power (mW)	$\approx 150$ [86]	$\approx 260$ [87]
Slope Efficiency per Facet <sup>‡</sup> (W/A)	0.39[88]	0.55[89]
Maximum CW Operation Temperature ( $^{\circ}\text{C}$ )	$\approx 170$ [90]	$\approx 220$ [91]
Characteristic Temperature (K)	40 - 70 [92,93]	$\geq 200$ [87,94]
Modulation Bandwidth <sup>†</sup> (GHz)	25 (120 mA) [48,95]	$\geq 40$ (155 mA) [96]
Linewidth Enhancement Factor <sup>†</sup>	1 - 2 [48]	1.4 [96]

<sup>†</sup> In the GaInAsP QW structure, a de-tuned DFB laser is used which improves things as compared to a Fabry-Perot laser for the case of GaInAs/GaAs.

<sup>‡</sup> This is out of the anti-reflection coated facet of a AR/HR laser cavity.

**Table 1-2.** Typical Material Parameters for 1.55  $\mu\text{m}$  (InP-Based) and 0.98  $\mu\text{m}$  (GaAs-Based) Lasers.

Parameter	$\text{Ga}_{0.2}\text{In}_{0.8}\text{As}_{0.75}\text{P}_{0.25}$ QWs	$\text{Ga}_{0.2}\text{In}_{0.8}\text{As}$ QWs
	$\text{Ga}_{0.23}\text{In}_{0.77}\text{As}_{0.5}\text{P}_{0.5}$ barriers	$\text{Al}_{0.2}\text{Ga}_{0.8}\text{As}$ barriers
P-type Absorption per $10^{18} \text{ cm}^{-3}$ doping ( $\text{cm}^{-1}$ )	20	6 - 10
Thermal Conductivity ( $\text{W}/(\text{cm}\cdot^{\circ}\text{C})$ )	0.877 (InP) < 0.1 (GaInAsP)	0.9 (AlAs) 0.45 (GaAs) $\approx 0.1$ (AlGaAs)
Auger Recombination Coefficient ( $\text{cm}^6/\text{s}$ )	$3\text{-}5 \times 10^{-29}$	$\approx 3 \times 10^{-30}$
Conduction Band Barrier (meV)	93	275

With the use of visible (AlGaInP-based) lasers, I can now introduce one important idea that will be shown later in this dissertation. In terms of temperature sensitivity as defined by a characteristic temperature, one sees that 1.55  $\mu\text{m}$  lasers lag far behind 0.98  $\mu\text{m}$  lasers ( $\leq 70 \text{ K}$  vs.  $\geq 200 \text{ K}$ ). Many have proposed either Auger recombination [64-72] or carrier overflow [73-80] as the main cause for this discrepancy. Looking at 0.67  $\mu\text{m}$  lasers -- where the Auger recombination should be low due to its wide band gap -- similar problems related to the characteristic temperature are seen as in the case of 1.55  $\mu\text{m}$  lasers. This is attributed to the low level of electron confinement in these lasers and this

problem gets worse as the wavelength is reduced further. One of the key advances in this field was the use of multiple quantum well barriers (MQBs) to better confine electrons. When MQBs are employed, one sees that the characteristic temperatures are in the range of 140-160 K[81-85]. This has important implications for 1.55  $\mu\text{m}$  which will be explored in Chapters 3 and 4. The results of AlGaInP-based lasers show that the Auger recombination difference between GaAs-based and InP-based lasers cannot explain all of the difference in temperature sensitivity. As will be shown in Section 3.4, carrier overflow also has a dramatic effect.

#### 1.4 Dissertation Overview

This dissertation on the improved temperature performance of 1.55  $\mu\text{m}$  lasers is organized as follows. Chapter 2 lays the groundwork for a theoretical analysis of semiconductor lasers. The method employed here, which uses theoretical gain curves and experimental measurements of carrier-induced loss, is explained in detail. Chapter 3 presents my results on the modeling of 1.55  $\mu\text{m}$  edge-emitting lasers. The main result from this analysis is that both Auger recombination and carrier-induced effects are responsible for the reduced temperature performance of 1.55  $\mu\text{m}$  lasers. Since Auger recombination is inherent at this wavelength, carrier-induced effects provide the most direct means of improving device performance. This is investigated in chapter 4 where the various ways researchers in 1.55  $\mu\text{m}$  lasers have tried to improve device performance are examined. In the methods tried to date, improvements in the carrier confinement for 1.55  $\mu\text{m}$  lasers are limited. This is due to GaInAsP/InP material system where improved carrier confinement leads to reduced optical confinement. To break these limitations, I propose the use of  $\text{Al}_x\text{Ga}_{1-x}\text{As}$  for the cladding layers of the device since, for  $x > 0.45$ , the index is lower than InP. The net result is that laser structures can be designed where the carrier confinement is *improved by  $\approx 5 kT$  without a significant loss of optical*

*confinement*. The structures that achieve this result – the single-fused and double-fused laser – are proposed and theoretically modeled. Chapter 5 is concerned with the creation of 1.55  $\mu\text{m}$  in-plane lasers using wafer-fused cladding layers. Following this, Chapter 6 presents experimental data on these novel 1.55  $\mu\text{m}$  in-plane lasers. What I show is that  $T_0$  values comparable to 1.55  $\mu\text{m}$  lasers with InP cladding layers have been achieved. The major improvement seen with these novel laser structures is that a regime of constant slope efficiency exists as the temperature increases. This behavior is not seen in typical 1.55  $\mu\text{m}$  lasers and resembles the performance of GaAs-based lasers. Finally, in Chapter 7, I will summarize the major findings of this work and point to areas where improvements need to be made for these devices to improve further.

## 1.5 References

- [1] A. Yariv, *Optical Electronics*, Fourth ed. (Saunders College Publishing, San Francisco, 1991). See Chapter 6.
- [2] J. Hecht, *Understanding Lasers: An Entry-Level Guide*, First ed. (IEEE Press, New York, 1991).
- [3] B. J. Thibeault, E. R. Hegblom, P. D. Floyd, R. Naone, Y. Akulova, and L. A. Coldren, "Reduced optical scattering loss in vertical-cavity lasers using a thin (300 Å) oxide aperture", *IEEE Photonics Technology Letters* **8**, 593 (1996).
- [4] D. L. Huffaker, L. A. Graham, H. Deng, and D. G. Deppe, "Sub-40  $\mu$  A continuous-wave lasing in an oxidized vertical-cavity surface-emitting laser with dielectric mirrors", *IEEE Photonics Technology Letters* **8**, 974 (1996).
- [5] C. Yong, P. D. Dapkus, M. H. MacDougal, and Y. Gye Mo, "Lasing characteristics of high-performance narrow-stripe InGaAs-GaAs quantum-well lasers confined by AlAs native oxide", *IEEE Photonics Technology Letters* **8**, 176 (1996).
- [6] G. M. Yang, M. H. MacDougal, and P. D. Dapkus, "Ultralow threshold current vertical-cavity surface-emitting lasers obtained with selective oxidation", *Electronics Letters* **31**, 886 (1995).
- [7] K. D. Choquette, K. L. Lear, R. P. Schneider, and K. M. Geib, "Cavity characteristics of selectively oxidized vertical-cavity lasers", *Applied Physics Letters* **66**, 3413 (1995).
- [8] G. P. Agrawal, *Fiber-optic communication systems* (Wiley, New York, 1992).
- [9] A. Jones, *Historical Sketch of the Electrical Telegraph* (Putnam, New York, 1852).
- [10] A. G. Bell, USA Patent # 174,465 (1876).
- [11] W. K. Pratt, *Laser Communication Systems* (Wiley, New York, 1969).
- [12] G. P. Agrawal, N. K. Dutta, and G. P. Agrawal, *Semiconductor lasers*, 2nd ed ed. (Van Nostrand Reinhold, New York, 1993).
- [13] H. C. Casey and M. B. Panish, *Heterostructure lasers* (Academic Press, New York, 1978).

- [14] R. Dupuis, "An introduction to the development of the semiconductor laser" *IEEE Journal of Quantum Electronics* **QE-23**, 651 (1987).
- [15] J. von Neumann, "Notes on the photon-disequilibrium-amplification scheme (JvN), September 16, 1953" *IEEE Journal of Quantum Electronics* **QE-23**, 659 (1987).
- [16] J. P. Gordon, H. J. Zeiger, and C. H. Townes, "Molecular microwave oscillator and new hyperfine structure in the microwave spectrum on  $\text{NH}_3$ ", *Physical Review* **95**, 282 (1954).
- [17] M. G. A. Bernard and G. Duraffourg, "Possibilities de lasers a semi-conducteurs" *Journal de Physique* **22**, 836 (1961).
- [18] M. G. A. Bernard and G. Duraffourg, "Laser Conditions in Semiconductors", *Physica Status Solidi* **1**, 699 (1961).
- [19] R. N. Hall, G. E. Fenner, J. D. Kingsley, T. J. Soltys, and R. O. Carlson, "Coherent Light Emission from GaAs junctions", *Physical Review Letters* **9**, 366 (1962). Nov. 1 issue (recieved Sept. 24)
- [20] M. I. Nathan, W. P. Dunke, G. Burns, J. F.H. Dill, and G. Lasher, "Stimulated Emission of Radiation from GaAs p-n Junctions", *Applied Physics Letters* **1**, 62 (1962). Nov. 1 issue (recieved Oct. 6)
- [21] T. M. Quist, H. R. R, R. J. Keyes, W. E. Krag, B. Lax, A. L. McWhorter, and H. J. Zeiger, "Semiconductor MASER of GaAs", *Applied Physics Letters* **1**, 91 (1962). Dec. 1 issue (recieved Oct. 23)
- [22] J. N. Holonyak and S. F. Bevacqua, "Coherent (visible) light emission from  $\text{Ga}(\text{As}_{1-x}\text{P}_x)$  junctions", *Applied Physics Letters* **1**, 82 (1962). Dec. 15 issue (recieved Oct. 17)
- [23] I. Hayashi, M. B. Panish, P. W. Foy, and S. Sumski, "Junction lasers which operate continuously at room temperature", *Applied Physics Letters* **17**, 109 (1970).
- [24] Z. I. Alferov, V. M. Andreev, D. Z. Garbuzov, Y. V. Zhilyaev, E. P. Morozov, E. L. Portnoi, and V. G. Trofim, "Investigation of the influence of the AlAs-GaAs heterostructure parameters on the laser threshold current and realization of continuous emission at room temperature", *Fizika i Tekhnika Poluprovodnikov* **4**, 1826 (1970).
- [25] E. A. Rezek, N. Holonyak, Jr., B. A. Vojak, G. E. Stillman, J. A. Rossi, D. L. Keune, and J. D. Fairing, "Liquid phase epitaxial InGaPAs multilayered heterojunction lasers exhibiting quantum size effects", *Device Research Conference 1976*, Ithaca, NY, USA, 1976, 1204.
- [26] N. Holonyak, Jr., R. M. Kolbas, W. D. Laidig, B. A. Vojak, R. D. Dupuis, and P. D. Dapkus, "Low-threshold continuous laser operation (300-

- 337K) of multilayer MOCVD  $\text{Al}_x\text{Ga}_{1-x}\text{As-GaAs}$  quantum-well heterostructures" *Applied Physics Letters* **33**, 737 (1978).
- [27] R. D. Dupuis, P. D. Dapkus, R. M. Kolbas, N. Holonyak, Jr., and H. Shichijo, "Photopumped laser operation of MOCVD  $\text{Al}_x\text{Ga}_{1-x}\text{As}$  near a GaAs quantum well ( $\lambda \approx 6200 \text{ \AA}$ , 77K)" *Applied Physics Letters* **33**, 596 (1978).
- [28] N. Holonyak, Jr., R. M. Kolbas, R. D. Dupuis, and P. D. Dapkus, "Room-temperature continuous operation of photopumped MOCVD  $\text{Al}_x\text{Ga}_{1-x}\text{As-GaAs-Al}_x\text{Ga}_{1-x}\text{As}$  quantum-well lasers" *Applied Physics Letters* **33**, 73 (1978).
- [29] R. D. Dupuis, P. D. Dapkus, N. Holonyak, Jr., E. A. Rezek, and R. Chin, "Room-temperature laser operation of quantum-well  $\text{Ga}_{1-x}\text{Al}_x\text{As-GaAs}$  laser diodes grown by metal-organic chemical vapour deposition" *Applied Physics Letters* **32**, 295 (1978).
- [30] W. D. Laidig, P. J. Caldwell, Y. F. Lin, and C. K. Peng, "Strained-layer quantum-well injection laser" *Applied Physics Letters* **44**, 653 (1984).
- [31] W. D. Laidig, Y. F. Lin, and P. J. Caldwell, "Properties of  $\text{In}_x\text{Ga}_{1-x}\text{As-GaAs}$  strained-layer quantum-well-heterostructure injection lasers" *Journal of Applied Physics* **57**, 33 (1985).
- [32] D. Feketa, K. T. Chan, J. M. Ballantyne, and L. F. Eastman, "Graded-index separate-confinement  $\text{InGaAs/GaAs}$  strained-layer quantum well laser grown by metalorganic chemical vapor deposition" *Applied Physics Letters* **49**, 1659 (1986).
- [33] Y. J. Yang, K. Y. Hsieh, and R. M. Kolbas, "Continuous room-temperature operation of an  $\text{InGaAs-GaAs-AlGaAs}$  strained-layer quantum well laser", *45th Annual Device Research Conference*, Santa Barbara, CA, USA, 1987, 2379.
- [34] R. W. Kaliski, N. Holonyak, Jr., K. C. Hsieh, D. W. Nam, J. W. Lee, H. Shichijo, R. D. Burnham, J. E. Epler, and H. F. Chung, "Continuous (300 K) photopumped laser operation of  $\text{Al}_x\text{Ga}_{1-x}\text{As-GaAs}$  quantum well heterostructures grown on strained-layer GaAs on Si" *Applied Physics Letters* **50**, 836 (1987).
- [35] S. E. Fischer, D. Fekete, G. B. Feak, and J. M. Ballantyne, "Ridge waveguide injection laser with a  $\text{GaInAs}$  strained-layer quantum well ( $\lambda = 1 \mu\text{m}$ )" *Applied Physics Letters* **50**, 714 (1987).
- [36] E. P. O'Reilly, K. C. Heasman, A. R. Adams, and G. P. Witchlow, "Calculations of the threshold current and temperature sensitivity of a  $(\text{GaIn})\text{As}$  strained quantum well laser operating at  $1.55 \mu\text{m}$ ", *2nd International Conference*



*on Superlattices, Microstructures and Microdevices*, Goteborg, Sweden, 1986, 99.

- [37] A. R. Adams, "Band-structure engineering for low-threshold high-efficiency semiconductor lasers", *Electronics Letters* **22**, 249 (1986).
- [38] E. Yablonovitch and E. O. Kane, "Band structure engineering of semiconductor lasers for optical communications", *Journal of Lightwave Technology* **6**, 1292 (1988).
- [39] E. Yablonovitch and E. O. Kane, "Reduction of lasing threshold current density by the lowering of valence band effective mass", *Journal of Lightwave Technology* **LT-4**, 504 (1986).
- [40] K. C. Kao and G. A. Hockham, "Dielectric-fibre surface waveguides for optical frequencies", *Proceedings of the IEE* **113**, 1151 (1966).
- [41] F. P. Kapron, D. B. Keck, and R. D. Maurer, "Radiation losses in glass optical waveguides", *Applied Physics Letters* , 423 (1970).
- [42] K. Oe, S. Ando, and K. Sugiyama, "1.3  $\mu\text{m}$  CW operation of GaInAsP/InP DH diode lasers at room temperature", *Japanese Journal of Applied Physics* **16**, 1273 (1977).
- [43] T. Miya, Y. Terunuma, T. Hosaka, and T. Miyashita, "Ultra low loss single-mode fibers at 1.55  $\mu\text{m}$ ", *Review of the Electrical Communication Laboratories* **27**, 497 (1979).
- [44] T. Miya, Y. Terunuma, T. Hosaka, and T. Miyashita, "Ultimate low-loss single-mode fibre at 1.55  $\mu\text{m}$ ", *Electronics Letters* **15**, 106 (1979).
- [45] J. B. MacChesney and D. J. DiGiovanni, "Materials development of optical fiber", *Journal of the American Ceramic Society* **73**, 3537 (1990).
- [46] J. A. Jay and E. M. Hopiavuori, "Dispersion-shifted fiber hits its stride", *Photonics Spectra* **24**, 153 (1990).
- [47] R. Baker, "Optical amplification", *Physics World* **3**, 41 (1990).
- [48] P. A. Morton, T. Tanbun-Ek, R. A. Logan, N. Chand, K. W. Wecht, A. M. Sergent, and P. F. Sciortino, Jr., "Packaged 1.55  $\mu\text{m}$  DFB laser with 25 GHz modulation bandwidth", *Electronics Letters* **30**, 2044 (1994).
- [49] K. Morito, R. Sahara, K. Sato, and Y. Kotaki, "Penalty-free 10 Gb/s NRZ transmission over 100 km of standard fiber at 1.55  $\mu\text{m}$  with a blue-chirp modulator integrated DFB laser", *IEEE Photonics Technology Letters* **8**, 431 (1996).
- [50] S. Mohrdiek, H. Burkhard, F. Steinhagen, H. Hillmer, R. Losch, W. Schlapp, and R. Gobel, "10-Gb/s standard fiber transmission using directly modulated 1.55- $\mu\text{m}$  quantum-well DFB lasers", *IEEE Photonics Technology Letters* **7**, 1357 (1995).

- [51] L. V. T. Ngugen, A. J. Lowery, P. C. R. Gurney, and D. Novak, "Spectral study of a 1.55  $\mu\text{m}$  multimode FP semiconductor laser using the transmission-line laser model", *Optical and Quantum Electronics* **27**, 663 (1995).
- [52] M. Kawano, T. Aoyagi, H. Watanabe, T. Takiguchi, Y. Nakajima, A. Takemoto, and R. Hirano, "Extremely low power penalty in 2.5-Gb/s transmission experiment using 1.55- $\mu\text{m}$  MQW-DFB lasers with optimized QW number", *Microwave and Optical Technology Letters* **7**, 150 (1994).
- [53] U. Fischer, "10 Gbit/s transmission over 69 km of non-dispersion-shifted singlemode fibre with CPFSK direct modulation of 1.55  $\mu\text{m}$  BH DFB laser", *Electronics Letters* **28**, 1305 (1992).
- [54] S. J. Wang, C. Y. Kuo, P. Parayanthal, T. M. Shen, M. P. Melley, and R. L. Hartman, "A 1.7 Gb/s ASK and a 622 Mb/s incoherent FSK transmission experiment using a 1.55- $\mu\text{m}$  multiquantum well distributed feedback laser", *IEEE Photonics Technology Letters* **2**, 920 (1990).
- [55] M. S. Lin, S. J. Wang, C. Y. Kuo, and M. P. Melley, "Nearly dispersion-penalty-free transmission using blue-shifted 1.55- $\mu\text{m}$  distributed feedback lasers", *IEEE Photonics Technology Letters* **2**, 741 (1990).
- [56] K. Sato, Y. Kondo, M. Nakao, and M. Fukuda, "1.55- $\mu\text{m}$  narrow-linewidth and high-power distributed feedback lasers for coherent transmission systems", *Twelfth Conference on Optical Fiber Communications, OFC*, Houston, TX, USA, 1989, 1515.
- [57] K. L. Monham, R. Plastow, A. C. Carter, and R. C. Goodfellow, "1.3 Gbit/s transmission over 107 km of dispersion-shifted monomode fibre using a 1.55  $\mu\text{m}$  multimode laser", *Electronics Letters* **21**, 619 (1985).
- [58] Y. Nakano, Y. Itaya, M. Fukuda, Y. Noguchi, H. Yasaka, and K. Oe, "1.55  $\mu\text{m}$  narrow-linewidth multielectrode DFB laser for coherent FSK transmission", *Electronics Letters* **23**, 826 (1987).
- [59] S. J. Wang, Y. Twu, N. K. Dutta, and R. L. Hartman, "Two-section distributed feedback lasers for incoherent frequency-shift-keying transmission systems", *Electronics Letters* **26**, 1243 (1990).
- [60] M. Suzuki, H. Tanaka, H. Taga, S. Yamamoto, and Y. Matsushima, " $\lambda/4$ -shifted DFB laser/electroabsorption modulator integrated light source for multigigabit transmission", *Journal of Lightwave Technology* **10**, 90 (1992).
- [61] H. Haisch, W. Baumert, C. Hache, E. Kuhn, M. Klenk, K. Satzke, M. Schilling, J. Weber, and E. Zielinski, "10 Gbit/s standard fibre TDM transmission at 1.55  $\mu\text{m}$  with low chirp monolithically integrated MQW electroabsorption modulator/DFB-laser realized by selective area MOVPE", *20th European Conference on Optical Communication Proceedings of ECOC'94*.

20th European Conference on Optical Communications, Firenze, Italy, 1994, 801.

[62] G. C. Wilson, T. H. Wood, J. L. Zyskind, J. W. Sulhoff, S. B. Krasulick, J. E. Johnson, T. Tanbun-Ek, and P. A. Morton, "Analogue transmission at 1.55  $\mu\text{m}$  using linearised electroabsorption modulator/DFB laser and fibre amplifier", *Electronics Letters* **31**, 1934 (1995).

[63] D. M. Adams, C. Rolland, N. Puetz, R. S. Moore, F. R. Shepherd, H. B. Kim, and S. Bradshaw, "Mach-Zehnder modulator integrated with a gain-coupled DFB laser for 10 Gbit/s, 100 km NDSF transmission at 1.55  $\mu\text{m}$ ", *Electronics Letters* **32**, 485 (1996).

[64] A. Haug, "Evidence of the importance of Auger recombination for InGaAsP lasers", *Electronics Letters* **20**, 85 (1984).

[65] A. Haug, "Theory of the temperature dependence of the threshold current of an InGaAsP laser", *IEEE Journal of Quantum Electronics* **QE-21**, 716 (1985).

[66] A. Haug and H. Burkhard, "Temperature dependence of threshold current of  $\text{In}_{1-x}\text{Ga}_x\text{As}_y\text{P}_{1-y}$  lasers with different compositions", *IEEE Proceedings J (Optoelectronics)* **134**, 117 (1987).

[67] M. Asada and Y. Suematsu, "The effects of loss and nonradiative recombination on the temperature dependence of threshold current in 1.5-1.6  $\mu\text{m}$  GaInAsP/InP lasers", *8th IEEE International Semiconductor Laser Conference*, Ottawa, Ont., Canada, 1982, 917.

[68] K. D. Chik, "A theoretical analysis of Auger recombination induced energetic carrier leakage in GaInAsP/InP double heterojunction lasers and light emitting diodes", *Journal of Applied Physics* **63**, 4688 (1988).

[69] N. K. Dutta and R. J. Nelson, "Temperature dependence of threshold of the InGaAsP/InP double-heterostructure lasers and Auger recombination", *Applied Physics Letters* **38**, 407 (1981).

[70] N. K. Dutta and R. J. Nelson, "The case for Auger recombination in  $\text{In}_{1-x}\text{Ga}_x\text{As}_y\text{P}_{1-y}$ ", *Journal of Applied Physics* **53**, 74 (1982).

[71] A. Sugimura, "Auger recombination effect on threshold current of InGaAsP quantum well lasers", *8th IEEE International Semiconductor Laser Conference*, Ottawa, Ont., Canada, 1982, 932.

[72] W. Zhuang, B. Zheng, J. Xu, Y. Li, J. Xu, and P. Chen, "Carrier loss resulting from Auger recombination in InGaAsP/InP double heterojunction laser diodes: spectroscopy of 950 nm high energy emission", *IEEE Journal of Quantum Electronics* **QE-21**, 712 (1985).

- [73] M. Yano, H. Imai, and M. Takusagawa, "Analysis of threshold temperature characteristics for InGaAsP/InP double heterojunction lasers", *Journal of Applied Physics* **52**, 3172 (1981).
- [74] T. R. Chen, B. Chang, L. C. Chiu, K. L. Yu, S. Margalit, and A. Yariv, "Carrier leakage and temperature dependence of InGaAsP lasers", *Applied Physics Letters* **43**, 217 (1983).
- [75] V. Mikhaelashvili, N. Tessler, R. Nagar, G. Eisenstein, A. G. Dentai, S. Chandrasakhar, and C. H. Joyner, "Temperature dependent loss and overflow effects in quantum well lasers", *IEEE Photonics Technology Letters* **6**, 1293 (1994).
- [76] N. Tessler, A. Berenzon, and G. Eisenstein, "Analysis of pump-probe measurements and carrier overflow effects in quantum well optical amplifier", *Proceedings of 1994 Conference on Lasers and Electro-Optics and The International Electronics Conference CLEO/QEC*, Anaheim, CA, USA, 1994, 253.
- [77] N. Tessler, V. Mikhaelashvili, R. Nagar, G. Eisenstein, A. G. Dentai, C. H. Joyner, and S. Chandrasekhar, "Temperature and output power dependence of carrier overflow and internal loss in InGaAs/InGaAsP multiple quantum well lasers", *Proceedings of IEEE 14th International Semiconductor Laser Conference*, Maui, HI, USA, 1994, 67.
- [78] N. Tessler, A. Berenzon, and G. Eisenstein, "Analysis of pump probe measurements and carrier overflow effects in multiple quantum-well optical amplifiers", *IEEE Journal of Quantum Electronics* **30**, 2767 (1994).
- [79] J. Mark, J. Mork, N. Tessler, and G. Einstein, "Barrier dynamics in quantum well amplifiers measured by a broad band femtosecond pump-probe set-up", *Proceedings of 1994 Conference on Lasers and Electro-Optics and The International Electronics Conference CLEO/QEC*, Anaheim, CA, USA, 1994, 253.
- [80] J. Mark, N. Tessler, G. Eisenstein, and J. Mork, "Broadband femtosecond pump-probe setup operating at 1300 and 1550 nm", *Applied Physics Letters* **64**, 1899 (1994).
- [81] P. M. Smowton and P. Blood, "Threshold current temperature dependence of GaInP/(Al<sub>y</sub>Ga<sub>1-y</sub>)InP 670 nm quantum well lasers", *Applied Physics Letters* **67**, 1265 (1995).
- [82] P. M. Smowton and P. Blood, "GaInP-(Al<sub>y</sub>Ga<sub>1-y</sub>)InP 670 nm quantum-well lasers for high-temperature operation", *IEEE Journal of Quantum Electronics* **31**, 2159 (1995).

- [83] P. M. Smowton, H. D. Summers, P. Bees, and P. Blood, "Optimisation of 670 nm strained-quantum-well laser diodes for high-temperature operation", *JEE Proceedings-Optoelectronics* **141**, 136 (1994).
- [84] K. Jong-Seok, Y. Min, C. Won-Jin, C. Ji-Ho, C. In-Seong, C. Won-Taek, and Y. Tae-Kyung, "670 nm AlGaInP/GaInP strained multi-quantum well laser diode with high characteristic temperature ( $T_0$ )", *Optical and Quantum Electronics* **27**, 435 (1995).
- [85] D. P. Bour, D. W. Treat, R. L. Thornton, T. L. Paoli, R. D. Bringans, B. S. Krusor, R. S. Geels, D. F. Welch, and T. Y. Wang, "Low threshold  $\text{Ga}_x\text{In}_{1-x}\text{P}/(\text{Al}_y\text{Ga}_{1-y})_{0.5}\text{In}_{0.5}\text{P}$  strained quantum well lasers", *Journal of Crystal Growth* **124**, 751 (1992).
- [86] D. Z. Garbuzov, I. E. Berishev, Y. V. Ilyin, N. D. Ilyinskaya, A. V. Ovchinnikov, N. A. Pikhtin, and I. S. Tarasov, "High-power buried heterostructure in InGaAsP/InP laser diodes produced by an improved regrowth process", *Journal of Applied Physics* **72**, 319 (1992).
- [87] Y. K. Chen, M. C. Wu, W. S. Hobson, S. J. Pearton, A. M. Sergent, and M. A. Chin, "High-power 980-nm AlGaAs/InGaAs strained quantum-well laser grown by OMVPE", *IEEE Photonics Technology Letters* **3**, 406 (1991).
- [88] T. R. Chen, J. Ungar, J. Iannelli, S. Oh, H. Luong, and N. Bar-Chaim, "High power operation of InGaAsP/InP multiquantum well DFB lasers at 1.55  $\mu\text{m}$  wavelength", *Electronics Letters* **32**, 898 (1996).
- [89] H. Chida, K. Fukagai, T. Miyazaki, and S. Ishikawa, "25-100 degrees C automatic power control free 600 Mbit/s modulation of 0.98  $\mu\text{m}$  InGaAs/AlGaAs laser for high-speed data link", *Electronics Letters* **31**, 2006 (1995).
- [90] H. Nobuhara, K. Tanaka, T. Yamamoto, T. Machida, T. Fujii, and K. Wakao, "High-temperature operation of InGaAs/InGaAsP compressive-strained QW lasers with low threshold currents", *IEEE Photonics Technology Letters* **5**, 961 (1993).
- [91] P. L. Derry, H. E. Hager, K. C. Chiu, D. J. Booher, E. C. Miao, and C. S. Hong, "Low threshold current high-temperature operation of InGaAs/AlGaAs strained-quantum-well lasers", *IEEE Photonics Technology Letters* **4**, 1189 (1992).
- [92] H. Temkin, D. Coblenz, R. A. Logan, J. P. van der Ziel, T. Tanbun-Ek, R. D. Yadvish, and A. M. Sergent, "High temperature characteristics of InGaAsP/InP laser structures", *Applied Physics Letters* **62**, 2402 (1993).
- [93] P. J. A. Thijs, L. F. Tiemeijer, P. I. Kuindersma, J. J. M. Binsma, and T. Van Dongen, "High-performance 1.5  $\mu\text{m}$  wavelength InGaAs-InGaAsP strained

quantum well lasers and amplifiers" *IEEE Journal of Quantum Electronics* **27**, 1426 (1991).

[94] H. Lang, H. D. Wolf, L. Korte, H. Hedrich, C. Hoyler, and C. Thanner, "GaAs/AlGaAs quantum well laser for high-speed applications" *IEEE Proceedings J (Optoelectronics)* **138**, 117 (1991).

[95] P. A. Morton, R. A. Logan, T. Tanbun-Ek, P. F. Sciortino, Jr., A. M. Sergent, R. K. Montgomery, and B. T. Lee, "25 GHz bandwidth 1.55  $\mu\text{m}$  GaInAsP p-doped strained multiquantum-well lasers" *Electronics Letters* **28**, 2156 (1992).

[96] S. Weisser, E. C. Larkins, K. Czotscher, W. Benz, J. Daleiden, I. Esquivias, J. Fleissner, J. D. Ralston, B. Romero, R. E. Sah, A. Schonfelder, and J. Rosenzweig, "Damping-limited modulation bandwidths up to 40 GHz in undoped short-cavity In/sub 0.35/Ga/sub 0.65/As-GaAs multiple-quantum-well lasers" *IEEE Photonics Technology Letters* **8**, 608 (1996).

## **2. Modeling In-Plane Semiconductor Lasers: Approach**

A lot of work in the area of 1.55  $\mu\text{m}$  in-plane lasers has been directed at understanding how the properties of the materials used (GaInAs(P) quantum wells, barriers, and separate confinement heterostructure (SCH) regions) translate into device performance. As shown in Section 1.3, there are some striking differences between the materials structures used for 1.55  $\mu\text{m}$  in-plane lasers and their short infra-red (GaAs-based) and visible (AlGaInP-based) counterparts; in addition, the resulting device performance is different. In this Chapter I will build up a foundation for modeling the static performance of 1.55  $\mu\text{m}$  Fabry Perot lasers. Fabry Perot lasers are used due to the much simpler modeling procedure that is required when the temperature is changed as compared to more complicated distributed feedback (DFB) lasers which are more widely used in fiber-optic communication systems. First, a baseline 1.55  $\mu\text{m}$  laser structure is introduced as well as factors that are important in understanding its performance. After this, my modeling approach is then described in general terms. Three important aspects of this model are described in greater detail: the generation of GaInAsP quantum well gain curves, how the effects of carrier occupation in the barrier and SCH regions affect the operation of 1.55  $\mu\text{m}$  in-plane lasers, and how heating effects are included. Finally, I conclude by looking at three of the current methods used to characterize the temperature dependence of 1.55  $\mu\text{m}$  lasers.

### **2.1 Introduction to 1.55 $\mu\text{m}$ Lasers: Design Aspects and General Features**

For any modeling algorithm of 1.55  $\mu\text{m}$  lasers, a device structure needs to be defined. The general device structure used in the calculations of Chapter 3 is

shown below in Figure 2-1. Here, the standard 1.55  $\mu\text{m}$  laser structure used by most researchers in the field is chosen; the structure consists of n-InP and p-InP cladding layers surrounding a GaInAsP active region. In the case of the calculations in chapter 3, I use 1% compressively strained 7 nm GaInAsP quantum wells with 10 nm GaInAsP barriers with a bandgap of 1.25  $\mu\text{m}$ . This well thickness is such that the emission wavelength is 1.55  $\mu\text{m}$  at 20°C. The composition of these layers is  $\text{Ga}_{0.2}\text{In}_{0.8}\text{As}_{0.75}\text{P}_{0.25}$  for the quantum well and  $\text{Ga}_{0.231}\text{In}_{0.769}\text{As}_{0.502}\text{P}_{0.498}$  for the barrier.

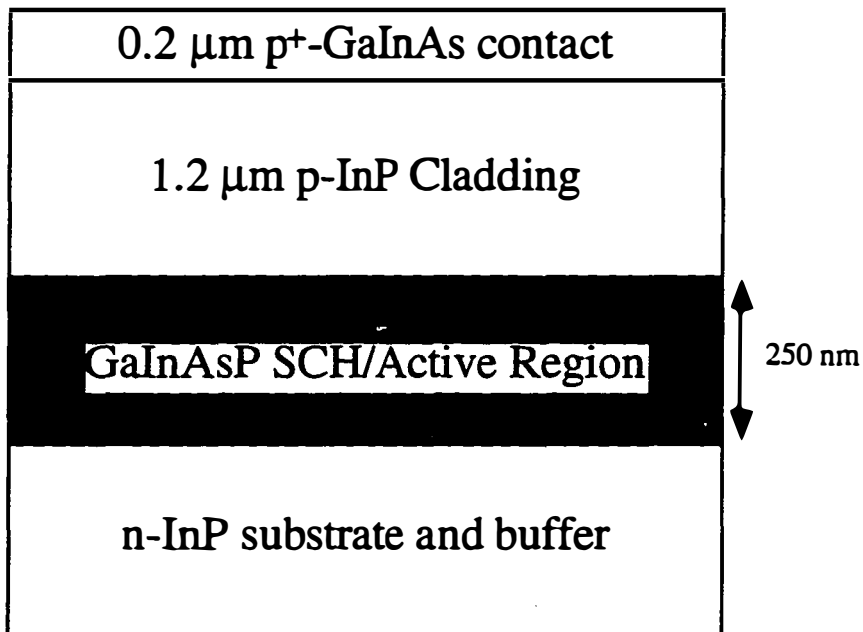


**Figure 2-1** General 1.55  $\mu\text{m}$  laser structure used in the calculation results presented in Chapter 3.

Separate confinement heterostructure (SCH) layers of  $\text{Ga}_{0.176}\text{In}_{0.824}\text{As}_{0.368}\text{P}_{0.632}$  (bandgap of 1.15  $\mu\text{m}$ ) are used on each side of the quantum wells to improve optical confinement. The total waveguide width is 250 nm. In this structure, the



conduction band offset is approximately 93 meV at room temperature while the valence band offset is approximately 163 meV. Now that the general parameters of the laser structure are defined, I will move onto the adjustable parameters are at the disposal of the crystal grower or device designer. After that, two of the most important effects that affect 1.55  $\mu\text{m}$  laser performance are described in general terms.

### 2.1.1 Design Issues and Definitions

Before making a quantum well laser for a specific application, several factors that affect the resulting device performance need to be addressed. For reference in the following discussion, a pair of gain curves are shown in Figure 2-2.

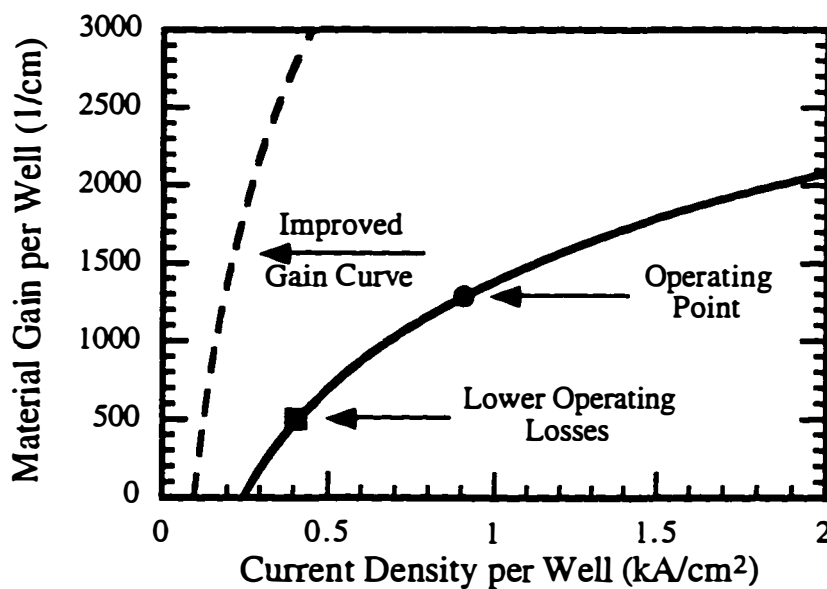


**Figure 2-2** Representative quantum well gain curves for a semiconductor laser.

When one has a gain curve (dark solid curve) as shown in Figure 2-2, the important parameter to be decided is where on this gain curve to operate the device. This can be controlled in three important ways.

### *Change in Cavity Length*

This results in changing the operation point of the device by changing the gain required to reach threshold (i.e., moving from the circle to the square in Figure 2-2). If one increases the cavity length only, the threshold current tends to increase because the gain curve is sub-linear and a decrease in the required gain by this means generally means an increase in threshold current. So, for continuous-wave (CW) operation of a laser, cavity lengths of 500  $\mu\text{m}$  or less are typically used with as low a length as possible being the norm. In order to reduce the mirror losses of the laser, while maintaining a low  $I_{\text{th}}$ , high reflection (HR) coatings can be applied to one or both laser facets.

### *Composition of quantum wells used in active region*

In current semiconductor lasers, quantum wells are the active region of choice for high performance devices. The size, on the order of 10 nm, allows for quantum mechanical effects which improve the device. These effects include a reduction in the band edge density-of-states and a lifting of the heavy-hole/light-hole degeneracy in the valence band. In addition, the quantum well can be designed in order to give better characteristics. Biaxial strain in the quantum wells has been shown to improve device performance both theoretically [1-5] and experimentally [6-12]. Strain can be used to change the gain curve from the solid to dashed curve as shown in Figure 2-2. The net result of this change is that the current needed to achieve a particular amount of gain is lower. This improvement is mainly attributed to three things: a reduction of the in-plane effective mass in the valence band, an further increase in the splitting of the degeneracy between the heavy hole and light hole bands beyond that

provided by quantization, and a reduction of Auger currents and intervalence band absorption. In this section, 1% compressively strained GaInAsP quantum wells are used to take advantage of all of these factors.

### *The number of quantum wells*

Increasing the number of wells in the active region is an attractive approach since (i) the length of the cavity is not changed (low  $L_m$ ) and (ii) the operation point on the gain curve is reduced since each quantum well needs to provide less gain. The main problem with this approach -- especially using strained quantum wells -- is that there is a practical limit to how many quantum wells can be used<sup>1</sup> (in terms of a critical thickness [15,16]). Furthermore, there is evidence in the literature that uniform pumping of the active region becomes a bad assumption if the number of quantum wells is made too large [17-22].

#### *2.1.2 Auger Recombination and 1.55 $\mu\text{m}$ Lasers*

In semiconductor lasers, large injected carrier densities ( $\geq 10^{18} \text{ cm}^{-3}$ ) are needed to obtain lasing. However, with this many carriers in the active region, coulomb interactions between electrons in the conduction band and holes in the valence bands may cause recombination to occur without the production of a photon. This type of recombination is known as Auger recombination which is known to be a major concern in narrow-band gap semiconductors. Auger recombination can be broken into two classes: band-to-band Auger processes and phonon-assisted Auger processes. In evaluating the magnitude of these Auger processes, energy and momentum conservation is needed between all carriers involved. In the case of band-to-band processes, a minimum activation energy exists; for the phonon-assisted processes, there is no minimum energy needed to

---

<sup>1</sup> With strain compensation[13,14], this limit can be further increased.

initiate this processes due to the inclusion of a phonon in the conservation equations. However, in the narrow-band gaps used in 1.55  $\mu\text{m}$  laser structures, the band-to-band Auger processes dominate and will be the only Auger recombination considered here. For 1.55  $\mu\text{m}$  lasers, the CCCH and CHHS Auger processes<sup>ii</sup> dominate and are depicted schematically in Figure 2-3. In the CCCH process, an electron in the conduction band (state 1) recombines with a hole in the valence band (state 2). For energy and momentum conservation, another electron is kicked into a higher state in the conduction band (states 3 and 4); this electron then cools down to the bottom of the band via optical phonons. This Auger process involves two conduction band electrons and a valence band hole and varies with the carrier density as  $n^2p$ . In addition, this Auger recombination has an exponential temperature dependence with an activation energy given by

$$E_a = \frac{m_4 E_g}{2m_1 + m_2 - m_4} \quad (2-1)$$

where the numerical subscripts refer to the states in Figure 2-3. The CHHS process involves the same initial recombination as the CCCH process: an electron from the conduction band recombines with a hole in the valence band (states 1 and 2).

---

<sup>ii</sup> The CHHL processes is not considered here. I expect it to be low due to the use of compressive strain in the quantum well active region which has been seen by others.

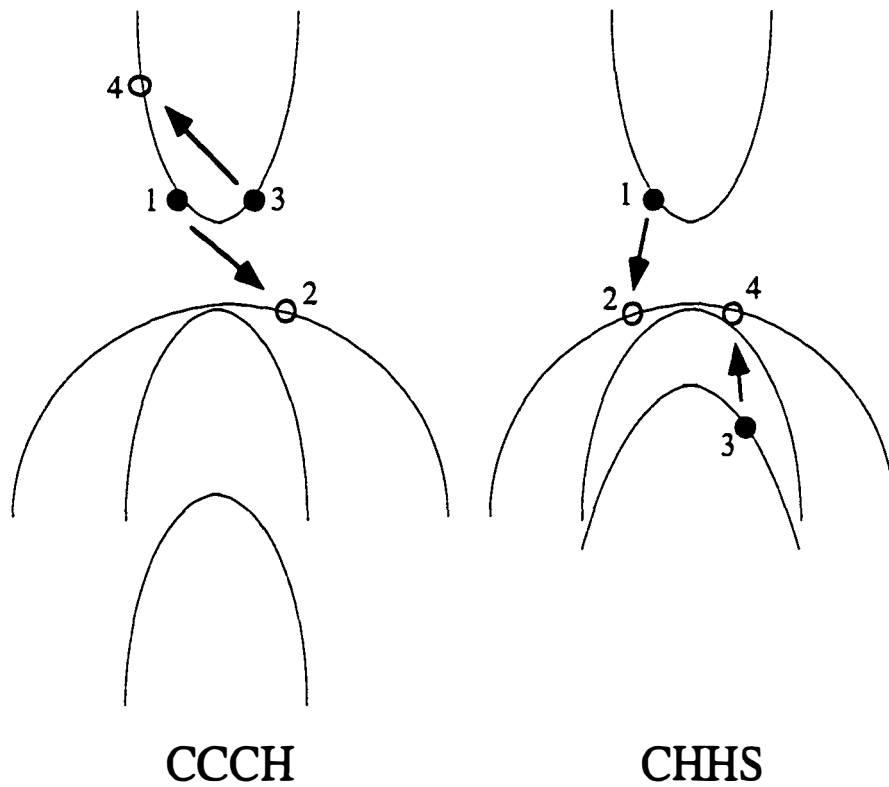


**Figure 2-3** The two dominant band-to-band Auger processes for 1.55  $\mu\text{m}$  lasers.

For energy and momentum conservation, the CHHS process has an electron from the split-off band (state 3) recombine with a hole in the valence band (state 4). Since two hole states are involved in the CHHS process, this Auger process varies with carrier density as  $np^2$  and also has an exponential temperature dependence with an activation energy of

$$E_a = \frac{m_3(E_g - \Delta) + m_1\Delta}{2m_2 + m_1 - m_3} \quad (2-2)$$

Due to the material properties of InP-based alloys and the fact that  $n^2p = np^2$  due to the dominance of injected carriers<sup>iii</sup>, the CHHS process is dominant in 1.55  $\mu\text{m}$  lasers.

One of the benefits of using biaxial strain in the quantum wells of semiconductor lasers was the prediction of a reduction of Auger recombination due to structural changes in the valence band [1,3]. Although this has been predicted, experimental results are inconclusive as to the amount of the reduction of Auger currents [23-27]. However, one thing is clear: besides some theoretical results [28-30], no one has experimentally measured a complete elimination of Auger or a reduction to the levels of GaAs-based lasers ( $\approx 3 \times 10^{-30} \text{ cm}^6/\text{s}$ ). So, in the area of 1.55  $\mu\text{m}$  lasers, Auger current is important. It is generally accepted that the Auger current has a cubic dependence on the injected carriers given by

$$J_{AUG} = eLC_{po} \exp\left(-\frac{E_a}{kT}\right) np^2 \quad (2-3)$$

### 2.1.3 Carrier Overflow and Device Performance

In this section, the effect that carrier overflow on device performance is illustrated. What is meant by carrier overflow here is the occupation of barrier

---

<sup>iii</sup> Also, the CCHS is dominant in 1.55  $\mu\text{m}$  lasers due to the use of p-doping to improve performance.

and SCH regions in the laser by a significant number of electrons<sup>iv</sup>. One important type of carrier overflow – carrier leakage out of the active region -- is not included here<sup>v</sup>.

The complete elimination of these carrier-induced effects leads, theoretically, to improved device performance in a number of areas. These areas are addressed in the next section.

### *1. Improved Gain Curve Characteristics*

It is known from solid-state physics that the density of states for a 2D system (a quantum well) is smaller than a 3D system[31]. As a result, for the same change in carrier density, one would expect the quasi-Fermi level in a 2D system to go farther in the bands. Thus, for the same carrier density change, more gain is available. In addition, the current that these overflow carriers provided to the total threshold current is now eliminated and less current is needed to get the same gain. Thus, the gain curve is improved and this is shown in Figure 2-4 at 20°C and 100°C.

---

<sup>iv</sup> Both electrons and holes actually overflow into the barrier and waveguide regions. Because of the low conduction band offsets for 1.55  $\mu\text{m}$  lasers, it is the electron overflow that is dominant.

<sup>v</sup> This issue is taken up in Chapter 4.

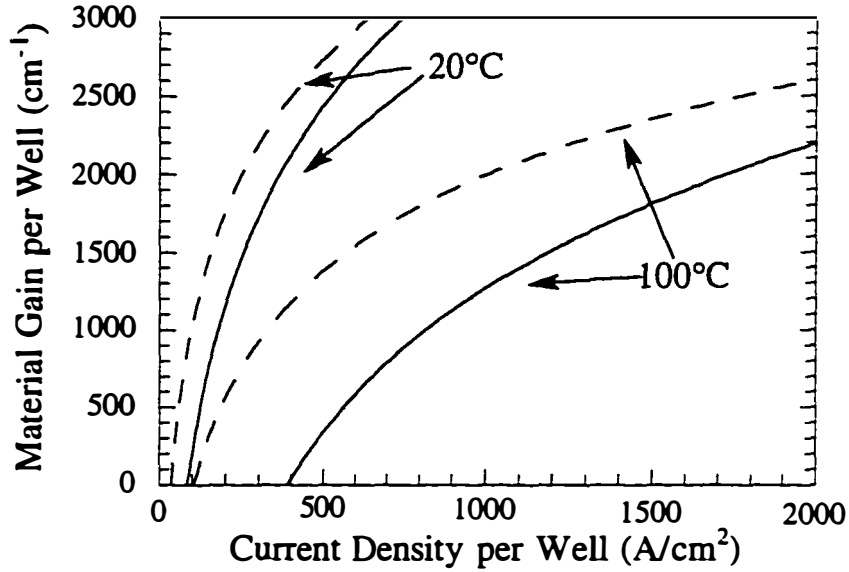


**Figure 2-4** Material gain versus current density curves for a 3 quantum well 1.55  $\mu\text{m}$  lasers with (—) and without (----) carrier overflow into the barrier and SCH regions at 20°C and 100°C. The reason for the crossover of the gain curves is explained in Appendix A.

## 2. Reduced Losses

Elimination of overflow carriers will also result in lower losses for the laser. From Equation (2-19), the losses of the device are now given by

$$\alpha_T = \alpha_i^o + \alpha_m + \Gamma_w \sigma_{IVBA}^{2D} n_{QW} N'_{QW} \quad (2-4)$$



Comparing equations ( 2-4) and (2-19) leads to a reduction in loss of

$$\Delta\alpha = \left( \sigma_{FCA}^{3D} + \sigma_{IVBA}^{3D} \right) \left( \left[ n_{QW} + 1 \right] \Gamma_B N'_{QW} + \Gamma_S N'_{SCH} \right) \quad (2-5)$$

This reduction in internal losses – coupled with improved gain curves at higher temperatures -- leads to a marked improvement in threshold current. This change in loss makes the required gain to achieve threshold lower when carrier overflow is eliminated.

### 3. Improved Modulation Characteristics

If all the carriers injected into the device go into the quantum wells, the quasi-Fermi level would be able to move much farther into the bands as the carrier density changes. This leads to an increase in differential gain. Modeling of the gain curves shows an expected increase in differential gain at  $1000 \text{ cm}^{-1}$  of gain per well from  $4$  to  $8 \times 10^{-16} \text{ cm}^2$ .

Another improvement that should occur with the elimination of carrier overflow is a reduction in the frequency chirp. The amount of chirp is given by (for large signal modulation)<sup>vi</sup>

$$\Delta\nu = \frac{\alpha_l}{4\pi} \left( \frac{1}{P_o} \frac{\partial P_o}{\partial t} \right)_{\max} \quad (2-6)$$

where  $\alpha_l$  is the linewidth enhancement factor which is given by

---

<sup>vi</sup> This simplified expression is for the condition that the output power varies rapidly (order of nanoseconds). See Reference [32] for an explanation

$$\alpha_l = -\frac{4\pi}{\lambda_o} \left( \frac{\partial n_g / \partial N}{\partial g / \partial N} \right) \quad (2-7)$$

There are two reasons that frequency chirp will decrease with an elimination of carrier overflow. First, the differential gain of the laser will increase; this alone will decrease  $\alpha_l$ . Second, changes in the group index of the lasing mode,  $n_g$ , with injected carriers will be less because -- even as more carriers are put in the quantum well -- the small overlap of the lasing mode with the quantum wells retards group index changes.

## 2.2 General Modeling Approach

In order to accurately model the static performance of 1.55  $\mu\text{m}$  lasers (or any semiconductor lasers for that matter), several elements are needed. In this section I introduce my approach of modeling the static characteristics of 1.55  $\mu\text{m}$  lasers. Figure 2-5 show the approach in flowchart form. The modeling method goes as follows. After the device structure has been defined, several important parameters are now known: the optical confinement factor, the gain curves for the active region, and the dimensions of the device. Given an operating temperature for the laser, the internal losses and the operating point on the gain curve can be determined. Using well known laser equations, the threshold current and the L-I curve (not including heating effects) can be determined.

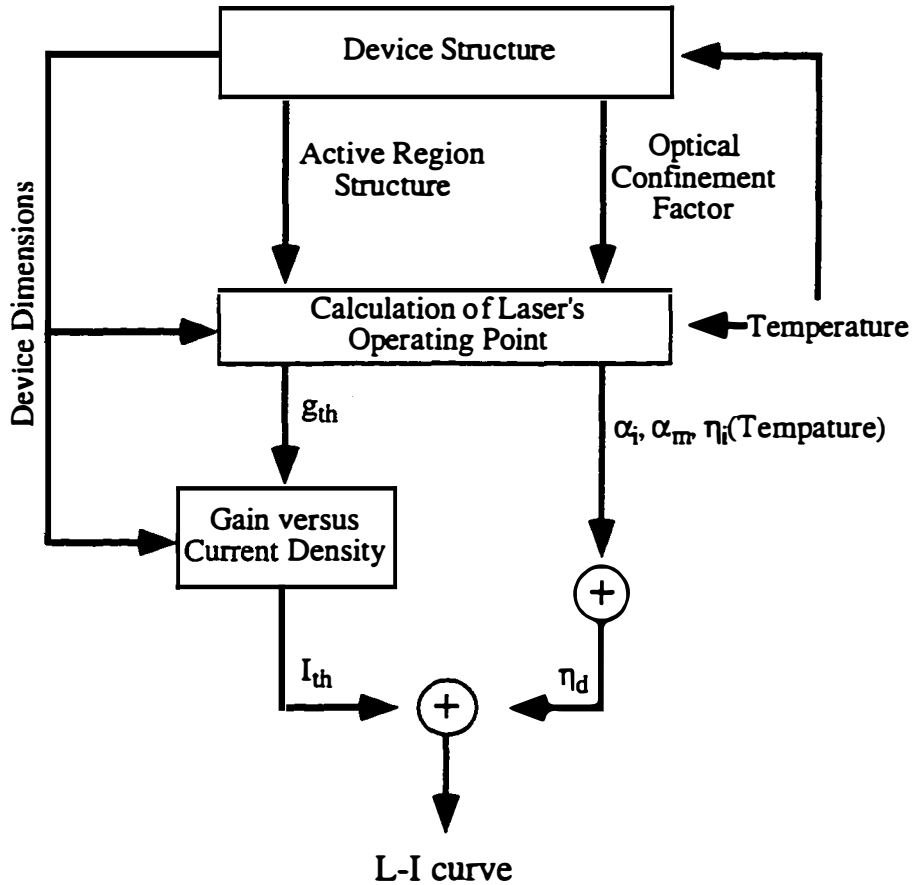


**Figure 2-5** Flow chart of procedure used to model the static characteristics of 1.55  $\mu\text{m}$  lasers. Note that the heating part of the model is not included here. See Section 2.2.3 for more information.

The next three sections are concerned with the most important parts of the calculation method used to obtain static laser characteristics: modeling of the GaInAsP quantum well gain curves, the determination of the operating point of the laser with the effect of carrier occupation in the barrier and SCH regions (i.e., carrier overflow or state-filling) included, and how device heating effects are included in the modeling algorithm.

### 2.2.1 Gain Curves of GaInAsP Quantum Wells for 1.55 $\mu\text{m}$ Emission

In order for a laser to operate, optical gain provided by the active region must overcome any losses (mirror as well as internal) that exist in the cavity. This section is concerned with looking at the theoretical GaInAsP quantum well gain curves used in this chapter – which are an extension of the work done by Scott Corzine in the Ga(In)As/(Al)GaAs system [5,33,34]. Here, I will only present relevant results; those interested in more details about these calculations are encouraged to read Appendix A. In all cases for this chapter the nominal room temperature Auger coefficient is  $5 \times 10^{-29} \text{ cm}^6/\text{s}$  with an activation energy of 60 meV. Figure 2-6 shows the calculation of the gain curve of a 7 nm 1% compressively strained GaInAsP quantum well at both 20°C and 100°C as a function of injected sheet carrier density. A couple of comments about these gain curve are in order here. First, notice that the gain curve changes as a function of temperature. This is due to two effects. The first is the increased occupation of barrier and SCH regions due to Fermi-function broadening alone. The Fermi function is given by

$$f(E) = \left[ 1 + \exp\left\{ \frac{(E - E_f)}{kT} \right\} \right]^{-1} \quad (2-8)$$

Note that the exponential dependence in the denominator make it such that the Fermi function alone has a very minor effect.

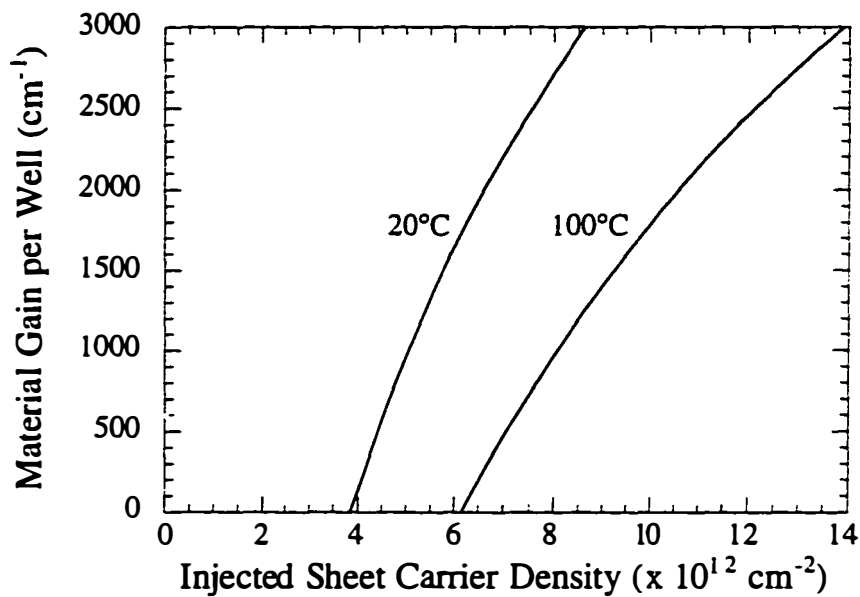
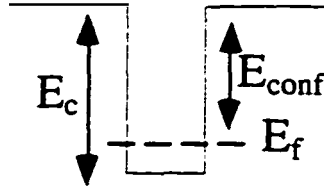


**Figure 2-6** Gain curve of GaInAsP quantum well at  $1.55 \mu\text{m}$  as a function of total injected sheet carrier density at  $20^\circ\text{C}$  and  $100^\circ\text{C}$ .

The main effect that causes a change in the gain curve as a function of temperature is the requirement that the quasi-Fermi levels must be pushed farther into each band in order to get to the required gain for lasing. Figure 2-7 show a schematic of the quantum well structure along with the requirements for various levels of optical gain. Note that the Fermi level changes by only a few meV as the temperature changes from  $20^\circ\text{C}$  to  $100^\circ\text{C}$ . In order to explain the gain curves of Figure 2-6, there are two important points to be made about the data in Figure 2-7.



Gain per QW @ 20°C	0 cm <sup>-1</sup>	300 cm <sup>-1</sup>	1000 cm <sup>-1</sup>
$E_{fc}$	59.7 meV	62.5 meV	70.8 meV
$E_{conf}$ in Conduction Band (meV)	23.3 meV	20.6 meV	12.3 meV
Electrons in QW (x 10 <sup>18</sup> cm <sup>-3</sup> )	0.9	0.96	1.15
Electrons in Barrier (x 10 <sup>18</sup> cm <sup>-3</sup> )	1.4	1.4	1.9
$E_{fv}$	2.4 meV	5.9 meV	13.9 meV

Gain per QW @ 100°C	0 cm <sup>-1</sup>	300 cm <sup>-1</sup>	1000 cm <sup>-1</sup>
$E_{fc}$	66 meV	68.8 meV	76 meV
$E_{conf}$ in Conduction Band (meV)	16.9 meV	14.1 meV	6.9 meV
Electrons in QW (x 10 <sup>18</sup> cm <sup>-3</sup> )	1.17	1.22	1.39
Electrons in Barrier (x 10 <sup>18</sup> cm <sup>-3</sup> )	2.85	3.17	3.8
$E_{fv}$	2.1 meV	4.5 meV	11.1 meV

**Figure 2-7** Effective confinement and carrier occupation values for a 7 nm 1% compressively strained GaInAsP quantum well with 10 nm GaInAsP barriers at 20°C and 100°C.

First, the effective confinement (which is the difference between the conduction band barrier for the quantum well and the electron's quasi-Fermi level) changes quite a bit for the temperature change. In the case of transparency (gain = 0 cm<sup>-1</sup>),  $E_{conf}$  is reduced by about 27%; for a gain of 1000 cm<sup>-1</sup>, the reduction is about 44%. Second, as the number of electrons needed in the quantum well to provide

the gain increases ( $1.15$  to  $1.39 \times 10^{18} \text{ cm}^{-3}$  for a gain of  $1000 \text{ cm}^{-1}$ ), there is a large corresponding increase in carriers in the barrier region ( $1.9$  to  $3.8 \times 10^{18} \text{ cm}^{-3}$  for a gain of  $1000 \text{ cm}^{-1}$ ). This increase in carriers leads to an increase in current density since the radiative and Auger currents have a square and cubic dependence on carrier density. Figure 2-8 shows the resulting gain curve as a function of current density for the  $7 \text{ nm}$   $1\%$  compressively strained GaInAsP quantum well at  $20^\circ\text{C}$  and  $100^\circ\text{C}$ .

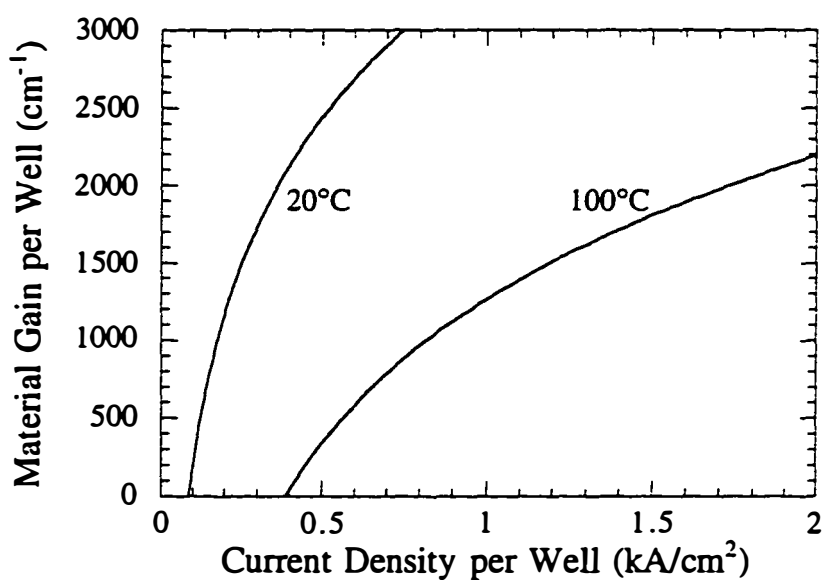


**Figure 2-8** Gain curve of GaInAsP quantum well at  $1.55 \mu\text{m}$  as a function of current density at  $20^\circ\text{C}$  and  $100^\circ\text{C}$ . Here, the current density per well contains both the radiative and Auger components.

Since the carriers in the quantum well and barrier regions changes as a function of temperature, the question that needs to be answered is what other effects -- if any -- do these carriers have. These effects are explored in the next section.

### 2.2.2 Determining the Operating Point of a In-plane Laser

This section is concerned with how the operation point of the laser is determined. The general approach is outlined in flow chart form in Figure 2-9.

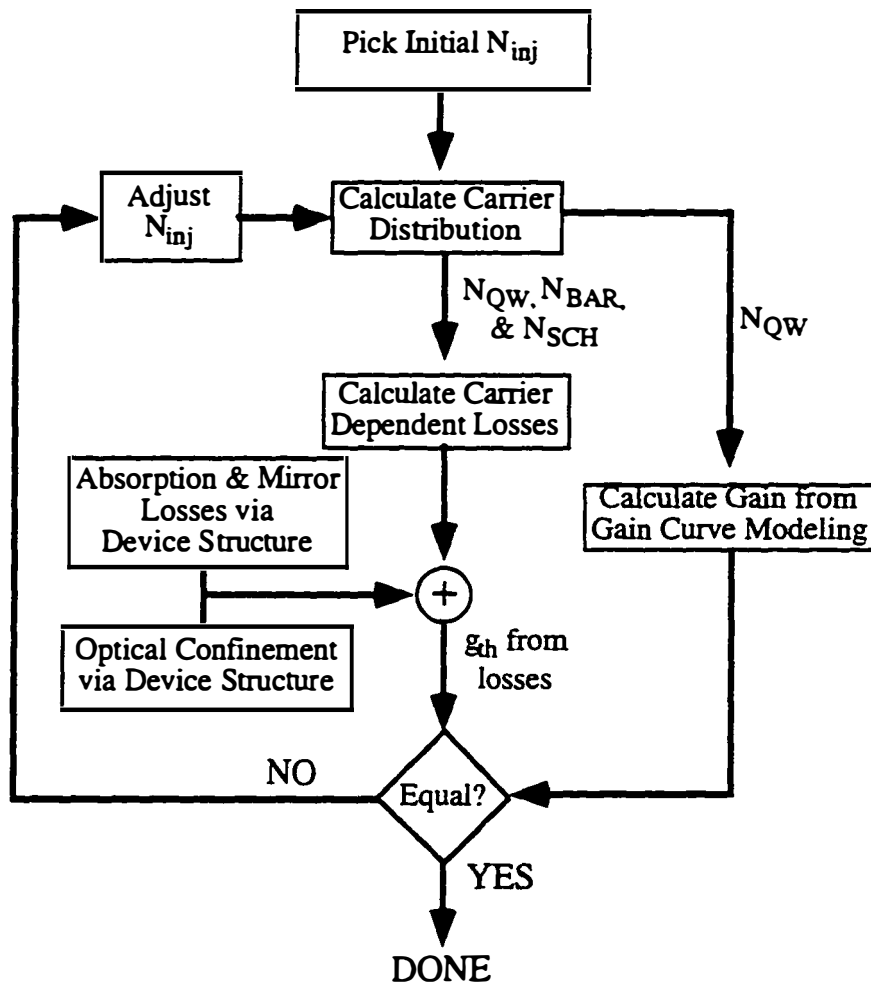


**Figure 2-9** Flow chart of procedure used to calculate the operating point of in-plane semiconductor lasers.



The approach used is as follows. An initial injected carrier density is assumed for the device. It is further assumed that these carriers occupy only the quantum wells, the barrier regions, and the SCH regions of the laser. Using charge neutrality across the active region (see Equations (A-1) and (A-2)), the number of actual carriers in each of the three regions mentioned above is defined. Knowing this, the losses and gain can be calculated. The injected carrier density is adjusted until threshold is reached (i.e., the losses of the laser equal the gain supplied by the quantum well active region). These losses for the laser consist of three parts. The first two parts are the *carrier-independent losses*; this includes the mirror loss due to the laser's cavity length and the absorption, recombination, and scattering losses due to the device's material structure. In addition to being independent of carrier concentration, these two loss mechanisms are also assumed to be temperature independent. The final part of the losses of the laser is due to carrier effects: free carrier absorption and intervalence band absorption. These loss mechanisms – since they are carrier density dependent – are also temperature dependent since the number of carriers in all regions of the device changes as the operating temperature is changed. In equation form, the total losses of the device are shown below:

$$\alpha_T = \alpha_m + \alpha_i^\circ + \alpha_c(N'_{QW}, N'_{BAR}, N'_{SCH}) \quad (2-9)$$

where  $\alpha_m$  is the mirror losses,  $\alpha_i^\circ$  is the sum of all doping and scattering losses in the laser structure and the carrier dependent loss term ( $\alpha_c$ ) which is given by

$$\Gamma_w \sigma_{IVBA}^{2D} n_{QW} N'_{QW} + \left( \sigma_{FCA}^{3D} + \sigma_{IVBA}^{3D} \right) \left( [n_{QW} + 1] \Gamma_B N'_{BAR} + \Gamma_S N'_{SCH} \right) \quad (2-10)$$

In the above, the ( $N'$ )s and  $\Gamma$ s represent the *actual* carrier densities in and percentage of overlap that the lasing mode has with the individual quantum wells, barriers, and SCH regions;  $\sigma_{FCA}^{3D}$  is the loss coefficient for 3D carriers ( $N'_{BAR}$  and  $N'_{SCH}$ ) due to free carrier absorption; and  $\sigma_{IVBA}^{2D}$  and  $\sigma_{IVBA}^{3D}$  are the loss coefficients for 2D carriers ( $N'_{QW}$ ) and 3D carriers respectively due to intervalence band absorption. Based upon the work of [35], the following values were assigned to the coefficients in terms of  $\text{cm}^{-1}$  of loss per  $10^{18} \text{ cm}^{-3}$  of electrons:  $\sigma_{IVBA}^{2D} = 10 \text{ cm}^{-1}$ ,  $\sigma_{FCA}^{3D} = 5 \text{ cm}^{-1}$ , and  $\sigma_{IVBA}^{3D} = 50 \text{ cm}^{-1}$ . In the case of Reference [35], these numbers were generated for 6 nm strained GaInAs quantum wells. The gain needed to be supplied by the quantum well active region in order to overcome the losses in equation (2-9) are obtained from the quantum well gain curve modeling discussed in section 2.2.1. In order to be able to later take out the effects of carrier overflow into the barrier and SCH regions of the device, the gain curves are fitted to a logarithmic function of  $N'_{QW}$  which has the form of

$$\Gamma_w g_o \ln \left( \frac{N'_{QW}}{N_{tr}} \right) \quad (2-11)$$

where  $g_o$  and  $N_{tr}$  (the carrier density needed to get to transparency) are the fitting parameters.

### 2.2.3 Heating Effects in In-plane Laser Operation

The final important piece to the modeling approach outlined in this chapter is how heating effects are included in the model. The general procedure is outlined in Figure 2-10 below. An initial heat sink temperature is assumed. Using the procedure illustrated in Figure 2-5, the operating point of the laser is calculated. However, due to the resistance and finite thermal conductivity of the structure,

heat is generated which changes the actual active region temperature. For the modeling presented here, this heating is only included at threshold.

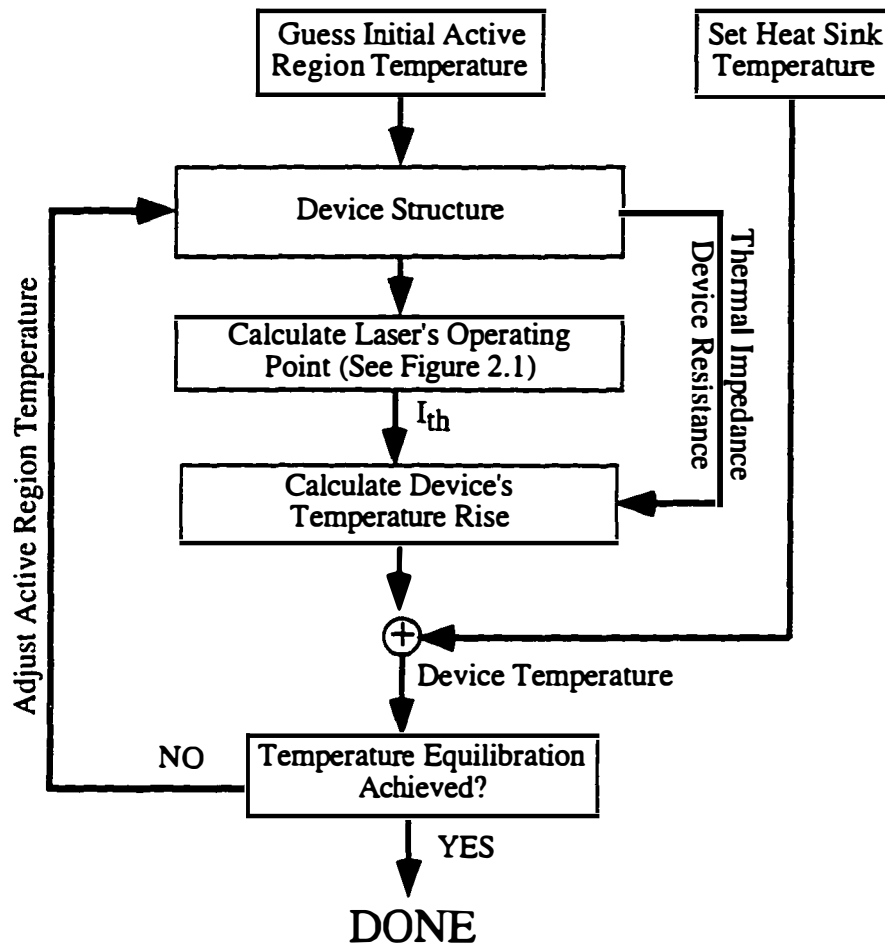


**Figure 2-10** Flow chart of procedure used to model the static characteristics of 1.55  $\mu\text{m}$  lasers where the effects of device heating are included.

This is important in that the results for  $T_o^{10mW}$  that are presented in Chapter 3 will overestimate what is seen experimentally. The power dissipated at threshold is given by

$$P_D = (V_o + I_{th}R)I_{th} \quad (2-12)$$

where  $V_o$  is the turn-on voltage of the structure and  $R$  is the structure resistance. For the results in Chapter 3, these parameters are assigned the values 0.8V and 5  $\Omega$  respectively. Once the power dissipated is known, the increase in temperature is given by

$$\Delta T = P_D Z_{th} \quad (2-13)$$

where  $Z_{th}$  is the laser's thermal impedance. In order to account for changes in the geometry of the structure, I will represent the laser as a linear heat source of length  $L$  and width  $w$  on a thick substrate which is wider than it is thick. In this approximation [32],  $Z_{th}$  is given by

$$Z_{th} = \frac{\ln(4h/w)}{\pi\sigma_s L} \quad (2-14)$$

In Equation (2-14),  $h$  is the thickness of the substrate (assumed to be 100  $\mu\text{m}$ ) and  $\sigma_s$  is the thermal conductivity of the substrate. For example, a  $3 \times 300 \mu\text{m}^2$  device on an InP substrate,  $Z_{th}$  has a thermal impedance of  $59.2^\circ\text{C/W}$ . However, in 1.55  $\mu\text{m}$  lasers, the thermal impedance of the active region may be higher than the above simple expression due to the very poor thermal conductivity of GaInAsP. In the modeling work here, this difference is ignored; however, its ramifications on the results will be discussed.

#### 2.2.4 Calculation of Threshold Current and Light vs. Current Curves

Now that I have covered the modeling approach used to determine the operating point of the laser, the last modeling step is concerned with the calculation of the current at which threshold is achieved as well as the generation of light versus current curves. In determining the operating point of the laser, the threshold gain ( $g_{th}$ ) was determined. This value is used in another set of gain curves calculated as outlined in Appendix A which relates the gain to the current density and as a logarithmic form similar to equation ( 2-11). Solving that equation for the threshold current density gives the following relationship between the threshold current density and the threshold gain

$$J_{th} = \frac{n_{qw}}{\eta_i} J_{tr} \exp\left(\frac{g_{th}}{g_{opt}}\right) \quad (2-15)$$

Here,  $g_{opt}$  and  $J_{tr}$  (the transparency current density) are also fitting parameters. Once  $J_{th}$  is known, the threshold current itself is given by

$$I_{th} = J_{th} wL \quad (2-16)$$

where  $w$  and  $L$  are the width and length of the laser cavity. To obtain the light versus current characteristics of a laser, the following expression is used

$$P_o = \frac{h\nu}{q} \eta_d (I - I_{th}) \Big|_{I \geq I_{th}} \quad (2-17)$$

where  $P_o$  is the total power out of the device (both mirrors),  $h\nu/q$  is the energy of the emitted photons, and  $\eta_d$  is the external differential quantum efficiency of the device. To generate the actual light versus current curves that are measured,

I need to take into account that -- in general -- different amounts of light may come out of each facet. To account for this, the external differential quantum efficiency can be defined as

$$\eta_{dn} = F_n \eta_i \frac{\alpha_m}{\alpha_i + \alpha_m} \quad (2-18)$$

where  $F_n$  is related to the reflectivity and transmission through each mirror (#1 or #2) by

$$F_\alpha = \frac{t_\alpha^2}{(1 - r_\alpha^2) + \frac{r_\alpha}{r_\beta} (1 - r_\beta^2)} \quad (2-19)$$

where  $\alpha=1$  and  $\beta=2$  or  $\alpha=2$  and  $\beta=1$ . It is assumed here that the reflectivity and transmission of each facet is the same and that there is no additional loss at the facets. These conditions result in  $F_1=F_2=0.5$ . Furthermore,  $\eta_i$  is the fractional amount of the injected sheet carrier density that is in the quantum wells which is given by<sup>vii</sup>

$$\eta_i = \frac{n_{QW} N_{QW} L_{QW}}{\sigma_{no}} \quad (2-20)$$

where  $\sigma_{no}$  is given in equation A-1 in Appendix A .

---

<sup>vii</sup> This definition of  $\eta_i$  does not include carrier leakage out of the waveguide region of the laser.

## 2.3 Measuring the Temperature Dependence of 1.55 $\mu\text{m}$ Lasers

In the previous section I developed a complete modeling algorithm for the static properties of 1.55  $\mu\text{m}$  in-plane lasers. However, in order for this model to be useful, a means of comparing the modeling results to experiment must be developed. In this section, the three main experimental approaches of quantifying the temperature behavior of 1.55  $\mu\text{m}$  lasers are explored. They are the characteristic temperature, or  $T_o$ , approach; the maximum operation temperature, or  $T_{max}$ , approach; and the critical temperature, or  $T_c$ , approach. In this section, I will delve further into each of these methods.

### 2.3.1 Characteristic Temperature ( $T_o$ ) Approach

The most widely used method for characterizing the temperature dependence of semiconductor lasers is the characteristic temperature approach proposed by Pankove in 1968 [36]. In this approach, Pankove observed that the temperature dependence of the external quantum efficiency as measured by the slope of the sub-threshold light versus current data followed an exponential relationship. It was further seen that there was an exponential dependence of the threshold current ( $I_{th}$ ) with temperature which could be represented as

$$I_{th} = I_o \exp\left(\frac{T}{T_o}\right) \quad (2-1)$$

where  $I_o$  and  $T_o$  are the characteristic current and temperature respectively. In measurements done to quantify  $T_o$ , it has been shown that  $T_o$  is much lower for 1.55  $\mu\text{m}$  lasers than for GaAs-based lasers (see Table 1-1). Much work has been done in several laboratories [36-62] to try and explain the physical

significance of  $T_o$ . Using Equation ( 2-1),  $T_o$  – in terms of the current densities at threshold – can be defined as

$$T_o = \frac{T' - T_{ref}}{\ln\left(\frac{J'}{J_{ref}}\right)} \quad (2-2)$$

where  $T_{ref}$  and  $T'$  are two different temperatures ( $\Delta T = T' - T_{ref}$ ). Using a logarithmic description for the gain from a quantum well in the form of

$$g_{QW} = g_{opt} \ln\left(\frac{J_{QW}}{J_{tr}}\right) \quad (2-3)$$

$T_o$  can be redefined in terms of measurable parameters and changes in these parameters with temperature. Solving for  $J_{QW}$  in ( 2-3) and substituting those expressions into ( 2-1) yields

$$T_o = \frac{\Delta T}{\ln\left(\frac{J'}{J_{tr}}\right) + \ln\left(\frac{\eta_i}{\eta_i}\right) + \frac{g_{th}}{n_{QW} g_{opt}} - \frac{g_{th}}{n_{QW} g_{opt}}} \quad (2-4)$$

where  $J_{th} = (n_{QW}/\eta_i)J_{QW}$  and  $g_{th} = n_{QW} g_{QW}$ . If changes in the parameters with temperature are defined as shown below<sup>viii</sup>

---

<sup>viii</sup> Note that since the wavelength of lasing changes with the temperature of the active region, the optical confinement factor will also change. This is considered to be a small effect and is ignored.



$$\begin{aligned}
 J_{tr}' &= J_{tr}^{\dagger} J_{tr} & g_{opt}' &= g_{opt}^{\dagger} g_{opt} \\
 \eta_i' &= \eta_i^{\dagger} \eta_i & g_{th}' &= g_{th}^{\dagger} g_{th} = \left(1 + \frac{\Delta g_{th}}{g_{th}}\right) g_{th}
 \end{aligned}$$

where  $X'$  represents the fractional change in parameter  $X$  from  $T_{ref}$  to  $T'$ . Using these changes in Equation ( 2-4) leads to the final result of

$$T_o = \frac{\Delta T}{\ln J_{tr}' - \ln \eta_i' + \frac{1}{n_{QW} \Gamma_{act} g_{opt}'} \left( \frac{\alpha_o}{g_{opt}^{\dagger}} - \alpha_o + \frac{\Delta \alpha}{g_{opt}^{\dagger}} \right)} \quad (2-5)$$

where  $\alpha_o$  represents the total losses in the laser at  $T_{ref}$ . Note that in Equation (2-5), the temperature sensitivity is related to *how things change as a function of temperature and not on the values at  $T_{ref}$* . This will be further explored in the design-related issues in Chapter 4. In lasers for fiber optic communications, the temperature sensitivity of the threshold current is not the important parameter. These devices -- when in use -- are set to provide a fixed output power into an optical fiber. Thus, the temperature sensitivity of the current required to maintain this output power is important. In the theoretical results of Chapters 3 and 4, the temperature sensitivity of the current needed to provide  $P_o$  mW out of one of the laser's facets ( $\equiv T_o(P_o)$ ) will be used as a figure of merit as well as  $T_o$  at threshold.  $T_o(P_o)$  can be written in a similar manner to  $T_o$  in Equation ( 2-5). Ignoring spontaneous emission, the light output power out of one of the laser's facets is given by

$$P_o = F \eta_d \frac{h\nu}{q} (I - I_{th}) \quad (2-6)$$

where  $F$  is the fraction of the total light in the laser cavity coming out of the facet. Using Equations ( 2-2) and ( 2-6),  $T_o(P_o)$  can be reduced to

$$T_o = \frac{\Delta T}{\ln\left(\frac{X}{\eta_a^\dagger v^\dagger} + I_{th} \exp[\Delta T/T_o]\right) - \ln(X + I_{th})} \quad (2-7)$$

where  $X \equiv qP_o/(F\eta_a h\nu)$ .

Recently, there has been work that suggest that  $T_o$  is not the most important parameter for judging the temperature dependence of 1.55  $\mu\text{m}$  lasers. From this recent work, two additional methods of evaluating the temperature dependence of 1.55  $\mu\text{m}$  lasers has emerged. They are detailed below.

### 2.3.2 *The Maximum Temperature ( $T_{max}$ ) Approach*

J.D. Evans and co-workers have recently argued that the concept of  $T_o$  is not valid for long wavelength semiconductor lasers[63,64]. In its place, they have generated a semi-empirical approach to explain the temperature performance of these devices by examining the threshold current density ( $J_{th}$ ) in terms of its gradient with respect to temperature as defined below

$$\nabla_T J_{th} \equiv \frac{\partial J}{\partial T} \equiv \frac{J_{i+1} - J_i}{T_{i+1} - T_i} \quad (2-8)$$

In this analysis, the inverse of the threshold current temperature gradient ( $\nabla_T J_{th}$ )<sup>-1</sup> versus  $J_{th}$  was found to be independent of the device length and the temperature

at which the measurements were taken [63]. So, this indicates that two different lasers with the same active region and identical  $J_{th}$  will have the same  $\nabla_T J_{th}$  even though they may have been measured under different conditions<sup>ix</sup>. From a fit to the data, they found that  $(\nabla_T J_{th})^{-1}$  versus  $J_{th}$  can be fit to a power law relation

$$\nabla_T J_{th} = K \left( \frac{J_{th}}{J_c} \right)^m = \frac{J_{th}^m}{C} \quad (2-9)$$

where  $K$  is a constant with units of  $(A/(cm^2 \cdot K))$ ,  $J_c$  is in units of threshold current density, and  $C$  is a constant that depends on the magnitude of the parameter  $m$ . Experimentally, they found that  $m$  was always  $\approx 3/2$  and  $C$  was active region dependent [63]. More specifically,  $C$  was found to increase with an increase in the amount of biaxial strain and the number of quantum wells used in the laser. Although no direct evidence has been shown to equate  $m$  to a physical parameter of the device, the authors believe that  $m$  is related to the thermal impedance of the device which affects the amount of excess heat generated during operation. Furthermore, since  $m$  and  $C$  appear to be relatively temperature independent in their results, Equation (2-9) can be integrated with respect to temperature to yield an expression for  $J_{th}$  of

$$J_{th} = \left[ \frac{n}{C} (T_{max} - T) \right]^{-1/n} \quad (2-10)$$

where  $n = m-1$  and  $T_{max}$  is defined as the point where  $J_{th}$  approaches infinity which is determined by plotting  $J^{-n}$  versus temperature. In practice, however, there is a limit as to the maximum current density possible due to heating

---

<sup>ix</sup> This does not include -- in my opinion -- differences in the duty cycle used in the measurement (i.e., pulsed or continuous-wave). This must be the same.

concerns. In looking at the literature for 1.3 and 1.55  $\mu\text{m}$  lasers of many types [63,65-69], I have found that a reasonable practical limit for the total threshold current density is between 10 and 20  $\text{kA/cm}^2$ ; this current density will be used Chapter 3 to define  $T_{max}$  in the evaluation of different laser structures. In addition, these values will be compared to the case where heating effects are included in the model. As will be shown in Chapter 3, this definition allows me the flexibility to adjust certain device parameters without affecting  $T_{max}$  to first order. This is only true for cases where  $J_{th}$  is independent of the changed-device parameter while other parameters (such as  $I_{th}$  or the device resistance) change<sup>\*</sup>. To equate  $T_{max}^m (\equiv T_{max} \text{ as } J_{th} \rightarrow \infty)$  to device parameters, the peak modal gain of the device is related to the injected current by

$$\Gamma_{act} g_{th} = \Gamma_{act} n_{QW} g_{opt} \ln \left( \frac{J_{QW}}{J_{ir}} \right) = \alpha_o \quad (2-11)$$

Solving Equation (2-11) for  $J_{QW}$  yields an expression for  $J_{th}$  of

$$J_{th} = \frac{n_{QW}}{\eta_i} J_{ir} \exp \left[ \frac{\alpha_o}{\Gamma_{act} n_{QW} g_{opt}} \right] \quad (2-12)$$

which when substituted into equation(2-10) yields a final result for  $T_{max}^m$  of

---

<sup>\*</sup> When heating is included in the model, this scaling approximation is no longer valid.

$$T_{\max}^{\infty} = T_{\text{ref}} + \frac{C}{n \left( n_{\text{QW}} J_{\text{tr}} / \eta_i \right)^n \exp \left[ n \alpha_o / \Gamma_{\text{act}} n_{\text{QW}} g_{\text{opt}} \right]} \quad (2-13)$$

In order to maximize  $T_{\max}^{\infty}$  several things can be done: maximize  $C$ , minimize  $n$ , minimize  $J_{\text{tr}}$ , and operate at a low point on the gain curve. I will re-visit these issues when discussing design-related issues in Chapter 4.

### 2.3.3 The Critical Temperature ( $T_c$ ) Approach

The idea of a critical temperature to quantitatively characterize 1.55  $\mu\text{m}$  lasers was first proposed by Seki and co-workers [70-74]. In this approach, the external quantum efficiency is used as a measure of the temperature dependence. The expression for the external quantum efficiency used by Seki is shown below

$$\eta_d = \eta_i \frac{\alpha_m}{\alpha_i^o + \alpha_m} \quad (2-14)$$

where  $\eta_i$  is the internal quantum efficiency;  $\alpha_i^o$  is the internal loss in the lasers due to absorption, scattering, etc.; and  $\alpha_m$  is the facet mirror loss. The internal losses can be further divided into two components: one dealing with losses in the quantum well<sup>xi</sup> and one dealing with losses in the barriers and SCH. The expression for the internal loss is then given<sup>xii</sup> by

---

<sup>xi</sup> By their method, this component of the loss also includes absorption loss ( $\alpha_i^o$ ) from the cladding and contact lasers and other non-injected carrier induced loss mechanisms.

<sup>xii</sup> Note that in Seki's definitions, the optical overlap of the lasing mode with the quantum wells and SCH regions is implicit in his definition of  $\alpha$ . In the next section, I do not make this assumption.

$$\alpha_i = n_w \alpha_i^{QW} + \alpha_i^{SCH} \quad (2-15)$$

Experimentally, it has been observed [62] that the temperature dependence of the loss due to the quantum well can be approximated as a linear function of temperature

$$\alpha_i^{QW} = \alpha_1 + \gamma(T - T_1) \quad (2-16)$$

where  $\alpha_1$  is the loss at  $T_1$  and  $\gamma$  is an empirical coefficient which indicates the rate of change of quantum well loss with temperature which is mainly due to carrier effects. Using equations (2-15) and (2-16), the external quantum efficiency can be re-written as

$$\eta_d(T) = \eta_i(T) \frac{\alpha_m}{N_w [\alpha_1 + \gamma(T - T_1)] + \alpha_i^{SCH}(T) + \alpha_m} \quad (2-17)$$

When the losses in the barrier/SCH regions are small compared to other loss mechanisms, equation (2-17) can be reduced to

$$\eta_d \propto \eta_i(T) \exp \left[ - \frac{\gamma}{\alpha_m / N_w + \alpha_1} (T - T_1) \right] \quad (2-18)$$

What equation (2-18) shows is that in the regime of low barrier/SCH loss regime, the external quantum efficiency will have an exponential dependence (as

long as  $\eta_i$  is not temperature dependent). If the approximation regarding the barrier/SCH losses cannot be made, then the external quantum efficiency will decrease much more quickly than an exponential decay. The strength of this approach is that  $T_c$  can be related to the structural parameters of the laser quite easily. For example,  $T_c$  increases with an increase in the number of quantum wells in the active region and a reduction in the mirror losses. In addition,  $T_m$  (as defined below) increases with  $T_c$  and the temperature dependence of the external quantum efficiency decreases with increasing number of wells for  $T \leq T_c$ .

The authors further defined two different regions of operation for long wavelength lasers. The first ( $T \leq T_c$ ) I will call the *carrier-independent regime*. In this case, the losses in the barrier/SCH are small compared to the losses in the quantum well. From their work, Seki and co-workers found that the losses in the quantum well and Auger currents dominate in this regime. In the *carrier-dependent regime* ( $T > T_c$ ), the losses in the barrier/SCH cannot be ignored. In this regime, it is the losses in the barrier/SCH that dominate the temperature characteristics. The main effect they see is the effect of electrostatic deformation of the bands [74,75] which leads to a further reduction in carrier confinement. As the carrier loss continues to increase, a phenomena known as loss multiplication occurs. Here as the internal losses of the device increase due to carrier overflow into the barriers and SCH regions. As a result, the threshold gain increases which causes more carriers to be injected into the device in order to reach threshold. These extra carriers further exacerbate this problem by contributing more electrostatic deformation; thus, a positive feedback mechanism exists. The net effect is that the losses increase faster than the gain as a function of temperature and thus the lasing conditions is never met. This is where they define the  $T_m$ , the maximum operating temperature of the device. Note that this has a similar, albeit different, definition as the  $T_{max}$  used by Evans as discussed in Section 2.3.2.

In this section, I have detailed the three most used approaches to characterizing the temperature sensitivity of 1.5  $\mu\text{m}$  lasers. Throughout this dissertation, all three of these methods will be used in order to make accurate comparisons to the literature.

## 2.4 Summary

In the chapter, the general framework I have developed to model the static properties of semiconductor lasers has been outlined. Key aspects of this model are (i) the generation of gain curves of the GaInAsP quantum wells typically used in 1.55  $\mu\text{m}$  lasers, (ii) determination of the operating point on the gain curves taking into account many of the common loss mechanisms, and (iii) how device heating effects are included into the model. When all of these factors are accounted for, the threshold current of the device and the information to generate light versus current curves of the laser at different temperatures is known. I will now turn – in Chapter 3 – to the results of this model and a comparison of the simulated results to experimental data published in the literature.



## 2.5 References

- [1] A. R. Adams, "Band-structure engineering for low-threshold high-efficiency semiconductor lasers", *Electronics Letters* **22**, 249 (1986).
- [2] E. Yablonovitch and E. O. Kane, "Band structure engineering of semiconductor lasers for optical communications", *Journal of Lightwave Technology* **6**, 1292 (1988).
- [3] E. Yablonovitch and E. O. Kane, "Reduction of lasing threshold current density by the lowering of valence band effective mass", *Journal of Lightwave Technology* **LT-4**, 504 (1986).
- [4] S. W. Corzine and L. A. Coldren, "Theoretical gain in compressive and tensile strained InGaAs/InGaAsP quantum wells", *Applied Physics Letters* **59**, 588 (1991).
- [5] S. W. Corzine, R. H. Yan, and L. A. Coldren, "Theoretical gain in strained InGaAs/AlGaAs quantum wells including valence-band mixing effects", *Applied Physics Letters* **57**, 2835 (1990).
- [6] W. D. Laidig, P. J. Caldwell, Y. F. Lin, and C. K. Peng, "Strained-layer quantum-well injection laser", *Applied Physics Letters* **44**, 653 (1984).
- [7] W. D. Laidig, Y. F. Lin, and P. J. Caldwell, "Properties of  $\text{In}_x\text{Ga}_{1-x}\text{As}$ -GaAs strained-layer quantum-well-heterostructure injection lasers", *Journal of Applied Physics* **57**, 33 (1985).
- [8] D. Feketa, K. T. Chan, J. M. Ballantyne, and L. F. Eastman, "Graded-index separate-confinement InGaAs/GaAs strained-layer quantum well laser grown by metalorganic chemical vapor deposition", *Applied Physics Letters* **49**, 1659 (1986).
- [9] Y. J. Yang, K. Y. Hsieh, and R. M. Kolbas, "Continuous room-temperature operation of an InGaAs-GaAs-AlGaAs strained-layer quantum well laser", *45th Annual Device Research Conference*, Santa Barbara, CA, USA, 1987, 2379.
- [10] R. W. Kaliski, N. Holonyak, Jr., K. C. Hsieh, D. W. Nam, J. W. Lee, H. Shichijo, R. D. Burnham, J. E. Epler, and H. F. Chung, "Continuous (300 K) photopumped laser operation of  $\text{Al}_x\text{Ga}_{1-x}\text{As}$ -GaAs quantum well heterostructures grown on strained-layer GaAs on Si", *Applied Physics Letters* **50**, 836 (1987).

- [11] S. E. Fischer, D. Fekete, G. B. Feak, and J. M. Ballantyne, "Ridge waveguide injection laser with a GaInAs strained-layer quantum well ( $\lambda = 1 \mu\text{m}$ )" *Applied Physics Letters* **50**, 714 (1987).
- [12] E. P. O'Reilly, K. C. Heasman, A. R. Adams, and G. P. Witchlow, "Calculations of the threshold current and temperature sensitivity of a (GaIn)As strained quantum well laser operating at  $1.55 \mu\text{m}$ ", *2nd International Conference on Superlattices, Microstructures and Microdevices*, Goteborg, Sweden, 1986, 99.
- [13] B. I. Miller, U. Koren, M. G. Young, and M. D. Chien, "Strain-compensated strained-layer superlattices for  $1.5 \mu\text{m}$  wavelength lasers." *Applied Physics Letters* **58**, 1952 (1991).
- [14] D. C. Houghton, M. Davies, and M. Dion, "Limits of strain compensation in MQW InGaAsP/InP  $1.5 \mu\text{m}$  lasers.", *(1993) Conference Proceedings Fifth International Conference on Indium Phosphide and Related Materials*, 187 (1993).
- [15] J. W. Matthews and A. E. Blakeslee, "Defects in epitaxial multilayers. I. Misfit dislocations" *Journal of Crystal Growth* **27**, 118 (1974).
- [16] C. A. B. Ball and J. H. van der Merwe, "The growth of dislocation-free layers", *Dislocations in solids. Vol.6. Applications and recent advances*, 121 (1983).
- [17] C. H. Lin, C. L. Chua, Z. H. Zhu, and Y. H. Lo, "On nonuniform pumping for multiple-quantum well semiconductor lasers" *Applied Physics Letters* **65**, 2383 (1994).
- [18] C. H. Lin, C. Y. Tsai, C. L. Chua, and Y. H. Lo, "Effects of transport limited nonuniform pumping for multiple quantum well semiconductor lasers", *Conference Proceedings. IEEE Lasers and Electro-Optics Society 1994 7th Annual Meeting (Cat. No.94CH3371-2) Proceedings of LEOS'94*, Boston, MA, USA, 1994, 121.
- [19] M. Grupen, "Simulating carrier dynamics in quantum well lasers", *Physics and Simulation of Optoelectronic Devices IV*, San Jose, CA, USA, 1996, 374.
- [20] S. Seki, K. Yokoyama, and P. Sotirelis, "The influence of valence-band well depth on optical gain uniformity in  $1.3\text{-}\mu\text{m}$  InP-based strained-layer multiple-quantum-well lasers", *Proceedings of IEEE 14th International Semiconductor Laser Conference*, Maui, HI, USA, 1994, 135.
- [21] N. Tessler and G. Eisenstein, "On carrier injection and gain dynamics in quantum well lasers" *IEEE Journal of Quantum Electronics* **29**, 1586 (1993).
- [22] N. Tessler and G. Eisenstein, "Distributed nature of quantum-well lasers" *Applied Physics Letters* **62**, 10 (1993).

- [23] D. Patel, H. Temkin, C. S. Menoni, R. A. Logan, D. Coblenz, and C. Tome, "Enhanced characteristics of InGaAsP buried quaternary lasers with pressure in the diamond anvil cell" *Joint International Association for Research and Advancement of High Pressure Science and Technology and American Physical Society Topical Group on Shock Compression of Condensed Matter Conference*, Colorado Springs, CO, USA, 1993, 577.
- [24] D. Patel, C. S. Menoni, H. Temkin, R. A. Logan, and D. Coblenz, "Enhanced characteristics of InGaAsP buried quaternary lasers with pressures up to 1.5 GPa" *Applied Physics Letters* **62**, 2459 (1993).
- [25] L. Davis, Y. Lam, D. Nichols, J. Singh, and P. K. Bhattacharya, "Auger recombination rates in compressively strained  $\text{In}_x\text{Ga}_{1-x}\text{As}/\text{InGaAsP}/\text{InP}$  ( $0.53 \leq x \leq 0.73$ ) multi-quantum well lasers" *IEEE Photonics Technology Letters* **5**, 120 (1993).
- [26] Y. Zou, J. S. Osinski, P. Grodzinski, P. D. Dapkus, W. Rideout, W. F. Sharfin, and F. D. Crawford, "Experimental verification of strain benefits in 1.5- $\mu\text{m}$  semiconductor lasers by carrier lifetime and gain measurements" *IEEE Photonics Technology Letters* **4**, 1315 (1992).
- [27] M. Kot and K. Zdansky, "Measurement of radiative and nonradiative recombination rate in InGaAsP-InP LED's" *IEEE Journal of Quantum Electronics* **28**, 1746 (1992).
- [28] W. W. Lui, T. Yamanaka, Y. Yoshikuni, S. Seki, and K. Yokoyama, "Unifying explanation for recent temperature sensitivity measurements of Auger recombination effects in strained InGaAs/InGaAsP quantum-well lasers." *Applied Physics Letters* **63**, 1616 (1993). D2-68
- [29] W. W. Lui, T. Yamanaka, U. Yoshikuni, S. Seki, and K. Yokoyama, "A suppression mechanism of Auger recombination effects in strained quantum wells induced by local negative curvature of the energy band structure." *IEEE Journal of Quantum Electronics* vol. **30**, 392 (1994). G5-11
- [30] W. W. Lui, T. Yamanaka, Y. Yoshikuni, S. Seki, and K. Yokoyama, "Temperature sensitivity of Auger-recombination effects in compressively strained  $\text{In}_x\text{Ga}_{1-x}\text{As}/\text{In}_x\text{Ga}_{1-x}\text{As}_{1-y}\text{P}_y$  quantum-well lasers." *Physical Review B (Condensed Matter)* **48**, 8814 (1993). D2-69
- [31] C. Weisbuch and B. Vinter, *Quantum Semiconductor Structures: Fundamentals and Applications*, First ed. (Academic Press, Inc., San Diego, 1991). Chapter 1
- [32] L. A. Coldren and S. W. Corzine, *Diode lasers and photonic integrated circuits* (Wiley, New York, 1995).

- [33] S. W. Corzine, "Design of vertical-cavity surface-emitting lasers with strained and unstrained quantum well active regions," Dissertation, University of California – Santa Barbara, 1993.
- [34] S. W. Corzine, R. H. Yan, and L. A. Coldren, "Optical Gain in III-V Bulk and Quantum Well Semiconductors," in *Quantum Well Lasers*, edited by Jr. P.S. Zory (Academic Press, Boston, 1993), pp. 17.
- [35] V. Mikhaelashvili, N. Tessler, R. Nagar, G. Eisenstein, A. G. Dentai, S. Chandrasakhar, and C. H. Joyner, "Temperature dependent loss and overflow effects in quantum well lasers", *IEEE Photonics Technology Letters* **6**, 1293 (1994).
- [36] J. A. I. Pankove, "Temperature Dependence of Emission Efficiency and Lasing Threshold in Laser Diodes", *IEEE Journal of Quantum Electronics* **4**, 119 (1968).
- [37] D. A. Ackerman, P. A. Morton, R. F. Kazarinov, M. S. Hybertsen, G. E. Shtengel, T. Tanbun-Ek, and R. A. Logan, "Study of gain in determining  $T_0$  of 1.3  $\mu\text{m}$  semiconductor lasers", *Proceedings of IEEE 14th International Semiconductor Laser Conference*, Maui, HI, USA, 1994, 239.
- [38] D. A. Ackerman, G. E. Shtengel, M. S. Hybertsen, P. A. Morton, R. F. Kazarinov, T. Tanbun-Ek, and R. A. Logan, "Analysis of gain in determining  $T_0$  in 1.3  $\mu\text{m}$  semiconductor lasers", *IEEE Journal on Selected Topics in Quantum Electronics* **1**, 250 (1995).
- [39] M. Asada, A. R. Adams, K. E. Stubkjaer, Y. Suematsu, Y. Itaya, and S. Arai, "The temperature dependence of the threshold current of GaInAsP/InP DH lasers", *1980 IEEE International Semiconductor Laser Conference*, Brighton, UK, 1980, 611.
- [40] M. Asada and Y. Suematsu, "The effects of loss and nonradiative recombination on the temperature dependence of threshold current in 1.5-1.6  $\mu\text{m}$  GaInAsP/InP lasers", *8th IEEE International Semiconductor Laser Conference*, Ottawa, Ont., Canada, 1982, 917.
- [41] H. C. Casey, Jr., "Temperature dependence of the threshold current density in InP-Ga<sub>0.28</sub>In<sub>0.72</sub>As<sub>0.6</sub>P<sub>0.4</sub> ( $\lambda = 1.3 \mu\text{m}$ ) double heterostructure lasers", *Journal of Applied Physics* **56**, 1959 (1984).
- [42] T. R. Chen, B. Chang, L. C. Chiu, K. L. Yu, S. Margalit, and A. Yariv, "Carrier leakage and temperature dependence of InGaAsP lasers", *Applied Physics Letters* **43**, 217 (1983).
- [43] K. D. Chik, "A theoretical analysis of Auger recombination induced energetic carrier leakage in GaInAsP/InP double heterojunction lasers and light emitting diodes", *Journal of Applied Physics* **63**, 4688 (1988).

- [44] N. K. Dutta and R. J. Nelson, "Temperature dependence of threshold of the InGaAsP/InP double-heterostructure lasers and Auger recombination", *Applied Physics Letters* **38**, 407 (1981).
- [45] N. K. Dutta and R. J. Nelson, "The case for Auger recombination in  $\text{In}_{1-x}\text{Ga}_x\text{As}_y\text{P}_{1-y}$ ", *Journal of Applied Physics* **53**, 74 (1982).
- [46] N. K. Dutta, J. Lopata, D. L. Sivco, and A. Y. Cho, "Temperature dependence of threshold of strained quantum well lasers", *Applied Physics Letters* **58**, 1125 (1991).
- [47] M. Ettenberg, C. J. Nuese, and H. Kressel, "The temperature dependence of threshold current for double-heterojunction lasers", *Journal of Applied Physics* **50**, 2949 (1979).
- [48] B. Etienne, S. Jagdeep, R. F. Leheny, and R. E. Nahory, "Influence of hot carriers on the temperature dependence of threshold in 1.3  $\mu\text{m}$  InGaAsP lasers", *Applied Physics Letters* **41**, 1018 (1982).
- [49] A. Haug, "Evidence of the importance of Auger recombination for InGaAsP lasers", *Electronics Letters* **20**, 85 (1984).
- [50] A. Haug, "Theory of the temperature dependence of the threshold current of an InGaAsP laser", *IEEE Journal of Quantum Electronics* **QE-21**, 716 (1985).
- [51] A. Haug and H. Burkhard, "Temperature dependence of threshold current of  $\text{In}_{1-x}\text{Ga}_x\text{As}_y\text{P}_{1-y}$  lasers with different compositions", *IEEE Proceedings J (Optoelectronics)* **134**, 117 (1987).
- [52] M. M. Leopold, A. P. Specht, C. A. Zmudzinski, M. E. Givens, and J. J. Coleman, "Temperature-dependent factors contributing to  $T_0$  in graded-index separate-confinement-heterostructure single quantum well lasers", *Applied Physics Letters* **50**, 1403 (1987).
- [53] H. Jung, E. Gobel, K. M. Romanek, and M. H. Pilkuhn, "Temperature dependence of optical gain spectra in GaInAsP/InP double-heterostructure lasers", *Applied Physics Letters* **39**, 468 (1981).
- [54] W. W. Lui, T. Yamanaka, Y. Yoshikuni, S. Seki, and K. Yokoyama, "Unifying explanation for recent temperature sensitivity measurements of Auger recombination effects in strained InGaAs/InGaAsP quantum-well lasers", *Applied Physics Letters* **63**, 1616 (1993).
- [55] W. W. Lui, T. Yamanaka, Y. Yoshikuni, S. Seki, and K. Yokoyama, "Temperature sensitivity of Auger-recombination effects in compressively strained  $\text{In}_x\text{Ga}_{1-x}\text{As}-\text{In}_x\text{Ga}_{1-x}\text{As}_{1-y}\text{P}_y$  quantum-well lasers", *Physical Review B (Condensed Matter)* **48**, 8814 (1993).

- [56] J. O'Gorman and A. F. J. Levi, "Effect of fixed emission wavelength on threshold current of InGaAsP semiconductor laser diodes" *Electronics Letters* **28**, 2091 (1992).
- [57] J. O'Gorman, A. F. J. Levi, T. Tanbun-Ek, D. L. Coblentz, and R. A. Logan, "Temperature dependence of long wavelength semiconductor lasers" *Applied Physics Letters* **60**, 1058 (1992).
- [58] J. O'Gorman, A. F. J. Levi, S. Schmitt-Rink, T. Tanbrun-Ek, D. L. Coblentz, and R. A. Logan, "On the temperature sensitivity of semiconductor lasers" *Applied Physics Letters* **60**, 157 (1992).
- [59] J. O'Gorman and A. F. J. Levi, "Wavelength dependence of  $T_0$  in InGaAsP semiconductor laser diodes" *Applied Physics Letters* **62**, 2009 (1993).
- [60] W. Zhuang, B. Zheng, J. Xu, Y. Li, J. Xu, and P. Chen, "Carrier loss resulting from Auger recombination in InGaAsP/InP double heterojunction laser diodes: spectroscopy of 950 nm high energy emission" *IEEE Journal of Quantum Electronics* **QE-21**, 712 (1985).
- [61] M. Yano, H. Imai, and M. Takusagawa, "Analysis of threshold temperature characteristics for InGaAsP/InP double heterojunction lasers" *Journal of Applied Physics* **52**, 3172 (1981).
- [62] Y. Zou, J. S. Osinski, P. Grodzinski, P. D. Dapkus, W. C. Rideout, W. F. Sharfin, J. Schlafer, and F. D. Crawford, "Experimental study of Auger recombination, gain, and temperature sensitivity of 1.5  $\mu\text{m}$  compressively strained semiconductor lasers" *IEEE Journal of Quantum Electronics* **29**, 1565 (1993).
- [63] J. D. Evans, J. G. Simmons, D. A. Thompson, N. Puetz, T. Makino, and G. Chik, "An investigation into the temperature sensitivity of strained and unstrained multiple quantum-well, long wavelength lasers: new insight and methods of characterization" *IEEE Journal on Selected Topics in Quantum Electronics* **1**, 275 (1995).
- [64] J. D. Evans and J. G. Simmons, "The dependence of the maximum operating temperature of long wavelength semiconductor lasers on physical and material device parameters" *IEEE Photonics Technology Letters* **7**, 614 (1995).
- [65] H. Temkin, D. Coblentz, R. A. Logan, J. P. van der Ziel, T. Tanbun-Ek, R. D. Yadvish, and A. M. Sergent, "High temperature characteristics of InGaAsP/InP laser structures" *Applied Physics Letters* **62**, 2402 (1993).
- [66] T. Makino, H. Lu, and J. D. Evans, "Temperature dependence of the threshold current in gain-coupled distributed feedback lasers with periodically etched quantum wells: mechanism for an appearance of infinite  $T_0$ " *Applied Physics Letters* **68**, 1892 (1996).

- [67] H. Lu, C. Blaauw, and T. Makino, "High-temperature single-mode operation of 1.3- $\mu\text{m}$  strained MQW gain-coupled DFB lasers", *IEEE Photonics Technology Letters* **7**, 611 (1995).
- [68] T. Makino and H. Lu, "Wide temperature-range singlemode operation of MQW gain-coupled DFB lasers", *Electronics Letters* **30**, 1948 (1994).
- [69] P. J. A. Thijs, L. F. Tiemeijer, P. I. Kuindersma, J. J. M. Binsma, and T. Van Dongen, "High-performance 1.5  $\mu\text{m}$  wavelength InGaAs-InGaAsP strained quantum well lasers and amplifiers", *IEEE Journal of Quantum Electronics* **27**, 1426 (1991).
- [70] S. Seki, H. Oohasi, H. Sugiura, T. Hirono, and K. Yokoyama, "Dominant mechanisms for the temperature sensitivity of 1.3  $\mu\text{m}$  InP-based strained-layer multiple-quantum-well lasers", *Applied Physics Letters* **67**, 1054 (1995).
- [71] S. Seki, H. Oohashi, H. Sugiura, T. Hirono, and K. Yokoyama, "Design criteria for highly-efficient operation of 1.3  $\mu\text{m}$  InP-based strained-layer multiple-quantum-well lasers at elevated temperatures", *IEEE Photonics Technology Letters* **7**, 839 (1995).
- [72] S. Seki, K. Yokoyama, and P. Sotirelis, "Theoretical analysis of high-temperature characteristics of 1.3  $\mu\text{m}$  InP-based quantum-well lasers", *IEEE Journal on Selected Topics in Quantum Electronics* **1**, 264 (1995).
- [73] S. Seki and K. Yokoyama, "Theoretical analysis of temperature sensitivity of differential gain in 1.55  $\mu\text{m}$  InGaAsP-InP quantum-well lasers", *IEEE Photonics Technology Letters* **7**, 251 (1995).
- [74] S. Seki, H. Oohasi, H. Sugiura, T. Hirono, and K. Yokoyama, "Dominant mechanism for limiting the maximum operating temperature of InP-based multiple-quantum-well lasers", *Journal of Applied Physics* **79**, 2192 (1996).
- [75] S. Seki and K. Yokoyama, "Electrostatic deformation in band profiles of InP-based strained-layer quantum-well lasers", *Journal of Applied Physics* **77**, 5180 (1995).





### 3. Modeling In-Plane Semiconductor Lasers: Results

This chapter is concerned with the modeling results of 1.55  $\mu\text{m}$  in-plane lasers using the approach of Chapter 2. Many of the factors that affect device performance were covered in Chapter 2. Here, the results of all of these factors are presented with an emphasis on the effects of Auger current and carrier overflow specifically. The baseline active region for the 1.55  $\mu\text{m}$  laser structure modeled is three 7 nm 1% compressively strained GaInAsP quantum wells with two 10 nm GaInAsP barriers separating them. This device structure is described in more detail in Section 2.1. Table 3-1 summarizes the other important parameters for the laser structure modeled in this chapter.

**Table 3-1** Parameters used in the modeling of 1.55  $\mu\text{m}$  in-plane lasers for a 3 quantum well active region.

Parameter	Value	Units
Device Width	3	$\mu\text{m}$
Internal Losses ( $\alpha_i^o$ )	10	1/cm
QW Confinement Factor ( $\Gamma_w$ )	3.84	%
Barrier Confinement Factor ( $\Gamma_B$ )	14.13	%
SCH Confinement Factor ( $\Gamma_s$ )	29.88	%
Auger Coefficient at 20°C	$5 \times 10^{-29}$	$\text{cm}^6/\text{s}$
Auger Activation Energy	60	meV

### 3.1 Effect of Structural Parameters

Using Equation (2.5), the predicted  $T_0$  values versus cavity length are shown below in Figure 3-1 for temperatures between 20°C and 80°C. The temperature dependence of the threshold current is pretty strong as shown by the relatively low  $T_0$  values.

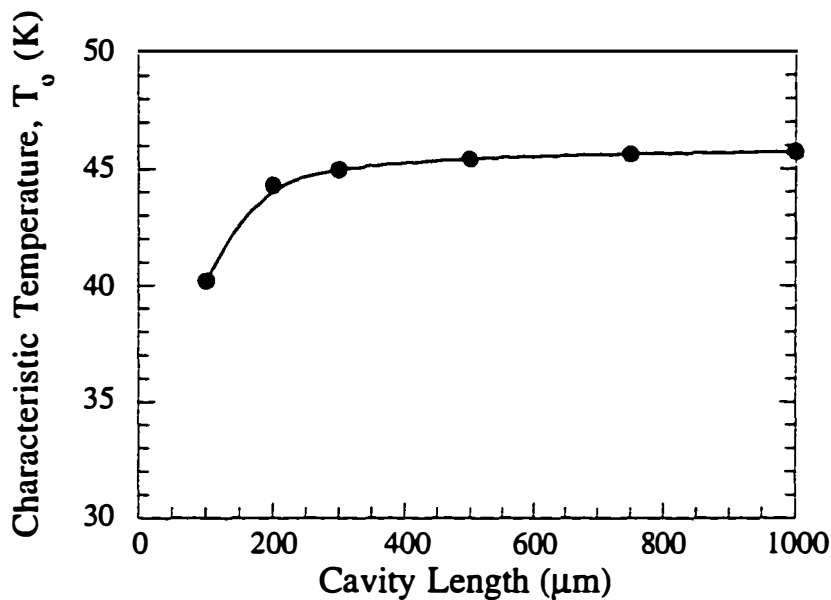


**Figure 3-1** Calculated  $T_0$  values for a 3 quantum well device with a 3  $\mu\text{m}$  stripe width. Other important information is found in Table 3-1. Note that heating has been ignored in this calculation.

What Figure 3-1 shows is that for high losses (i.e., short cavities), the characteristic temperature decreases rapidly. As the cavity length is made longer the value increases – reaching a value of 45.7K for a  $3 \times 1000 \mu\text{m}^2$  device. In the

case of Figure 3-1,  $T_o$  is not limited by a change in the operating point on the gain curve.

For the device modeled here, the change in losses is calculated to vary from 40 to 7  $\text{cm}^{-1}$  for a  $3 \times 100$  and a  $3 \times 1000 \mu\text{m}^2$  device respectively. Looking at Equation (2.5) more closely shows that there are three factors that determine  $T_o$ :  $J_{tr}^\dagger$ ,  $\eta_i^\dagger$ , and  $\Delta\alpha$ . In the best case scenario, Equation (2.5) reduces to

$$T_o = \frac{\Delta T}{\ln J_{tr}^\dagger + \frac{1}{n_{QW} \Gamma_{act} g_{opt}} \left( \frac{\alpha_o}{g_{opt}^\dagger} - \alpha_o \right)} \quad (3-1)$$

where  $\eta_i^\dagger$  is one and  $\Delta\alpha$  is zero. Using Equation (3-1) in Figure 3-2 below shows that – even if losses and changes in internal efficiency are neglected – the  $T_o$  values only improves to 51.7K at a cavity length of 1000  $\mu\text{m}$ . Thus in this case,  $J_{tr}^\dagger$  is the dominant term in the determination of  $T_o$ . For the laser here,  $J_{tr}^\dagger$  has a value of 3.2.

One structural change that is typically made in 1.55  $\mu\text{m}$  lasers is an increase in the number of quantum wells. The  $T_o$  values for 3 and 5 quantum wells is shown in Figure 3-3. When the number of quantum wells is increased, the optical confinement factor increases to 6.65% and the threshold is lower for small cavities since the operation point has been moved down on the gain curve.

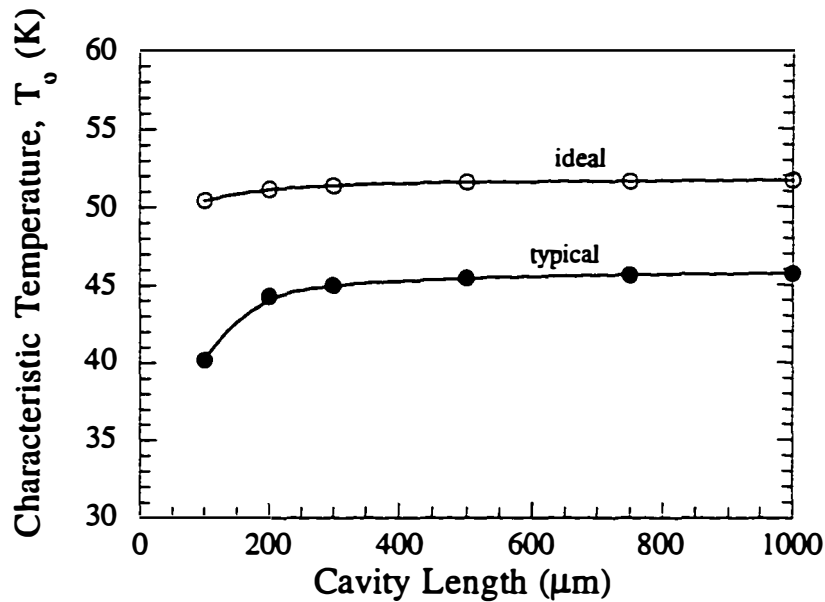


**Figure 3-2** Calculated  $T_0$  values for a 3 quantum well device with a 3  $\mu\text{m}$  stripe width with the loss mechanisms included (typical) and ignored (ideal). Other important information is found in Table 3-1. Note that heating has been ignored in this calculation.

The results shown in Figure 3-2 and Figure 3-3 suggest that there are other effects at work in the determination of  $T_0$  for 1.55  $\mu\text{m}$  lasers. Even if the ideal case is used for a 5 quantum well active region, the  $T_0$  value is only 51.9 K for a  $3 \times 1000 \mu\text{m}^2$  device – well below that values of 980-nm in-plane lasers. The two main issues that determine the  $T_0$  for 1.55  $\mu\text{m}$  lasers – Auger recombination and carrier overflow – will be addressed in the next two sections.

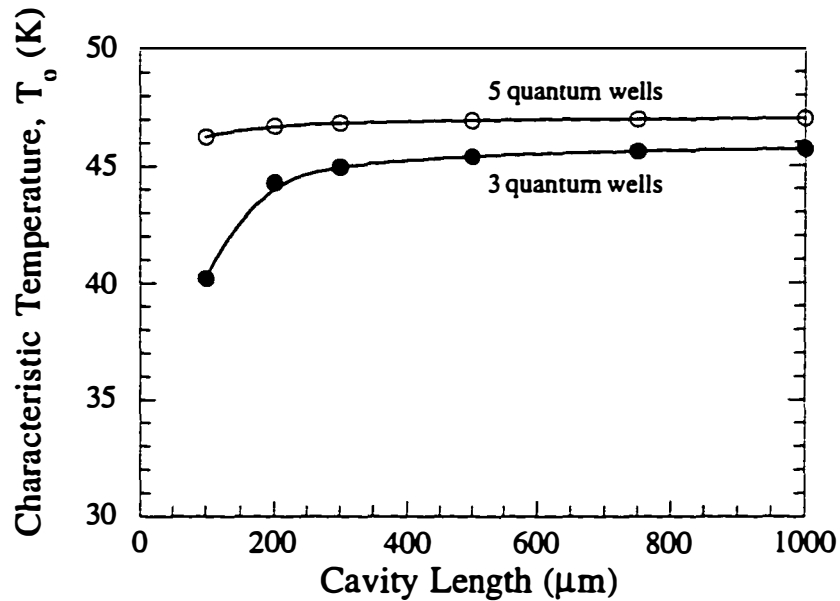


**Figure 3-3** Calculated  $T_o$  values for a 3  $\mu\text{m}$  stripe width device with 3 or 5 quantum well active region. Other important information is found in Table 3-1. Note that heating has been ignored in this calculation.

The other important parameters for 1.55  $\mu\text{m}$  lasers in fiber-optic communication systems is the change in the slope efficiency of the laser as the temperature changes and  $T_o^{10\text{mW}}$ . For this structure, the slope efficiency with cleaved facets ( $R_1=R_2=0.3$ ) is 0.23 W/A per facet at 20°C. This value decreases to 0.18 and 0.09 W/A as the temperature increases (without heating included) to 100°C and 200°C respectively. What this change in slope efficiency means is that it more current will be needed to reach an output power of 10 mW.  $T_o^{10\text{mW}}$  versus cavity length is shown below for cleaved facets with 3 quantum wells and 5 quantum wells in the active region.

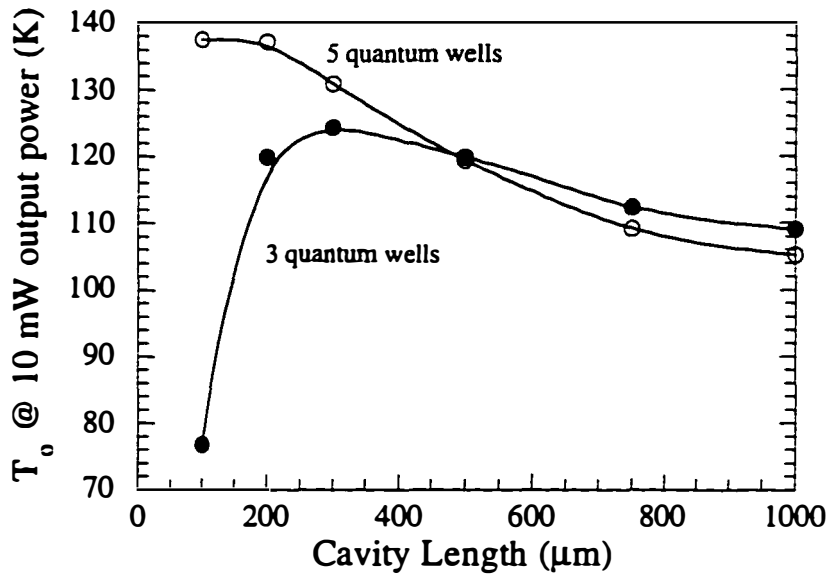


**Figure 3-4** Calculated current to maintain 10 mW per facet versus operating temperature for a three quantum well 1.55  $\mu\text{m}$  laser with a 300  $\mu\text{m}$  cavity length. Other important information is found in Table 3-1. Note that heating has been ignored in this calculation.

Figure 3-4 shows that cavity length changes do affect  $T_o^{10mW}$  due to changes in the differential efficiency. For 3 quantum wells, the peak  $T_o^{10mW}$  value is 124.3 K at a 300  $\mu\text{m}$  cavity length; for 5 quantum wells, the peak  $T_o^{10mW}$  value is 134.5 K at a 100  $\mu\text{m}$  cavity length.

Before leaving this section, the maximum operating temperature,  $T_{\text{max}}$ , is calculated in two ways. The first is to determine the temperature at which the threshold current density is between 10 and 20  $\text{kA}/\text{cm}^2$ . The second is to use the theoretical model with heating. Figure 3-5 shows the threshold current as a

function of temperature for a 3 and 5 quantum well active region. In both cases, a deviation of the slope of  $I_{th}$  vs. temperature occurs between 60 and 80 °C. In the case of the 3 quantum wells, the deviation is closer to 60°C while it occurs near 80°C for the 5 quantum well active region. This is in accordance to the work of Seki outlined in Section 2.1.3. The values of  $T_{max}$  which correspond to a threshold current density of 10 kA/cm<sup>2</sup> are 131°C for a 3 quantum well active region and 148°C for a 5 quantum well active region. The effects of heating as determined using the iterative approach of Section 2.2.3 is shown in Figure 3-6.

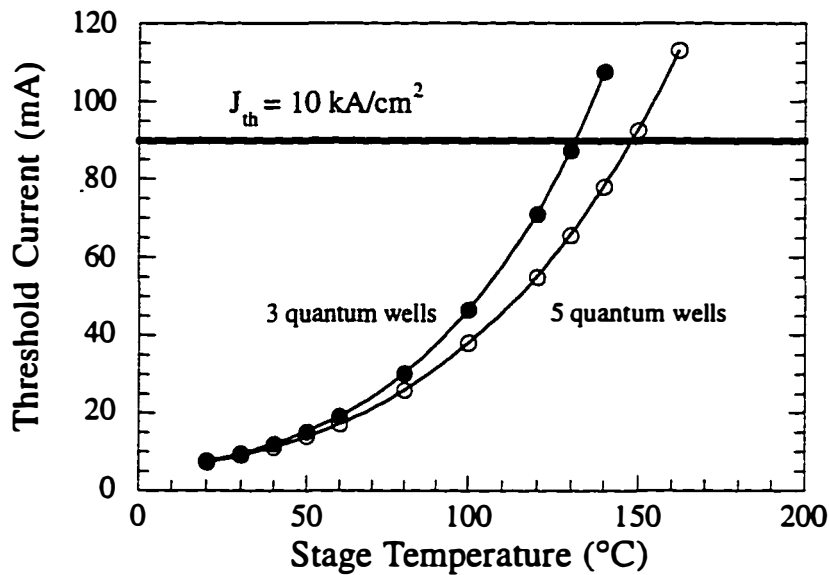


**Figure 3-5** Threshold current versus temperature for a 3 or 5 quantum well active region with a 300  $\mu\text{m}$  cavity length. In this calculation heating has been ignored. Other important parameters can be found in Table 3-1.

The extra threshold current needed to overcome the heating effects increases monotonically with temperature. Below about 100°C, the extra current needed is small (< 4 and 2 mA for the 3 and 5 quantum wells active regions).

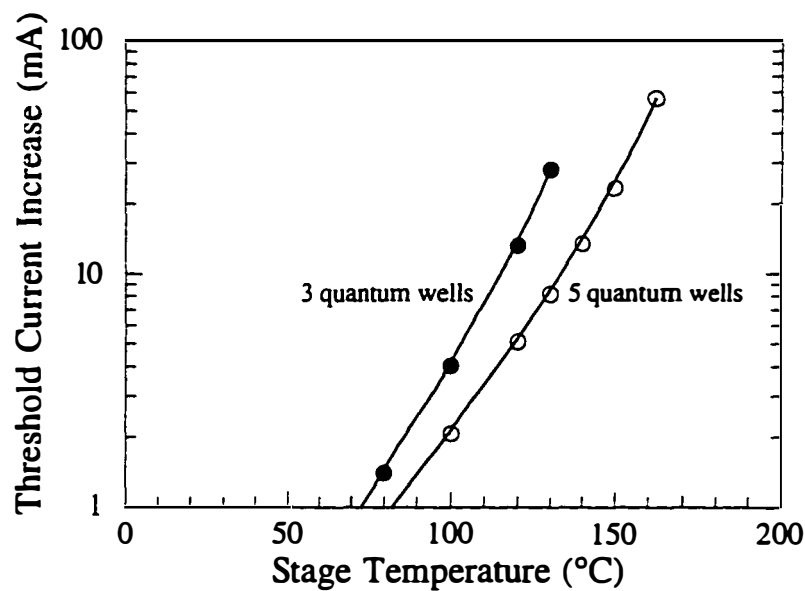


**Figure 3-6** Threshold current increase as a function of the heat sink temperature for a 3 and 5 quantum well active region at a cavity length of 300  $\mu\text{m}$ . Other important information about the laser can be found in Table 3-1.

As the temperature increases beyond 100°C, this extra current increase dramatically until the iterative approach of Section 2.2.3 no longer achieves a solution. For the 3 quantum well active region,  $T_{\text{max}}$  occurs at 136°C; for the 5 quantum well active region  $T_{\text{max}}$  increases to 164°C due to the lower operating point on the gain curve. In fact, the 5 quantum well sample can accommodate more heating before the device no longer works. This is illustrated by the



change in active region temperature as shown in Figure 3-7. Here we see that a 1°C increase in active region temperature at threshold does not occur until about 50-60°C. However, the temperature continues to rise monotonically until it reaches a maximum value of 13.3 and 25°C for a 3 and 5 quantum well active region.

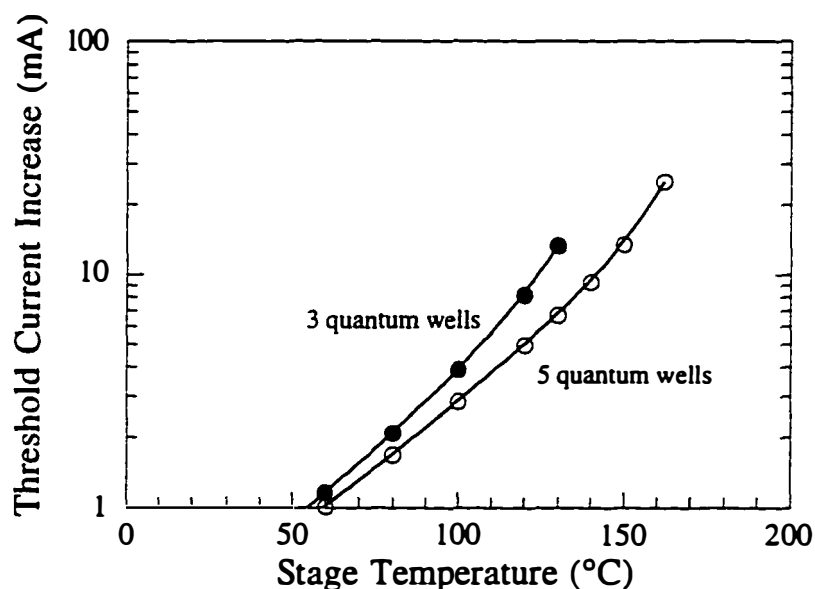


**Figure 3-7** Active region temperature increases as a function of the heat sink temperature for a 3 and 5 quantum well active region at a cavity length of 300  $\mu\text{m}$ . Other important information about the laser can be found in Table 3-1.

In making direct comparisons to the literature the losses in short cavity devices are reduced using some type of HR coating applied to the facets. To look at these effects in more detail, the total losses of the laser (mirror losses plus *non-carrier* losses) were changed by changing the reflectivity of the laser facets.

The results, in terms of  $T_{\max}$ , are shown in Figure 3-8.

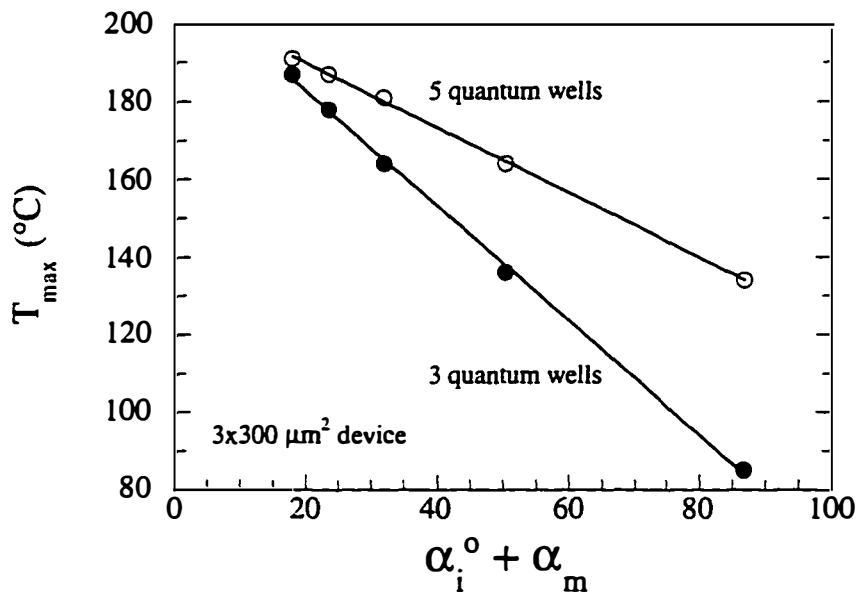


**Figure 3-8** Theoretical maximum operating temperature of a 1.55  $\mu\text{m}$  laser as a function of non-carrier losses. This calculation assumes the optical confinement factors defined in Table 3-1 and device heating effects are included.

From Figure 3-8,  $T_{\max}$  can be fitted to a linear function of loss given by

$$\begin{array}{ll}
 214 - 1.43(\alpha_i^o + \alpha_m) \text{ } ^\circ\text{C} & \text{3 quantum wells} \\
 206.4 - 0.835(\alpha_i^o + \alpha_m) \text{ } ^\circ\text{C} & \text{5 quantum wells}
 \end{array} \quad (3-2)$$

Equation (3-2) shows that  $T_{\max}$  values of greater than 200°C should be achievable.

This does not correspond with experimental results presented in the literature. The discrepancy, I believe, is due to the simple expression used to calculate the thermal impedance of the device which does not take into account the high difference in thermal conductivity between InP and GaInAsP alloys. Figure 3-9 shows the effects of a change in the thermal conductivity used in Equation (2-25) on  $T_{\max}$ .

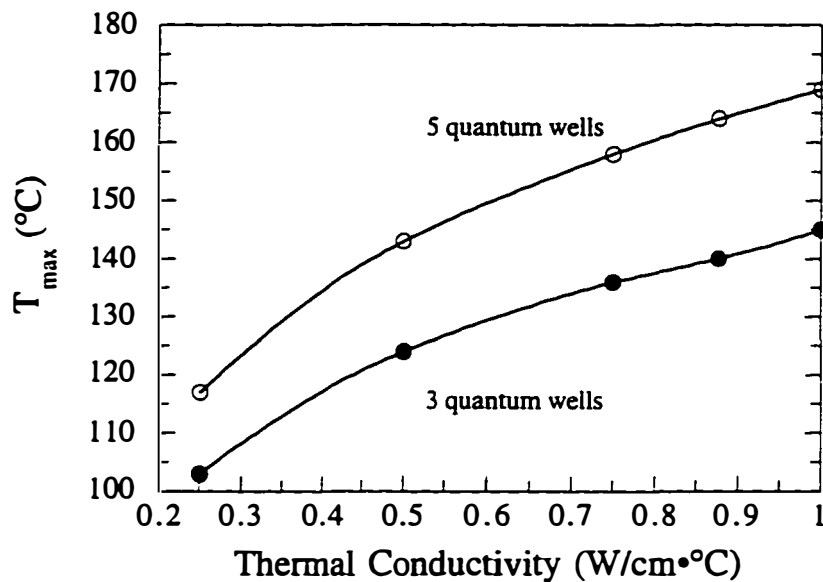


**Figure 3-9** The maximum operating temperature of a 3 or 5 quantum well laser with a 300  $\mu\text{m}$  cavity length as the thermal conductivity used in Equation (2-25) is changed. In this calculation cleaved facets are assumed. Other important parameters are shown in Table 3-1.

What Figure 3-9 shows is that the thermal conductivity used to determine a thermal impedance is important in calculating a maximum operating temperature. From the work of Dubravko Babic in 1.55  $\mu\text{m}$  VCSELs[1] a simple analytical expression for the thermal impedance leads to a conductivity of 0.5 W/cm $\cdot$ °C. Using this value in my calculations leads to a much more realistic  $T_{\text{max}}$  value when compared to the literature.

### 3.2 Auger Recombination Effects

In this section, the effects of a change in Auger recombination are investigated. The gain versus current density curves are shown in Figure 3-10 for different Auger coefficients at 20°C. Here we see the improvement clearly. For example, the transparency current density per well (the current density at zero material gain) is reduced from 144 A/cm $^2$  to 40 A/cm $^2$  for an order of magnitude reduction in the Auger coefficient. Figure 3-11 show the  $T_0$  values calculated between 20 and 80°C for a 3 quantum well active region. An increase in  $T_0$  from 42.2 K to 68.4 K for a 1000  $\mu\text{m}$  cavity length is calculated when the Auger coefficient is reduced by a order of magnitude; this improvement has been predicted by others [2-5]. This is due to the improvement in the parameter  $J_{tr}^{\dagger}$  of Equation (2-5). For the quantum active region here,  $J_{tr}^{\dagger}$  varies from 3.55 for an Auger coefficient of  $10^{-28}$  cm $^6$ /s at 20°C to 2.04 for a  $10^{-29}$  cm $^6$ /s Auger coefficient. Thus  $J_{tr}^{\dagger}$  is the only factor in the expression of  $T_0$  that is drastically affected by a change in Auger. The other two parameters --  $\eta_i^{\dagger}$  and  $\Delta\alpha$  -- are affected by changes in the carrier density and not the current. Therefore their values are not a function of the Auger recombination.

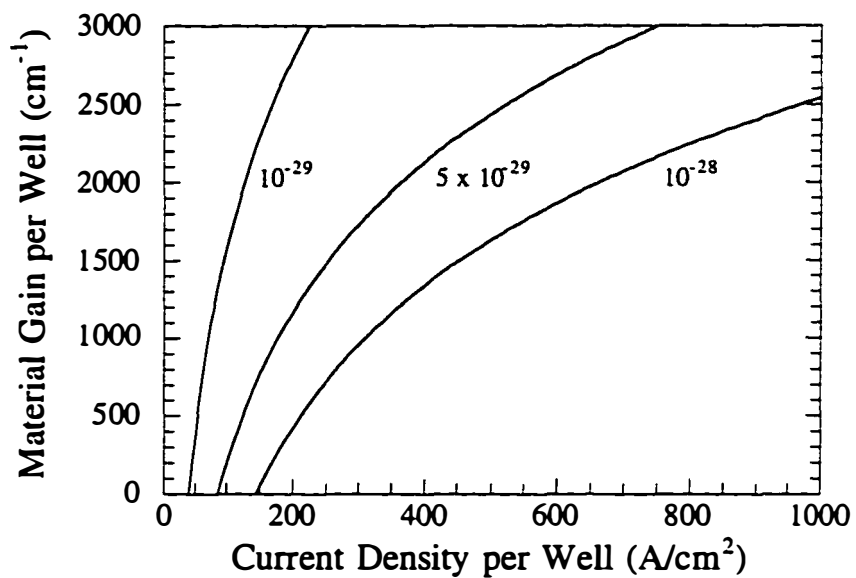


**Figure 3-10** Gain versus current density curves with Auger coefficients from  $10^{-28}$  to  $10^{-29}$  cm<sup>6</sup>/s at 20°C.

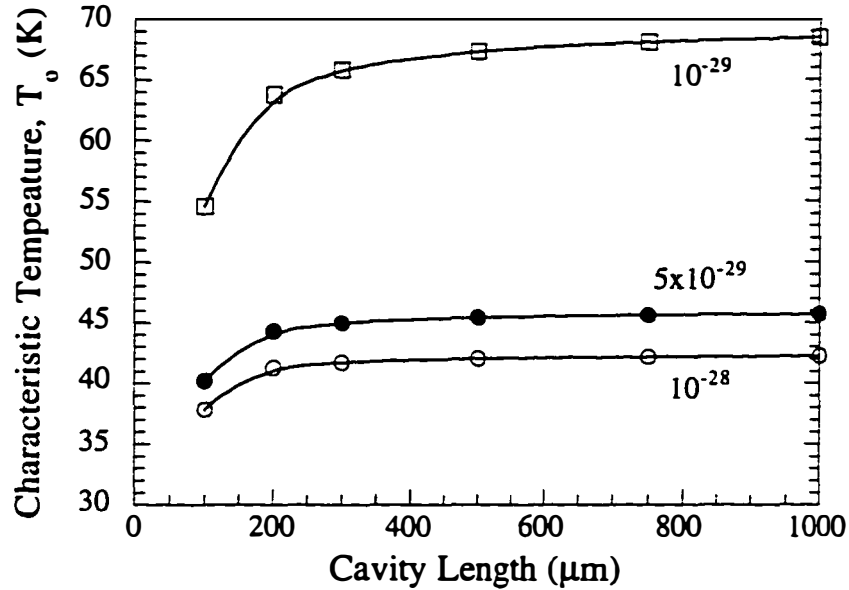


**Figure 3-11** Plot of  $T_0$  values versus cavity length for a 3 quantum well active region with different Auger coefficients. In all cases a 60 meV activation energy is assumed. The  $T_0$  values for each case is also shown above without the presence of device heating.

One important thing to note here is that it takes a significant reduction in Auger to improve the  $T_0$  values for 1.55  $\mu\text{m}$  lasers. In fact, even with a reduction to  $10^{-29}$   $\text{cm}^6/\text{s}$ , the  $T_0$  values are still much lower than those of GaAs-based lasers -- an issue I will address further in the next section. Another parameter which can be changed is the activation energy assumed for the Auger process. In Table 3-1 I have assumed an activation energy of 60 meV. As the activation energy changes,  $T_0$  and other parameters are affected. The effect on  $T_0$  is shown below in Figure 3-12.

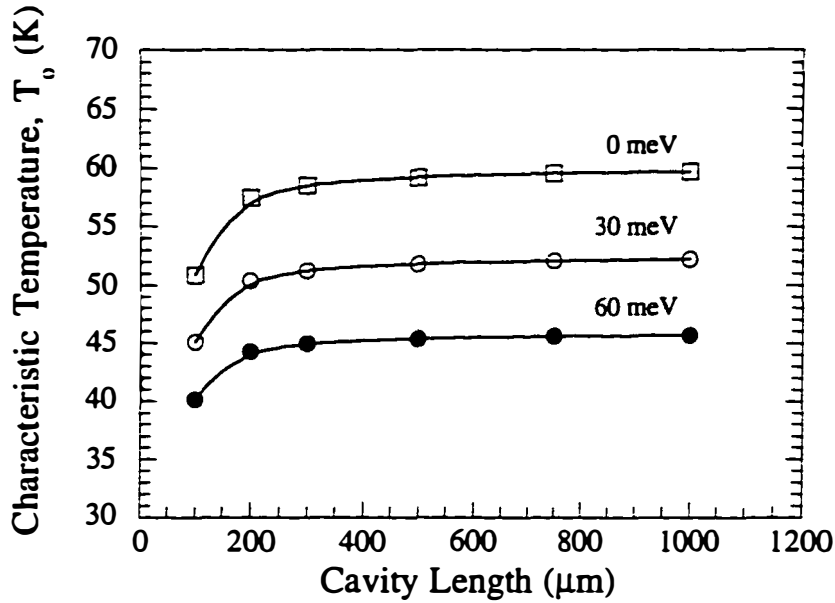


**Figure 3-12** Plot of  $T_o$  values versus cavity length for different Auger activation energies. The  $T_o$  values for each case is also shown above without the presence of device heating.

In terms of the parameter that is important for optical communications,  $T_o^{10mW}$ , a reduction in the amount of Auger recombination leads to a significant improvement. These results are summarized in Table 3-2. As opposed to the effect of Auger reduction on  $T_o$ , Auger reduction has a strong effect on  $T_{max}$ . An increase to an Auger coefficient of  $10^{-28}$  cm<sup>6</sup>/s leads to a reduction of  $T_{max}$  of 100°C; a decrease of Auger to  $10^{-29}$  cm<sup>6</sup>/s leads to an increase in  $T_{max}$  of above 200°C – near the value for GaAs-based lasers. This is due to a *reduction in the actual value of  $J_r$  with Auger* which matters in determining  $T_{max}$ .

**Table 3-2** Summary of the  $T_o$ ,  $T_o^{10mW}$ , and  $T_{max}$  values as the Auger coefficient at 20°C is changed. In all cases an activation energy of 60 meV is assumed. Other important information is found in Table 3-1.

Parameter	Auger Coefficient at 20°C (cm <sup>6</sup> /s)		
	10 <sup>-28</sup>	5 x 10 <sup>-29</sup>	10 <sup>-29</sup>
$T_o$ @ 500 $\mu$ m 3 quantum wells	42 K	45.4 K	65.8 K
$T_o$ @ 500 $\mu$ m 5 quantum wells	43.2 K	47 K	71.3 K
$T_o^{10mW}$ @ 300 $\mu$ m 3 quantum wells	91 K	124.3 K	200.6 K
$T_o^{10mW}$ @ 300 $\mu$ m 5 quantum wells	96.8 K	130.8 K	214.6 K
$T_{max}$ , 3 quantum wells	107°C	136°C	> 200°C
$T_{max}$ , 5 quantum wells	122°C	164°C	> 200°C

This again suggests that  $T_o$  is not necessarily the best parameter by which to characterize 1.55  $\mu$ m lasers and that a reduction in Auger can improve 1.55  $\mu$ m laser performance as expected. Table 3-2 summarizes the findings of how the Auger coefficient affects the results in terms of  $T_o$ ,  $T_o^{10mW}$ , and  $T_{max}$  with device heating effects included.



### 3.3 Carrier Overflow Effects

The procedure outlined in Chapter 2 is now used to model 1.55  $\mu\text{m}$  lasers without carrier overflow effects. Figure 3-13 shows a calculation of the threshold current versus temperature.

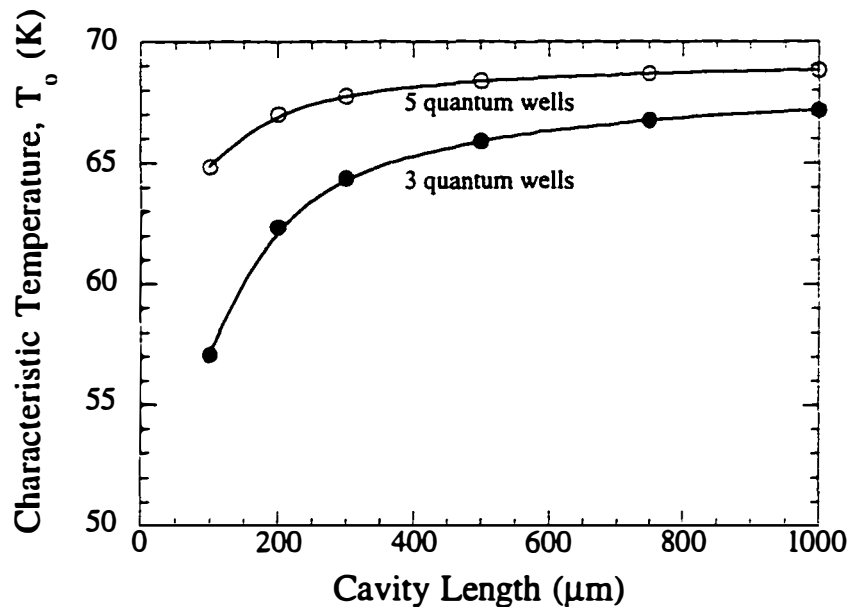


**Figure 3-13** Calculated  $T_0$  values for a 3 and 5 quantum well 1.55  $\mu\text{m}$  lasers without carrier overflow. Other important information is found in Table 3-1. Note that device heating is not included.

A comparison of Figure 3-1 and Figure 3-13 shows that the elimination of carrier overflow effects leads to improved characteristics in terms of  $T_0$ . For example, at a cavity length of 1000  $\mu\text{m}$ ,  $T_0$  improves from 45.7 and 51.9 K for a 3 or 5 quantum well active region with carrier overflow to 67.2 and 68.9 K

without it. This marks a predicted improvement of 47 and 33% respectively. When the amount of Auger recombination is changed by either a reduction in the actual coefficient or the activation energy, the improvement in  $T_0$  without carrier overflow improves. In the case of an elimination of carrier overflow, both  $J_{tr}^{\dagger}$  and  $\Delta\alpha$  are reduced. For an Auger coefficient of  $5 \times 10^{-29} \text{ cm}^6/\text{s}$  at  $20^\circ\text{C}$ ,  $J_{tr}^{\dagger}$  decreases to 1.38. In addition,  $\Delta\alpha$  – which is only due to losses in the quantum wells – is less than  $1.5 \text{ cm}^{-1}$ . Elimination of carrier overflow in  $1.55 \text{ }\mu\text{m}$  lasers also has an effect on  $T_c$  and  $T_{max}$ . As defined by Seki,  $T_c$  represents the point at which the external differential efficiency deviates from an exponential dependence. In the case of not carrier overflow, this will occur at high temperature since the only losses in the system are due to the quantum wells. From my calculations, this occurs around  $140^\circ\text{C}$ . Table 3-3 summarize the  $T_0$ ,  $T_0^{10mW}$  and  $T_{max}$  values calculated, with all factors included, in this chapter with and without carrier overflow.

### 3.4 Summary

In this and the preceding chapter, a modeling approach for in-plane semiconductor lasers has been presented. With respect to the results presented in this chapter, some important conclusions have been drawn. Using measurable parameters, I have shown that  $T_0$  is related to the *change in these parameters as the temperature is increased*. Most notably, the parameters  $J_{tr}^{\dagger}$  and  $\eta_i^{\dagger}$  have the largest effects on  $T_0$ . This suggest that minimization of the threshold current will not necessarily lead to improved  $T_0$  values since  $J_{tr}^{\dagger}$  and  $\eta_i^{\dagger}$  are related to the design of the laser structure.  $T_{max}$ , like  $T_0$ , is determined mainly by the value of  $J_{tr}$  at room temperature. However since heating effects ultimately determine the maximum operating temperature,  $T_{max}$  can be improved by minimizing the threshold current of the device.

**Table 3-3** Summary of  $T_o$ ,  $T_o^{10mW}$  and  $T_{max}$  values calculated using the procedure outlined in Chapter 2. In all cases, the data of Table 3-1 was used and cleaved facets were assumed.

Auger Coefficient @ 293 K (cm <sup>6</sup> /s)		10 <sup>-29</sup>	5 x 10 <sup>-29</sup>			10 <sup>-28</sup>	
Auger Activation Energy (meV)		60	0	30	60	60	
Carrier Overflow	$T_o$ (K) @ 1000 $\mu$ m	68.4	59.7	52.2	45.7	42.2	
	$T_o^{10mW}$ (K)	201 @ 300 $\mu$ m				124 @ 300 $\mu$ m	92.3 @ 300 $\mu$ m
	$T_{max}$ (°C)	> 200				136	100
No Carrier Overflow	$T_o$ (K) @ 1000 $\mu$ m	131.9	94.8				
	$T_o^{10mW}$ (K)	466 @ 300 $\mu$ m					288 @ 300 $\mu$ m
	$T_{max}$ (°C)	> 200		> 200	> 200		

In this chapter, I have shown that for an Auger coefficient at 20°C of  $5 \times 10^{-29}$  cm<sup>6</sup>/s and a 60 meV activation energy, a  $T_o$  value of 45.7 K is calculated for a  $3 \times 1000 \mu\text{m}^2$  device; for a  $3 \times 300 \mu\text{m}^2$  device,  $T_o^{10mW}$  and  $T_{max}$  have values of 124 K and 136 °C with cleaved facets.

In the literature, two factors -- Auger recombination and carrier overflow -- have been ascribed to be the main causes of the low  $T_o$  and  $T_{max}$  values in 1.55  $\mu$ m in-plane lasers. In both cases, these factors can be viewed in terms of

inefficiency. For Auger recombination, every electron and hole that recombines by this means does not provide gain to the lasing mode and thus more carriers (i.e., current) is needed to obtain the required gain from the active region. In the case of carrier overflow, carriers in the barrier and SCH regions of the device also do not provide gain to the lasing mode; furthermore, their interactions with the lasing mode cause additional losses which force the active region to provide more gain and hence need more current to obtain the required gain. In terms of the parameters  $T_o$ ,  $T_o^{10mW}$  and  $T_{max}$ , a reduction in Auger recombination has a sizable effect. For an order of magnitude reduction in the Auger coefficient,  $T_o$  increases from 45.7 K to 68.4 K for a  $3 \times 1000 \mu\text{m}^2$  device. Similarly,  $T_o$ ,  $T_o^{10mW}$  and  $T_{max}$  increases by 62% and  $T_{max}$  increases from 136°C to over 200°C for a  $3 \times 300 \mu\text{m}^2$  device. When carrier overflow effects are eliminated, the effects on  $T_o$ ,  $T_o^{10mW}$  and  $T_{max}$  are equally dramatic. The calculated  $T_o$  value increases from 45.7 K to 67.2 K for a  $3 \times 1000 \mu\text{m}^2$  device. This is nearly equivalent to *a five-fold reduction in Auger recombination!* If there is no temperature dependence in the Auger recombination (i.e., no activation energy), the increase is even more dramatic – up to 94.8 as compared to 59.7 K with carrier overflow effects. In terms of  $T_o^{10mW}$  the calculated values increases by 132 % over the case with carrier overflow effects;  $T_{max}$  is calculated to be over 200°C with no carrier overflow effects. When both carrier overflow and Auger recombination are reduced, the  $T_o$  values calculated start to approach those seen in GaAs-based lasers. This shows that both Auger recombination and carrier overflow effects are important.

From a device design perspective, Auger recombination comes with active regions at 1.55  $\mu\text{m}$  lasers. So, the main result in terms of designing 1.55  $\mu\text{m}$  lasers with improved temperature performance is a reduction in carrier overflow effects. The issues involved in designing 1.55  $\mu\text{m}$  lasers with reduced carrier overflow are the subject of the next chapter.

### 3.5 References

- [1] D. I. Babic, "Double-Fused Long-Wavelength Vertical-cavity Lasers." Dissertation, University of California, Santa Barbara, 1995.
- [2] S. Seki, H. Oohasi, H. Sugiura, T. Hirono, and K. Yokoyama, "Dominant mechanisms for the temperature sensitivity of 1.3  $\mu\text{m}$  InP-based strained-layer multiple-quantum-well lasers" *Applied Physics Letters* **67**, 1054 (1995).
- [3] S. Seki and K. Yokoyama, "Theoretical analysis of temperature sensitivity of differential gain in 1.55  $\mu\text{m}$  InGaAsP-InP quantum-well lasers" *IEEE Photonics Technology Letters* **7**, 251 (1995).
- [4] S. Seki, H. Oohasi, H. Sugiura, T. Hirono, and K. Yokoyama, "Dominant mechanism for limiting the maximum operating temperature of InP-based multiple-quantum-well lasers" *Journal of Applied Physics* **79**, 2192 (1996).
- [5] S. Seki, K. Yokoyama, and P. Sotirelis, "Theoretical analysis of high-temperature characteristics of 1.3  $\mu\text{m}$  InP-based quantum-well lasers" *IEEE Journal on Selected Topics in Quantum Electronics* **1**, 264 (1995).



## **4. Design of 1.55 $\mu\text{m}$ Lasers with Reduced Carrier Overflow**

In this chapter, methods of reducing carrier overflow in 1.55  $\mu\text{m}$  lasers are explored. First, a brief review of the literature on how other researchers have addressed this problem is given. Following this, my approach, which involves the technique of direct wafer bonding (referred to as wafer fusion in this dissertation) is described. An introduction to wafer fusion is followed by design issues for 1.55  $\mu\text{m}$  lasers using wafer fused structures and my structural designs.

### **4.1 Methods of Reducing Carrier Overflow in 1.55 $\mu\text{m}$ Lasers**

As shown in Chapter 3, there is a marked improvement in many device characteristics if the effects of carrier overflow can be eliminated. This section is concerned with methods of achieving this goal. By carrier overflow in this chapter, we are concerned not only with carrier occupation of barrier and waveguide regions (as was the case in Chapter 3) but also carrier leakage out of the entire waveguide region which was not included in the modeling approach described in Chapter 2. The different methods that are typically used to reduce these carrier overflow mechanisms are described below.

#### *4.1.1 Raising the Barrier Height in GaInAsP-based Multiple Quantum Well Lasers*

Compositional changes in the quaternary alloy GaInAsP lead to band gap energy changes while keeping it lattice-matched to InP. Thus, one approach to reduced carrier overflow is to make the band-gap of the GaInAsP barriers and waveguide regions larger. Using the structure of the laser in Chapter 2 (see

Figure 2-3), Figure 4-1 below shows the effect of raising the barrier and SCH region's GaInAsP composition on the barrier height and overlap of the lasing mode with the quantum well active region.

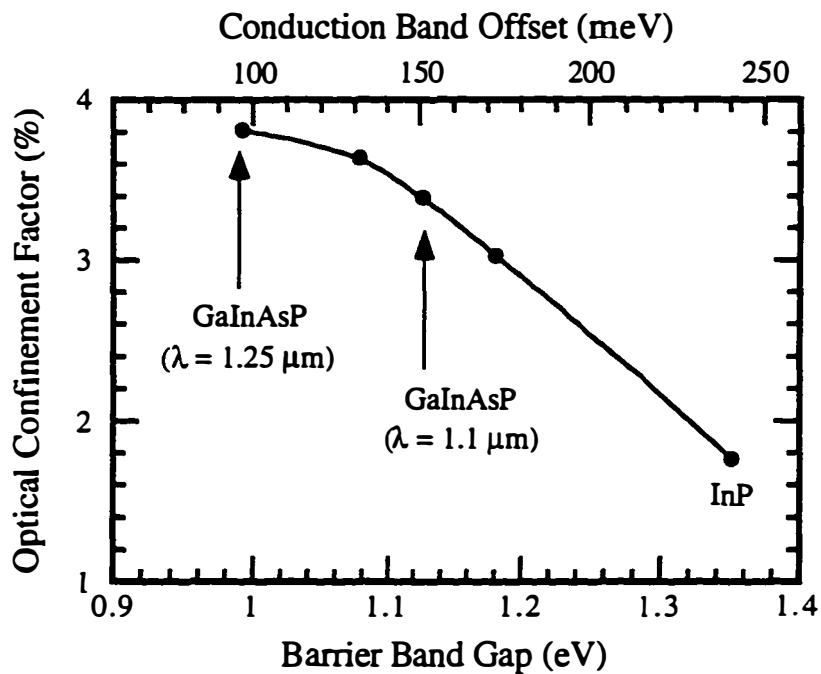


**Figure 4-1** Optical confinement factor for a 3 quantum well active region as the barrier height is changed.

What this shows is that a trade-off exists in the design of 1.55  $\mu\text{m}$  lasers. As the conduction band offset for the quantum wells is increased (reduced carrier occupation of barrier and SCH regions of the laser)<sup>1</sup>, the optical confinement

<sup>1</sup> The amount of carrier leakage out of the active region is not significantly changed by a change in the GaInAsP composition of the waveguide region at room temperature.



factor of the active region decreases. If InP is used as the barrier material, the electron confinement will increase by  $\approx 143$  meV (5.5 kT at room temperature) while the optical confinement factor decreases by 54 %. This reduction in the confinement factor causes the devices to operate on a higher point on the quantum well's gain curve leading to more current needed to achieve lasing. In addition, the temperature sensitivity of the laser increases.

The effect of the barrier band gap has been studied by Nobuhara and co.-workers where they varied the band gap of the GaInAsP from 1.4  $\mu\text{m}$  to 1.1  $\mu\text{m}$  [1]. This change in band gap resulted in a 34% decrease in the optical confinement factor. The results showed that at room temperature for five 4 nm quantum wells, the threshold current was constant for barrier band gaps from 1.4  $\mu\text{m}$  to 1.2  $\mu\text{m}$  and increased for larger ones. As the temperature increased, the small band gaps increased due to carrier overflow into the barrier regions (as measured by the emission spectra) and the larger band gap's current increased due to either a reduction in confinement or inhomogeneous carrier injection [1]. Inhomogeneous carrier<sup>ii</sup> injection is most likely the culprit because the threshold current was higher at 20°C for the 1.1  $\mu\text{m}$  barrier band gap.

#### 4.1.2 Use of AlGaInAs as a Barrier Material in 1.55 $\mu\text{m}$ Lasers

In order to reduce the problems of inhomogeneous carrier injection which are believed to hamper the performance of GaInAsP-based 1.55  $\mu\text{m}$  lasers, many groups turned to AlGaInAs as a barrier material. One of the main advantages of AlGaInAs over GaInAsP is that 70-75% of the band gap difference is predicted to be in the conduction band as compared to 40% for GaInAsP [2,3]. Many researchers have used AlGaInAs grown by either metalorganic chemical vapor

---

<sup>ii</sup> Probably the holes since their barrier height is now approximately 225 meV.

deposition [4-8] or molecular beam epitaxy [9-15]. One of the main difference in structures is that, usually, the MBE-grown structure use AlInAs as the p- and n-cladding layers of the laser while with MOCVD the choice of AlInAs and InP exists<sup>iii</sup>. Table 4-1 below details many of the material parameter differences between AlGaInAs and GaInAsP.

**Table 4-1** Material Parameters for AlGaInAs versus GaInAsP taken from Reference [2]

	AlGaInAs	GaInAsP
Band Gap @ 300K (eV)	0.75 to 1.45	0.75 to 1.34
$m_c/m_0$	0.041 to 0.083	0.041 to 0.08
$m_v/m_0$	0.47 to 0.87	0.47 to 0.85
$\mu$ ( $\text{cm}^2/\text{V}\cdot\text{s}$ )	13000 to 4600	13000 to 6000
$\Delta E_c/\Delta E_g$	0.75	0.4
Refractive Index	3.58 to 3.21	3.58 to 3.17

However, in either case, the same problem exists in these lasers as the barrier height is raised – the optical confinement factor of the lasing mode decreases. Device results for AlGaInAs barrier and quantum well structures are very comparable to that of GaInAsP-based lasers. For three 1.2% compressively strained  $\text{Ga}_{0.29}\text{In}_{0.71}\text{As}$  quantum wells with 5 nm  $\text{Al}_{0.28}\text{Ga}_{0.48}\text{In}_{0.42}\text{As}$  barriers, threshold current densities of 400  $\text{A}/\text{cm}^2$  were obtained for an infinite cavity

---

<sup>iii</sup> With the advent of three-zone solid phosphorus crackers in MBE technology [16-21], this distinction can be eliminated.

length [22]. Favorable results have also been achieved by MBE-grown structures where threshold current densities as low as  $538 \text{ A/cm}^2$  for three 10 nm  $\text{Al}_{0.1}\text{Ga}_{0.2}\text{In}_{0.7}\text{As}$  quantum wells with 5 nm  $\text{Al}_{0.3}\text{Ga}_{0.18}\text{In}_{0.52}\text{As}$  barriers have been achieved[14]. Other improvements that have been seen in these devices are an enhanced differential gain [23,24] and good high speed modulation characteristics [12,13,25].

An increase in  $T_0$  has been observed for these lasers. Reports of  $T_0$  values of 100K around  $20^\circ\text{C}$  and 60K between  $30\text{-}70^\circ\text{C}$  with  $\text{AlGaInAs}$  barriers [26] and a high of 86K with  $\text{AlInAs}$  barriers [27] have published. In the case of the study with  $\text{AlInAs}$  barriers described in Reference [27], different compositions of  $\text{AlGaInAs}$  were explored with no change in the quantum well composition. A summary of their data appears below.

**Table 4-2** Data taken from Reference [27] on the Performance of 1.55  $\mu\text{m}$  lasers with 1.5  $\mu\text{m}$  cavity widths and 300  $\mu\text{m}$  cavity lengths under CW conditions. In all cases, 9 nm unstrained  $\text{GaInAs}$  quantum wells were used with 3 nm barriers. No facet coating were used in these devices.

Well Number	$\Delta E_c$ (meV)	$\Delta E_v$ (meV)	$I_{th}$ (mA)	$T_0$ (K)	Barrier Composition
6	500	214	9.6	44	$\text{Al}_{0.47}\text{In}_{0.53}\text{As}$
10	270	116	11.5	69	$\text{Al}_{0.29}\text{Ga}_{0.18}\text{In}_{0.53}\text{As}$
10	380	163	10	75	$\text{Al}_{0.39}\text{Ga}_{0.08}\text{In}_{0.53}\text{As}$
10	500	214	19.5	74.2	$\text{Al}_{0.47}\text{In}_{0.53}\text{As}$
16	500	214	36.4	86	$\text{Al}_{0.47}\text{In}_{0.53}\text{As}$

Note that there are several similarities to this data and the data discussed for GaInAsP-based lasers in Reference [1]. As the barrier height increases, the threshold current displays a minimum and increases sharply for a continued increase in barrier height. In addition, for the highest conduction band offset, the threshold current increases by 380% from 6 to 16 wells -- strongly suggesting non-uniform carrier effects. For reference, valence band offsets of 163 and 214 meV in AlGaInAs roughly corresponds to GaInAsP barriers with a 1.21 and 1.12  $\mu\text{m}$  band gap respectively. Note however, that even though non-uniform injection of carriers exists, the  $T_0$  for the case of AlInAs barriers continues to increase as the number of wells increases. This suggests that even though there is non-uniform injection, most of the quantum wells are producing enough gain to keep the quasi-Fermi level in the conduction band low in the well.

#### 4.1.3 Other Approaches

Before ending this section on reducing carrier overflow, I would like to briefly mention briefly other studies that have been done to investigate carrier overflow effects. They are outlined below.

##### *Carrier Leakage Outside the Waveguide Region*

Many different approaches have been used to reduce carrier leakage out of the waveguide region of the laser. These approaches can be classified into two different classes: *band-gap engineered* designs and *doping-profile designs*. In the first class of designs, the goal is to find a method of providing an enhanced barrier for electrons on the p-side of the laser. Two different schemes have been used to achieve this: multi-quantum well barriers (MQBs) in the cladding and SCH regions [11,28,29] and the use of a thin AlInAs electron and/or hole stopper layers [30-32]. In all of the cases of these two methods, no or slight increases in

$T_0$  are seen. The main effect seen, however, is an improvement in the reduction of the differential quantum efficiency as the temperature increases. In the doping profile design approaches [33-35], it is proposed that the doping profile of the waveguide/p-cladding interface is important in reducing carrier leakage. Direct measurements using an integrated  $p^+ n^- n^+$  electron collector on the p-side of the device [36] show that this leakage current can account for 20% of the total threshold current at 50°C and can be reduced by providing a high p-doping at this interface.

#### *Growth on Ternary Substrate for Deep Potential Wells*

Another method that has been used to reduced carrier overflow is the growth of laser active regions on GaInAs substrates [37-41]. Based upon the calculations in Reference [38], the conduction band offset increases from 179 meV to 308 meV and the valence band offset increase from 40 meV to 145 meV. Theoretical calculations predict modulation bandwidths of greater than 75 GHz and  $T_0$  for a 1.3  $\mu\text{m}$  lasers of 173K [38,39]. Experimentally, the researcher have achieved a threshold current density of 222 A/cm<sup>2</sup> and a characteristic temperature of 221K at a wavelength of 1.03  $\mu\text{m}$  [41]. The ability to incorporate indium into the quantum wells currently limits the wavelength to values shorter than 1.3 or 1.55  $\mu\text{m}$ .

In summary, many approaches can be used to reduce the carrier overflow in 1.55  $\mu\text{m}$  lasers. In the design of any laser, the following factors should be addressed:

- high electron confinement for reduced occupation of barrier and waveguide states without a significant decrease in  $\Gamma_{acr}$ .
- low hole confinement for uniform injection.
- high offsets into the p-cladding for reduced carrier leakage

These issues are addressed in the next section where I describe my approach to the design of 1.55  $\mu\text{m}$  lasers with reduced carrier overflow.

## 4.2 Wafer Fusion for 1.55 $\mu\text{m}$ Lasers with Reduced Carrier Overflow

In the previous section, many methods for reducing the effects of carrier overflow were described. In this section, my approach to the design of 1.55  $\mu\text{m}$  lasers using wafer fused structures is outlined. After an introduction to wafer fusion, the design issues of 1.55  $\mu\text{m}$  lasers are investigated again and my solutions to the issues are detailed.

### 4.2.1 Introduction to Wafer Fusion

The idea of wafer fusion, or direct wafer bonding, has been around for awhile in the silicon industry -- mainly in the area of silicon-on-insulator technology [42-48]. However, in the use of wafer fusion for improving the performance of 1.55  $\mu\text{m}$  lasers, compound semiconductors must be used. Wafer fusion of III-V semiconductors was first demonstrated in 1984[49]; however, it was in 1990 that the results became encouraging for optoelectronic devices [50]. Since then, wafer fusion has been used in a variety of applications. The main advantage of wafer fusion is that compounds with large lattice and thermal expansion mismatches can be joined permanently -- something that has been very hard to achieve by heteroepitaxy without threading dislocations forming<sup>iv</sup>. Before giving the reader a sense of the diversity of applications for which wafer fusion has been used, I will first delve into what is known about wafer fusion

---

<sup>iv</sup> For a good discussion of why this is the case, the reader is referred to Reference [51].

### *The Fusion Process*

The actual process of direct wafer involves three main steps: (i) the contacting of two samples (typically at room temperature in air), (ii) annealing the bonded samples to elevated temperatures to strengthen the bond, and (iii) selective removal of one of the substrates. Most of the work that has been done to date to understand this process on a fundamental level has been done in silicon and is outlined here.

In the direct wafer bonding of silicon to either silicon or silicon dioxide, surface preparation was found to be important. In the early days of this technology, it was believed that hydrophilic surfaces were needed for bonding to occur [52]. Later, successful bonding of both hydrophilic and hydrophobic surfaces was achieved[48]. A three step model has been proposed to explain the bonding mechanism. First, the samples are initially bonded via hydrogen bonds -- a type of van der Waals interaction. A hydrogen atom can participate in a hydrogen bond if it is bound to oxygen, nitrogen, or fluorine [48]. This type of bonding is fairly weak ( $\approx 0.22$  eV) and will not keep the samples in contact throughout subsequent processing. When the samples is annealed, two other processes take place to strengthen the bond. First, the hydrogen bonds between silanol groups connect the wafers. As this process takes place, water is still at the bonding interface. Finally, siloxane bonds develop between the wafers and a water monomer is released[53]. This monomer diffuses away from the bonding interface. Stengl and co.-workers estimated that the surface energy increases from  $100 \text{ erg/cm}^2$  to  $2 \times 980 \text{ erg/cm}^2$  -- or the surface energy of quartz[53] in the case of silicon to silicon direct wafer bonding.

In order to make direct wafer bonding technology feasible, the factors that affect successful and unsuccessful bonding must be understood. In this field, three factors that have been found to be most important.

- The sample surface must be flat and smooth. Small gaps can exist between the wafers and will – in many cases – be enclosed during the annealing process. Work done determined a threshold of 0.57 nm as the point at which a rougher surface will not bond routinely [54].
- The surface must be clean and free of particles. Particles can lead to large unbonded regions as well as point where the stress exceeds the critical shear stress of the material and leads to dense network of dislocations which can spread by gliding away from the particle [55].
- The surface must be free of hydrocarbons. Hydrocarbons are trapped at the bonding interface, break up into small gaseous molecules, and lead to “gas” pockets<sup>v</sup> that are under pressure and exploded upon removal of one of the substrates [48].

Outside of the work of silicon wafer bonding, no fundamental work has been done to understanding the process of wafer bonding. This holds for the case needed here – GaAs-to-InP bonding. The fusion of InP to GaAs that are done for this work proceeded as follows. First, a target sample and a source sample are cleaved to a size of  $(8\pm 2)$  by  $(8\pm 2)$  mm<sup>2</sup>. After each sample is cleaned thoroughly, they are placed together (epi-side to epi-side) and put into a graphite fixture in which a uniform pressure is applied to maintain intimate contact between the samples<sup>vi</sup>. The fixture is annealed under either a H<sub>2</sub> or N<sub>2</sub> ambient to elevated temperatures (typically  $\approx 600^\circ\text{C}$ ) for 30–45 minutes to allow mass transport to occur at the interface of the source and target wafers. After cooling

---

<sup>v</sup> Gas pockets of this nature can also be formed by air being trapped between the wafers when contacted.

<sup>vi</sup> For silicon wafer bonding, uniform pressure during annealing is not used. Hence, I believe this results in higher annealing temperatures being needed.



down, the substrate of the source wafer is selectively removed. More details of this process is covered in Chapter 5.

At the elevated temperatures that are used in wafer fusion mass transport of the InP occurs via dissociation of  $\text{P}_2$  from the InP layer. This results in an excess of mobile In atoms near the InP/GaAs interface[56]. The nature of the contact of the GaAs wafer to the InP wafer is such that a concentration gradient of In exists. This gradient causes the InP to move and makes the InP conform to the GaAs[57]. A collaborative effort was initiated between UCSB and Hewlett Packard Labs to study the details of GaAs to InP fusion [51]. From this work, the following conclusions were drawn:

- Two-beam transmission electron microscopy (TEM) analysis showed no threading dislocation formation from the InP/GaAs interface. In addition, strain relaxation was seen to occur within 40 nm of this interface
- From electron-beam induced current (EBIC) measurements, a significant number of dark lines was observed at distances less than 0.4  $\mu\text{m}$  to the fusion interface.
- Room temperature photoluminescence of a multiple quantum well structure showed no degradation for quantum wells greater than 200 nm from the fusion interface<sup>vii</sup>.
- With the fusion junction in the depletion of a diode, EBIC measurements showed a dark current of 5  $\text{mA}/\text{cm}^2$  at 2 V.
- No significant amount of absorption was found at the fusion interface. This was determined by measuring and modeling distributed bragg reflector (DBR) mirrors before and after fusion.

---

<sup>vii</sup> Not that this was done in a undoped structure such that dopant effects (mainly Be and Zn) may require that this distance be changed.

These results suggest that the effects of wafer fusion on the material structure are slight and that devices can be made by this technique.

#### 4.2.2 Applications of Wafer Fusion

The ability to marry two different semiconductors with little regards to lattice and thermal mismatch has spawned a number of different efforts in novel device structures. In general, these efforts can be placed into two different classes. The first class I will call the *free-orientation integration* class. The approach is to place a device from one substrate -- on which it is easy to make -- onto another substrate where it may be more useful for device integration. Efforts in this area include:

- Long wavelength GaInAs photodetectors on Si and GaAs substrates where dark currents of 0.29 nA and 57 pA have been achieved on Si and Ga respectively[58,59]. Responsivities of 1 A/W and 80% efficiencies have been reported.
- 1.5  $\mu\text{m}$  lasers on Si [60-69] and GaAs [70-73] substrates where no major degradation in device performance has been seen.

The second class of wafer fusion applications is what I will call the *materials integration* class. This approach uses specific material properties of the two materials being joined by wafer fusion. This is done to either make a novel device or improve an existing device's performance. Efforts in the area include:

- 1.5  $\mu\text{m}$  vertical cavity surface emitting lasers [74-78]. Here the active region is made of InP-based alloys for 1.5  $\mu\text{m}$  emission and Al(Ga)As/GaAs DBR mirrors for high reflectivity epitaxial mirrors that are difficult to do in the InP system. As of now, this approach has lead to the best device results for VCSELs at this wavelength.

- A novel long wavelength avalanche photodetector which use a GaInAs absorption region for 1.3 and 1.5  $\mu\text{m}$  light and a Si multiplication region for gain [79,80]. Results to date are gains of 130 at 1.3  $\mu\text{m}$  and a gain bandwidth product of 81 GHz.
- High power AlGaInP/GaP light-emitting diodes (LEDs) [81-84] where the GaP substrate is transparent to the emitted light from the LED leading to higher efficiencies and output flux. In addition, GaP's high thermal conductivity also helps provide better heat sinking. This work has also lead to successful wafer fusion over a 50-nm wafer [85].

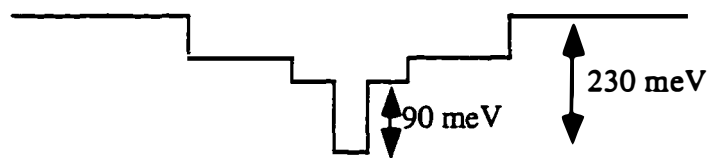
As I move on to my designs for 1.55  $\mu\text{m}$  lasers with reduced carrier overflow, I should point out that the approach taken here differs from the approaches used as examples in the above discussion of 1.55  $\mu\text{m}$  lasers on GaAs and Si substrates. In my approach, the material design must (i) provide electron confinement against carrier leakage and occupation of the barrier states in the active region and (ii) provide optical confinement of the mode such that enough amplification of the lasing mode occurs at reasonable threshold currents. In References[60-73] the fusion junction is placed  $> 1 \mu\text{m}$  away from the active region. This distance provides no additional optical confinement. The method by which these requirements are achieved is the subject of the next section.

### 4.3 Design of 1.55 $\mu\text{m}$ Lasers Using Wafer Fused Structures

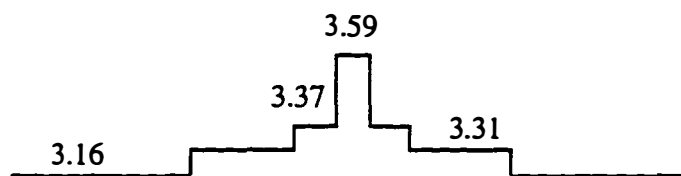
#### 4.3.1 *General Issues and Definitions*

In this section, two designs that allow for 1.55  $\mu\text{m}$  lasers with reduced carrier overflow are presented. As stated in the previous section, my goal is to achieve more electron and optical confinement than is possible in current 1.55  $\mu\text{m}$  laser designs. To illustrate this improvement, Figure 4-2 below shows the conduction

band and index of refraction profile of a 1.55  $\mu\text{m}$  laser employing a GaInAsP waveguide region and InP cladding layers.



(a) Conduction Band Profile



(b) Index of Refraction Profile

**Figure 4-2** The conduction band profile (a) and index of refraction profile (b) for the 1.55  $\mu\text{m}$  laser modeled in Chapter 3. The approximate band offsets and index values are labeled in the figure for reference and only one quantum well is shown for clarity.

If we want to improve the electron confinement of 1.55  $\mu\text{m}$  lasers with InP cladding layers<sup>viii</sup> by raising the barrier height, a reduction in the optical confinement must be accepted. In order to obtain the higher electron confinement obtainable by raising the barrier height, a different material with a smaller index of refraction than InP at 1.55  $\mu\text{m}$  must be used for the cladding. Using semiconductors that are lattice matched to InP will not achieve this since InP has the smallest index of materials lattice matched to it. My solution to this dilemma is to use AlGaAs that is lattice matched to GaAs. This material has two

<sup>viii</sup> This is also true for an AlInAs cladding whose index is slightly higher than InP.

main advantages. As shown in Figure 4-3 below, its index is smaller than InP for Al mole fractions greater than 0.45.

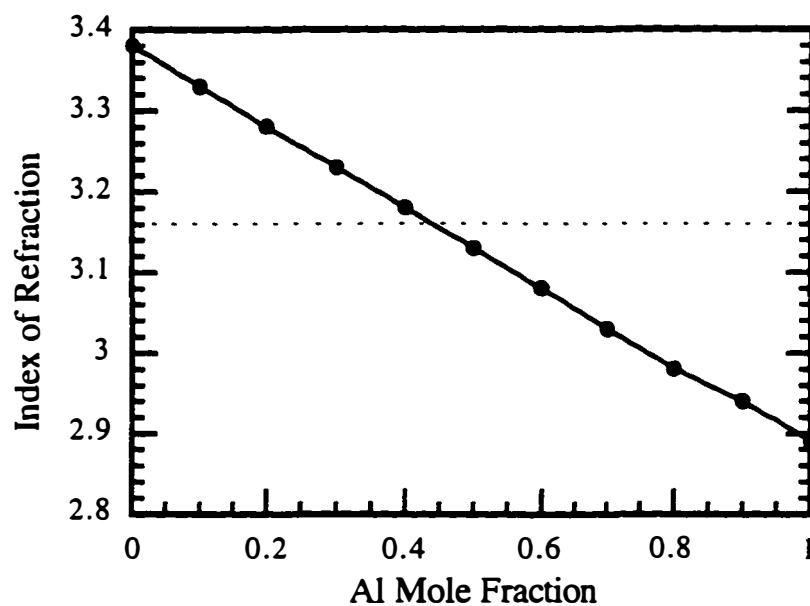


**Figure 4-3** The index of refraction for AlGaAs at 1.55  $\mu\text{m}$  as a function of Al mole fraction. The thin dashed line represents the index of InP. Thus, Al mole fractions of greater than 0.45 will have a lower index than InP. This data is taken from the work of Afromowitz in Reference [86].

The change in cladding material from InP to AlGaAs leads to a higher optical confinement factor when the barrier height is raised due to better waveguiding. This is illustrated later in the section. Second, the band gap of AlGaAs with mole fractions greater than 0.45 is large such that using AlGaAs as a cladding layer significantly reduces electron leakage out of the active region that has been seen in 1.55  $\mu\text{m}$  lasers with InP claddings[33,36].The requirement of reduced carrier

leakage out of the waveguide region of the laser only requires that AlGaAs be used on the p-side of the device. Therefore, there are two possible types of structures that can be used to create 1.55  $\mu\text{m}$  lasers with reduced carrier overflow using wafer fusion. These structures – the *single-fused laser* and the *double-fused laser* – are shown in Figure 4-4.

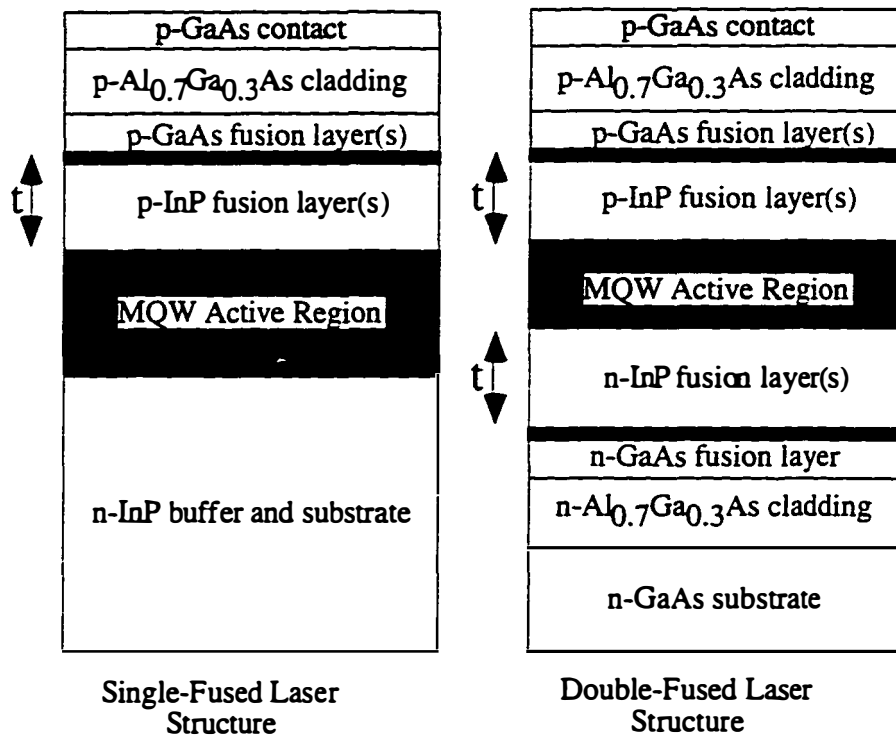
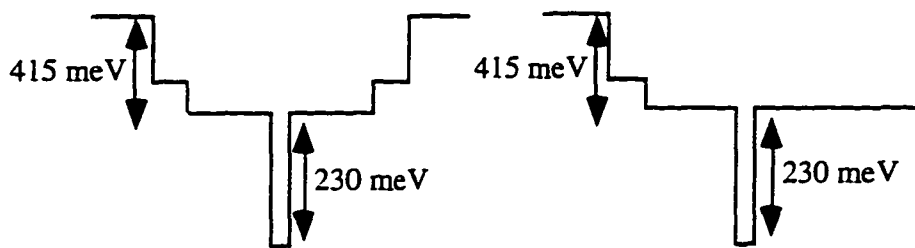
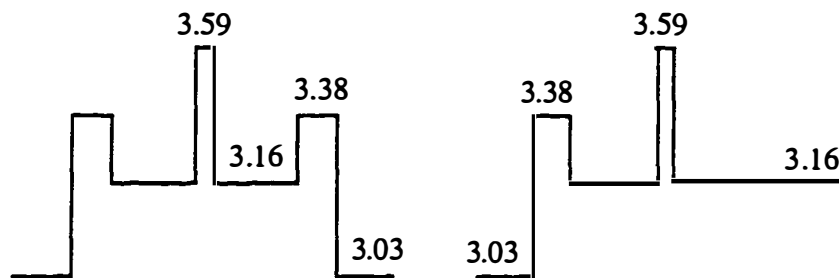


**Figure 4-4** General schematic of the single-fused laser and double-fused laser where the white portions are MOCVD-grown (active region in dark gray) and the shaded portions are MBE-grown. The specific thickness and doping values for the laser are covered in Chapter 5. The point where the fusion interface resides is denoted by the thick solid line

The index of refraction of AlGaAs decreases with increasing Al mole fraction – which leads to better waveguiding. I chose to use  $\text{Al}_{0.7}\text{Ga}_{0.3}\text{As}$  so as to minimize potential problems with high Al mole fraction cladding layers. Figure 4-5 shows the conduction band and index of refraction profiles for each of these structures.



(a) Conduction Band Profile



(b) Index of Refraction Profile

**Figure 4-5** The conduction band (a) and index of refraction (b) profiles for the double-fused (left side) and single-fused (left side) lasers. The approximate band offsets and index values are shown. Only one quantum well is shown for clarity and the p-side of the device is on the left side.

Each of these structures in Figure 4-4 have certain advantages. As will be shown in the next section, the *double-fused laser* leads to a higher optical

overlap of the lasing mode with the gain media (i.e., the quantum wells). This should lead to lower threshold currents. However, this structure also requires a more complicated process (2 fusions) in order to fabricate lasers and may lead to lower yields. The *single-fused laser*, on the other hand, has a simpler fabrication procedure albeit with lower  $\Gamma_{\text{act}}$ . In addition, if single mode operation is desired, the *single-fused laser* -- regardless of the waveguide thickness -- always has one transverse mode. In the *double-fused laser*, too large of a waveguide will lead to more than one transverse mode<sup>ix</sup>. Before moving on to design issues related to the use of wafer fusion, issues related to minimizing the temperature sensitivity of 1.55  $\mu\text{m}$  lasers and maximizing their ultimate CW operating temperature need to be addressed. In the case of the temperatures sensitivity, I will use the  $T_o$  expression developed in Chapter 2. This expression is repeated below

$$T_o = \frac{\Delta T}{\ln J_{tr}^{\dagger} + \ln \eta_i^{\dagger} + \frac{1}{n_{QW} \Gamma_{\text{act}} g_{\text{opt}}^{\dagger}} \left( \frac{\alpha_o}{g_{\text{opt}}^{\dagger}} - \alpha_o + \frac{\Delta \alpha}{g_{\text{opt}}^{\dagger}} \right)} \quad (4-1)$$

In order to maximize  $T_o$ , the denominator of Equation (4-1) needs to be minimized. This can be achieved in the following ways:

- Minimizing the change of  $J_{tr}$  with temperature
- Minimizing changes in  $\eta_i$  with temperature
- Minimizing changes in  $g_{\text{opt}}$  with temperature

---

<sup>ix</sup> This may not be a big concern since the second transverse mode will have a much lower optical overlap with the active region and higher overlap with the rest of the structure. Therefore, its threshold gain should be much larger and may never reach threshold



- Minimizing changes in  $\Delta\alpha$  with temperature
- Using a high  $g_{\text{opt}}$  value (i.e., strained quantum well)
- Using a high number of quantum wells and a large optical overlap  $\Gamma_{\text{act}}$ .

As was shown in Chapter 3 many of these effects can be achieved by a reduction in carrier overflow. In terms of  $T_{\text{max}}^{\text{max}}$ , minimizing  $J_{\text{tr}}$  and  $\alpha_0$  will lead to a higher value (See Equation 2-11).

In order to assess the advantages and disadvantages of 1.55  $\mu\text{m}$  laser structures using wafer fusion, I need to define some design criteria. Ultimately, what is desired is as high an optical confinement factor as possible. But this goal comes with some trade-offs. As was mentioned in Section 4.2.1, the proximity of the fusion interface was shown to affect the photoluminescence from the quantum wells if placed closer than 200 nm<sup>2</sup>. This consideration affects the design because the optical confinement factor is directly related to how close the fusion junction is to the active region.

Furthermore, some roughness or contamination may exist at the fusion interface which could cause additional optical loss. As was mentioned previously, the fusion in my case is being used to provide both electron and optical confinement. Therefore, interaction of the optical mode with the fusion interface is necessary. This is not the case in any of the other structure I mentioned in Section 4.2.1. The closest case would be the 1.5  $\mu\text{m}$  vertical-cavity lasers. However, the fusion interface is placed at a null of the standing wave pattern so that any effects

---

<sup>2</sup> Recent work by my colleague at UCSB, Alexis Black, has shown that this distance is smaller without the presence of dopants. Dopants may require the fusion junction to be further away.

are negated<sup>xi</sup>. This is possible in a vertical-cavity device since the cavity and growth direction are parallel; in an in-plane lasers these two entities are perpendicular and no such scheme is available. In order to minimize any possible increased optical losses, the fusion junction may need to be moved even further away than 200 nm.

The last criterion that is considered in the designs is intervalence band absorption due to the p-doped regions of the structure. Based on the EBIC measurements detailed in Reference [51], it is desirable to have the fusion junction out of the depletion region of the device. In a typical p-i-n laser, this requires significant doping ( $> 10^{18} \text{ cm}^{-3}$ ) at this interface. However, this amount of doping also causes additional optical loss. In the GaInAsP material system, intervalence band absorption has been measured at  $20 \text{ cm}^{-1}$  per  $10^{18}$  active dopant atoms [87]. In GaAs, the loss is slightly higher –  $26 \text{ cm}^{-1}$  per  $10^{18}$  active dopant atoms[88]; for InP, this value increases linearly with doping while for GaAs it rises by the power of 1.3.

Before moving onto my designs, I would like to summarize the major criteria used in their determination.

- As high an optical overlap with the quantum well active region as possible
- A minimum distance of 200 nm from a fusion junction to the nearest quantum well. The smaller this value that larger the optical overlap with the active region
- As low an optical overlap with the fusion structure(s) in the device so as to minimize any possible loss mechanisms

---

<sup>xi</sup> This is true in principle. See Chapter 6 for more information.

### 4.3.2 Modeling Formulation

In this section the design methodology used to determine the material structures for wafer fused lasers is described. The general approach taken is as follows. The waveguide material composition and waveguide thickness are first determined. Then, the optical confinement factor of a single quantum well at the exact center of the waveguide is calculated within the structure desired – either *single-fused* or *double-fused*. As the thickness of waveguide is changed, the optical overlap with this quantum well also changes. This is shown in Figure 4-6 for a single-fused laser structure using a GaInAsP ( $\lambda = 1.1 \mu\text{m}$ ) waveguide. Note that in Figure 4-6 that there is a waveguide range for which the optical confinement factor is maximized<sup>xii</sup>. To extend this to a multiple quantum well active region, the optical confinement factor ( $\Gamma_{act}$ ) is given by

$$\Gamma_{act} = n_{QW} \Gamma_{SQW}(t_{QW}, t_{WG}) \quad (4-2)$$

where  $t_{WG}$  is the waveguide thickness and  $t_{QW}$  is the quantum well thickness. It is assumed that  $\Gamma_{SQW}$  is a linear function of  $t_{QW}$ . Equation (4-2) only holds for small  $n_{QW}$  [89,90] and is used here to give simple analytical results that have the same trend as a more formal calculation. Once the number and thickness of the quantum wells is known, the distance from the fusion junction to the closest quantum well ( $d_f$ ) is given by

$$d_f (nm) = 25 + \frac{t_{WG}}{2} - \frac{n_{QW}}{2} (t_{QW} + t_b) + \frac{t_b}{2} \quad (4-3)$$

---

<sup>xii</sup> This holds in general for wafer fused structures. However, there is a deviation when InP is used as described later in the section.

where  $t_b$  is the barrier thickness and the fusion structure consists of 50 nm of InP and 50 nm of GaAs.

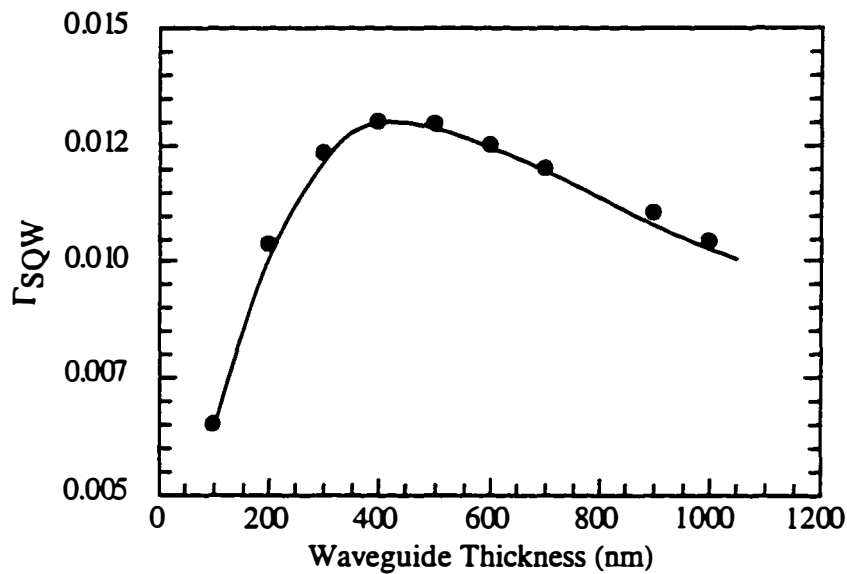


**Figure 4-6**  $\Gamma_{SQW}$  versus waveguide thickness for a single fused laser structure with a GaInAsP ( $\lambda = 1.1 \mu\text{m}$ ) waveguide. In this case,  $t_{InP}$  is 100 nm as defined in Figure 5.3

The last piece of information needed is the optical overlap of the lasing mode with the fusion structure ( $\Gamma_f$ ). It is calculated as a function of  $t_{WG}$  and -- in the plots below -- is assumed to be independent of the number of quantum wells in the active region.

### 4.3.3 Structures Using GaInAsP( $\lambda = 1.1 \mu\text{m}$ ) Waveguides

Using Equations (4-2) and (4-3), contour plots for  $\Gamma_{act}$  were calculated for the single-fused and double-fused structures with GaInAsP( $\lambda = 1.1 \mu\text{m}$ ) waveguides. These plots are shown in Figures 4-7 and 4-8.

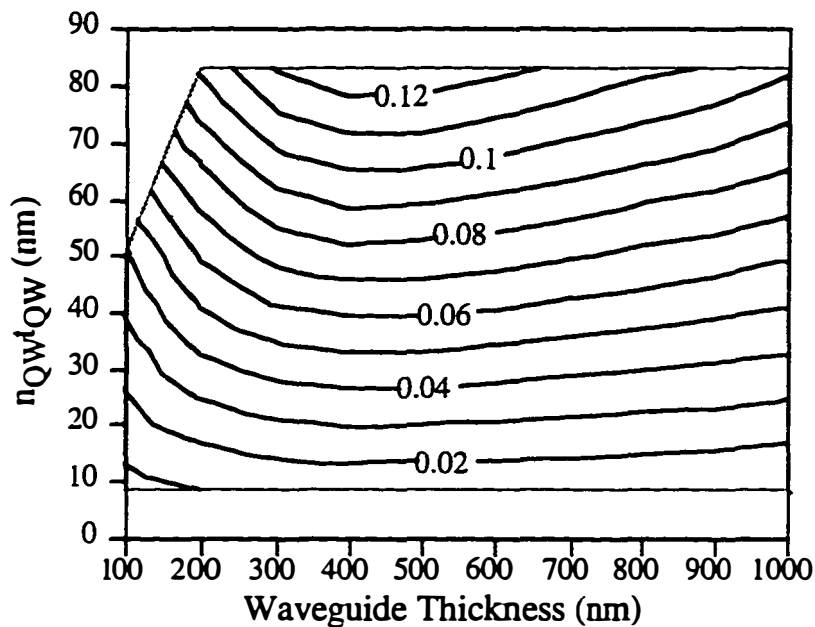


**Figure 4-7** Contour plots for  $\Gamma_{act}$  with a GaInAsP( $\lambda = 1.1 \mu\text{m}$ ) waveguide in a single-fused structure as the waveguide thickness and total active region thickness are changed.  $t_{inP}$  is assumed to be 150 nm as defined in Figure 5.3.

There is one major difference between the *single-fused* and *double-fused* laser structures: for the same waveguide thickness the double-fused structure will always have a higher  $\Gamma_{act}$ . It can be seen that in each case there is a waveguide thickness range at which  $\Gamma_{act}$  is maximized for a given  $n_{QW}t_{QW}$ . For the single-fused structure, this is between  $\approx 400$  and  $500$  nm; in the double-fused

structure, the value is below  $\approx 300$  nm. The other important parameters, as mention in Section 4.3, are the fusion junction distance from the quantum well active region and the overlap of the fusion structure with the lasing mode.

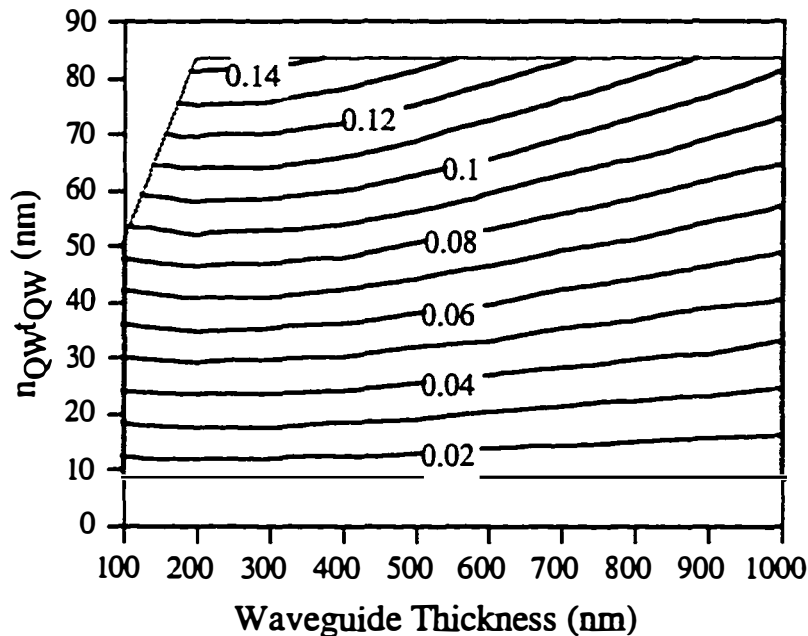


**Figure 4-8** Contour plots for  $\Gamma_{act}$  with a GaInAsP ( $\lambda = 1.1 \mu\text{m}$ ) waveguide in a double-fused structure as the waveguide thickness and total active region thickness are changed.  $t_{InP}$  is assumed to be 150 nm.

Using Equation (4-3), an InP spacer of 100 nm or more leads to the minimum distance of the fusion junction from the active region required. In terms of designs of high speed lasers, where carrier transport is important [91-93], this distance may be too large.

Figure 4-9 shows the overlap of the lasing mode with the fusion structure. As with  $\Gamma_{act}$ , there are different values for  $\Gamma_{\beta}$  with the different fusion structures. In

this case for the same waveguide thickness the double-fused structure will always have a higher  $\Gamma_{\text{fj}}$ .

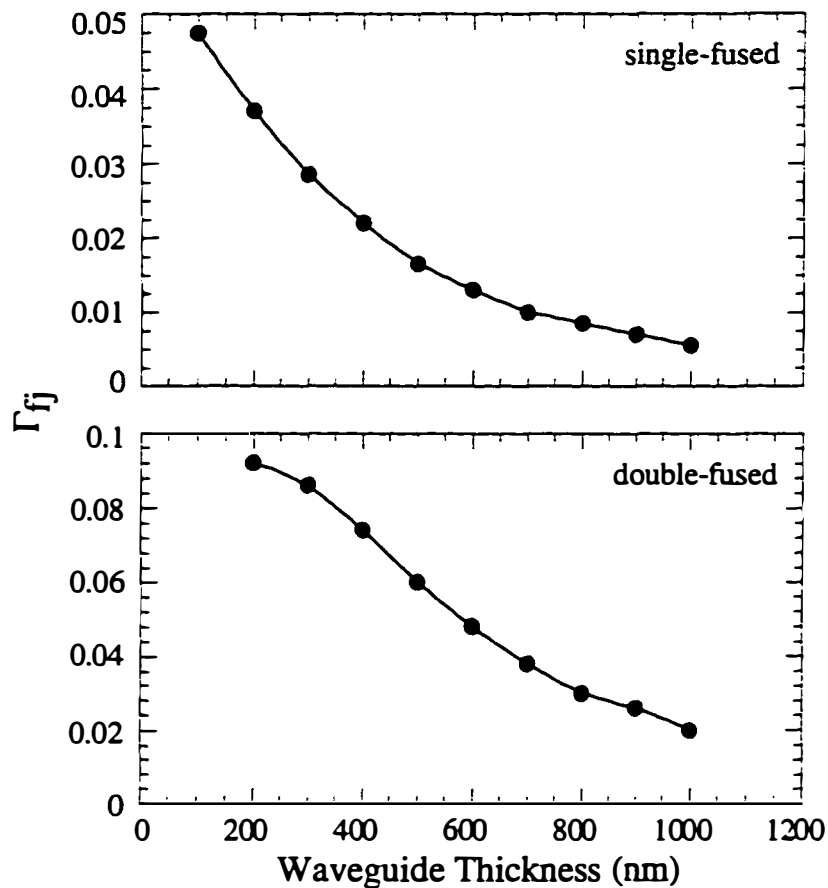


**Figure 4-9** Overlap of the lasing mode with the fusion structure (50 nm each of InP and GaAs) as the waveguide thickness changes. For this calculation  $t_{\text{InP}}$  is assumed to be 150 nm.

In fact the overlap for a double-fused structure can be twice as high as the single-fused case. This is due to the asymmetry of the index profile in the

single-fused structure's case (Figure 4-5). The parameters  $\Gamma_{acr}$ ,  $d_f$ , and  $\Gamma_f$  can be further adjusted by changing the InP spacer thickness –  $t_{InP}$ . A reduction in  $t_{InP}$  increases  $\Gamma_{acr}$  and  $\Gamma_f$  while decreasing  $d_f$  in both *single-fused* and *double-fused* structures. An increase in  $t_{InP}$  has the opposite effect:  $\Gamma_{acr}$  and  $\Gamma_f$  both decrease while  $d_f$  increases. Thus, depending on the application of the 1.55  $\mu\text{m}$  wafer fused structure, both the waveguide thickness and the InP spacer thickness can be adjusted to meet that application's needs.

#### 4.3.4 Structures Using InP Waveguides

As mentioned in Section 4.3, the use of AlGaAs for the cladding later material allows the barrier height of the quantum well active region to be increased substantially without a large decrease in  $\Gamma_{acr}$  (see Figure 4-1). In the GaInAsP material system, the highest barrier height achievable is by the use of InP barriers. below shows the contour plot of  $\Gamma_{acr}$  for a double-fused structure using an InP waveguide<sup>xiii</sup>. As is seen above, there is no range of waveguide thickness where a maximum  $\Gamma_{acr}$  exists as was the case with the GaInAsP ( $\lambda = 1.1 \mu\text{m}$ ) waveguides. This is due to the relatively poor waveguiding that still exists in the structure – even with the use of AlGaAs cladding layers. Thus maximizing  $\Gamma_{acr}$  means making the InP waveguide as thin as possible. This reduction in waveguide thickness also leads to an increase in  $\Gamma_f$  and a decrease in  $d_f$ .

---

<sup>xiii</sup> Using the single-fused structure in Figure 4-4 does not lead to a guided mode with an InP waveguide.



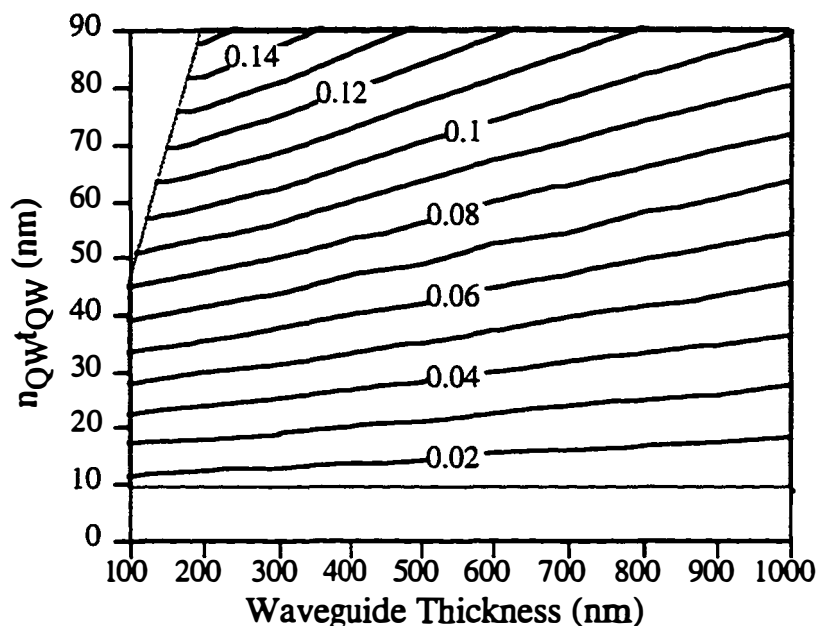


**Figure 4-10** Contour plots for  $\Gamma_{act}$  with a InP waveguide in a double-fused structure as the waveguide thickness and total active region thickness are changed.

The overlap of the lasing mode with the fusion structure is shown in Figure 4-11.

#### 4.4 Summary

In this chapter, various aspects of laser design for reduced electron overflow in 1.55  $\mu\text{m}$  lasers have been examined. In structures using InP (or AlInAs) cladding layers, a serious trade-off exists between the overlap of the lasing mode with the quantum well active region ( $\Gamma_{act}$ ) and the amount of electron confinement to these same quantum wells. My solution to this problem was to use a material for the cladding layer that had a lower index than InP: AlGaAs with a 70% Al mole fraction.

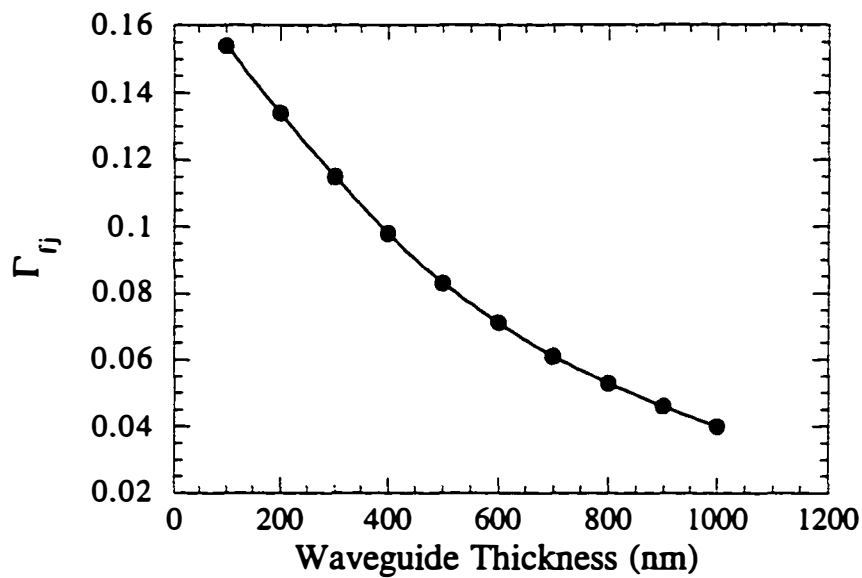


**Figure 4-11** Overlap of the lasing mode with the fusion structure (50 nm each of InP and GaAs) as the waveguide thickness and active region thickness are changed.

The improvement with the use of AlGaAs cladding layers in a single-fused or double-fused structure is summarized in Table 4-3 below. Therefore *confinement factors approaching the case with InP cladding layers can be achieved with between 2 and 5.5  $kT$  additional electron confinement at room temperature.*

**Table 4-3** Summary of  $\Gamma_{act}$  values for single-fused and double-fused laser structures – under optimized waveguide conditions -- with 3 +1% quantum well active region as compared to the InP cladding case. The quantum well thickness have been adjusted for 1.55  $\mu\text{m}$  emission. 10 nm barriers are assumed and  $t_{InP}$  is 100 nm for the 1.1  $\mu\text{m}$  GaInAsP waveguide wafer fused cases.

Waveguide Material	$\Delta E_c$ (meV)	Active Region Confinement Factor ( $\Gamma_{act}$ )-		
		InP Cladding	Single-Fused Structure	Double-Fused Structure
1.25 $\mu\text{m}$ GaInAsP	97	3.86	4.57	4.89
1.1 $\mu\text{m}$ GaInAsP	151	3.39	4.35	5
InP	240	1.76	does not exist	3.93

In the next chapter, the procedure used to create these novel wafer fused structures is described.

#### 4.5 References

- [1] H. Nobuhara, K. Tanaka, T. Yamamoto, T. Machida, T. Fujii, and K. Wakao, "High-temperature operation of InGaAs/InGaAsP compressive-strained QW lasers with low threshold currents", *IEEE Photonics Technology Letters* **5**, 961 (1993).
- [2] M. Quillec, "Material for future InP based optoelectronics: InGaAsP versus InGaAlAs.", *Proceedings of the SPIE - The International Society for Optical Engineering* **1361**, pt.1, 34 (1991).
- [3] M. Allovon and M. Quillec, "Interest in AlGaInAs on InP for optoelectronic applications", *IEE Proceedings J (Optoelectronics)* **139**, 148 (1992).
- [4] R. Bhat, C. E. Zah, M. A. Koza, D. M. D. Hwang, F. J. Favire, and B. Pathak, "OMCVD growth of strained  $\text{Al}_x\text{Ga}_y\text{In}_{1-x-y}\text{As}$  for low threshold 1.3  $\mu\text{m}$  and 1.55  $\mu\text{m}$  quantum well lasers", *No.92CH3104-7*, Newport, RI, USA, 1992, 453.
- [5] A. Kasukawa, R. Bhat, C. E. Zah, M. A. Koza, S. A. Schwarz, and T. P. Lee, "200-A/cm<sup>2</sup> threshold current density 1.5-  $\mu\text{m}$  GaInAs/AlGaInAs strained-layer GRIN-SCH quantum-well laser diodes grown by OMCVD", *49th Annual Device Research Conference (papers in summary form only received)*, Boulder, CO, USA, 1991, 2690.
- [6] A. Kasukawa, R. Bhat, C. E. Zah, M. A. Koza, and T. P. Lee, "Very low threshold current density 1.5  $\mu\text{m}$  GaInAs/AlGaInAs graded-index separate-confinement-heterostructure strained quantum well laser diodes grown by organometallic chemical vapor deposition", *Applied Physics Letters* **59**, 2486 (1991).
- [7] C. E. Zah, R. Bhat, F. J. Favire, M. Koza, T. P. Lee, D. Darby, D. C. Flanders, and J. J. Hsieh, "Low threshold 1.3  $\mu\text{m}$  strained-layer  $\text{Al}_x\text{Ga}_y\text{In}_{1-x-y}\text{As}$  quantum well lasers", *Electronics Letters* **28**, 2323 (1992).
- [8] C. E. Zah, M. C. Wang, R. Bhat, T. P. Lee, S. L. Chuang, Z. Wang, D. Darby, D. Flanders, and J. J. Hsieh, "High-temperature modulation dynamics of 1.3  $\mu\text{m}$   $\text{Al}_x\text{Ga}_y\text{In}_{1-x-y}\text{As}/\text{InP}$  compressive-strained multiple-quantum-well lasers", *Proceedings of IEEE 14th International Semiconductor Laser Conference*, Maui, HI, USA, 1994, 215.
- [9] K. Nishikata, H. Shimizu, Y. Hirayama, K. Hiraiwa, T. Fukushima, Y. Ikegami, T. Matsuda, F. Iwase, and M. Irikawa, "MBE growth of GaInAs/AlGaInAs superlattices on InP and application to 1.5  $\mu\text{m}$  MQW lasers", *Furukawa Electric Review*, **8** (1994).

- [10] H. Hillmer, R. Losch, W. Schlapp, A. Pocker, and H. Burkhard, "MBE grown strain-compensated AlGaInAs/AlGaInAs/InP MQW laser structures", *Electronics Letters* **31**, 1346 (1995).
- [11] M. Irikawa, H. Shimizu, I. Fukushima, K. Nishikata, and Y. Hirayama, "Strained GaInAs-AlGaInAs 1.5- $\mu\text{m}$ -wavelength multiquantum-well lasers loaded with GaInAs-AlInAs multiquantum barriers at the p-side optical confinement layer", *IEEE Journal on Selected Topics in Quantum Electronics* **1**, 285 (1995).
- [12] F. Steinhagen, H. Hillmer, R. Losch, W. Schlapp, H. Walter, R. Gobel, E. Kuphal, H. L. Hartnagel, and H. Burkhard, "AlGaInAs/InP 1.5  $\mu\text{m}$  MQW DFB laser diodes exceeding 20 GHz bandwidth", *Electronics Letters* **31**, 274 (1995).
- [13] M. Blez, C. Kazmierski, D. Mathoorasing, M. Quillec, M. Gilleron, H. Nakajima, and B. Sermage, "High speed ultralow chirp 1.55  $\mu\text{m}$  MBE grown GaInAs/AlGaInAs MQW DFB lasers", *Electronics Letters* **28**, 1040 (1992).
- [14] M. J. Mondry, Z. M. Chuang, M. G. Peters, and L. A. Coldren, "Low threshold current density 1.5  $\mu\text{m}$  (In, Ga, Al)As quantum well lasers grown by MBE", *Electronics Letters* **28**, 1471 (1992).
- [15] M. Blez, C. Kazmierski, M. Quillec, D. Robein, M. Allovon, A. Gloukhian, and B. Sermage, "First DFB GRIN-SCH GaInAs/AlGaInAs 1.55  $\mu\text{m}$  MBE MQW active layer buried ridge structure lasers", *Electronics Letters* **27**, 93 (1991).
- [16] J. N. Baillargeon and A. Y. Cho, "Solid source MBE growth of lattice matched GaInAsP with phosphorus and arsenic valved cracking cells", *Conference Proceedings. IEEE Lasers and Electro-Optics Society 1994 7th Annual Meeting (Cat. No.94CH3371-2) Proceedings of LEOS'94*, Boston, MA, USA, 1994, 347.
- [17] J. N. Baillargeon, K. Y. Cheng, A. Y. Cho, and S. N. G. Chu, "All solid source molecular beam epitaxy growth of  $\text{Ga}_x\text{In}_{1-x}\text{As}_y\text{P}_{1-y}/\text{InP}$  lasers using phosphorus and arsenic valved cracking cells", *15th North American Conference on Molecular Beam Epitaxy*, College Park, MD, USA, 1995, 2244.
- [18] J. N. Baillargeon, A. Y. Cho, and R. J. Fischer, "Evaluation of the performance and operating characteristics of a solid phosphorus source valved cracking cell for molecular beam epitaxy growth of III-V compounds", *Journal of Vacuum Science & Technology B (Microelectronics and Nanometer Structures)* **13**, 64 (1995).
- [19] J. N. Baillargeon, A. Y. Cho, and K. Y. Cheng, "Incorporation of arsenic and phosphorus in  $\text{Ga}_x\text{In}_{1-x}\text{As}_y\text{P}_{1-y}$  alloys grown by molecular-beam epitaxy using solid phosphorus and arsenic valved cracking cells", *Journal of Applied Physics* **79**, 7652 (1996).

- [20] T. P. Chin, J. C. P. Chang, J. M. Woodall, W. L. Chen, G. I. Haddad, C. Parks, and A. K. Ramdas, "Operation and device applications of a valved-phosphorus cracker in solid-source molecular-beam epitaxy", *14th North American Conference on Molecular-Beam Epitaxy*, Urbana, IL, USA, 1994, 750.
- [21] G. W. Wicks, M. W. Koch, F. G. Johnson, J. A. Varriano, G. E. Kohnke, and P. Colombo, "Operation of a molecular-beam epitaxy machine employing a valved solid phosphorus source", *13th North American Molecular-Beam Epitaxy Conference*, Stanford, CA, USA, 1993, 1119.
- [22] A. Kasukawa, R. Bhat, C. E. Zah, M. A. Koza, and T. P. Lee, "Very low threshold current density 1.5  $\mu\text{m}$  GaInAs/AlGaInAs graded-index separate-confinement-heterostructure strained quantum well laser diodes grown by organometallic chemical vapor deposition.", *Applied Physics Letters* **59**, 2486 (1991).
- [23] H. Shimizu, T. Fukushima, K. Nishikata, Y. Hirayama, and M. Irikawa, "1.5  $\mu\text{m}$  wavelength compressively strained GaInAs/AlGaInAs multi-quantum-well lasers grown by molecular-beam epitaxy with high differential gain and low threshold current density", *Applied Physics Letters* **67**, 449 (1995).
- [24] M. L. Xu, G. L. Tan, J. M. Xu, M. Irikawa, H. Shimizu, T. Fukushima, Y. Hirayama, and R. S. Mand, "Ultra-high differential gain in GaInAs-AlGaInAs quantum wells: experiment and modeling", *IEEE Photonics Technology Letters* **7**, 947 (1995).
- [25] M. Blez, C. Kazmierski, D. Mathoorasing, M. Quillec, M. Gilleron, H. Nakajima, and B. Sermage, "High speed narrow linewidth 1.55  $\mu\text{m}$  GaInAs/AlGaInAs MQW DFB lasers", *No.92CH3104-7*, Newport, RI, USA, 1992, 618.
- [26] T. Mamijoh, H. Horikawa, Y. Matsui, Y. K. Sin, M. Nakajima, C. Q. Xu, and Y. Ogawa, "Improved operation characteristics of long-wavelength lasers using strained MQW active layers", *IEEE Journal of Quantum Electronics* **30**, 524 (1994).
- [27] A. Wakatsuki, Y. Kawamura, Y. Noguchi, and H. Iwamura, "Effect of conduction-band discontinuity on lasing characteristics of 1.5  $\mu\text{m}$  InGaAs/In(Ga)AlAs MQW-FP lasers", *IEEE Photonics Technology Letters* **5**, 383 (1993).
- [28] T. Fukushima, H. Shimizu, K. Nishikata, Y. Hirayama, and M. Irikawa, "Carrier confinement by multiple quantum barriers in 1.55  $\mu\text{m}$  strained GaInAs/AlGaInAs quantum well lasers", *Applied Physics Letters* **66**, 2025 (1995).

- [29] H. Shimizu, T. Fukushima, K. Nishikata, Y. Hirayama, and M. Irikawa, "1.55  $\mu\text{m}$  strained GaInAs/AlGaInAs MQW lasers with a multi-quantum barrier", *Proceedings of IEEE 14th International Semiconductor Laser Conference*, Maui, HI, USA, 1994, 26.
- [30] R. F. Kazarinov and G. L. Belenky, "Novel design of semiconductor lasers for optical communication", *Physics and Simulation of Optoelectronic Devices III*, San Jose, CA, USA, 1995, 386.
- [31] R. F. Kazarinov and G. L. Belenky, "Novel design of AlGaInAs-InP lasers operating at 1.3  $\mu\text{m}$ ", *IEEE Journal of Quantum Electronics* **31**, 423 (1995).
- [32] H. Murai, Y. Matsui, Y. Ogawa, and T. Kunii, "Lasing characteristics under high temperature operation of 1.55  $\mu\text{m}$  strained InGaAsP/InGaAlAs MQW laser with InAlAs electron stopper layer", *Electronics Letters* **31**, 2105 (1995).
- [33] G. L. Belenky, C. L. Reynolds, Jr., R. F. Kazarinov, V. Swaminathan, S. Luryi, and J. Lopata, "Effect of p-doping profile on performance of strained multi-quantum-well InGaAsP-InP lasers", *Physics and Simulation of Optoelectronic Devices IV*, San Jose, CA, USA, 1996, 612.
- [34] G. L. Belenky, C. L. Reynolds, Jr., R. F. Kazarinov, V. Swaminathan, S. L. Luryi, and J. Lopata, "Effect of p-doping profile on performance of strained multi-quantum-well InGaAsP-InP lasers", *IEEE Journal of Quantum Electronics* **32**, 1450 (1996).
- [35] P. A. Andrekson, R. F. Kazarinov, N. A. Olsson, T. Tanbun-Ek, and R. A. Logan, "Effect of thermionic electron emission from the active layer on the internal quantum efficiency of InGaAsP lasers operating at 1.3  $\mu\text{m}$ ", *IEEE Journal of Quantum Electronics* **30**, 219 (1994).
- [36] G. L. Belenky, R. F. Kazarinov, J. Lopata, S. Luryi, T. Tanbun-Elk, and P. A. Garbinski, "Direct measurement of the carrier leakage out of the active region in InGaAsP/InP laser heterostructures", *IEEE Transactions on Electron Devices* **42**, 215 (1995).
- [37] H. Ishikawa, "Theoretical gain of strained quantum well grown on an InGaAs ternary substrate", *Applied Physics Letters* **63**, 712 (1993).
- [38] H. Ishikawa and I. Suemune, "Large estimated frequency response increase from deep potential well strained quantum well lasers", *IEEE Photonics Technology Letters* **6**, 1315 (1994).
- [39] H. Ishikawa and I. Suemune, "Analysis of temperature dependent optical gain of strained quantum well taking account of carriers in the SCH layer", *IEEE Photonics Technology Letters* **6**, 344 (1994).

- [40] H. Shoji, T. Uchida, T. Kusunoki, M. Matsuda, H. Kurakake, S. Yamazaki, K. Nakajima, and H. Ishikawa, "InGaAs/InGaAsP strained SQW LD grown on  $\text{In}_{0.05}\text{Ga}_{0.95}\text{As}$  ternary substrate", *Proceedings of IEEE 14th International Semiconductor Laser Conference*, Maui, HI, USA, 1994, 22.
- [41] H. Shoji, T. Uchida, T. Kusunoki, M. Matsuda, H. Kurakake, S. Yamazaki, K. Nakajima, and H. Ishikawa, "Fabrication of  $\text{In}_{0.25}\text{Ga}_{0.75}\text{As}/\text{InGaAsP}$  strained SQW lasers on  $\text{In}_{0.05}\text{Ga}_{0.95}\text{As}$  ternary substrate", *IEEE Photonics Technology Letters* 6, 1170 (1994).
- [42] W. P. Maszara, "SOI by wafer bonding: a review", *Proceedings of the Fourth International Symposium on Silicon-on-Insulator Technology and Devices*, Montreal, Que., Canada, 1990, 199.
- [43] W. P. Maszara, "SOI material by wafer bonding: an overview", *No.91CH3053-6*, Vail Valley, CO, USA, 1991, 18.
- [44] K. D. Wise, "Integrated silicon sensors: technology and microstructures", *No.91CH3092-4*, Ithaca, NY, USA, 1991, 412.
- [45] C. Harendt, C. E. Hunt, W. Appel, H. G. Graf, B. Hofflinger, and E. Penteker, "Silicon on insulator material by wafer bonding", *Journal of Electronic Materials* 20, 267 (1991).
- [46] S. Cristoloveanu, "Advanced silicon on insulator materials: processing, characterization and devices", *Materials Science and Technology. Proceedings of the Summer School*, Erice, Italy, 1988, 223.
- [47] S. Bengtsson, "Semiconductor wafer bonding: a review of interfacial properties and applications", *Journal of Electronic Materials* 21, 841 (1992).
- [48] Q. Y. Tong and U. Gosele, "Semiconductor wafer bonding: recent developments", *Materials Chemistry and Physics* 37, 101 (1994).
- [49] Z. L. Liao, J. N. Walpole, and D. Z. Tsang, "Fabrication, characterization, and analysis of mass-transported GaInAsP/InP buried-heterostructure lasers", *IEEE Journal of Quantum Electronics* QE-20, 855 (1984).
- [50] Z. L. Liao and D. E. Mull, "Wafer fusion: a novel technique for optoelectronic device fabrication and monolithic integration", *Applied Physics Letters* 56, 737 (1990).
- [51] R. J. Ram, J. J. Dudley, J. E. Bowers, L. Yang, K. Carey, S. J. Rosner, and K. Nauka, "GaAs to InP wafer fusion", *Journal of Applied Physics* 78, 4227 (1995).
- [52] R. Stengl, K. Mitani, V. Lehmann, and U. Gosele, "Silicon wafer bonding: chemistry, elasto-mechanics, and manufacturing", *No.89CH2796-1*, Stateline, NV, USA, 1989, 123.



- [53] R. Stengl, T. Tan, and U. Gosele, "A model for the silicon wafer bonding process", *Japanese Journal of Applied Physics, Part 2 (Letters)* **28**, 1735 (1989).
- [54] T. Abe and J. H. Matlock, "Wafer bonding technique for silicon-on-insulator technology", *Solid State Technology* **33**, 39 (1990).
- [55] H. Baumgart, R. D. Pinker, E. F. Steigmeier, H. Auderset, and A. J. R. de Kock, "Impact of interface preparation on defect generation during wafer bonding", *No.89CH2796-1*, Stateline, NV, USA, 1989, 95.
- [56] Z. L. Liau, "Prevention of In evaporation and preservation of smooth surface in thermal annealing and mass transport of InP", *Applied Physics Letters* **58**, 1869 (1991).
- [57] K. Hansen, E. Peiner, G. P. Tang, and A. Schlachetzki, "A theoretical model of InP mass transport", *Japanese Journal of Applied Physics, Part 1 (Regular Papers & Short Notes)* **32**, 234 (1993).
- [58] F. E. Ejeckam, C. L. Chua, Z. H. Zhu, and Y. H. Lo, "High-efficiency picoamperes dark current InGaAs P-I-N photodetectors on Si and GaAs substrates", *IEEE Lasers and Electro-Optics Society 1995 Annual Meeting. 8th Annual Meeting. Conference Proceedings (Cat. No.95CH35739) LEOS '95. IEEE Lasers and Electro-Optics Society 1995 Annual Meeting. 8th Annual Meeting. Conference Proceedings*, San Francisco, CA, USA, 1995, 23.
- [59] F. E. Ejeckam, C. L. Chua, Z. H. Zhu, and Y. H. Lo, "High-performance InGaAs photodetectors on Si and GaAs substrates", *IEEE/Cornell Conference on Advanced Concepts in High Speed Semiconductor Devices and Circuits (Cat. No.95CH35735) Proceedings IEEE/Cornell Conference on Advanced Concepts in High Speed Semiconductor Devices and Circuits*, Ithaca, NY, USA, 1995, 194.
- [60] M. Sugo, H. Mori, M. Tachikawa, Y. Itoh, and M. Yamamoto, "Room-temperature operation of an InGaAsP double-heterostructure laser emitting at 1.55  $\mu\text{m}$  on a Si substrate", *Applied Physics Letters* **57**, 593 (1990).
- [61] M. Sugo, H. Mori, Y. Itoh, Y. Sakai, and M. Tachikawa, "1.5  $\mu\text{m}$  long-wavelength MQW laser on a Si substrate", *Extended Abstracts of the 1991 International Conference on Solid State Devices and Materials*, Yokohama, Japan, 1991, 317.
- [62] M. Sugo, H. Mori, Y. Itoh, Y. Sakai, and M. Tachikawa, "1.5  $\mu\text{m}$  long-wavelength multiple quantum well laser on a Si substrate", *Japanese Journal of Applied Physics, Part 1 (Regular Papers & Short Notes)* **30**, 3876 (1991).
- [63] M. Sugo, H. Mori, Y. Sakai, and Y. Itoh, "Stable CW operation at room temperature of a 1.5  $\mu\text{m}$  wavelength multiple quantum well laser on a Si substrate", *Applied Physics Letters* **60**, 472 (1992).

- [64] M. Sugo, H. Mori, Y. Itoh, and M. Tachikawa, "Long-wavelength laser diodes on Si substrates", *Nat R & D* **42**, 527 (1993).
- [65] X. P. Jiang, H. Temkin, M. MacDonald, R. A. Logan, and D. Coblenz, "High performance InGaAsP/InP lasers on Si substrates", *Electronics Letters* **30**, 1680 (1994).
- [66] H. Wada, T. Kamijoh, and Y. Ogawa, "Direct bonding of InP to different materials for optical devices", *Proceedings of the Third International Symposium on Semiconductor Wafer Bonding: Physics and Applications Proceedings of Third International Symposium Semiconductor Wafer Bonding: Science, Technology and Applications*, Reno, NV, USA, 1995, 579.
- [67] K. Mori, K. Tokutome, and S. Sugou, "Direct bonding of high quality InP on Si and its application to low threshold semiconductor lasers", *Seventh International Conference on Indium Phosphide and Related Materials (Cat. No.95CH35720) Seventh International Conference on Indium Phosphide and Related Materials*, Hokkaido, Japan, 1995, 781.
- [68] K. Mori, K. Tokutome, and S. Sugou, "Low-threshold pulsed operation of long-wavelength lasers on Si fabricated by direct bonding", *Electronics Letters* **31**, 284 (1995).
- [69] H. Wada and T. Kamijoh, "Room-temperature CW operation of InGaAsP lasers on Si fabricated by wafer bonding", *IEEE Photonics Technology Letters* **8**, 173 (1996).
- [70] Y. H. Lo, R. Bhat, D. M. Hwang, M. A. Koza, and T. P. Lee, "Bonding by atomic rearrangement of InP/InGaAsP 1.5  $\mu\text{m}$  wavelength lasers on GaAs substrates", *Applied Physics Letters* **58**, 1961 (1991).
- [71] Y. Okuno, M. Aoki, T. Tsuchiya, and K. Uomi, "Free-orientation integration by direct bonding: fabrication of (001) InP-based 1.55  $\mu\text{m}$ -wavelength lasers on (110) GaAs substrate", *Seventh International Conference on Indium Phosphide and Related Materials (Cat. No.95CH35720) Seventh International Conference on Indium Phosphide and Related Materials*, Hokkaido, Japan, 1995, 785.
- [72] Y. Okuno, K. Uomi, M. Aoki, T. Taniwatari, M. Suzuki, and M. Kondow, "Anti-phase direct bonding and its application to the fabrication of InP-based 1.55  $\mu\text{m}$  wavelength lasers on GaAs substrates", *Applied Physics Letters* **66**, 451 (1995).
- [73] Y. Okuno, M. Aoki, T. Tsuchiya, and K. Uomi, "Fabrication of (001) InP-based 1.55  $\mu\text{m}$  wavelength lasers on a (110) GaAs substrate by direct bonding (a prospect for free-orientation integration)", *Applied Physics Letters* **67**, 810 (1995).
- [74] D. I. Babic, K. Streubel, R. P. Mirin, J. Piprek, N. M. Margalit, J. E. Bower, E. L. Hu, D. E. Mars, L. Yang, and K. Carey, "Room-temperature

performance of double-fused 1.54  $\mu\text{m}$  vertical-cavity laser", *Eighth International Conference on Indium Phosphide and Related Materials (Cat. No.96CH35930) Proceedings of 8th International Conference on Indium Phosphide and Related Materials*, Schwabisch-Gmund, Germany, 1996, 719.

[75] J. Piprek, D. I. Babic, and J. E. Bowers, "Modeling and optimization of 1.54  $\mu\text{m}$  double-fused VCSELs for cw operation above room temperature", *Physics and Simulation of Optoelectronic Devices IV*, San Jose, CA, USA, 1996, 149.

[76] Y. Ohiso, C. Amano, Y. Itoh, K. Tateno, T. Tadokoro, H. Takenouchi, and T. Kurokawa, "1.55  $\mu\text{m}$  vertical-cavity surface-emitting lasers with wafer-fused InGaAsP/InP-GaAs/AlAs DBRs", *Electronics Letters* **32**, 1483 (1996).

[77] N. M. Margalit, D. I. Babic, K. Streubel, R. P. Mirin, D. E. Mars, J. E. Bowers, and E. L. Hu, "Laterally oxidized long wavelength cw vertical-cavity lasers", *Applied Physics Letters* **69**, 471 (1996).

[78] D. I. Babic, K. Streubel, R. P. Mirin, N. M. Margalit, J. E. Bowers, E. L. Hu, D. E. Mars, Y. Long, and K. Carey, "Room-temperature continuous-wave operation of 1.54  $\mu\text{m}$  vertical-cavity lasers", *IEEE Photonics Technology Letters* **7**, 1225 (1995).

[79] A. R. Hawkins, T. E. Reynolds, D. R. England, D. I. Babic, M. J. Mondry, K. Streubel, and J. E. Bowers, "Silicon heterointerface photodetector", *Applied Physics Letters* **68**, 3692 (1996).

[80] A. R. Hawkins, T. Reynolds, D. R. England, D. I. Babic, M. Mondry, and J. E. Bowers, "Silicon hetero-interface photodetector", *IEEE Lasers and Electro-Optics Society 1995 Annual Meeting. 8th Annual Meeting. Conference Proceedings (Cat. No.95CH35739) LEOS '95. IEEE Lasers and Electro-Optics Society 1995 Annual Meeting. 8th Annual Meeting. Conference Proceedings*, San Francisco, CA, USA, 1995, 29.

[81] F. A. Kish, D. A. Vanderwater, D. C. DeFever, D. A. Steigerwald, G. E. Hofler, K. G. Park, and F. M. Steranka, "Highly reliable and efficient semiconductor wafer-bonded AlGaInP/GaP light-emitting diodes", *Electronics Letters* **32**, 132 (1996).

[82] F. A. Kish, D. A. Vanderwater, M. J. Peanasky, M. J. Ludowise, S. G. Hummel, and S. J. Rosner, "Low-resistance ohmic conduction across compound semiconductor wafer-bonded interfaces", *Applied Physics Letters* **67**, 2060 (1995).

[83] F. A. Kish, F. M. Steranka, D. C. DeFever, D. A. Vanderwater, K. G. Park, C. P. Kuo, T. D. Osentowski, M. J. Peanasky, J. G. Yu, R. M. Fletcher, D. A. Steigerwald, M. G. Craford, and V. M. Robbins, "Very high-efficiency semiconductor wafer-bonded transparent-substrate  $(\text{Al}_x\text{Ga}_{1-x})_{0.5}\text{In}_{0.5}\text{P}/\text{GaP}$  light-emitting diodes", *Applied Physics Letters* **64**, 2839 (1994).

- [84] F. A. Kish, D. A. DeFever, D. A. Vanderwater, G. R. Trott, R. J. Weiss, and J. S. Major, Jr., "High luminous flux semiconductor wafer-bonded AlGaInP/GaP large-area emitters", *Electronics Letters* **30**, 1790 (1994).
- [85] G. E. Hofler, D. A. Vanderwater, D. C. DeFever, F. A. Kish, M. D. Camras, F. M. Steranka, and I. H. Tan, "Wafer bonding of 50-mm diameter GaP to AlGaInP-GaP light-emitting diode wafers", *Applied Physics Letters* **69**, 803 (1996).
- [86] M. A. Fromowitz, "Refractive index of  $\text{Ga}_{1-x}\text{Al}_x\text{As}$ ", *Solid State Communications* **15**, 59 (1974).
- [87] C. H. Henry, R. A. Logan, F. R. Merritt, and J. P. Luongo, "The effect of intervalence band absorption on the thermal behavior of InGaAsP lasers", *8th IEEE International Semiconductor Laser Conference*, Ottawa, Ont., Canada, 1982, 947.
- [88] D. Babic, unpublished results.
- [89] S. Ohke, T. Umeda, and Y. Cho, "Optical waveguides using GaAs- $\text{Al}_x\text{Ga}_{1-x}\text{As}$  multiple quantum well", *Optics Communications* **56**, 235 (1985).
- [90] W. X. Zou, J. L. Merz, and L. A. Coldren, "Analysis and optimization of quantum-well thickness for GaAs/AlGaAs and InGaAs/GaAs/AlGaAs quantum-well lasers", *Journal of Applied Physics* **72**, 5047 (1992).
- [91] T. Fukushima, R. Nagarajan, M. Ishikawa, and J. E. Bowers, "High-speed dynamics in InP based multiple quantum well lasers", *Japanese Journal of Applied Physics, Part 1 (Regular Papers & Short Notes)* **32**, 70 (1993).
- [92] R. Nagarajan, "Carrier Transport Effects in High Speed Quantum Well Lasers," Dissertation, University of California - Santa Barbara, 1992.
- [93] M. Zimmermann, S. Kramer, A. Hangleiter, F. Steinhagen, H. Hillmer, and H. Burkhard, "Carrier transport in asymmetrically confined 1.55  $\mu\text{m}$  multiple quantum well laser structures", *Applied Physics Letters* **69**, 2324 (1996).

## 5. Materials Growth and Fusion for 1.55 $\mu\text{m}$ Wafer Fused Laser Structures

This chapter is concerned with the experimental details of the growth and wafer fusion steps used to create the wafer-fused 1.55  $\mu\text{m}$  lasers described in the previous chapter. The first section of this chapter details aspects of the materials growth. Specifically, two different growth technologies are used in these 1.55  $\mu\text{m}$  wafer fused lasers: metalorganic chemical vapor deposition (MOCVD) for the active region and molecular beam epitaxy (MBE) for the AlGaAs cladding layers<sup>1</sup>. Details of the growth technologies and the conditions used in this work are outlined. The next section details the fusion process used to combine these two different samples together.

### 5.1 Materials Growth

Two different types of material are needed for the 1.55  $\mu\text{m}$  lasers outlined in Chapter 4. Figure 5-1 shows a plot of the energy versus lattice constant space for non-nitride III-V semiconductors. For my laser structures, quantum well active regions that emit light at 1.55  $\mu\text{m}$  are used. Figure 5-1 shows that this is most easily met by semiconductor alloys lattice-matched to InP. The second requirement is Al<sub>x</sub>Ga<sub>1-x</sub>As alloys for the cladding regions. This is most easily achieved by growth on GaAs. In this section, the details of the growth of each of these materials is detailed.

---

<sup>1</sup> Technologically, this does not have to be the case. Here at UCSB, the InP-based work is done by MOCVD and most of the GaAs-based work is done by MBE.

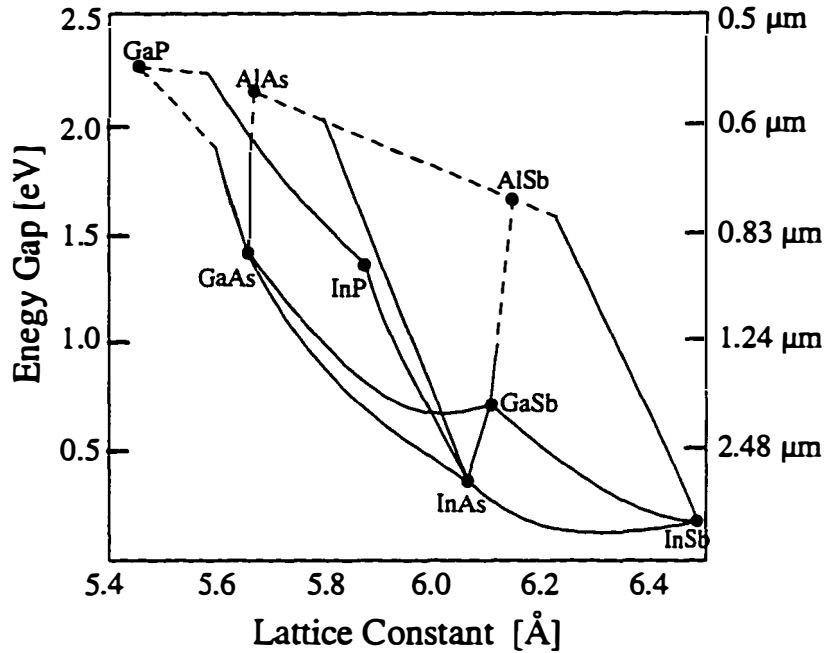


**Figure 5-1** Band gap energy versus lattice constant for common III-V semiconductors.

### 5.1.1 Active Region Growth by Metalorganic Chemical Vapor Deposition: An Introduction

Metalorganic chemical vapor deposition, or MOCVD, is a common technique for semiconductor synthesis. In this section, I will discuss some of the details that were used in the growth of quantum well active regions at 1.55  $\mu\text{m}$ . My purpose here is to give a quick general overview. Details about the process of obtaining the growth conditions detailed below is not my goal. This will be covered in detail by my colleagues here at the University of California at Santa Barbara in their dissertations; some of this work has already been published by our group[1-3].

A key feature of MOCVD is the use of organometallic compounds to provide the source material needed for compound semiconductor growth. A general schematic of an MOCVD reactor is shown below in Figure 5-2.

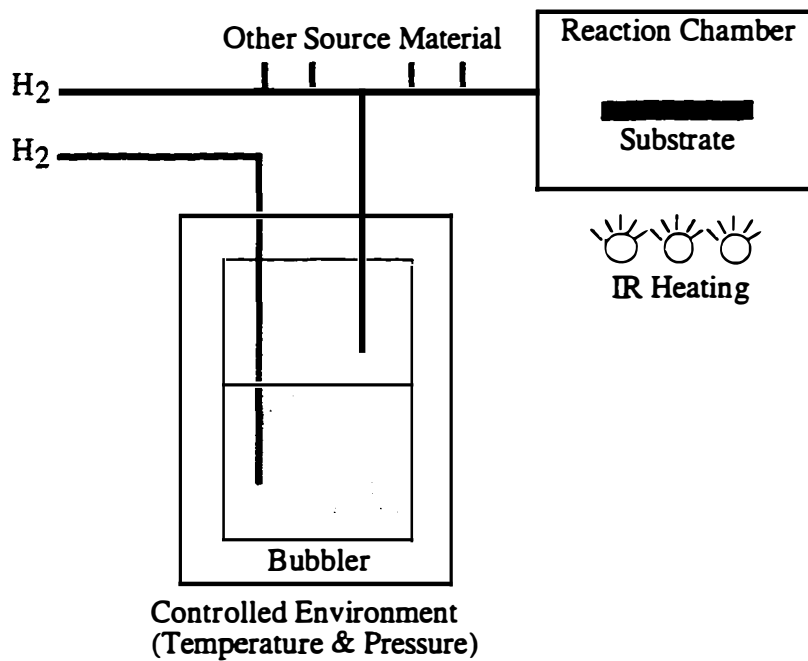


**Figure 5-2** General schematic of the MOCVD process. Note that only one source is shown for simplicity.

The process of MOCVD can be described as follows. A carrier gas (in our case hydrogen purified by a palladium diffuser) flows through a container that houses the source material (called a bubbler). The amount of the source that enters the carrier gas stream is controlled by the temperature and over-pressure of the source. This material, after mixing with other source material, then flows to a heated reaction chamber where a substrate awaits. For the growths by MOCVD in this dissertation, (100) oriented InP wafers – supplied by InPact – are used.

These n-type wafers are S-doped at  $6-8 \times 10^{18} \text{ cm}^{-3}$  with a 0.2 misorientation towards the  $\{111\}$ A.

At the temperatures typically used in MOCVD ( $\approx 600^\circ\text{C}$ ), a number of chemical processes take place both in the gas phase (known as homogeneous reactions) or at the surface of the substrate (known as heterogeneous reactions) which lead to the formation of the desired semiconductor alloy. In our MOCVD system, the source materials used are trimethylindium (TMIn) and trimethylgallium (TMGa) for the column III elements. Instead of using arsine and phosphine, as was common in MOCVD five to ten years ago, we used the organometallic compounds tertiarybutylarsine (TBA) and tertiarybutylphosphine (TBP) for the column V elements. The main advantage of these organometallic sources is that they are pyrophoric liquids with a lower toxicity than their hydride counterparts. Therefore, in the event of a catastrophic bubbler failure, the danger risk is much reduced. In addition, TBA and TBP have lower pyrolysis temperatures than arsine and phosphine; so lower growth temperatures and V/III ratios should be possible and have been reported [4,5]. In order to obtain conduction in the grown layers, sources are needed to introduce dopants. For the work here, diethylzinc was used for p-doping and disilane (at  $\approx 50 \text{ ppm}$ ) was used for n-doping. Table 5-1 details these and other important growth parameters.

In the growth of high quality quantum well active regions, where the thickness of the layers is on the order of 10 nm, the effect of interfaces is very important. This is especially true of  $\text{Ga}_x\text{In}_{1-x}\text{As}_y\text{P}_{1-y}$ -based materials. There are a couple of reasons for this. First, the column V species (As and P) are volatile at the growth temperatures used in MOCVD. This requires an over-pressure of these species to be present during growth. In addition, the quaternary alloy requires tight composition control of these volatile species. To ensure this on the atomic level, growth interruptions are typically used to control the abruptness of the



GaInAsP alloy's compositional change. Figure 5-3 shows the typical growth interruption scheme that we have found optimal in our reactor.

**Table 5-1** Important Growth Parameters used in the MOCVD synthesis of GaInAsP-based quantum well active regions at 1.55  $\mu\text{m}$ . Unless specified, all samples were grown on S-doped InP substrates with a  $0.2^\circ$  misorientation towards the  $\{111\}$ A direction.

Parameter	Units	Value
Column III sources	—	Trimethylindium, Trimethylgallium
Column V sources	—	Tertiarybutylarsine, Tertiarybutylphosphine
P-Dopant Source	—	Diethylzinc
N-Dopant Source	—	Disilane
Carrier Gas Flow	slpm	16 of $\text{H}_2$
Reactor Pressure	torr	350
Growth Temperature	$^\circ\text{C}$	610
InP Substrate Bake Time and Temperature	min.	10 @ $610^\circ\text{C}$
InP Substrate Bake TBP Flow	$\mu\text{mol}/\text{min.}$	1382

Growth is terminated by stopping the flow of the column III sources. To maintain the stoichiometry of the just completed layer an over-pressure of the column V gases is maintained for a time  $t_i$ .

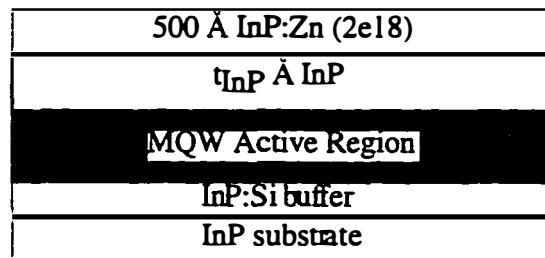
Source	InP Growth	$t_1$ (sec.)	$t_2$ (sec.)	GaInAs Growth	$t_3$ (sec.)	$t_4$ (sec.)	InP Growth
TMGa				█			
TMIn	█			█			█
TBA				█			
TBP	█					█	█

**Figure 5-3** Growth interruption scheme used in our MOCVD reactor for optimized interfaces using TBA and TBP. For our reactor,  $t_1=t_2=t_3=t_4=0.5$  s was found to be optimal [1-3].

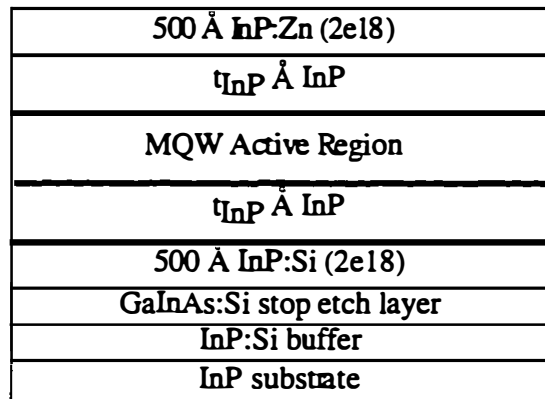
The gas composition above the substrate is then changed to flush out any species that are undesired for the next layer for a time  $t_2$ . After the next layer is grown, the process is repeated. This growth interruption can cause two detrimental effects. The first is *diffusion* of the gaseous species from the gas phase into the solid material. The other is incorporation of material that adsorbs (physi-sorbed) to the growth surface without being chemically incorporated -- a process known as *carry-over*. With the use of TBA and TBP, we have found that the use of TBA during these interruptions leads to poor interface properties that can affect device performance [2]. As shown in Figure 5-3, we do not use TBA in the purge between InP and GaInAs; only hydrogen is used during this phase of the growth interruption ( $t_2$  and  $t_3$ ). In the growth of GaInAsP, we do not use any column V flow for the growth interruptions around the *high-As* containing quaternary alloy -- the analogous situation to the case for InP and GaInAs.

### 5.1.2 Active Region Structures for 1.55 $\mu\text{m}$ Wafer Fused Lasers

In Chapter 4, I discussed some of the general features that were important in the design of 1.55  $\mu\text{m}$  lasers using wafer fusion. Here, more explicit details of the structures are presented. Figure 5-4 shows the two different structures used in this work – an active region for a *single-fused* and a *double-fused* laser.



(a)



(b)

**Figure 5-4** General multiple-quantum well (MQW) active region schematics for single-fused (a) and double-fused (b) lasers. Here,  $t_{\text{InP}}$  is the InP spacer layer thickness.

The only difference between the two structures is on the n-side of the device where there is a GaInAs stop etch layer for the *double-fused* laser. As will be discussed later, this distinction is necessary for processing the *double-fused laser's* material structure. As stated in Chapter 4, the p-doping side of the structure was assumed to be the region where high optical loss could occur in the structure. To minimize possible losses in the final device structure, two design factors are used. First, an InP spacer region,  $t_{\text{InP}}$  Å thick, is used to move the fusion junction away from the MQW active region. As stated in Chapter 4, increasing  $t_{\text{InP}}$  leads to a lower optical confinement factor. Second, a 50 nm p-InP layer doped at  $2 \times 10^{18} \text{ cm}^{-3}$  is used to minimize optical loss and ensure that the fusion junction is not in a bipolar region of the device. To investigate the progression of carrier overflow reduction on device performance, two different MQW active regions are investigated. These are illustrated in Figure 5-5. In order to grow these structures accurately, calibration of the GaInAsP compositions used must be done. This was done for all of the compositions here, except for the low compressively strained GaInAsP quantum well, by my colleagues Greg Fish and Dr. Patrick Abraham. The details of the growth of these InP-based alloys is shown in Table 5-2 below. The procedure employed at UCSB to control the GaInAsP composition most accurately involved fixing the amount of TMIn and TBP used and adjusting the TMGa and TBA to change compositions. For these compositions, the growth rate varies from 6.5 Å/s for InP to approximately 12 Å/s for GaInAs. It is found that the growth rate is linear with column III flow as would be expected in the mass-transport regime of growth in which we operate.

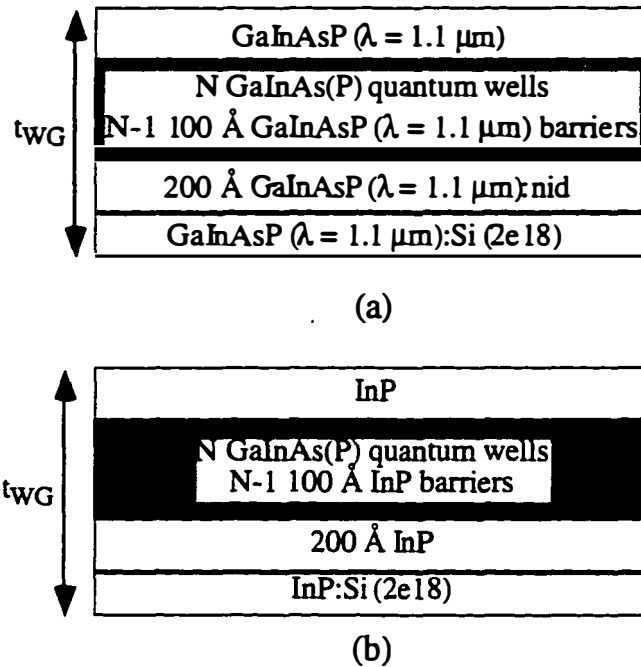


**Figure 5-5** MOCVD-grown active regions for 1.55  $\mu\text{m}$  wafer fused lasers. In case (a) GaInAsP ( $\lambda = 1.1 \mu\text{m}$ ) barriers are used and in case (b) InP barriers are used. The specific GaInAsP quantum well values as well as  $N$  and  $t_{\text{WG}}$  are detailed in Table 5-4.

### 5.1.3 Cladding Layer Growth by Molecular Beam Epitaxy

In the previous section, details of the MOCVD growth of the active region for 1.55  $\mu\text{m}$  wafer fused lasers was described. Here, the growth of the AlGaAs cladding layers by MBE<sup>ii</sup> is covered. MBE is a very popular synthesis techniques for the development of novel and state-of-the-art semiconductor, metallic, and other structures for various applications.

<sup>ii</sup> These growths were done by my colleagues at UCSB – Dr. Richard P. Mirin and Yi-Jen Chiu.

**Table 5-2** Partial Pressures for the various GaInAsP compositions used in the 1.55  $\mu\text{m}$  wafer-fused lasers.

Material	Solid Composition (%)		Partial Pressure (mtorr)			
	Ga	As	Ga	In	As	P
InP	0	0		17.9		667
GaInAs	46.8	100	15.7	17.9	100	
GaInAsP ( $\lambda=1.1 \mu\text{m}$ )	13.6	29.6	2.3	17.9	12.5	667
GaInAsP ( $\lambda = 1.25 \mu\text{m}$ )	23.1	50.2	4.3	17.9	28.8	667
Low Strain GaInAsP QW	35	90	8.4	17.9	466	667

Whereas MOCVD uses organometallic sources to provide the chemical constituents for the growing layer, MBE uses molecular or atomic sources<sup>iii</sup>. These sources are placed in temperature controlled effusion cells where thermal evaporation controls the amount of the source used in growth. For reliable composition and thickness control, the temperature inside the effusion cell needs to be controlled to  $\pm 1^\circ\text{C}$ . These beam fluxes are directed to a heated growth substrate in an ultra-high vacuum (UHV) chamber. UHV Base pressures of  $\leq 10^{-9}$  Torr (UHV) are used to minimize the amount of impurity species in the growth chamber as well as increasing the mean free path of the atomic or molecular species. To maintain equilibrium-like conditions inside of the effusion cell, the source is always heated; its introduction into the growth chamber is controlled by a mechanical shutter placed in front of the cell's orifice. In

<sup>iii</sup> A hybrid of MOCVD and MBE -- CBE or MOMBE -- is also gaining wider use.

addition, the substrate is rotated to improve uniformity where  $\pm 1\%$  over a 2-inch wafer is achievable. These and other features of a MBE system are shown schematically below.

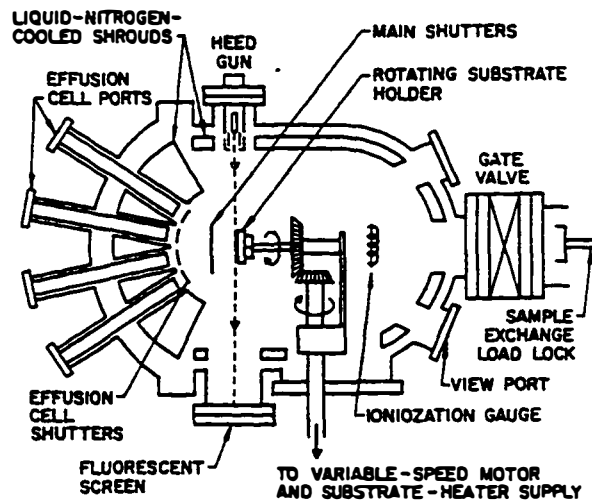


**Figure 5-6** Schematic of a molecular beam epitaxy system. This diagram was taken from Reference [6].

Since MBE is done in an UHV environment, there are a number of analytical tools that can be used to monitor the substrate before, after, or during growth. A popular tool -- Reflection High Energy Electron Diffraction (RHEED) -- is typically used to measure the growth rate of a semiconductor composition by measuring the intensity oscillations of a specularly reflected electron beam off the substrate<sup>iv</sup>. Under typical MBE growth conditions it is assumed that every group III atom incident on the substrate is incorporated (a unity sticking

---

<sup>iv</sup> At UCSB, this measurement is done on a separate wafer prior to growth of the actual structure.

coefficient). Thus, the composition is controlled by the relative column III fluxes.

Two different structures were grown by MBE for the cladding layers in 1.55  $\mu\text{m}$  wafer fused laser structures. They are shown in Figure 5-7 below.

500 Å GaAs:Be ( $2e18$ )
0.5 $\mu\text{m}$ AlGaAs( $x=0.7$ ):Be ( $5e17$ )
1 $\mu\text{m}$ AlGaAs( $x=0.7$ ):Be ( $2e18$ )
0.15 $\mu\text{m}$ Å GaAs:Be contact ( $5e19$ )
AlAs:Be buffer
GaAs:Be buffer
GaAs substrate

(a)

500 Å GaAs:Si ( $2e18$ )
1.5 $\mu\text{m}$ AlGaAs( $x=0.7$ ):Si ( $5e17$ )
GaAs:Si buffer
GaAs:Si substrate

(b)

**Figure 5-7** The p-AlGaAs structure (a) and n-AlGaAs structures (b) grown by MBE for 1.55  $\mu\text{m}$  wafer fused laser structure.

In the growth of these structures, substrate preparation is done in three parts. A bake is done in the buffer chamber to drive off  $\text{H}_2\text{O}$ , hydrocarbons, and any other impurities that may be on the wafer before introduction to the growth



chamber. Another – slightly higher – bake temperature is done in the growth chamber with the wafer facing way from the sources. This is done to ensure that as many impurities as possible are removed. After this, an oxygen desorption bake is done under an arsenic over-pressure to remove the native oxide on the GaAs substrate<sup>v</sup>. The substrate preparation parameters as well as other growth-related parameters are detailed in Table 5-3. Another important aspect to note about the growth of the structures in Figure 5-7 is the manner by which the AlGaAs is grown. At UCSB, digital alloys – thin alternating layers of AlAs and GaAs -- are used to represent the random alloys [7-9]. This allows for various Al mole fractions to be grown without a change in the Al or Ga effusion cell temperature. In digital alloys, the percentage of AlAs that makes up the AlAs/GaAs period denotes the Al mole fraction; in addition, this period must be made sufficiently small so that the mini-band structure of the superlattice and its electron transport behaves like a bulk alloy.

#### *5.1.4 Final Growth Structures*

In this section, the two growth technologies used to create the material structures needed for 1.55  $\mu\text{m}$  wafer fused laser structures have been detailed. Before leaving this section, the various device structures that were grown for fabrication into lasers are summarized in Table 5-4.

---

<sup>v</sup> RHEED is used to monitor the removal of the oxide.

**Table 5-3** Various parameters used in the growth of the AlGaAs cladding layer structure in Figure 5-7. The Be and Si cell temperatures are varied to achieve the desired doping levels.

Parameter	p-AlGaAs Structure	n-AlGaAs Structure
Buffer Chamber Bake	350°C / 2 hrs.	350°C / 2 hrs.
Growth Chamber Bake	450°C/40 min.	450°C/30 min.
Oxide Desorption Temp. [a]	630°C	625°C
Ga cell Temp.	1076°C	973°C
Ga BEP [b]	$7.3 \times 10^{-7}$ T	$2.3 \times 10^{-7}$ T
Al Cell Temp.	1370°C	1289°C
Al BEP [b]	$5.2 \times 10^{-7}$ T	$3.5 \times 10^{-7}$ T
As Cell Temp [c]	355°C	385°C
As cracker voltage	13.3 mV	13.2 mV
As BEP [b]	$12 \times 10^{-7}$ T	$95 \times 10^{-7}$ T
Rotation Speed	15 rpm	6 rpm
Growth Temp	655°C	690°C

#### Notes

- [a] The oxide desorption is monitored via RHEED
- [b] BEP stands for Beam Equivalent Pressure
- [c] A valved As cracker source is used.

**Table 5-4** Descriptions of the MOCVD-grown 1.55  $\mu\text{m}$  quantum well active regions grown for 1.55  $\mu\text{m}$  in-plane wafer-fused structure. The results of these devices are shown in Chapter 6.

Label	Description
SF-A	4 0.7% 5.5 nm GaInAsP quantum wells GaInAsP( $\lambda = 1.25 \mu\text{m}$ ) waveguide with 10 nm barriers 300 nm total waveguide thickness; 100 nm InP spacer
SF-B	4 0.7% 6.5 nm GaInAsP quantum wells GaInAsP( $\lambda = 1.1 \mu\text{m}$ ) waveguide with 10 nm barriers 396 nm total waveguide thickness; 100 nm InP spacer
DF-A	4 0.7% 6.5 nm GaInAsP quantum wells GaInAsP( $\lambda = 1.1 \mu\text{m}$ ) waveguide with 10 nm barriers 246 nm total waveguide thickness; 250 nm InP spacer
DF-B	3 0.7% 7 nm GaInAsP quantum wells InP waveguide with 10 nm barriers 641 nm total waveguide thickness; 250 nm InP spacer

## 5.2 Fusion Process for 1.55 $\mu\text{m}$ In-Plane Lasers

The process of fusion used here was developed in a collaboration with UCSB and Hewlett Packard Laboratories. General details and characterization of the procedure have been published elsewhere [10,11]. The procedure outlined here was adapted from the one developed by Dubravko Babic; it was this procedure that led to the first continuous-wave operation of a 1.55  $\mu\text{m}$  vertical-cavity surface-emitting laser above room temperature [12]. Key points in the procedure are illustrated in Figure 5-8 below and this figure is referred to throughout this section.

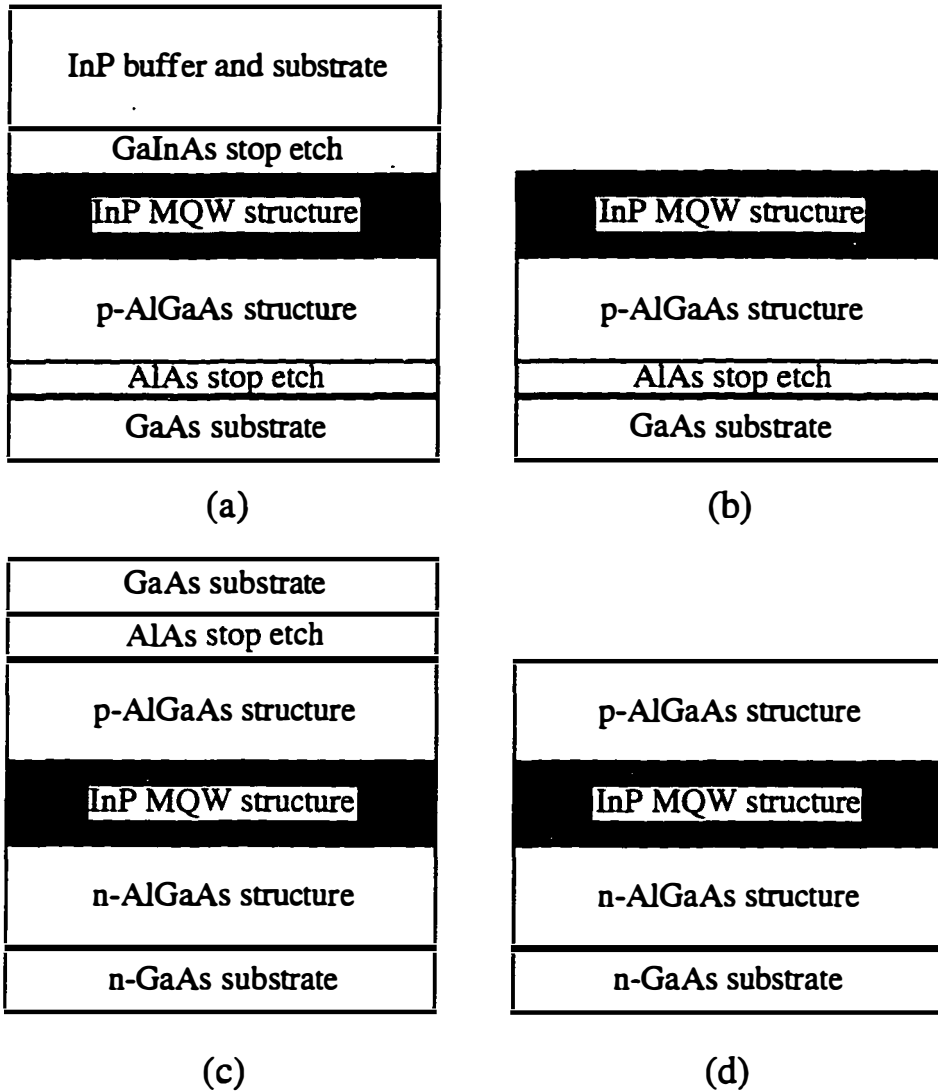


**Figure 5-8** Schematic of four important points in the fusion process as discussed in Section 5.2. The procedure shown here is for a double-fused 1.55  $\mu\text{m}$  laser. The single-fused structure is different in that the n-GaAs structure and substrate are replaced by an n-InP substrate and steps (a) and (d) are the only ones that occur.

An important thing to note here: the procedure below is for a *double-fused* laser structure. For a *single-fused* laser structure, Section 5.2.3 is not done.

### 5.2.1 Initial Sample Preparation

The first main step in the preparation of the samples for wafer fusion is to etch channels into the InP sample. This sample, as well as the p-GaAs sample, are made to be approximately 8x8 mm<sup>2</sup>. The procedure used to achieve these channels is outlined below:

- Sample is cleaned in acetone and isopropanol
- Positive photoresist (AZ4110) is spun on the sample at 6000 rpm for 35 seconds.
- The resist is then baked on a hot plate at 95°C for 1 minute.
- After allowing the sample to cool, 5 μm lines are transferred into the photoresist via exposure through a mask. The nominal exposure intensity is 7.5 mW/cm<sup>2</sup> with a time of 30 seconds. A long time is used in ensure complete exposure of resist at the edge of the samples where it is higher than in the center.
- The resist was then hard baked at 115°C for 2 minutes to make it more resistant to acid etching.
- After exposure, the sample is placed in a 20% developer solution (1 part developer: 4 parts deionized (DI) water) for 1 minute. Visual inspection was used to confirm the completion of the photoresist removal.
- The sample was then placed in an acid solution (3 H<sub>3</sub>PO<sub>4</sub>:1 HCl) to etch the InP.
- The photoresist is then removed in acetone. The samples is placed in isopropanol to remove the acetone and then dried with N<sub>2</sub>.

This step is typically done days before the actual fusion takes place. Before fusion, a complete cleaning of both the InP and p-GaAs samples is done. This cleaning of the samples can be broken down into four parts. The first is a heated solvent clean of the samples. The steps are outlined below:

- The samples are first scrubbed lightly with a constant acetone flow.
- The sample is placed in isopropanol to remove the acetone.
- The samples are placed in acetone which has been heated to just below the boiling point for 3 minutes. After this, the samples are placed into room temperature isopropanol to cool down the sample and remove residual acetone. This step is repeated a couple of times with the acetone and isopropanol being replaced between cleans

The next step in the process is a removal of any native oxide that still may be on the sample. This is done by placing both samples in pure ammonium hydroxide ( $\text{NH}_4\text{OH}$ ) for 5 minutes. After this, the samples are rinsed in DI water and dried thoroughly with nitrogen and then placed in a deep ultraviolet ozone system. This step has two purposes: to aid in the removal of any additional hydrocarbon-based contaminants and to grow an oxide layer on the samples. After 1 hour in the ozone system, the samples are removed and placed into pure  $\text{NH}_4\text{OH}$  for transport to the fusion system.

### 5.2.2 *First Fusion*

When this step commences, the InP and p-GaAs samples are in  $\text{NH}_4\text{OH}$ . They are removed and placed into methanol which dissolves the  $\text{NH}_4\text{OH}$  and puts the samples in an environment where oxidation does not occur. The samples are manually mated with a thin layer of methanol on both surfaces. After joining, the sample configuration is that shown in Figure 5-8(a). This combination is

then loaded into a graphite fixture for fusion. A calibrated torque wrench is used to place an even pressure of  $\approx 2.5$  MPa on the sample. When this is completed, the graphite fusion fixture is placed into the fusion system under nitrogen. A venturi pump is used to pump out the system from atmosphere ( $\approx 14.8$  psi) to 0.9 psi three times. On the first two pump downs, the system is back filled with nitrogen and on the last one the system is back filled with the ambient gas for the temperature cycle, either hydrogen or nitrogen. This gas flows through the system for a few minutes before the temperature cycle begins. The temperature sequence used for the fusion process is summarized in Figure 5-9.

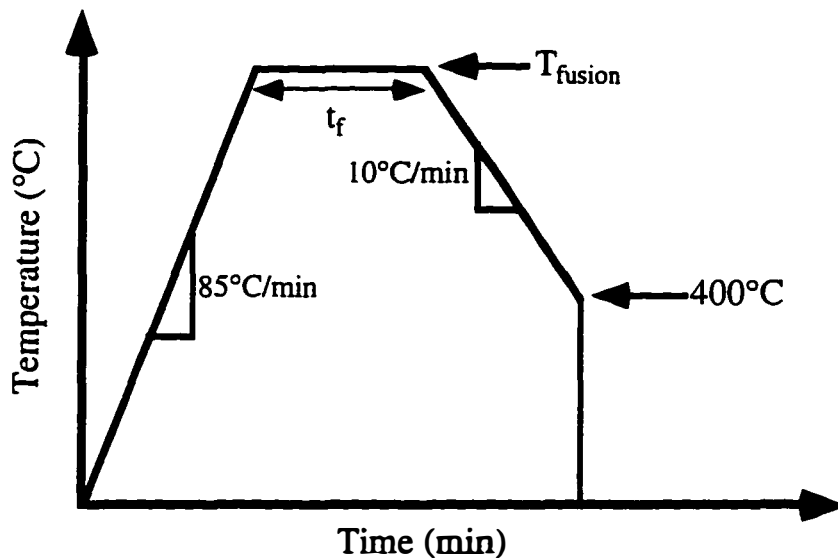


**Figure 5-9** The temperature set point of the fusion heater controller as a function of time. The stabilization point is at  $T_{fusion}$  for a time  $t_f$ .

Measurements of the system response revealed a ten minute delay between the sample reaching the fusion temperature and the controller. The ramp down time of 10°C/min. is used to minimize the amount of time that additional thermal

stress are applied to the sample [13]. This additional stress could lead to strain relaxation of the quantum well active region[14].

### 5.2.3 InP Substrate Removal

After the sample has cooled to room temperature, it is removed from the graphite fusion fixture and then is ready for InP substrate removal. InP is convenient in that a fast, highly selective ( $> 1000$ ) etch exists for InP over GaInAs (where the gallium content can be as little as 10%). This etch is 3 HCl: 1 H<sub>2</sub>O. The sample is placed in solution and it takes approximately 40 minutes to remove the entire InP substrate. The GaInAs stop etch layer is also removed. Another selective etch, 3 H<sub>3</sub>PO<sub>4</sub>:1 (H<sub>2</sub>O<sub>2</sub>): 50 DI H<sub>2</sub>O is used. The structure of the wafer fused material is now shown in Figure 5-8(b).

### 5.2.4 Second Fusion and GaAs Substrate Removal

For the next fusion, the sample is then re-processed for fusion along with an n-GaAs sample<sup>vi</sup>. For the work presented here channels were not etched for the second fusion. These two samples are joined and fused in the same manner discussed in Section 5.2.2. After the fusion has been completed, the sample (see Figure 5-8(c)) need to have the GaAs substrate of the p-AlGaAs structure removed. This is done in NH<sub>4</sub>OH: 30 H<sub>2</sub>O<sub>2</sub> using a spray etch setup developed by Dubravko Babic to speed up the process. This etch stops on AlAs and takes about 3 hours to complete. The completion of the etch can be seen by a color change of the surface due to the AlAs. After completing the GaAs substrate removal, the sample is placed into 5% hydrofluoric acid to remove the AlAs.

---

<sup>vi</sup> For the single-fused case, a p-GaAs sample is used here.



After the removal of the GaAs substrate the sample (see Figure 5-8(d)) is ready to be processed.

### 5.3 Summary

In this chapter, I have covered the creation of a 1.55  $\mu\text{m}$  wafer-fused laser. The process starts with three samples: one with InP-based quantum wells grown by MOCVD and two AlGaAs structures, one p-type and one n-type, grown by MBE. These samples are then joined via wafer fusion and processed into either *50  $\mu\text{m}$  broad-area lasers* or *narrow ridge waveguide lasers with a PMGI bond pad configuration* for testing. In the next chapter, the experimental results of the lasers fabricated by the processes in this chapter are detailed.

## 5.4 References

- [1] S. P. Denbaars, A. L. Holmes, M. E. Heimbuch, V. J. Jayaraman, C. M. Reaves, J. B. Shealy, U. K. Mishra, L. S. Coldren, and J. E. Bowers, "Indium Phosphide (InP) Based Heterostructure Materials and Devices Grown By Mocvd Using Tertiarybutylarsine (TBA) Tertiarybutylphosphine (TBP)", *Journal Of the Korean Physical Society*, S37 (1995).
- [2] A. L. Holmes, Jr., M. E. Heimbuch, G. Fish, L. A. Coldren, and S. P. Denbaars, "InP-based multiple quantum well structures grown with tertiarybutylarsine (TBA) and tertiarybutylphosphine (TBP): effects of growth interruptions on structural and optical properties", *Journal of Electronic Materials* **25**, 965 (1996).
- [3] M. E. Heimbuch, A. L. Holmes, Jr., C. M. Reaves, M. P. Mack, S. P. Denbaars, and L. A. Coldren, "Tertiarybutylarsine and tertiarybutylphosphine for the MOCVD growth of low threshold 1.55  $\mu\text{m}$  In/sub  $x$ /Ga/sub  $1-x$ /As/InP quantum-well lasers.", *Journal of Electronic Materials* vol.23,, 87 (1994).
- [4] M. Horita, M. Suzuki, and Y. Matsushima, "MOVPE growth of InGaAsP using TBA and TBP with extremely low V/III ratio", *Sixth International Conference*, Cambridge, MA, USA, 1992, 123.
- [5] M. Horita, M. Suzuki, and Y. Matsushima, "Electrical and optical properties of InP grown by metalorganic vapor phase epitaxy with extremely low V/III ratios using tertiarybutylphosphine", *Applied Physics Letters* **62**, 882 (1993).
- [6] V. Swaminathan and A. T. Macrander, *Materials aspects of GaAs and InP based structures* (Prentice Hall, Englewood Cliffs, N.J., 1991).
- [7] K. J. Moore, G. Duggan, P. Dawson, and C. T. Foxon, "Short-period GaAs-AlAs superlattices: optical properties and electronic structure", *Physical Review B (Condensed Matter)* **38**, 5535 (1988).
- [8] T. J. Drummond, E. D. Jones, H. P. Hjalmarson, and B. L. Doyle, "Growth and characterization of GaAs/AlAs superlattice alloys", *Growth of Compound Semiconductors*, Bay Point, FL, USA, 1987, 2.
- [9] K. Ploog, "Molecular beam epitaxy of artificially layered III-V semiconductors: ultrathin-layer (GaAs)<sub>m</sub>/(AlAs)<sub>m</sub> superlattices and delta-doping in GaAs", *7th General Conference of the Condensed Matter Division of the European Physical Society*, Pisa, Italy, 1987, 136.
- [10] D. I. Babic, "Double-Fused Long-Wavelength Vertical-cavity Lasers," Dissertation, University of California, Santa Barbara, 1995.

- [11] R. J. Ram, J. J. Dudley, J. E. Bowers, L. Yang, K. Carey, S. J. Rosner, and K. Nauka, "GaAs to InP wafer fusion", *Journal of Applied Physics* **78**, 4227 (1995).
- [12] D. I. Babic, K. Streubel, R. P. Mirin, J. Piprek, N. M. Margalit, J. E. Bower, E. L. Hu, D. E. Mars, L. Yang, and K. Carey, "Room-temperature performance of double-fused 1.54  $\mu\text{m}$  vertical-cavity laser", *Eighth International Conference on Indium Phosphide and Related Materials (Cat. No.96CH35930) Proceedings of 8th International Conference on Indium Phosphide and Related Materials*, Schwabisch-Gmund, Germany, 1996, 719.
- [13] Q. Y. Tong and U. Gosele, "Semiconductor wafer bonding: recent developments", *Materials Chemistry and Physics* **37**, 101 (1994).
- [14] J. Y. Tsao and B. W. Dodson, "Time, temperature and excess stress: relaxation in strained heterostructures", *Fourth International Conference on Modulated Semiconductor Structures*, Ann Arbor, MI, USA, 1989, 260.



## 6. Theoretical Predictions and Experimental Results

In this chapter the results I have obtained on 1.55  $\mu\text{m}$  wafer-fused laser structures are presented. Using the procedure of Chapter 2, the theoretical predictions for these *single-fused* and *double-fused* laser structures are presented in the first section. Following this, experimental results for lasers fabricated using the procedure outlined in Chapter 5. First, the effects of temperature on 1.55  $\mu\text{m}$  laser active regions is explored. Then, a comparison between *identical* active regions with either a p-InP or p-AlGaAs cladding layer is presented. Finally, narrow ridge laser results on *single-fused* and *double-fused* laser structures are detailed.

### 6.1 Theoretical Predictions

In Chapter 4, a design methodology was presented in which lasers with reduced carrier overflow could be made without a corresponding reduction in optical confinement. This section is concerned with a theoretical comparison of these structures with the 1.55  $\mu\text{m}$  in-plane laser results of Chapter 3. For convenience, the structure from Chapter 3 will be referred to as the conventional (*Conv.*) laser structure. Table 6-1 below details the important parameters for each of the three wafer-fused structures: a single-fused laser with a GaInAsP( $\lambda = 1.1 \mu\text{m}$ ) waveguide [called *SF-Q*], a double-fused laser with a GaInAsP( $\lambda = 1.1 \mu\text{m}$ ) waveguide [called *DF-Q*], and a double-fused laser with an InP waveguide [called *DF-B*].

**Table 6-1** Summary of the various confinement factors for *SF-Q*, *DF-Q*, and *DF-B*. The other parameters can be found in Table 3.1.

Structure	$\Gamma_w$	$\Gamma_B$	$\Gamma_s$
<b>3 Quantum Well Active Region</b>			
SF-Q	4.24 %	3.4 %	49.9 %
DF-Q	4.83 %	3.9 %	35.5 %
DF-B	4.6 %	3.42 %	56 %
<b>5 Quantum Well Active Region</b>			
SF-Q	7.56 %	7.32 %	45.7 %
DF-Q	8.42 %	8.16 %	29.6 %
DF-B	8.13 %	7.27 %	54.4 %

In addition, these structure have  $p\text{-Al}_{0.7}\text{Ga}_{0.3}\text{As}$  cladding layers; this will reduce the carrier leakage out of the active region which is seen in GaAs-based lasers [1.2]. As was mentioned in Chapter 4, these values for the optical confinement factor of the active region as improved over the device modeled in Chapter 3. The various structures – using the procedure of Chapter 2 – are modeled. Figure 6-1 below shows the results for  $T_o$  values as a function of cavity length.

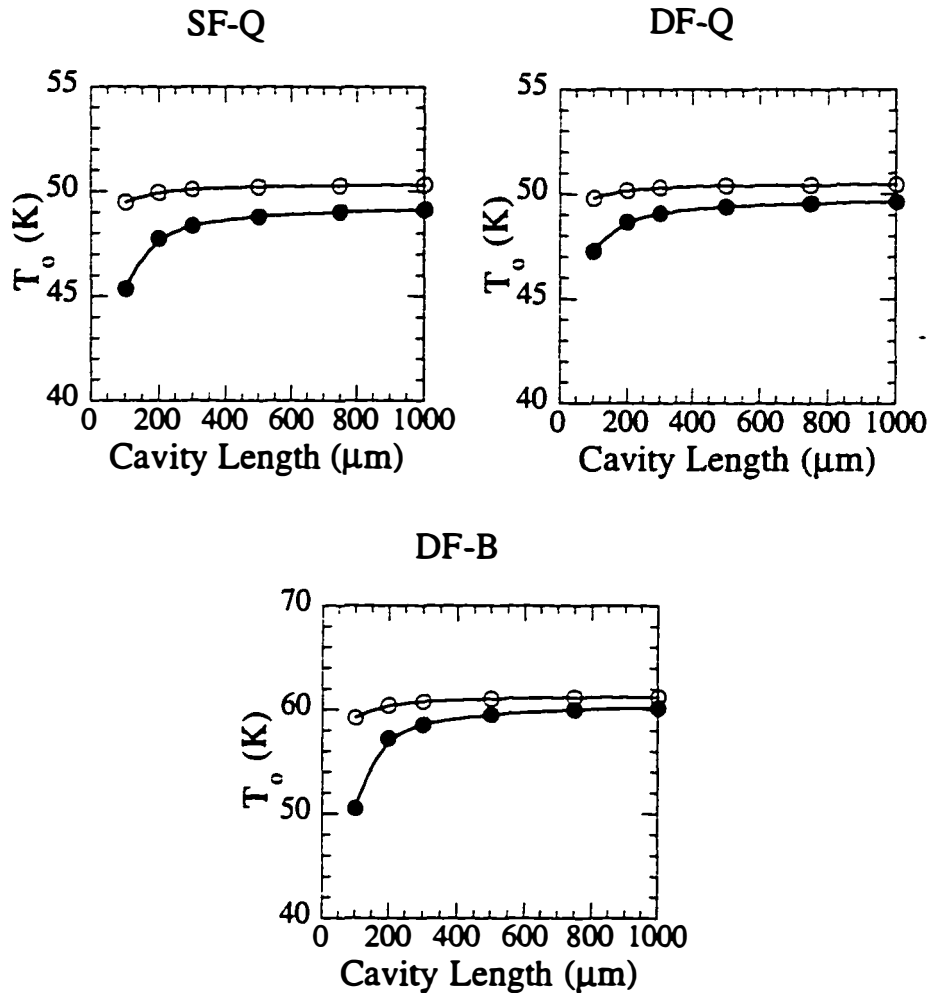


**Figure 6-1** Predicted  $T_0$  values for the *SF-Q*, *DF-Q*, and *DF-B* structures of Table 6-1 with a 3 (closed circles) or 5 (open circles) quantum well active region.

Various things can be derived from the results of  $T_0$  in Figure 6-1. For all of the wafer-fused  $1.55 \mu\text{m}$  laser structures, I predict an increase in  $T_0$  over the *Conv.* structure without a corresponding decrease in Auger recombination. This is due

to the improved carrier confinement in each of these structure which is accomplished by the increased barrier heights<sup>1</sup>. An important thing to note is that the two structure with GaInAsP( $\lambda = 1.1 \mu\text{m}$ ) waveguide – *SF-Q* and *DF-Q* – do not vary significantly in terms of  $T_o$ . This is even with a  $\approx 14\%$  increase in the confinement factor for the active region. As was discussed in Chapter 3, this shows that other effects are determining  $T_o$ . In the case of *SF-Q* and *DF-Q*, the increase over the *Conv.* structure by approximately 7.4% for a  $3 \times 1000 \mu\text{m}^2$  device with a three quantum well active region. This improvement gets better for a  $3 \times 100 \mu\text{m}^2$  device with a three quantum well active region where the improvement rises to nearly 13%. In terms of *DF-B*, which has a much higher electron confinement, the improvement is even more dramatic. The predicted improvements in this case are 31.6 % and 25.6 % for a  $3 \times 1000 \mu\text{m}^2$  and  $3 \times 100 \mu\text{m}^2$  devices with a three quantum well active region respectively<sup>ii</sup>. Figure 6-2 show the theoretical results for  $T_o^{10mW}$ . There is a difference in all of the structures. *SF-Q* has a value for  $T_o^{10mW}$  of 197 K for a  $3 \times 300 \mu\text{m}^2$  device. This value improves to 236 K for the *DF-Q* structure and finally to 415 K for *DF-B*. The improvement in terms of  $T_o^{10mW}$  is due to the improved confinement (i.e., lower  $I_{th}$  values) for *DF-Q* and *DF-B* structures as compared to *SF-Q* structure. In comparison with the *Conv.* structure, the increase is 58.8%, 89.7%, and 234% for *SF-Q*, *DF-Q*, and *DF-B* respectively.

Before ending this section and moving onto the experimental results, Table 6-2 summarizes the data presented in and as well as calculations of  $T_{max}$  for each of these structures.

---

<sup>1</sup> Again, uniform pumping of the quantum wells in the active region is assumed.

<sup>ii</sup> If the Auger coefficient is different that  $5 \times 10^{-29} \text{ cm}^6/\text{s}$  with a 60 meV activation energy, this improvement will increase.



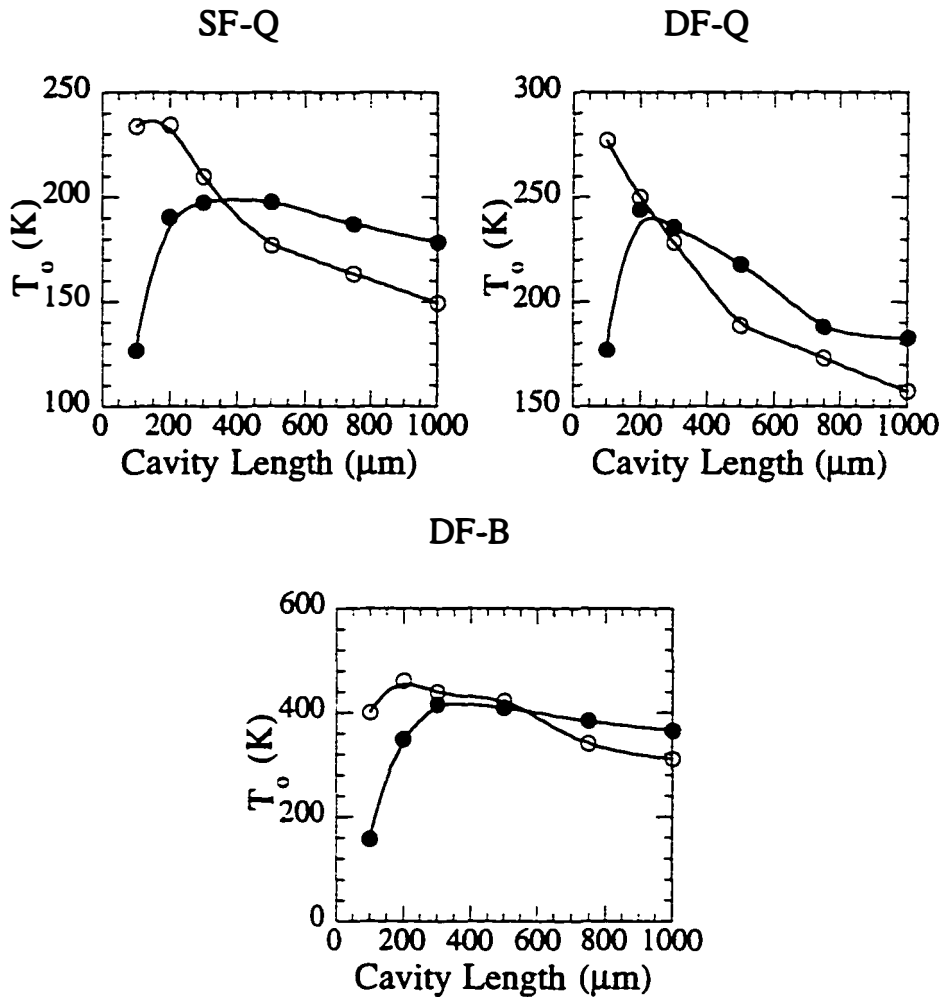


**Figure 6-2** Predicted  $T_0^{10mW}$  values for the *SF-Q*, *DF-Q*, and *DF-B* structures of Table 6-1 with a 3 (closed circles) or 5 (open circles) quantum well active region.

In terms of  $T_{max}$ , the prediction is that the *SF-Q* structure will have a higher value than the *DF-Q* structure which has a lower threshold current at 20°C. The reason for this is the use of a different thermal conductivity for the substrate.

**Table 6-2** Summary of the  $T_o$ ,  $T_o^{10mW}$ , and  $T_{max}$  values predicted for structures *SF-Q*, *DF-Q*, and *DF-B* structures of Table 6-1.

Structure		Conv.	SF-Q	DF-Q	DF-B
$T_o$ 3x500 $\mu\text{m}^2$ device	3 QWs	45.4 K	48.4 K	49.1 K	58.5 K
	5 QWs	47 K	50.1 K	50.3 K	60.7 K
$T_o^{10mW}$ 3x500 $\mu\text{m}^2$ device	3 QWs	124 K	190 K	244 K	349 K
	5 QWs	137 K	234 K	250 K	461 K
$T_{max}$ 3x300 $\mu\text{m}^2$ device	3 QWs	136°C	174°C	174°C	195°C
	5 QWs	164°C	192°C	177°C	> 200°C
$I_{th}$ 3x500 $\mu\text{m}^2$ device	3 QWs	8.6 mA	5.8 mA	5.1 mA	3.3 mA
	5 QWs	10.2 mA	6.9 mA	6.5 mA	3.8 mA

In the case of *SF-Q*, the substrate is InP which has a thermal conductivity value of 0.88 W/cm $\cdot$ °C. For *DF-Q* the substrate is GaAs which has a thermal conductivity of 0.45 W/cm $\cdot$ °C. If the thermal conductivity for *DF-Q* is equal to InP,  $T_{max}$  rises to 195 °C and >200°C for a three and five quantum well active region respectively. In all cases shown in Table 6-2, the values approach – but do not reach – the values calculated in Chapter 3 for no carrier overflow effects.

## 6.2 Experimental Results

In this section the experimental results obtained are explained. First, the effects of the fusion process on the 1.55  $\mu\text{m}$  laser structures is explored. This is followed by the experimental results of the laser structures fabricated using the procedure of Appendix B. Four different laser structures were used. They are outlined in Table 6-3.

**Table 6-3** Experimental structures fabricated into lasers for testing. The Active Regions refer to the structures outlined in Table 5.4.

Structure	Active Region	Comments	$\Gamma_{\text{act}}$
SF-Q1	SF-A	broad-area devices only	4.59 %
SF-Q2	SF-B	narrow ridge devices only one structure was annealed.	4.43 %
DF-Q1	DF-A	narrow ridge devices only	5.05 %
DF-B1	DF-B	narrow ridge devices only	3.1 %

### 6.2.1 Effects of the Fusion Process on 1.55 $\mu\text{m}$ Lasers: Structural, Optical, and Broad-Area Results

This sections covers experimental work done to determine the effect of the temperature chosen for wafer fusion. The final structure used in this study is shown below in Figure 6-3.

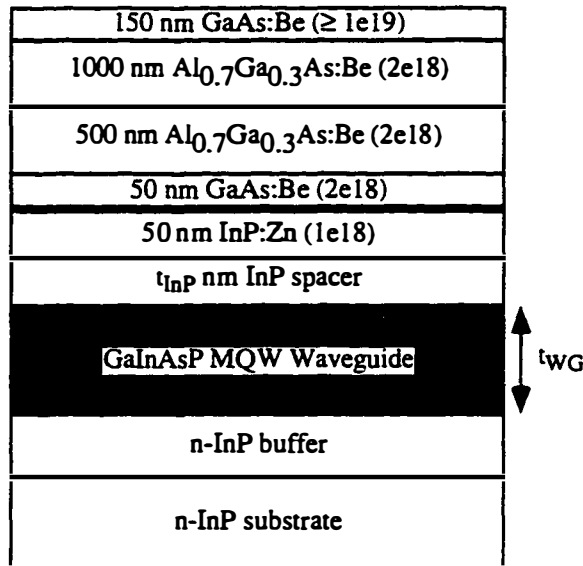


**Figure 6-3** Schematic of the final device structure of the material used in the fusion temperature characterization study. The lightly shaded region represents the MBE grown p-AlGaAs structure and the dark shaded region is the GaInAsP waveguide where the multiple quantum well active region resides. See Chapter 5 for more details. The dark solid line represents the fusion interface.

Here the structure similar to the one used in the modeling results presented in Chapter 3. The active region consists of four 0.7% compressively strained quantum wells and different compositions for the GaInAsP waveguide were used. This waveguide is placed into a single fused laser structure with a 100 nm InP spacer. The fusion temperature and time were used as variables as outlined in Table 6-4. The temperature was chosen as an important parameter for a two reasons. First, the quality of the fusion interface could be affected since the amount of mass transport that occurs at that interface (see Chapter 5); this mass transport should have an exponential dependence on temperature.

**Table 6-4** Samples used in the Fusion Temperature Study. The cleaning procedure, fusion pressure, heat-up rate, and cool-down rate are detailed in Chapter 5. For the waveguide material, 1.25Q stands for GaInAsP ( $\lambda = 1.25 \mu\text{m}$ ) and 1.1Q stands for GaInAsP ( $\lambda = 1.1 \mu\text{m}$ ). In all cases the fusion gas used was hydrogen.

Label	Waveguide		Fusion Conditions	
	Material	Thickness	Temperature	Time
A	1.25Q	300 nm	575°C	30 min.
B	1.25Q	300 nm	605°C	30 min.
C	1.25Q	300 nm	630°C	30 min.
E	1.1Q	400 nm	650°C	30 min.
F	1.1Q	400 nm	675°C	30 min.

A change in the quality of this interface could lead to changes in the turn-on voltage and internal losses of the laser structure. Another effect on the laser structure for which temperature could play a role is diffusion: both dopant diffusion (of the Zn and/or Be) and cation/anion interdiffusion of the GaInAsP quantum wells in the GaInAsP waveguide. A reduction of temperature should also minimize these effects since both diffusion mechanisms depend exponentially on temperature [3-5]. Other effects that may affect the results of this study as the fusion temperature is changed include a reduction in  $J_{th}$  due to a reduction in non-radiative defects in the quantum well active region [6,7] and an increase in  $J_{th}$  due to partial strain relaxation of the active region [8,9]. For structures A-C in Table 6-4, the active region's optical confinement factor is 4.59 %, the distance from the outermost quantum well to the bonding interface is 274 nm, and the overlap of the lasing mode with the fusion structure is 5.54 %. For structure D and E, the values are 4.82 %, 320 nm, and 4.66 % respectively.

**Structural Results**

To test the structural quality of the 1.55  $\mu\text{m}$  in-plane laser structure after the fusion process had been completed, a (004) reflection centered upon the InP Bragg angle was done on each sample in Table 6-4. The results are shown in Figure 6-4 for samples A-C and Figure 6-5 for samples D and E.

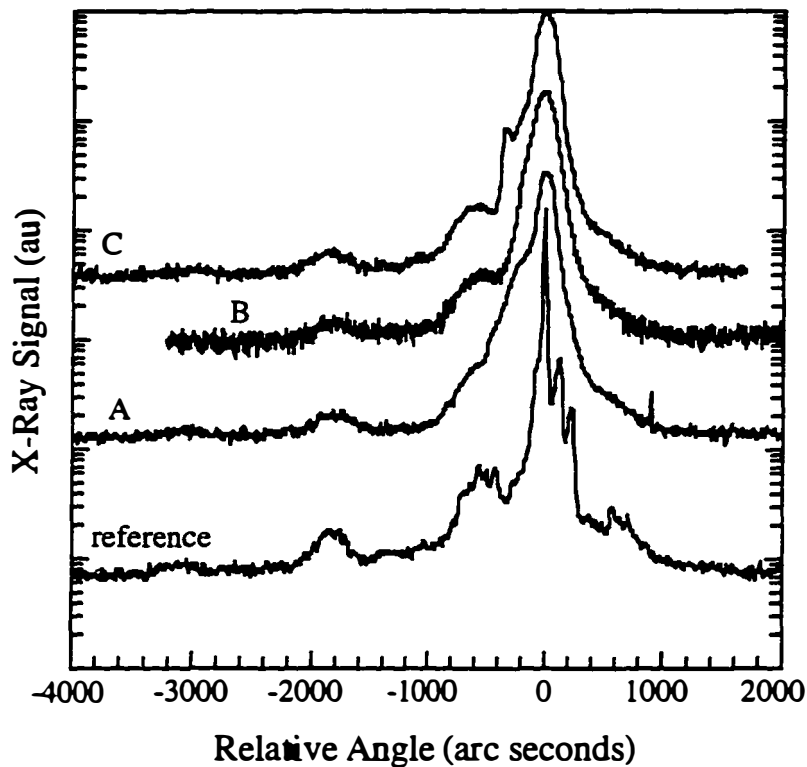


**Figure 6-4** (004) double crystal x-ray rocking curve of samples A, B, and C after fusion with a reference sample of the active region prior to fusion.

The results of the x-ray measurements show that the structure of the multiple quantum well active region is conserved over the entire temperature range

investigated. In addition, all of the peaks in the rocking curve are broadened as compared to the reference scan.

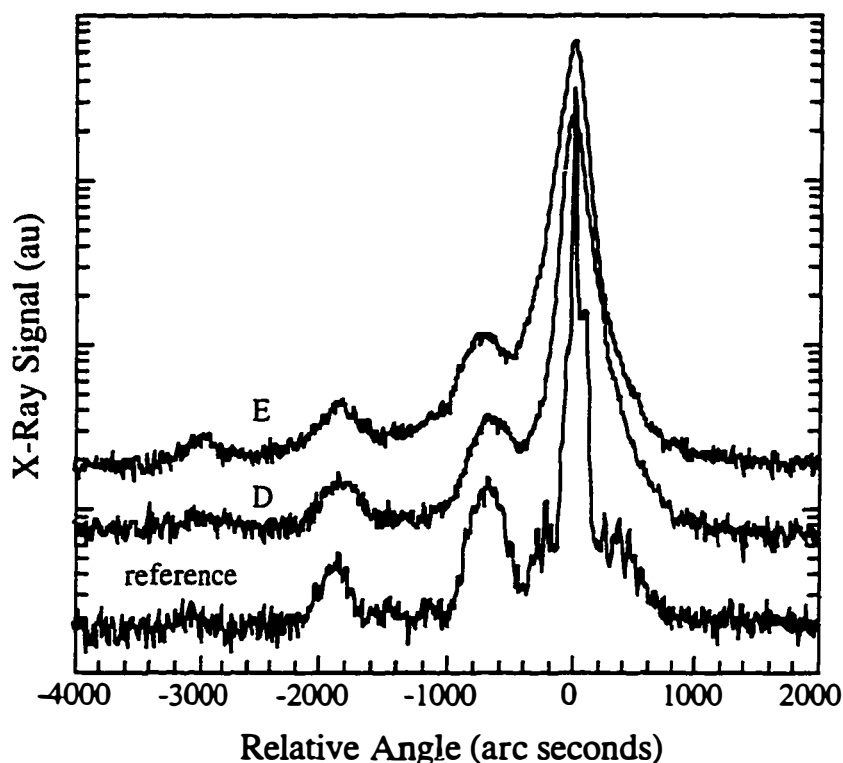


**Figure 6-5** (004) double crystal x-ray rocking curve of samples D and E after fusion with a reference sample of the active region prior to fusion.

This, I believe, is due to the formation of dislocations at the InP-to-GaAs fusion interface. For example, the full width at half maximum (FWHM) of the substrate peak in these samples increased from 16-20 arc seconds to 140-180 arc seconds for the various samples. In order to accurately measure the dislocation density, however, transmission electron microscopy would need to be done. The key result of the x-ray measurements is that there seems to be little change in the strain and structural integrity of the multiple quantum well active region as

the fusion temperature increases from 575°C to 675°C. Therefore, there is no reason, based upon the x-ray measurements, to pick a particular fusion temperature

### *Optical Results*

To test the optical quality of the 1.55  $\mu\text{m}$  laser structures after fusion, photoluminescence measurements are taken on the samples before and after the process. In the case of the measurements done in this work, the excitation source is an AlGaAs diode laser that emits light at 789 nm. This light is focused through objective lenses onto the sample. The resulting luminescence is focused again and then measured by a Si detector at room temperature. The results for samples A and E are shown below. Over the temperature range investigated, a reduction in the photoluminescence intensity of the 1.55  $\mu\text{m}$  in-plane laser structure is observed. There are a few things of note in order to interpret these results. First, this reduction is in part due to the structural differences of the samples when the measurement is taken. The duty cycle of the metal pattern on top of the 50  $\mu\text{m}$  broad-area lasers is 33%; this value is such that the pumping of the multiple quantum well structure and the collection of the emitted light are different before and after fusion. The measurement is not taken prior to fusion due to the 1.6  $\mu\text{m}$  of p-type  $\text{Al}_x\text{Ga}_{1-x}\text{As}$  on top of the active region. After device processing, this thickness is around 100 nm. These two effects suggest that a change in intensity should be seen. As shown by sample A, this change is only about 80% of the original intensity. In order to make direct comparisons between the different samples, the normalized integrated intensity is plotted for the samples in Figure 6-7. Although there is considerable scatter in the data, the trend is clear: increases in the fusion temperature lead to a reduction of the integrated intensity of approximately 40%.



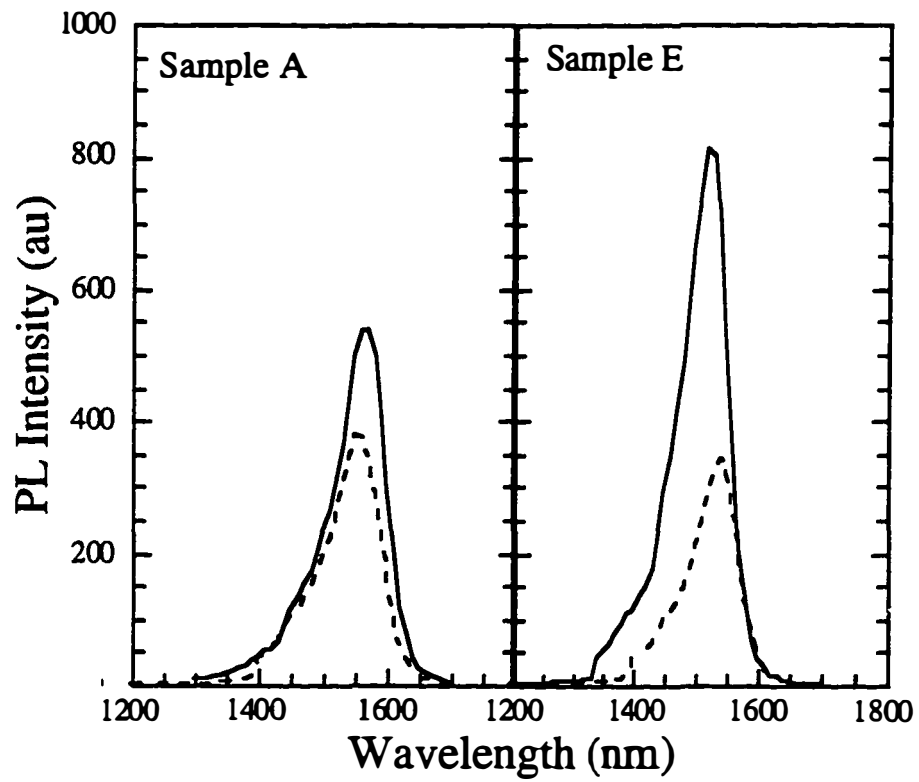


**Figure 6-6** Photoluminescence measurements for samples A and E before (—) and after (---) the fusion process and device processing.

Therefore, based upon the photoluminescence results, the fusion temperature should be as low as possible in order to keep the optical quality of the active region high.

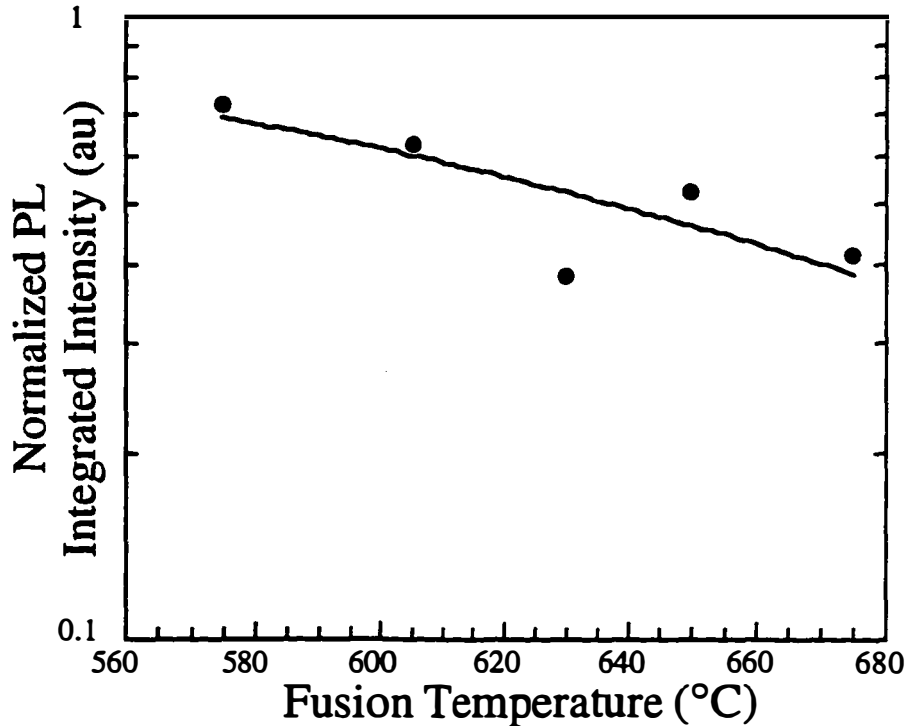


**Figure 6-7** Plot of the normalized PL intensity versus fusion temperature for samples A-E.

### ***Broad-Area Laser Results***

Ultimately, whatever the effects on the structural and optical characteristics of the 1.55  $\mu\text{m}$  in-plane laser structures the fusion process may have, the effects on device performance are the most important. In this section, the effects of the temperature cycle are explored on device results. Samples A-E were made into 50  $\mu\text{m}$  broad-area lasers by the procedure outlined in Appendix B. All of these structures were tested and only samples C, D, and E lased. In the cases of samples A and B, the turn-on voltages were over 2 V higher than the *reference* structure. Even though the fusion junction looked good when stain etched and

observed in a SEM, I believe that this high voltage is the sign of a bad fusion. Samples *E* and *F* lased, but the threshold current density was much higher than *SF-QI*:  $6 \text{ kA/cm}^2$  versus  $1.7 \text{ kA/cm}^2$ . As a result,  $630^\circ\text{C}$  was chosen as the temperature for fusion for the rest of the results presented in this section.

For comparison purposes, a  $2 \mu\text{m}$  regrowth of p-InP with a p<sup>+</sup>-GaInAs contact layer was performed on the same active region material as that used in samples A-C. A piece of this material serves as a *reference* sample. Another piece of the regrowth structure was fused to InP under the same conditions as samples C and will be called the *fused* structure. This InP substrate was then removed in 3 HCl: H<sub>2</sub>O with the original InP protected. To test the structural quality of the regrowth material, a (004) x-ray diffraction measurements was taken on samples on the *reference* and *fused* laser material prior to device processing. A comparison of the x-ray results of Figure 6-8 and Figure 6-4 shows that the amount of broadening in the multiple quantum well and InP substrate peaks is much less than in samples A-E.. This suggests that the broadening in samples A-E is not due to interdiffusion in the active region and is due to the InP-to-GaAs interface. Additionally, the *reference* and *fused laser material* was processed into  $50 \mu\text{m}$  broad-area lasers using a similar procedure to that outlined in Chapter 5. The results for a  $50 \times 1000 \mu\text{m}^2$  device are nearly identical in both the *reference* and *fused* case.

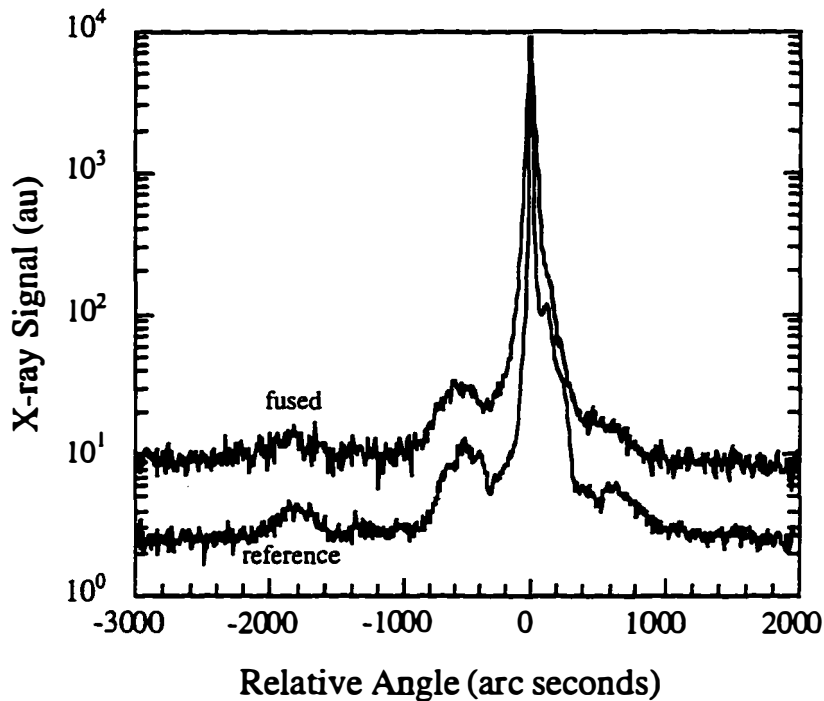


**Figure 6-8** (004) X-ray diffraction measurement of the *reference* and *fused* laser material.

At 20°C the threshold current density is 155 A/cm<sup>2</sup> per well. Measurement of  $1/\eta_d$  versus cavity length revealed an internal quantum efficiency of 73.2% and internal losses of 20.8 cm<sup>-1</sup> for the *reference* structure; for the *fused* structure, the values were 72.2% and 22.6 cm<sup>-1</sup>. Although these values are different, there is enough scatter to suggest that this difference is negligible. The threshold current was measured on these 50x1000 μm<sup>2</sup> devices between 20 and 60°C. An exponential fit of the data leads to a characteristic temperature of 59 K for both structures. This value is within those reported in the literature and shows that *the temperature cycling used in the wafer fusion process does not lead to any significant device degradation!*

Structure *SF-Q1* has the same active region as the *reference* and *fused* structures. However in this case, a p-AlGaAs cladding layer is used instead of the p-InP cladding. Similarly, the structure was processed into 50  $\mu\text{m}$  broad-area lasers via the process illustrated in Chapter 5. Figure 6-9 shows the L-I curves for the *reference* and *SF-Q1* structures at 20°C.

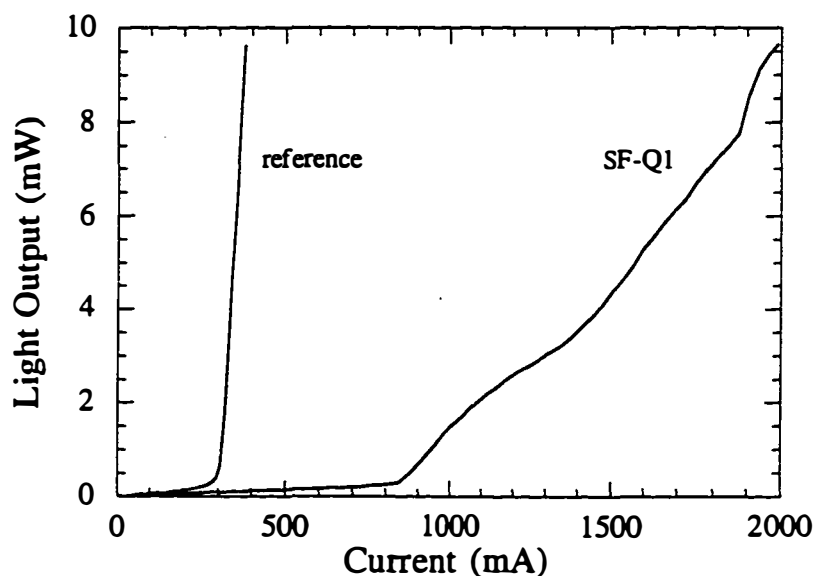


**Figure 6-9** Light versus current curves at 20°C for the *reference* and *SF-Q1* structures. The testing was done under pulsed conditions.

When a p-AlGaAs cladding layer is used, two important parameters get worse: the threshold current and the slope efficiency of the laser. For the *reference* structure,  $I_{\text{th}}$  is 303 mA ( $J_{\text{th}}$  of 0.628  $\text{kA}/\text{cm}^2$ ) and the slope efficiency is 0.123 W/A per facet. For *SF-Q1*,  $I_{\text{th}}$  rises to 849 mA ( $J_{\text{th}}$  of 1.7  $\text{kA}/\text{cm}^2$ ) while the slope efficiency drops to 0.0076 W/A per facet. There was also an increase of 0.3 V in the turn-on voltage of *SF-Q1*. It turns out that changes in either the

internal losses or the internal efficiency can lead to the discrepancy between the *reference* and *SF-Q1* results. Using Equations (2-26) and (2-29), the threshold current density and slope efficiency can be solved self-consistently to obtain approximate values for the internal efficiency and internal losses. The only assumption made is that the gain curve from the *fused* structure in Appendix B is the same for *SF-Q1*. A fit of the data for the *fused* structure leads to  $818.3 \text{ cm}^{-1}$  for  $g_0$  and  $244.1 \text{ A/cm}^2$  for  $J_{tr}$ . Doing this calculation leads to values of 14.3% for the internal quantum efficiency and  $55.9 \text{ cm}^{-1}$  for the additional loss in the *SF-Q1* structure. These values will be compared to values derived later for narrow ridge devices.

### 6.2.2 Single-Fused Laser Results: Narrow Ridge Devices

To explore the improvement of an increase in carrier confinement, structure *SF-Q2* was fabricated into narrow ridge lasers. The ridge width of the devices tested were measured to be 10 and  $7.5 \text{ }\mu\text{m}$ . Figure 6-10 shows a typical light versus current curve for these devices. As was the case for the broad-area lasers, the threshold current of 310 mA ( $J_{th}$  of  $6.7 \text{ kA/cm}^2$ ) was much higher than expected. As with the *SF-Q1* structures, the turn-on voltage is slightly higher:  $\approx 1.5 \text{ V}$ . However, I believe that there was an improvement in the fusion since the threshold current density is nearly identical to Samples *E* and *F* when the cavity length and stripe width were reduced; this type of area reduction typically leads to higher  $J_{th}$ . However, I cannot tell if the improvement is due to either an improvement in the fusion, a reduction in device area, or the use of nitrogen instead of hydrogen as the fusion gas<sup>iii</sup>.

---

<sup>iii</sup> A quick sidenote. Although my results were mixed on whether a change from hydrogen to nitrogen makes a difference, I believe now that changes in the fusion gas lead to negligible differences.

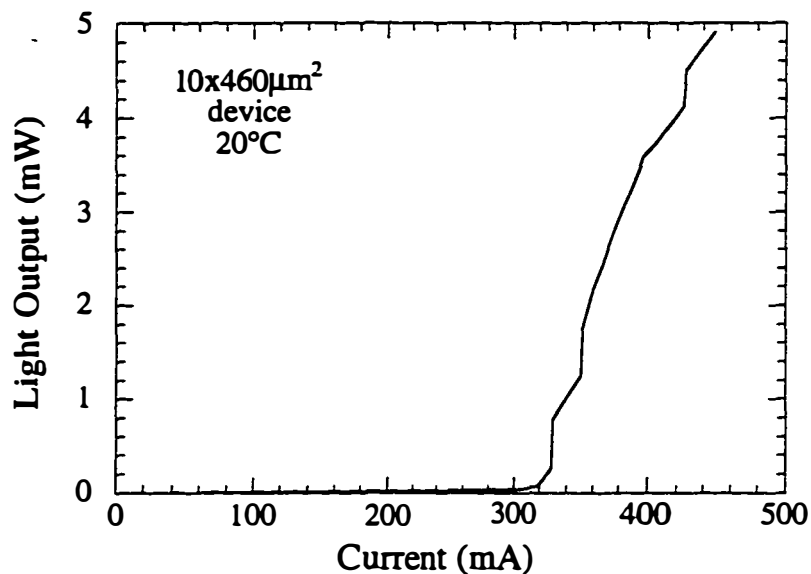


**Figure 6-10** Light versus current curve for structure *SF-Q2* at 20°C under pulsed conditions.

The spectrum from the laser at 1.2 and 1.7 times threshold are shown in Figures 6-11 and 6-12 below. Two different structure of type *SF-Q2* were processed into lasers. One was processed immediately upon completion of the GaAs substrate removal (see Section 5.2).

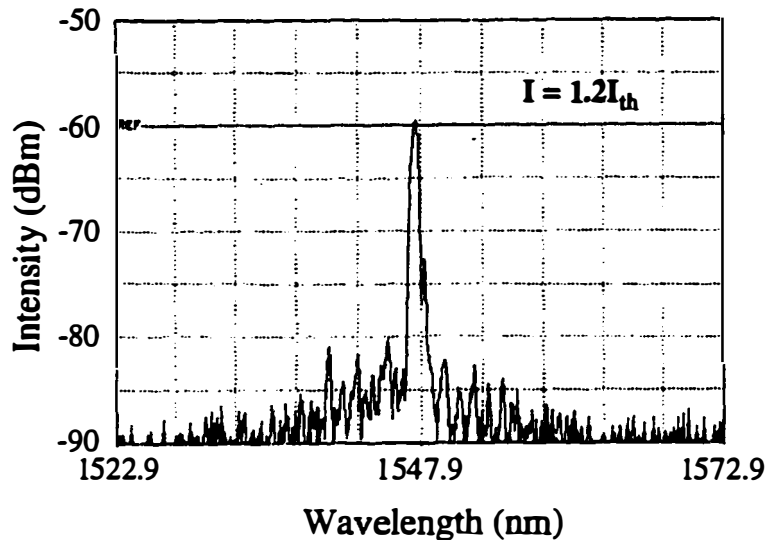


**Figure 6-11** Spectrum of the *SF-Q2* device from Figure 6-10 at  $1.2I_{th}$  under pulsed conditions.

The other, which I will call *SF-Q2 anneal*, was annealed in our MOCVD reactor at 630°C for 45 minutes. In addition to 16 slpm of hydrogen, a partial pressure of 1.5 torr of tertiarybutylarsine (TBA) was introduced to maintain the integrity of the GaAs surface. The idea behind this annealing step was to introduce hydrogen into the wafer-fused material via the decomposition of the TBA. This has been shown to improve the performance of 1.55  $\mu\text{m}$  lasers when arsine is used [10]. Hydrogen has been shown by others to passivate defects in the material and lead to improved optical and electrical properties [11-13]. The means by which this annealing step passivates defects is still an area of investigation. The effect could just be thermal or, as with hydrogen which is known to passivate p-type material [14], the effect could be hydrogen bonding with defects within the crystal structure. Much more will need to be done in order to measure which of these effects is at work here.



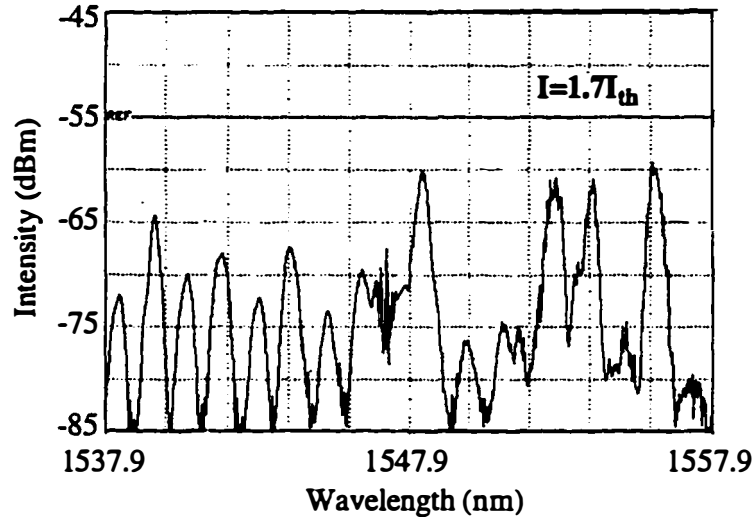


**Figure 6-12** Spectrum of the *SF-Q2* device from Figure 6-10 at  $1.7I_{th}$  under pulsed conditions.

After the *SF-Q2 anneal* structure is fabricated into narrow ridge lasers, the effects of the anneal were investigated. Figure 6-13 below shows the difference in light versus current curves for *SF-Q2* and *SF-Q2 anneal*. Since the devices have slightly different dimensions, a rigorous comparison is not completely possible. However, a few things can be deduced. In the case of *SF-Q2 anneal* the threshold current density is reduced to  $6.3 \text{ kA/cm}^2$  – still high but an improvement of  $\approx 6\%$  over *SF-Q2*. In addition, the turn-on voltage was  $0.2 \text{ V}$  lower and more devices worked in the case of *SF-Q2 anneal*; thus,  $1/\eta_d$  versus cavity length could be used to calculate internal losses and internal efficiencies although there is considerable scatter in the data. The results are shown in Figure 6-14.

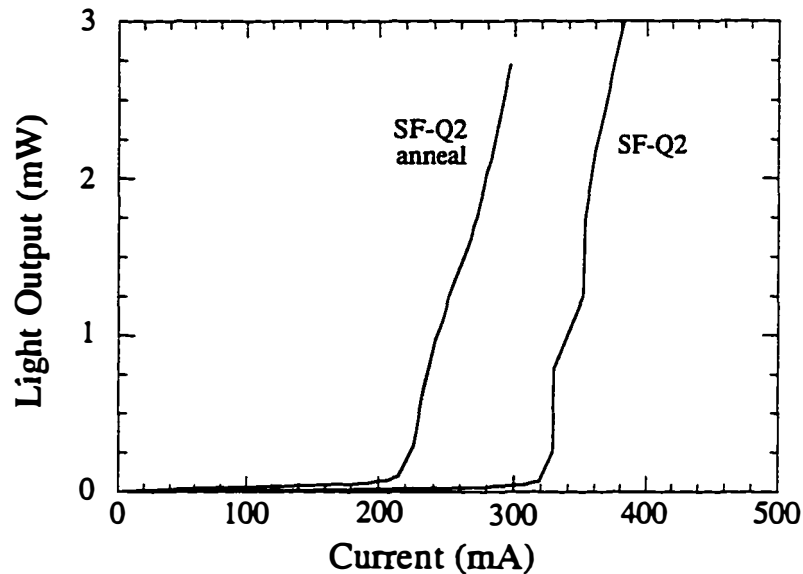


**Figure 6-13** Light versus current curves for *SF-Q2* and *SF-Q2 anneal*. The device dimensions are  $10 \times 460 \mu\text{m}^2$  for *SF-Q2* and  $7.5 \times 450 \mu\text{m}^2$  for *SF-Q2 anneal*.

From this measurement it was found that the *SF-Q2 anneal* structure has internal losses of  $40 \text{ cm}^{-1}$  and an internal efficiency of 40%. These values are worse than is typically seen in  $1.55 \mu\text{m}$  lasers with InP cladding layers. Based upon an increased buffer layer thickness for the MOCVD active region, the internal losses of the structure, without fusion, are expected to be between 10 and  $15 \text{ cm}^{-1}$ . This leaves between 29 and  $34 \text{ cm}^{-1}$  for either the fusion interface itself or the p-AlGaAs. In work on VCSELs here at UCSB, my colleague Near Margalit has inferred a loss of 0.05% per pass for the fusion junction [15]. Therefore the high internal losses are due to the fusion interface.

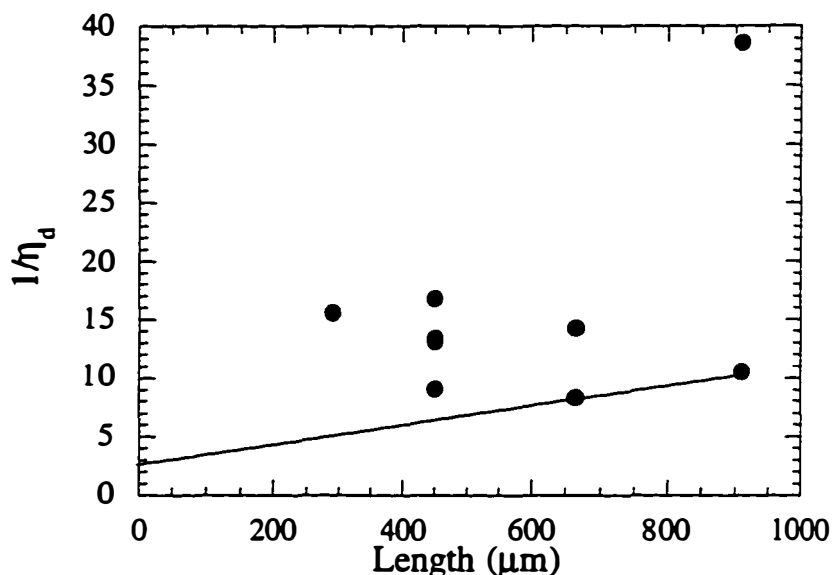


**Figure 6-14**  $1/\eta_d$  versus cavity length for *SF-Q2 anneal*.

However, one thing that is not seen in the double-fused VCSELs is a reduction in the internal efficiency. This may be due to the lower p-doping used around the fusion interface in these designs. Although nominally doped to  $2 \times 10^{18} \text{ cm}^{-3}$ , I believe that this value decreases due to diffusion that occurs during the fusion process. With this reduction in p-doping, it is quite possible that electrons can diffuse over to the fusion interface and recombine non-radiatively -- decreasing the internal efficiency. The equivalent measurement could not be done in the case of *SF-Q2* due to the low yield of devices at different cavity lengths. However, since the slope efficiencies are nearly identical and the threshold current densities are different, I believe that the effect of high temperature anneal is to passivate defects or remove defects that contribute optical loss. However,

this effect will need to be studied in much more detail before a mechanism is found.

For both *SF-Q2* and *SF-Q2 anneal*, the threshold current was measured from 20°C to 60°C.

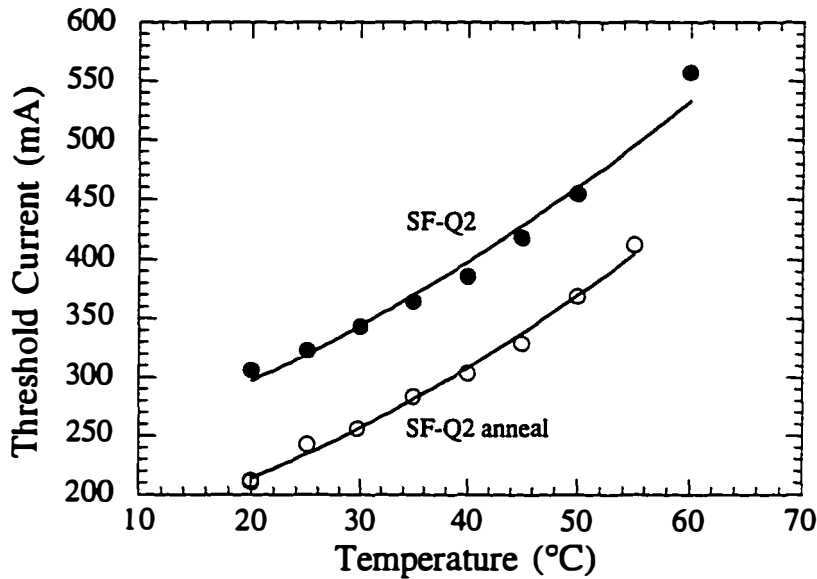


**Figure 6-15** Threshold current versus temperature for *SF-Q2* and *SF-Q2 anneal* tested under pulsed conditions. The device dimensions are  $10 \times 460 \mu\text{m}^2$  for *SF-Q2* and  $7.5 \times 450 \mu\text{m}^2$  for *SF-Q2 anneal*..

In terms of the characteristic temperature, *SF-Q2* has a higher value than *SF-Q2 anneal*: 68 K as compared to 55 K. The reason for this decrease for *SF-Q2 anneal* is not understood. Part of this may be due to the difference in the cavity length and device width. In narrow ridge devices, it has been shown that the losses and recombination effects increase significantly as the device width is

decreased [16]. This typically occurs for very small ridges. However, due to the high losses in this structure it is reasonable to assume that this may occur for the difference between *SF-Q2* and *SF-Q2 anneal*.

The other improvement that was predicted for single-fused lasers as compared to 1.55  $\mu\text{m}$  lasers with InP cladding layers was a reduction in the change of the slope efficiency with temperature. The data for *SF-Q2* and *SF-Q2 anneal* is shown below in Figure 6-16. Here there is an important improvement in terms of the slope efficiency for single-fused laser structures as compared to 1.55  $\mu\text{m}$  with InP cladding layers. For these devices, it has been reported that the slope efficiency steadily decreases with temperature [17,18]. This has been seen for broad-area material in our lab [19]. Both a decrease in internal efficiency and an increase in the internal losses has been shown to lead to such a behavior. In Figure 6-16 something very different is seen. For *SF-Q2*, the slope efficiency is constant from 20°C to 40°C. Above 40°C, the decrease in slope efficiency is rapid. I believe that this is due to the high losses in the structure. High losses and a short cavity lead to an operation point high on the gain curve. As the temperature increases, the current required increases and the amount of gain available decreases. Thus, there comes a point where the positive loss multiplication mechanism mentioned in Chapter 2 applies. Further increases in temperature leads to much higher losses. This explanation is somewhat inconsistent with the high  $T_0$  value for this material. Further work will need to be done in order to sort of the actual results. For *SF-Q2 anneal*, there was no decrease in slope efficiency measured from 20°C to 60°C. This type of result is consistent with the results seen for 980-nm GaAs-based lasers [2].

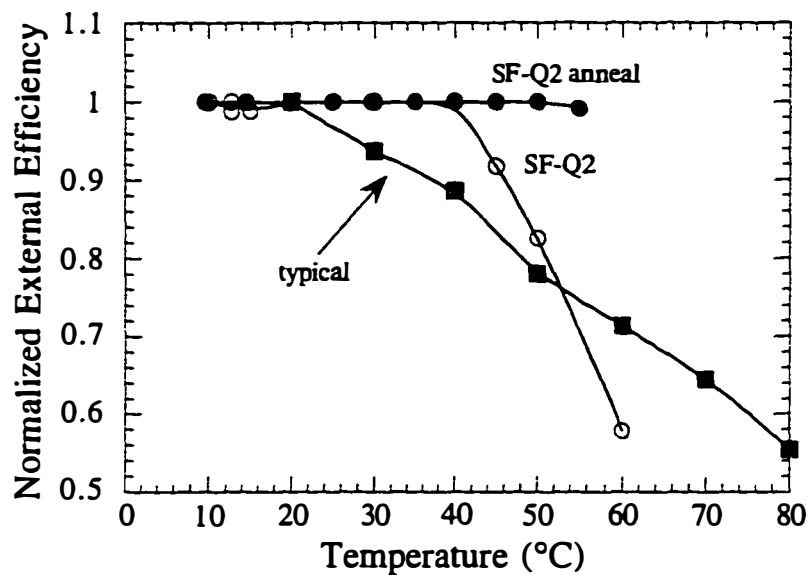


**Figure 6-16** Change in the slope efficiency of structures *SF-Q2* and *SF-Q2 anneal* tested under pulsed conditions. The device dimensions are  $10 \times 460 \mu\text{m}^2$  for *SF-Q2* and  $7.5 \times 450 \mu\text{m}^2$  for *SF-Q2 anneal*. The results for a typical  $1.55 \mu\text{m}$  laser [19] are also shown.

In these cases, both the internal efficiency and internal losses are not a function of temperature below about  $100^\circ\text{C}$ . This suggests that -- if the losses in the structures can be reduced further -- improvements in the change in efficiency with temperature should result.

### 6.2.3 Double-Fused Laser Results

The device results for double-fused structures was poor. The resulting light versus current curves as shown below. In a comparison to the results of the single-fused structures, the threshold current density are about the same.

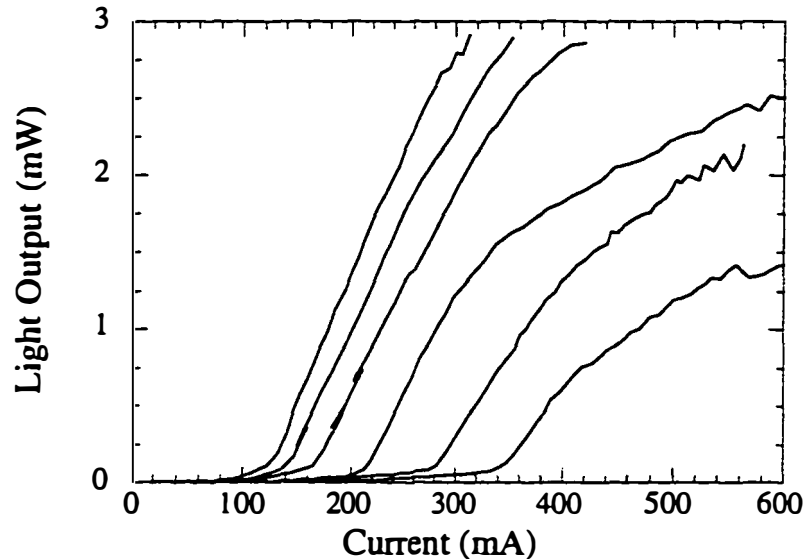


**Figure 6-17** Light versus current curves for the *DF-B* structure tested under pulsed conditions. The device dimensions are  $4.5 \times 610 \mu\text{m}^2$ . The temperatures shown are 4.2, 9.3, 14.3, 20, 29.6, and 34.6°C.

For the  $4.5 \times 610 \mu\text{m}^2$  device, the threshold current density is approximately 7.5  $\text{kA/cm}^2$  at 20°C. However, as shown in Table 6-3, there is one less quantum well and the optical confinement factor is reduced by 30%. For the results of Figure 6-17  $T_0$  is calculated to be 29.4 K. Changes in slope efficiency with

temperature are shown below. This data has a similar shape to *SF-Q2* of Figure 6-16. I believe that the lack of optical confinement and the increased losses due to two fusion interfaces are the cause of the reduced performance.

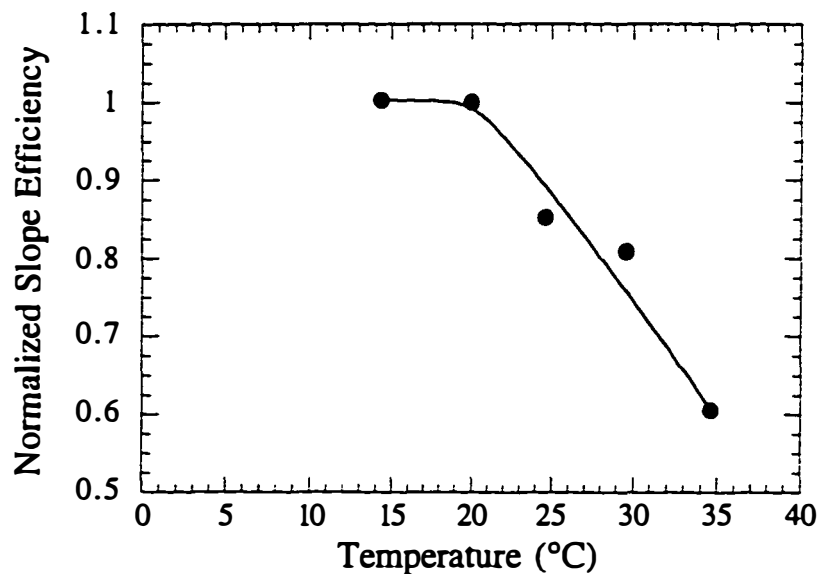


**Figure 6-18** Change in the slope efficiency of structures *DF-B* tested under pulsed conditions. The device dimensions are  $4.5 \times 610 \mu\text{m}^2$ .

### 6.3 Summary

In this chapter I presented both theoretical and experimental results for the proposed wafer-fused structures of Chapter 4. From the theoretical approach, all of the important parameters for  $1.55 \mu\text{m}$  lasers were expected to improve: the threshold current was lowered and  $T_o$ ,  $T_o^{10mW}$ , and  $T_{max}$  were raised. Experimental results showed the possibility of this improvement. A direct



comparison was presented between conventional and wafer-fused lasers with the identical active region. The results showed a 2.9 times increase in threshold current and the slope efficiency reduced. Both of these effects can be explained by a reduction in internal efficiency *or* an increase in internal loss. Narrow ridge device made with both a single-fused and double-fused structure showed some improvement. However, in both cases, the internal efficiency was reduced (41% versus 72.2%) and the internal losses were increased ( between 29 and 34  $\text{cm}^{-1}$ ) as compared to the *reference* structure of Appendix B. For the single-fused lasers, the  $T_0$  values measured were comparable to 1.55  $\mu\text{m}$  lasers reported in the literature.

## 6.4 References

- [1] U. Menzel, A. Barwolff, P. Enders, D. Ackermann, R. Puchert, and M. Voss, "Modelling the temperature dependence of threshold current, external differential efficiency and lasing wavelength in QW laser diodes", *Semiconductor Science and Technology* **10**, 1382 (1995).
- [2] R. F. Nabiev, E. C. Vail, and C. J. Chang-Hasnain, "Temperature dependent efficiency and modulation characteristics of Al-free 980-nm laser diodes", *IEEE Journal on Selected Topics in Quantum Electronics* **1**, 234 (1995).
- [3] S. Wai-Chee, J. Micallef, I. Ng, and E. H. Li, "Effects of different cation and anion interdiffusion rates in disordered In/sub 0.53/Ga/sub 0.47/As/InP single quantum wells", *Japanese Journal of Applied Physics, Part 1 (Regular Papers & Short Notes)* **34**, 1778 (1995).
- [4] J. Camassel, H. Peyre, and R. W. Glew, "Quantitative investigation of interdiffusion effects in balanced-strain InGaAs(P)/InGaAsP heterostructures: constant x vs. constant y", *2nd International Workshop on Expert Evaluation and Control of Compound Semiconductor Materials and Technologies*, Parma, Italy, 1994, 353.
- [5] R. M. Cohen, "Interdiffusion in alloys of the GaInAsP system", *Journal of Applied Physics* **73**, 4903 (1993).
- [6] J. Ko, C. H. Chen, and L. A. Coldren, "Low threshold MBE-grown AlInGaAs/AlGaAs strained multiquantum-well lasers by rapid thermal annealing", *Electronics Letters* **32**, 2099 (1996).
- [7] J. Ko, M. J. Mondry, D. B. Young, S. Y. Hu, L. A. Coldren, and A. C. Gossard, "Threshold reduction by rapid thermal annealing in MBE-grown AlInGaAs multiquantum well lasers on GaAs", *Electronics Letters* **32**, 351 (1996).
- [8] J. Y. Tsao, *Materials Fundamentals of Molecular Beam Epitaxy* (Academic Press, San Diego, CA, 1993). See Section 5.3.3
- [9] S. N. G. Chu, R. A. Logan, and W. T. Tsang, "Misfit stress-induced compositional instability in hetero-epitaxial compound semiconductor structures", *Journal of Applied Physics* **79**, 1397 (1996).
- [10] S. P. DenBaars, based upon a talk at a conference.
- [11] V. Swaminathan, U. K. Chakrabarti, W. S. Hobson, R. Caruso, J. Lopata, S. J. Pearton, and H. S. Luftman, "A photoluminescence study of

hydrogenated GaAs grown on an InP substrate by metalorganic chemical vapor deposition" *Journal of Applied Physics* **68**, 902 (1990).

[12] D. G. Yu, C. H. Chen, B. P. Keller, A. L. Holmes, Jr., E. L. Hu, and S. P. D. Baars, "Investigation of improved regrown material on InP surfaces etched with methane/hydrogen/argon", *40th International Conference on Electron, Ion, Photon Beam Tech and Nanofabrication*, Atlanta, GA, USA, 1996, 3674.

[13] B. Chatterjee and S. A. Ringel, "Hydrogen passivation and its effects on carrier trapping by dislocations in InP/GaAs heterostructures" *Journal of Applied Physics* **77**, 3885 (1995).

[14] B. Chatterjee and S. A. Ringel, "Effect of extended defects on the formation and dissociation kinetics of Zn-H complexes in heteroepitaxial p-type InP layers" *Applied Physics Letters* **69**, 839 (1996).

[15] N. Margalit, unpublished results.

[16] T. A. Strand, B. J. Thibeault, D. S. L. Mui, L. A. Coldren, P. M. Petroff, and E. L. Hu, "Low regrowth-interface recombination rates in InGaAs-GaAs buried ridge lasers fabricated by in situ processing" *Applied Physics Letters* **66**, 1966 (1995).

[17] P. A. Andrekson, R. F. Kazarinov, N. A. Olsson, T. Tanbun-Ek, and R. A. Logan, "Effect of thermionic electron emission from the active layer on the internal quantum efficiency of InGaAsP lasers operating at 1.3  $\mu\text{m}$ " *IEEE Journal of Quantum Electronics* **30**, 219 (1994).

[18] A. A. Bernussia, H. Temkin, D. L. Coblenz, and R. A. Logan, "Effect of barrier recombination on the high temperature performance of quaternary multiquantum well lasers." *Applied Physics Letters* vol. **66**, 67 (1995). D5-1

[19] P. A. Abraham, A. L. Holmes, M. E. Heimbuch, G. Fish, S. P. DenBaars, and J. E. Bowers, "1.55  $\mu\text{m}$  Lasers with Separate Strain Heterostructures", *submitted to Journal of Electronic Materials* (1997).

**Experiemental Results**

**184**

## 7. Recapitulation and Future Work

### 7.1 Recapitulation of Dissertation

In this dissertation, a new approach to the design of 1.55  $\mu\text{m}$  lasers for improved performance has been presented. In Chapter 1, the importance of 1.55  $\mu\text{m}$  lasers was detailed along with specific performance parameters and their relation to device characteristics. A comparison was also made between these 1.55  $\mu\text{m}$  lasers and their shorter wavelength (0.98  $\mu\text{m}$  and 0.67  $\mu\text{m}$ ) counterparts. In all cases, the 1.55  $\mu\text{m}$  lasers showed reduced performance: the threshold currents were higher and changed more rapidly with temperature, the maximum operating temperature lower, the modulation speed was lower, and the frequency chirp during this modulation was larger. Two specific differences – changes in the threshold current and slope efficiency of the laser with temperature – were chosen to be the parameters of focus. For 0.98  $\mu\text{m}$  lasers, the characteristic temperature ( $T_0$ ) approach gives values above 200 K. For 1.55  $\mu\text{m}$  lasers, the values are typically in the range of 40-70 K. The slope efficiency for 0.98  $\mu\text{m}$  lasers is typically constant from 20°C up to  $\approx$  100°C before a decrease is observed; for 1.55  $\mu\text{m}$  a continual decrease in slope efficiency is observed as the temperature is elevated above room temperature.

To understand the problem and the effect of material parameters, Chapters 2 and 3 presented a theoretical approach that I developed to calculate the various static parameters of 1.55  $\mu\text{m}$  in-plane lasers. The approach of this method was to use the quantum well gain curve calculation algorithm developed by Scott Corzine, with modifications done by me for 1.55  $\mu\text{m}$  lasers. In his procedure, the quasi-Fermi levels are determined by placing a set sheet carrier density into the active region. I use this information about carrier distribution to calculate the

gain being provided by the quantum wells as well as the optical loss due to these carriers. An iterative approach is used to determine the operating point of the laser. In addition, heating effects are added to the calculations via a simple expression for the thermal impedance whose determining parameter is the thermal conductivity for the laser. With this modeling methodology, several important things about the performance of 1.55  $\mu\text{m}$  lasers were theoretically observed.

- *Auger Current Effects.* As shown in Section 3.2, Auger recombination does have an effect on the important parameters for 1.55  $\mu\text{m}$  lasers: threshold current and the characteristic temperature,  $T_o$ . However, a simple reduction in the amount of Auger recombination does not lead to greatly improved  $T_o$  values. This is because there are other factors at play. For a reduction in Auger recombination from  $10^{-28}$  to  $10^{-29}$   $\text{cm}^6/\text{s}$ ,  $T_o$  improves by 62 %: from 42.2 K to 68.4 K. The other important parameters for 1.55  $\mu\text{m}$  lasers also improve with a reduction in Auger recombination.
- *Carrier Overflow Effects.* As shown in Section 3.3, carrier overflow effects -- mainly occupation of the barrier and SCH regions of the device -- has a dramatic effect on  $T_o$  and the threshold current. For a complete elimination of carrier overflow effects,  $T_o$  is predicted to increase from 45.7 K to 67.2 K at an Auger recombination rate of  $5 \times 10^{-29}$   $\text{cm}^6/\text{s}$  with a 60 meV activation energy. Also, the threshold current decreases greatly and  $T_o^{10mW}$  improves dramatically. These improvements are due to a more efficient use of the carriers that are placed into the active region.

The net result of Chapters 2 and 3 is that it takes a decrease in Auger recombination *and* carrier overflow to obtain the  $T_o$  values of 0.98  $\mu\text{m}$  lasers.

Since -- in general -- one does not have control over the amount of Auger recombination for 1.55  $\mu\text{m}$  lasers, the only parameter available to the device designer for improved performance is the amount of carrier overflow. From Chapter 3, it was shown that carrier overflow effects are reduced by increasing the barrier band gap for the quantum wells. However, this change alone leads to a reduction in the optical confinement factor of the active region. The net result is that a trade-off exists: maximizing  $\Gamma_{acr}$  leads to large amounts of carrier overflow, minimizing carrier overflow leads to reduced  $\Gamma_{acr}$ . In addition to this trade-off, it has been shown experimentally that carrier leakage out of the active region is also a problem at elevated temperatures. In Chapter 4, my proposed structures -- the *single-fused* and *double-fused* laser -- were designed to alleviate both of these problems. The key feature of these structure is the use of  $\text{Al}_{0.7}\text{Ga}_{0.3}\text{As}$  as the cladding layer. This composition of AlGaAs has a lower index of refraction at 1.55  $\mu\text{m}$  than InP. Therefore, better waveguiding is provided for these structures as the barrier height increases in the active region. Also, the large band gap of  $\text{Al}_{0.7}\text{Ga}_{0.3}\text{As}$  provides a means of minimizing the carrier leakage problem out of the active region. For InP barriers -- the highest barrier height attainable in the GaInAsP material system -- the optical confinement factor is nearly the same as those values reported in the literature for 1.55  $\mu\text{m}$  GaInAsP lasers; in addition, the amount of electron confinement is improved by 5.5 kT at room temperature. These materials, however, cannot be grown in one step since the growth of InP on GaAs results in threading dislocations which causes device failure. To combine these materials in a way to be useful for lasers, an exciting new technology -- wafer fusion -- is used. Its use is described for this process.

Before these wafer-fused structure can be tested experimentally, the materials required -- a GaInAsP quantum well active region and AlGaAs cladding layers -- need to be grown. In Chapter 5, the growth processes used to prepare these semiconductor structures are detailed. The active region was grown by MOCVD

while the AlGaAs cladding layers were grown by MBE. In addition, detailed steps of the wafer fusion process are described. In Chapter 6, both the theoretical predictions and experimental results are presented. In terms of theoretical results, a reduction in the threshold current are predicted for each of the three structures of Chapter 4: *SF-Q*, *DF-Q*, and *DF-B*. Furthermore, improvements in  $T_o$  of up to 30% are predicted. Improvements in  $T_o^{10mW}$  and  $T_{max}$  are also expected. In terms of experimental results, the devices did not live up -- in all cases -- to the theoretical predictions. The threshold currents were quite a bit higher that expected. In addition, the slope efficiency of the laser was reduced. These two factors lead me to hypothesize that the fusion interface provides additional optical loss and a reduction in the structure's internal efficiency. In addition, for the single-fused laser structure, the  $T_o$  values were comparable to those in the literature. One thing that did improve over 1.55  $\mu\text{m}$  lasers with InP cladding layers is the sensitivity of the slope efficiency with temperature. For the single-fused structure, the slope efficiency was constant from 20°C up to 40°C before decreasing. When the sample was annealed to introduced hydrogen, no reduction in the slope efficiency was seen between 20°C and 60°C. The results show that these novel 1.55  $\mu\text{m}$  laser structures can lead to the improvements predicted by theory. In order to make further improvements, however, the reduction in efficiency and increase in losses seen due to the InP-to-GaAs fusion interface must be eliminated.

## 7.2 Future Work

In the extension of the results of this dissertation, there are a number of areas which need to be pursued. My thoughts on these areas are listed below



### 7.2.1 *Modeling Improvements*

Although quantitative agreement can be achieved via the modeling approach of Chapter 2, there are four areas that should be addressed. The first of these areas is the use of realistic thermal impedance values for the laser structures. As was stated in Chapters 2 and 3, GaInAsP alloys have a much lower thermal conductivity than binary compounds such as GaAs and InP. The effect of these differences in thermal conductivity needs to be addressed. Theoretical calculations are one way to go. However, I believe that experimental measurements on real devices will provide the best means of ascertaining the effect. Another area that needs to be addressed is non-uniform carrier injection into the active region. Some of the experimental results of other researchers -- presented in Chapter 4 -- pointed to the fact that as the barrier height in the active region increases, the quantum wells no longer provide the same amount of gain. This effect should be included in further theoretical work.

The last two areas which I feel should be addressed is the concept of Auger recombination and heating about threshold. In the literature, there are many different values reported in terms of the actual coefficient as well as the activation energy. These changes -- as the model now stands -- can be easily addressed. The two main areas not accounted for currently are the change in Auger recombination with the composition of GaInAsP and the (assumed) cubic dependence of Auger recombination. Theoretical predictions of the amount of Auger recombination show that the coefficient is expected to decrease with an increase in the amount of phosphorus in GaInAsP (i.e., from GaInAs to InP) [1]. In my work, the amount of Auger in the quantum wells, barrier, and SCH regions is assumed to be the same. Furthermore, work at USC where they measured the effects of strain on Auger showed that the recombination rate is not cubic and has a more complicated function with respect to carrier density [2]. Again, these ideas need to be sorted out and then they can be easily incorporated

into the modeling procedure. In terms of heating effects, I mentioned in the discussion of the modeling approach of Chapter 2 that the heating effects I have included only deal with the determination of the threshold condition. Things such as the roll-off of the light versus current curve are not included, but to make accurate predictions to experimental work, this effect must be added.

### 7.2.2 *Understanding the Fusion Process for in-plane Lasers*

In this work, the fusion process used was, in general, kept as constant as possible. Since I see increased loss and reduced efficiency with lasers that have an InP-to-GaAs fusion interface, the formation of this interface is crucial for improved performance of these and other devices where fusion interfaces interact strongly with the optical properties of the device. To this end, I think that following parameters are the ones that should be studied in most detail:

- *The Fusion Gas.* In this work I believe that I saw no difference between hydrogen and nitrogen as the fusion gas. In the literature both gases have been used. My belief is that as long as the gas is pure and does not introduce contaminants, the use of hydrogen, nitrogen, or some inert gas should not change the results.
- *Processing Procedure.* In the wafer fusion done at UCSB a lot of care is used to make sure the surface is as clean as possible and there is no oxide on either sample when mated. In silicon wafer fusion, the cleanliness procedure are also strictly followed, but there is little concern regarding oxide formation. Is this important in the case of InP-to-GaAs fusion? Furthermore, is the cleaning procedure currently being used the best? I feel that different oxide removal techniques and acid etching for surface cleaning should be tried to see if things improve.

- *Applied Pressure.* In my work, I lowered the pressure that was typically used in wafer fusion at UCSB. The rationale for this was the hope that more mass transport may occur at the fusion interface. This hypothesis needs to be tested. Pressure may also affect the amount of contaminants at the interfaces as well as the quality of the resulting bonds.
- *Temperature Effects.* Even though I studied these effects for the work presented in Chapter 6, more work should be done here. This is especially true in the regime of lower fusion temperatures which could provide a lot of benefits with lower dopant diffusion.

In order to see whether any of these changes in the process of wafer fusion have any effect, techniques other than devices should be used for characterization. In terms of the electrical quality of the fusion interface, simple *p-p*, *n-n*, *p-n*, or even *p-i-n* junctions (where the fusion interface is in the intrinsic region) can be fabricated and tested. For optical properties, waveguide loss measurements can be used. The other main issue is what -- if any -- contaminants exist at the fusion interface. For these type of measurements, some type of infrared spectroscopy needs to be used. This type of analysis is common in silicon direct wafer bonding [3,4]. However, the current size of InP-to-GaAs fusion ( $8 \times 8 \text{ mm}^2$ ) may be too small in order to get enough signal-to-noise ratio to see contaminants with a wave number less than  $1500 \text{ cm}^{-1}$ . Other possible techniques include planar-view TEM for dislocation studies and surface analysis techniques for bonding information. In the case of these last two techniques, the measurements may require the fusion interface to be very near ( $< 10 \text{ nm}$ ) the surface of the structure.

### 7.2.3 *Alternate Structures for 1.55 $\mu\text{m}$ Lasers with Wafer Fused Cladding Layers*

The last issue that I feel needs to be addressed is possible ways to further improve 1.55  $\mu\text{m}$  in-plane lasers with wafer fused cladding layers. In this discussion, two specific areas will be addressed: optical confinement and electron confinement improvements.

For optical confinement improvements, I have two suggestions. The first is to move the fusion junction even closer than the  $\approx 300$  nm used in this work. When this occurs, the overlap of the lasing mode with the quantum well active region increases. However, this comes at the cost of increased interaction of the lasing mode with the fusion junction(s). Until the loss are reduced, this improvement is not that practical. One thing that can be changed immediately is the cladding material used for the lasers. With  $\text{Al}_{0.7}\text{Ga}_{0.3}\text{As}$ , a thin layer of GaAs needs to be used for the fusion process. This high index layer reduces the optical confinement factor. An alternate approach would be to use either  $\text{Ga}_{0.5}\text{In}_{0.5}\text{P}$  lattice-matched to GaAs or GaP. Both materials should have a lower resistance and a higher thermal conductivity than AlGaAs alloys as well as a lower index than InP [5] and contain no Al such that a GaAs layer need not be used. In addition, both materials would have the same benefit in terms of carrier leakage reduction of AlGaAs and would remove possible reliability problems that are seen in GaAs-based lasers with AlGaAs cladding layers [6-8].

For improved electron confinement, the approach of Chapter 4 was to raise the barrier height of the GaInAsP barrier. One alternate would be to switch to AlGaInAs. As mentioned in Chapter 4, this would lead to higher electron confinement *and* higher optical confinement for the same barrier band gap due to 70% of the band gap difference being in the conduction band. Another approach is to deepen the quantum wells used. Recently, the addition of nitrogen to

arsenides and phosphides has been explored [9,10]. What small amounts of nitrogen provide is a significant reduction in the materials band gap. For high enough nitrogen content, semi-metallic behavior is predicted. While a lot of work is now trying to obtain 1.3 or 1.55  $\mu\text{m}$  emission on GaAs with GaInAsN, the use of wafer fused cladding layers allows for the GaInAsN to be grown on InP – an easier prospect for long wavelength emission. Even without the improvement in the carrier confinement via changes to the quantum wells or barriers, more quantum wells can be used to reduced the gain each quantum well must provide for lasing. In order to maintain high carrier confinement, InP barriers are not possible. An alternate would be to use GaInP for strain compensation [11].

### 7.3 References

- [1] G. P. Agrawal, N. K. Dutta, and G. P. Agrawal, *Semiconductor lasers*, 2nd ed ed. (Van Nostrand Reinhold, New York, 1993).
- [2] Y. Zou, J. S. Osinski, P. Grodzinski, P. D. Dapkus, W. Rideout, W. F. Sharfin, and F. D. Crawford, "Experimental verification of strain benefits in 1.5- $\mu\text{m}$  semiconductor lasers by carrier lifetime and gain measurements" *IEEE Photonics Technology Letters* **4**, 1315 (1992).
- [3] M. K. Weldon, V. E. Marsico, Y. J. Chabal, D. R. Hamann, S. B. Christman, and E. E. Chaban, "Infrared spectroscopy as a probe of fundamental processes in microelectronics: silicon wafer cleaning and bonding", *8th International Conference on Vibrations at Surfaces*, Birmingham, UK, 1996, 163.
- [4] D. Feijoo, Y. J. Chabal, and S. B. Christman, "Silicon wafer bonding studied by infrared absorption spectroscopy" *Applied Physics Letters* **65**, 2548 (1994).
- [5] C. H. Joyner, A. G. Dentai, R. C. Alferness, L. L. Buhl, M. D. Divino, and W. C. Dautremont-Smith, "InGaP/InP waveguides" *Applied Physics Letters* **50**, 1509 (1987).
- [6] M. Usami, Y. Matsushima, and Y. Takahashi, "Extremely high characteristic temperature  $T_0$  of 0.98  $\mu\text{m}$  InGaAs/InGaP strained quantum well lasers with GaAs/InGaP superlattice optical confinement layer" *Electronics Letters* **31**, 192 (1995).
- [7] R. F. Nabiev, E. C. Vail, and C. J. Chang-Hasnain, "Temperature dependent efficiency and modulation characteristics of Al-free 980-nm laser diodes" *IEEE Journal on Selected Topics in Quantum Electronics* **1**, 234 (1995).
- [8] T. Ijichi, M. Ohkubo, A. Iketani, and T. Kikuta, "High-power 0.98  $\mu\text{m}$  strained-layer quantum-well lasers with InGaP cladding" *Microwave and Optical Technology Letters* **7**, 139 (1994).
- [9] M. Kondow, S. Nakatsuka, T. Kitatani, Y. Yazawa, and M. Okai, "Room-temperature pulsed operation of GaInNAs laser diodes with excellent high-temperature performance" *Japanese Journal of Applied Physics, Part 1 (Regular Papers, Short Notes & Review Papers)* **35**, 5711 (1996).
- [10] M. Kondow, S. Natatsuka, T. Kitatani, Y. Yazawa, and M. Okai, "Room-temperature continuous-wave operation of GaInNAs/GaAs laser diode" *Electronics Letters* **32**, 2244 (1996).

[11] P. A. Abraham, A. L. Holmes, M. E. Heimbuch, G. Fish, S. P. DenBaars, and J. E. Bowers, "1.55  $\mu\text{m}$  Lasers with Separate Strain Heterostructures", *submitted to Journal of Electronic Materials* (1997).





## **A. Gain Curve Modeling of GaInAsP Quantum Wells**

As stated in Chapter 2, this appendix is concerned with a more detailed explanation of the modeling method used to generate gain versus sheet carrier density and current density curves for GaInAsP quantum wells. The calculations done here are an extension of the work done by Scott Corzine to calculate the quantum well gain curves for the unstrained GaAs/AlGaAs and the strained GaInAs/AlGaAs systems [1-5]. The first section of this appendix briefly outlines the method used by Scott Corzine to calculate gain curves. In the second section, I go into my modification for GaInAsP quantum wells: the calculation of GaInAsP material parameters, band offsets, occupation of electrons in the barrier and SCH regions, and temperature dependence effects. The final section is concerned with an illustration and explanation of the quantum well gain curve results.

### **A.1 General Gain Curve Calculation Procedure**

Figure A-1 shows a flowchart for the overall calculation procedure for quantum well gain curves used in Chapters 2 and 3. In words, the procedure goes as follows. The material parameters for the quantum well and barriers are calculated at the temperature specified (see Section A.2 for more information) including strain effects if necessary.

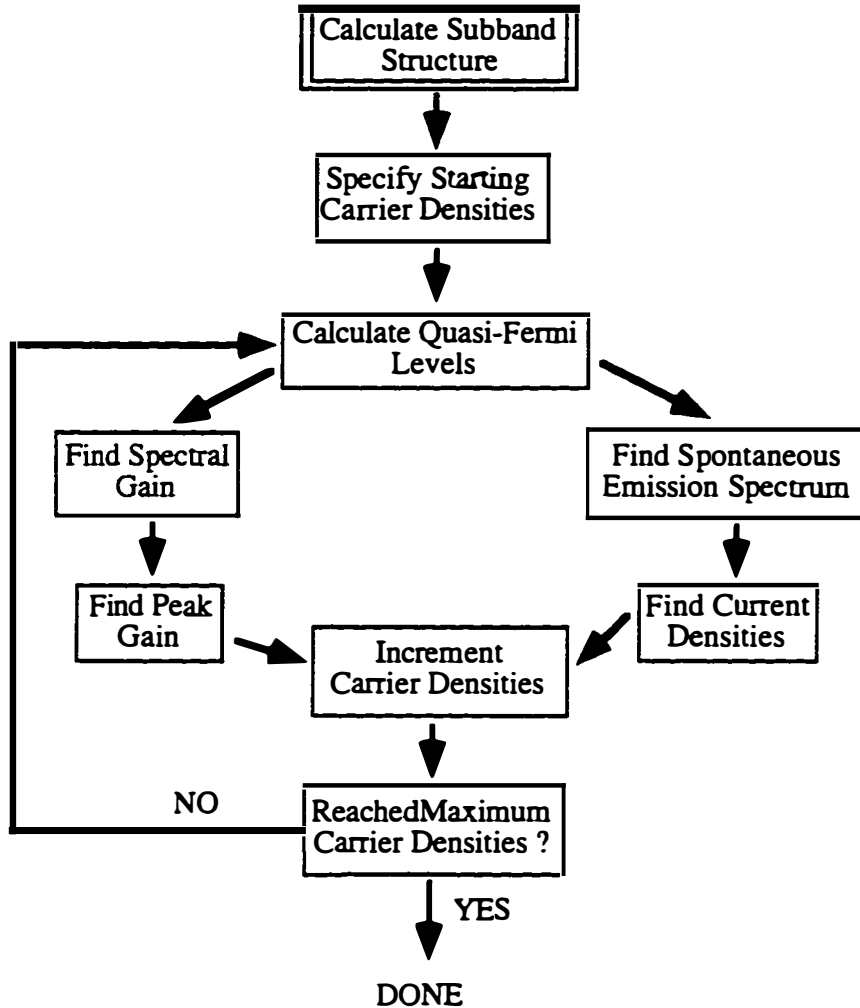


**Figure A-1** General Procedure for the calculation of GaInAsP quantum well gain curves from Reference [4].

When these are known, other important parameters such as the band offsets and emission wavelength are calculated along with the valence subband structure which includes both heavy/light hole coupling and split-off band effects. Next, a specific carrier sheet density (units of  $\text{cm}^{-2}$ ) is injected into the active region and

the carrier densities in the quantum well, barriers, and SCH regions are calculated according to charge neutrality across the entire active region which is given by

$$\sigma_{no}(E_{fc}) + \sigma_A^- = \sigma_{po}(E_{fc}) + \sigma_D^- \quad (\text{A-1})$$

In this expression  $\sigma_{no}(E_{fc})$  and  $\sigma_{po}(E_{fv})$  are related to carrier densities in the active region by

$$\begin{aligned} \sigma_{no}(E_{fc}) &= N_{QW}L_{QW} + N_{BAR}(n_{QW}L_{QW} + [n_{QW} + 1]L_{BAR}) + \\ &N_{SCH}(n_{QW}L_{QW} + [n_{QW} + 1]L_{BAR} + 2L_{SCH}) \\ \sigma_{po}(E_{fv}) &= P_{QW}L_{QW} + P_{BAR}(n_{QW}L_{QW} + [n_{QW} + 1]L_{BAR}) + \\ &P_{SCH}(n_{QW}L_{QW} + [n_{QW} + 1]L_{BAR} + 2L_{SCH}) \end{aligned} \quad (\text{A-2})$$

and  $\sigma_A^-$  and  $\sigma_D^+$  are the sheet charge densities of ionized acceptors or donors (if the active region is doped);  $E_{fc}$  and  $E_{fv}$  are the quasi-Fermi levels for electrons and holes; and the  $N$ 's,  $P$ 's, and  $L$ 's represents the electron and hole carrier densities (units of  $\text{cm}^{-3}$ ) and the lengths of the quantum well, barriers, and SCH regions. When charge neutrality is achieved, the quasi-Fermi levels are determined. Now we can calculate gain (see Equations 35, 36, and 38 in Reference [5]) and current densities (see Equations 2.23 and 2.36 in Reference [4]). The procedure is then repeated for different sheet carrier densities to generate a gain versus carrier density or gain versus current density curve. For the calculations in this dissertation, the injected sheet carrier density is varied from  $10^{12}$  to  $5 \times 10^{14} \text{ cm}^{-2}$  in  $5 \times 10^{12} \text{ cm}^{-2}$  steps; the temperature is varied from 20 to 200°C in 20°C steps.

In this approach there is one major assumption that need to be stated. It is assumed that the quasi-Fermi levels are flat across the entire active region. This is a dubious assumption at best since the width can be quite large, but is necessary to make the calculations efficient. In fact, Scott Corzine has argued in Chapter 7 of Reference [4] that interactions between the carriers in the quantum well and carriers in the barriers are significant enough that major band bending may be canceled out by a redistribution of carriers. Other work in InP-based quantum wells [6], however, states that the inclusion of band-bending is necessary. So, in comparing the results in this work to the work including electrostatic deformation, my results represent a best-case scenario.

## A.2 Modifications to Calculate GaInAsP Gain Curves

In this section, modifications to the gain calculation procedure outlined in Section 1 are now defined. Here I outline the methods used to calculate GaInAsP material parameters, quantum well band offsets, occupation of barrier and SCH regions, and temperature dependence.

### A.2.1 GaInAsP Material Parameters

One important aspect of any theoretical modeling of quantum well lasers is the determination of materials parameters. The approach taken here is based on the work of Gershoni and co.-workers [7]. For long wavelength lasers, the quaternary alloy  $\text{Ga}_x\text{In}_{1-x}\text{As}_y\text{P}_{1-y}$  is generally the material of choice for 1.3 and 1.55  $\mu\text{m}$  lasers due to the ability to change the band gap and lattice constant of the alloy independently'. As noted by Gershoni, the material parameters for

---

' This is also true of the quaternary alloy AlGaInAs; however, this alloy is not considered here.

quaternary alloys are not well known over the entire parameter space; thus some type of interpolation scheme is needed to extract the necessary parameters. The flexibility of the GaInAsP allows us to break down the material's parameter space into two groups: those compositions lattice-matched to InP and those that are biaxially strained. For the lattice-matched case, we consider the quaternary alloy to be composed of lattice-matched GaInAs and InP<sup>ii</sup>. Thus:

$$Ga_xIn_{1-x}As_yP_{1-y} = (Ga_{0.47}In_{0.53}As)_z(InP)_{1-z} \quad (A-3)$$

where  $z=y=x/0.47$ . This approach is used instead of the interpolation scheme outlined by Adachi [8] since the material properties of InP and Ga<sub>0.47</sub>In<sub>0.53</sub>As have been well studied. Material parameters can be linearly interpolated between these two alloys leading to a general expression of

$$A_Q(z) = (1-z)A_B + zA_T \quad (A-4)$$

where  $A$  is the material parameter and the subscripts  $Q$ ,  $B$ , and  $T$  stand for the quaternary, binary InP, and lattice-matched GaInAs alloys respectively.

---

<sup>ii</sup> A similar approach could be adopted for compositions near the lattice constant of GaAs by using GaAs and Ga<sub>0.3</sub>In<sub>0.7</sub>P.

A key feature of this interpolation scheme is the ease at which compositions of  $\text{Ga}_x\text{In}_{1-x}\text{As}_y\text{P}_{1-y}$  that are biaxially strained to InP can be handled<sup>iii</sup>. When the alloy is grown with a different lattice constant than InP, one generally changes the group III composition to add strain. For this interpolation scheme (equation (A-4)), the result amounts to changing only the ternary alloy's composition by some amount  $\Delta x$  away from the lattice-matched value. The amount of strain for a  $\Delta x$  change in the group III composition is given by

$$\varepsilon = \frac{a_Q(x_{lm}, z) - a_Q(x_{lm} + \Delta x, z)}{a_Q(x_{lm} + \Delta x, z)} = -\frac{1}{a_B} \frac{\partial A_Q(x_{lm}, z)}{\partial x} \Delta x \quad (\text{A-5})$$

where  $x_{lm} = 0.47$  and  $a_B$  is the lattice constant of InP. Using Equation (A-4), the strain can be rewritten as

$$\varepsilon = \frac{a_{InAs} - a_{GaAs}}{a_{InP}} z \Delta x \quad (\text{A-6})$$

where a similar expression to Equation (A-4) for  $A_T(x)$  is used. Equation (A-4) can be generalized for any material parameter leading to

$$A_Q(x, z) = A_B + (A_{GaAs} - A_{InAs})z\Delta x + z(A_T - A_B) \quad (\text{A-7})$$

---

<sup>iii</sup> Sidenote. This approach is probably only good for small ( $\leq \pm 2\%$ ) amounts of biaxial strain with respect to InP.

Note that one important material parameter that has not been interpolated in this manner is the unstrained band gap of GaInAsP. Instead, I have used the equation derived by Moon [9].

### *A.2.2 Quantum Well Band Offsets*

Another important aspect in the calculation of accurate quantum well gain curves is the calculation of the band offsets between the quantum well and barriers. The most widely used theoretical approach is the model-solid theory [10,11]. The main aspect of this model is that it aligns the band structure (at  $k=0$ ) of the quantum well active region to an “absolute” energy scale. This is done by relating the average electrostatic potential to the vacuum level by modeling a semiconductor as a superposition of neutral atoms [11]. After the bands are attached to an absolute energy scale, strain can be used to change the band offsets by use of the deformation potentials (see Reference [10] or Appendix C of Reference [4] for more information). However, I have found that using this method directly does not lead to the band offset values that have been measured [12,13]. So, the modification made to the calculation of band offsets follows the suggestion of Reference [12]. The initial band offset is calculated assuming 40% of  $\Delta E_g$  goes into the conduction band. Then, the effects of strain are added via the model-solid theory.

### *A.2.3 Occupation of Barrier and SCH Regions*

Equations ( A-1) and ( A-2) include sheet density terms that relates the carriers in the barrier and SCH regions. These are calculated via the quasi-Fermi levels. The important thing to note is that  $N_{BAR}$  and  $N_{SCH}$  do not represent the number of carriers in each individual barrier or SCH regions. The reason for this is illustrated in Figure A-2 below.

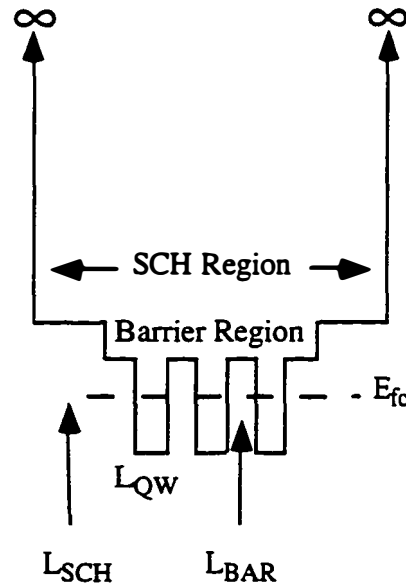


**Figure A-2** Schematic of carrier distribution calculation scheme for calculating the electron distribution in the active region.

where  $L_{QW}$ ,  $L_{BAR}$ , and  $L_{SCH}$  are the thickness of the individual quantum well, barrier, and SCH regions respectively. When the electron quasi-Fermi level is raised to some level within the quantum well, Fermi-Dirac statistics requires that not only will there be carriers in the quantum well, the barrier region and SCH regions will also be occupied. The importance of this is that the barrier region that is occupied is a sum of the 3D states above the quantum wells (whose thickness is given by  $n_{QW}L_{QW}$  and the barrier states (whose thickness is given by  $(n_{QW}+1)L_{BAR}$ ). Thus for three 9 nm quantum wells and 10 nm barriers, the resulting barrier state thickness is 67 nm. In the case of the SCH region in Figure A-2, the total thickness is increased by twice the SCH thickness. A similar procedure is used to calculate the hole distribution but I assume that the occupation of the holes in the SCH region is negligible because of their tight confinement. This distinction is important in Chapter 2 when I discuss how



these carriers affect the operating point of the laser. For example, in Equation (2-19) the actual carriers in each barrier region is defined as

$$N'_{BAR} = \frac{N_{BAR} [n_{QW} (L_{QW} + L_{BAR}) + L_{BAR}]}{L_{BAR}} \quad (A-8)$$

Thus for the conditions described above the carrier density in each barrier region ( $N'_{BAR}$ ) is 6.7 times higher than the carrier density ( $N_{BAR}$ ) calculation in the generation of gain curves.

Another important thing to note from Figure A-2 is that no carrier/current leakage out of the waveguide region is considered in this model. The ramifications of this carrier leakage will be explored in Chapters 4 and 6.

#### A.2.4 Temperature Dependence

The temperature dependence of several parameters is also included in the modeling procedure. For the band gap of InP, GaInAs, and GaInAsP, the band gap is assumed to vary with temperature by

$$E_s^Q(T) = E_s^Q(0) - \frac{\alpha T^2}{\beta + T} \quad (A-9)$$

where  $\alpha = 6.9 \times 10^{-4} \text{ eV/K}^2$  and  $\beta = 372 \text{ K}$ [14]. Note that in Reference [14] these constants were found to hold for a wide range of GaInAsP compositions; I have assumed in my modeling that they hold for all compositions. As a result, the quantum well band offsets changes only slightly with temperature. In addition, the lattice constant is assumed to change with temperature via the thermal expansion coefficient as calculated using a form of Equation (A-7).

Furthermore, the radiative current density is modeled to vary inversely with temperature and the Auger current density is modeled according to

$$J_{AUG} = eLC_{p0} \exp\left(-E_a/kT\right)NP^2 \quad (\text{A-10})$$

where  $E_a$  is the activation energy of the dominant CHHS Auger process which is assumed to be 60 meV. Note that this Auger coefficient is assumed to be the same for carriers in the quantum well and barrier regions.

### A.3 Modeling of GaInAsP quantum wells with GaInAsP or InP barriers.

Now that the general procedure for the calculation for GaInAsP quantum well gain curves has been illustrated, I will now concentrate on looking at the results in more detail than is presented in Chapter 2. Table A-1 shows that four different active regions that are examined in this appendix. For reference, the quantum well composition is for a 1% compressive strain with respect to InP; the well width in cases *A* and *B* is adjusted for 1.55  $\mu\text{m}$  emission. Note that case *A* is the quantum wells used in the active regions of the laser modeled in Chapter 3 while case *B* represents those used in the in-plane lasers with fused cladding lasers proposed and modeled in Chapters 4 and 6. Figure A-3 shows the gain curves for active regions *A* and *B* at 20°C with respect to current and injected sheet carrier density. For the same number of carriers in each quantum well, case *A* (GaInAsP barriers) will provide more gain for achieving lasing than case *B* (InP barriers).

**Table A-1** Active region parameters used in the simulations of this appendix. For cases A and C, an additional 40 nm of the GaInAsP barrier composition is used on each side of the quantum wells for additional optical confinement.

Parameter	Active Region Structure			
	A	B	C	D
QW Material	GaInAsP	GaInAsP	GaInAsP	GaInAsP
QW Width	7 nm	9 nm	4 nm	4 nm
% Ga/ % As	20/75	20/75	20/75	20/75
Barrier Material	GaInAsP	InP	GaInAsP	InP
Barrier Width	10 nm	10 nm	10 nm	10 nm
% Ga/ % As	23.1/50.2	0/0	23.1/50.2	0/0
SCH Material	GaInAsP	InP	GaInAsP	InP
SCH Width per side	75 nm	300 nm	75 nm	300 nm
% Ga/ % As	17.6/36.8	0/0	17.6/36.8	0/0
Conduction Band QW Offset (meV)	83	226	83	226
Valence Band QW Offset (meV)	163	378	163	378
Energies of Conduction Band QW States (meV)	38.3	41.6, 163	57	102
Energies of Heavy Hole QW States (meV)	12.2, 48, 105	8.7, 34.8, 78.1, 139, 215, 306	29, 108	33.5, 133, 291
Energies of Light Hole QW States (meV)	104	105, 231	127	169

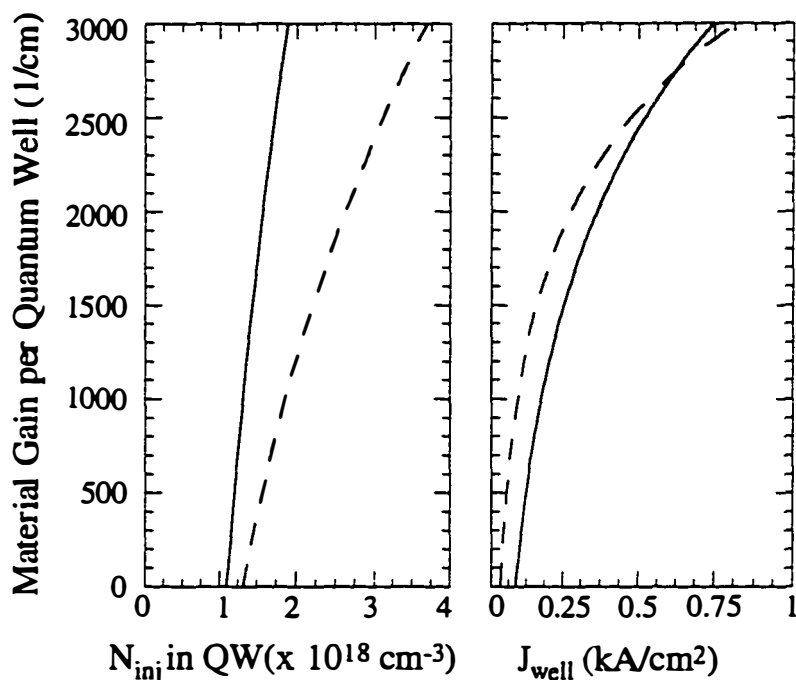


**Figure A-3** Modal gain per quantum well versus current density per well ( $J_{well}$ ) and injected carrier sheet carrier density ( $N_{inj}$ ) for a 3 GaInAsP quantum wells with GaInAsP (A, —) and InP (B, - - -) barriers. The temperature is 293 K and the Auger is assumed to be  $5 \times 10^{-29} \text{ cm}^6/\text{s}$ .

However, as will be shown later in Chapter 3, putting these carriers into the quantum well in case A also places a large number of carriers in the barrier and SCH regions. The net result being a higher threshold gain and current. Thus, when all carrier effects are included, the gain from the quantum well in case B requires less current than the quantum well in case A for gains less than  $2400 \text{ cm}^{-1}$  per well. In fact, since the number of carriers needed in case B is higher

than in case *A* for the same material gain, the differential gain ( $\partial g/\partial n$ ) is also worse. The reason for this improved gain curve characteristics (in terms of current density) without a corresponding improvement in differential gain is due to the conduction band of the quantum well. From Table A-1, we see that there are two confined states in the conduction band for case *B* whereas there is only one in case *A*. The effect of this is that the gain curve saturates more quickly than in case *B*. This is shown in the expression for the material gain of a quantum well [5]

$$g(\hbar\omega) = \left( \frac{1}{\hbar\omega} \right) \frac{\pi e^2 \hbar}{\epsilon_0 c m_0^2} \frac{\bar{n}_g}{\bar{n}^2} |M_T|^2 \rho_{red}(E_{eh} - E'_g) (f_c - f_v) \quad (\text{A-11})$$

where  $f_c$  and  $f_v$  are the Fermi functions for the conduction and valence bands respectively. The gain gets bigger as  $f_c$  tends towards one and  $f_v$  tends toward zero. With more than one state in the conduction band,  $f_c$  saturates very quickly for the lasing state. From that point on, increases in the material gain are then determined by changes in  $f_v$ , which is hampered by differences in the valence band structure as shown in Figure A-4. Note that the valence subband structures and density of states for case *A* and case *B* are quite different. Since case *B* has higher conduction and valence band offsets, there are more bound states in the quantum well [15-17]. This leads to a higher density of states for low energies into the valence band.

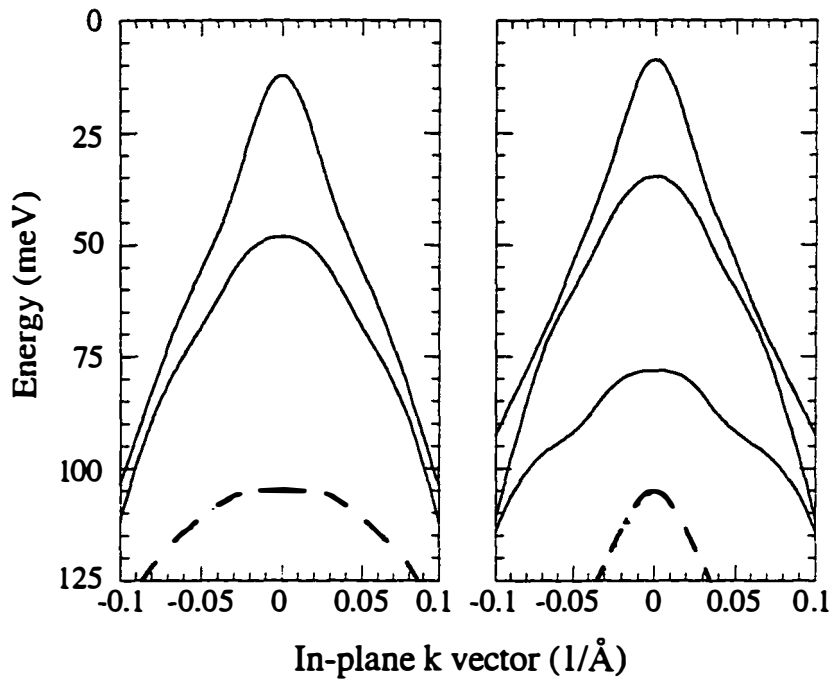


**Figure A-4** Some of valence subband substructure is plotted on the left for case *A* and on the right for case *B* of Table A-1 where coupling between the heavy hole (—) and light hole (---) states is included.

Thus as more carriers are injected into the active region of the laser, the quasi-Fermi levels must penetrate further into the bands in order to provide more gain. Since the density of states in the case of InP barriers is higher than for GaInAsP barriers, the quasi-Fermi level for holes is *slowed* in its penetrating into the valence band.

To show the effect of quantum well band structure, I have simulated two quantum wells with much thinner widths (4 nm) for comparison. As shown in Table A-1 for cases *C* and *D*, the conduction band and valence subband structure in terms of the number of bound states is a lot more similar than a comparison for cases *A* and *B*. The resulting gain curves are shown in Figure A-5.

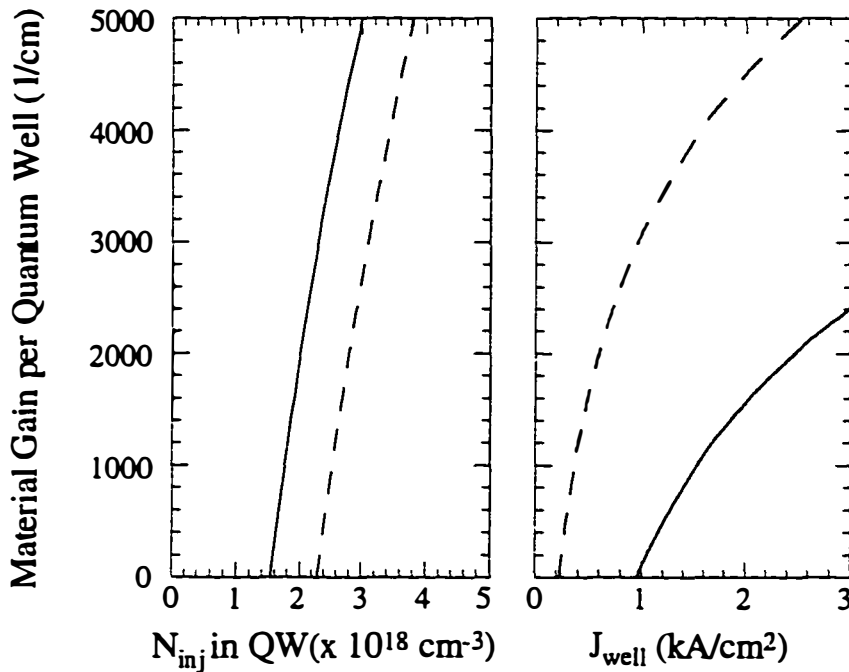


**Figure A-5** Peak modal gain per quantum well versus current density per well ( $J_{well}$ ) and injected carrier sheet carrier density ( $N_{inj}$ ) for a 3 GaInAsP quantum wells with GaInAsP (*C*, —) and InP (*D*, - - -) barriers. The temperature is 293 K and the Auger is assumed to be  $5 \times 10^{-29} \text{ cm}^6/\text{s}$ .

In this case, the gain curves never cross – showing that the case of InP barriers is always superior to GaInAsP barriers. The valence subband structure for these two cases are shown in Figure A-6.

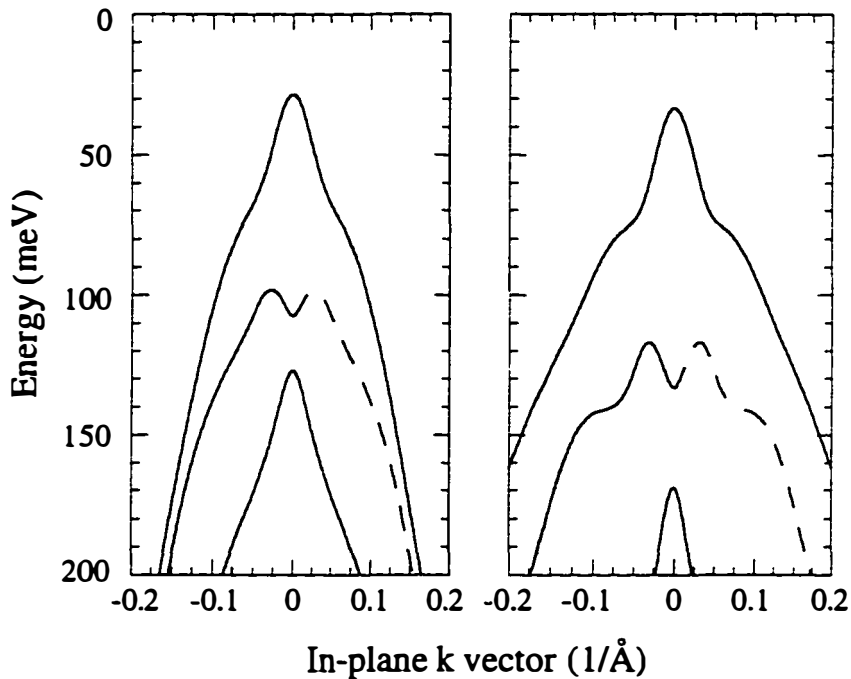
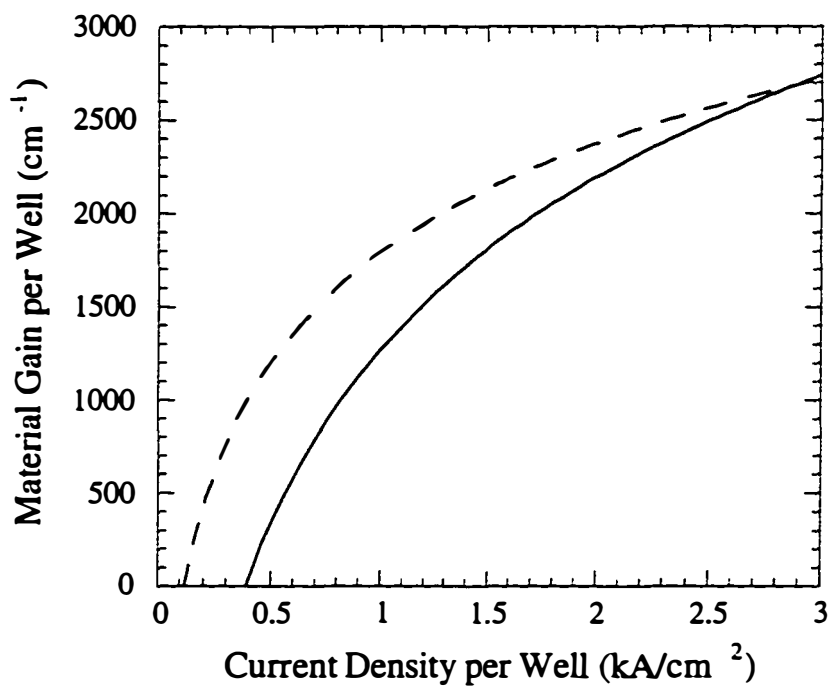


Figure A-6: Some of valence subband substructure is plotted on the left for case C and on the right for case D of Table A-1 where coupling between the heavy hole (—) and light hole (---) states is included.

The main advantage of going to InP barriers – as explained in chapter 3 – is the increase confinement of electrons at elevated temperatures. Figure A-7 shows the calculated gain curves for GaInAsP and InP barriers at 100°C. In this case the GaInAsP quantum well curve with InP barriers is superior to the case with



GaInAsP barriers. The effects of the change in gain curve characteristics on theoretical device performance results are explored in Chapters 3 and 6.



**Figure A-7** Modal gain per quantum well current density with GaInAsP (A, —) and InP (B, ----) barriers. The temperature is 373 K.

## A.4 References

- [1] S. W. Corzine, R. H. Yan, and L. A. Coldren, "Theoretical gain in strained InGaAs/AlGaAs quantum wells including valence-band mixing effects" *Applied Physics Letters* **57**, 2835 (1990).
- [2] S. W. Corzine and L. A. Coldren, "Theoretical gain in compressive and tensile strained InGaAs/InGaAsP quantum wells" *Applied Physics Letters* **59**, 588 (1991).
- [3] S. W. Corzine and L. A. Coldren, "Theoretical gain in strained-layer quantum wells" *Laser Diode Technology and Applications V*, Los Angeles, CA, USA, 1992, 177.
- [4] S. W. Corzine, "Design of vertical-cavity surface-emitting lasers with strained and unstrained quantum well active regions," Dissertation, University of California – Santa Barbara, 1993.
- [5] S. W. Corzine, R. H. Yan, and L. A. Coldren, "Optical Gain in III-V Bulk and Quantum Well Semiconductors," in *Quantum Well Lasers*, edited by Jr. P.S. Zory (Academic Press, Boston, 1993), pp. 17.
- [6] S. Seki and K. Yokoyama, "Electrostatic deformation in band profiles of InP-based strained-layer quantum-well lasers" *Journal of Applied Physics* **77**, 5180 (1995).
- [7] D. Gershoni, C. H. Henry, and G. A. Baraff, "Calculating the optical properties of multidimensional heterostructures: Application to the modeling of quaternary quantum well lasers" *IEEE Journal of Quantum Electronics* **29**, 2433 (1993).
- [8] S. Adachi, "Material parameters of  $\text{In}_{1-x}\text{Ga}_x\text{As}_y\text{P}_{1-y}$  and related binaries" *Journal of Applied Physics* **53**, 8775 (1982).
- [9] R. L. Moon, G. A. Antypas, and L. W. James, "Bandgap and lattice constant of GaInAsP as a function of alloy composition" *Journal of Electronic Materials* **3**, 635 (1974).
- [10] M. P. C. M. Krijn, "Heterojunction band offsets and effective masses in III-V quaternary alloys." *Semiconductor Science and Technology* **6**, 27 (1991).
- [11] C. G. Van de Walle, "Band lineups and deformation potentials in the model-solid theory." *Physical Review B* **39**, 1871 (1989).
- [12] R. W. Martin, S. L. Wong, R. J. Nicholas, A. Smith, M. A. Gibbon, E. J. Thrush, and J. P. Stagg, "Band offsets in strained InGaAsP/InGaAsP

quantum well optical modulator structures." *Journal de Physique IV (Colloque)* **3**, 327 (1993).

[13] S. R. Forrest, P. H. Schmidt, R. B. Wilson, and M. L. Kaplan, "Relationship between the conduction-band discontinuities and band-gap differences of InGaAsP/InP heterojunctions." *Applied Physics Letters* **45**, 1199 (1984).

[14] H. Temkin, V. G. Keramidas, M. A. Pollack, and W. R. Wagner, "Temperature dependence of photoluminescence of n-InGaAsP" *Journal of Applied Physics* **52**, 1574 (1981).

[15] G. Bastard, *Wave mechanics applied to semiconductor heterostructures* (Les Editions de Physique, Les Ulis Cedex, France, 1988).

[16] A. P. French and E. F. Taylor, *An introduction to quantum physics*, 1st ed ed. (Norton, New York, 1978).

[17] H. Kroemer, *Quantum mechanics : for engineering, materials science, and applied physics* (Prentice Hall, Englewood Cliffs, N.J., 1994).



## **B. Device Processing of 1.55 $\mu\text{m}$ Lasers with Wafer Fused Cladding Layers**

This appendix details the steps needed to take the wafer-fused material and make it into 1.55  $\mu\text{m}$  lasers. The growth and fusion processes are covered in Chapter 5. Two different structures were fabricated for this work: *50  $\mu\text{m}$  broad-area lasers* and *narrow ridge waveguide lasers with a PMGI bond pad configuration*. For the narrow ridge configuration, two different structures were used. One consists of nominally 3  $\mu\text{m}$  ridges with 50  $\mu\text{m}$  bond pads. The other consists of different ridge widths with approximately 20  $\mu\text{m}$  bond pads. The procedure by which this material is processed is outlined below.

### **B.1 Lithography for p-metal contact and p-metallization**

The first step in the laser processing is to define a pattern on top of the laser structure for metallization. An overview of the procedure described below appears in Figure B-1. First, the structure is clean in acetone and isopropanol. After this, photoresist (AZ 4210) is spun at 6000 rpm for 35 seconds. Before exposure, the photoresist is baked on a hot plate at 95°C for one minute. After this step, the sample is in the state shown in Figure B-1(a). The next step in the process is to open up windows in the photoresist for the p-metal contact. The photoresist is exposed to UV radiation at an intensity of 7.5 mW/cm<sup>2</sup> for 30 seconds. To help in the removal of the metal after evaporation, a soak of the resist in toluene is done for 12 to 15 minutes. Afterwards, it is developed in a 20% developer solution (AZ 4000K) for 60 seconds. Visual inspection was used to confirm the completion of the photoresist removal. At this point, the sample's state is shown in Figure B-1(b).

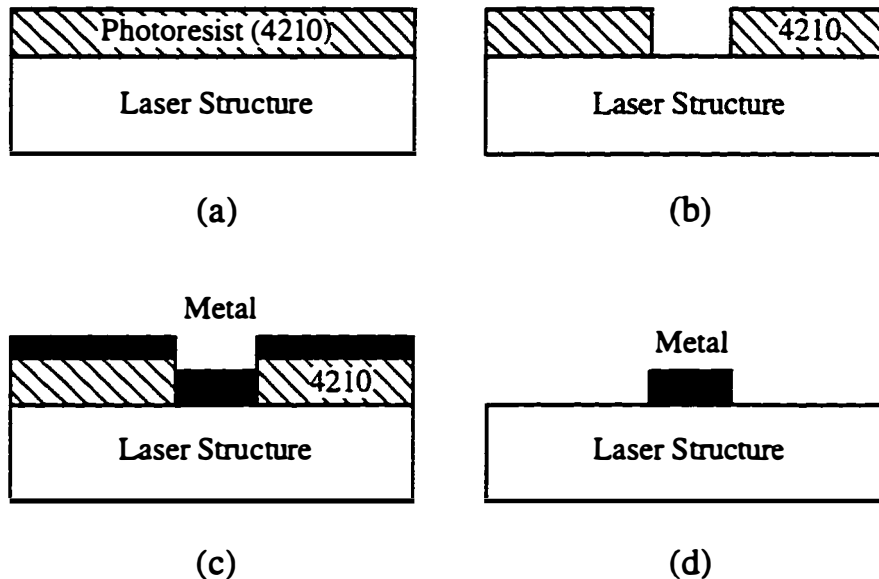


**Figure B-1** Schematic of four important points in the lithography and p-metal processes as discussed in Section B-1.

Now, the laser structure is ready for p-metallization. Since the doping level in the p-GaAs contact is very high ( $> 10^{19} \text{ cm}^{-3}$ ), a non-doping contact can be used without a significant increase in contact resistance. Due to its robustness, the titanium/platinum/gold metallization system is used (known as Ti/Pt/Au). This metal is deposited onto the sample in a electron beam (E-beam) evaporation system at a base pressure of  $2 \times 10^{-6}$  torr or less. For this step, the thickness of the Ti, Pt, and Au are 30 nm, 30 nm, and 350 nm respectively. For the ridge etch processing, a sacrificial 60 nm Ni layer is deposited as an etch mask. This process coats the entire sample with metal. As is shown in Figure B-1(c), the metal is discontinuous and allow for easy removal of the metal in the lift-off process. In order to remove the resist, acetone is used for the resist and the metal that lies on top of it. After the lithography process, the sample's state is shown in Figure B-1(d).

## B.2 Ridge Etch of Laser Structure and p-metal anneal

The next step of the laser process is to define a ridge from the p-metal to the active region. This is to allow the current that flows in the device to be restricted to this ridge (known as the ridge width in future discussions). For these devices, dry etching of the p-Al<sub>x</sub>Ga<sub>1-x</sub>As is used. Dry etching differs from wet etching in that the gaseous etch species can be excited such that both chemical and physical components of etching can be used to control the resulting etch profile [1-3]. In the case here vertical sidewalls are desired. However this comes at the small cost of possible damage to important layers [4]. The etch chemistry used in this step is BCl<sub>3</sub>:SiCl<sub>4</sub>:Cl<sub>2</sub> in the proportion of 10:2:1. For AlGaAs, the etch rate is approximately 380 nm/min. at a base pressure of 5x10<sup>-6</sup> Torr, an etch pressure of 5 mtorr, and a plasma power of 100 watts. A laser reflectometry system is used to determine the proper stopping point of the etch which is targeted for 150 nm above the fusion interface. After removing the sample from the etch chamber, the etch damage is removed in SBW: 2 HBr: 1 H<sub>2</sub>O for 15 seconds which can etch up to 70 nm of additional material. In addition, this etch solution etches off the remaining Ni mask [5].

After the ridge has been etched, the Ti/Pt/Au metal is annealed to improve contact resistance. The annealing conditions used here were 450°C in a forming gas ambient for 20 seconds. In the case of 50 μm broad-area lasers, the samples are now ready to be thinned for the n-metallization. For the narrow ridge structures, the processing for the bond pad needs to be done.

## B.3 Bond Pad Lithography and Metallization

In order to make good contact to ridges that are < 10 μm wide, some type of wider bonding pad is used for probing. The procedure for placing the bond pads over the ridges consists of three parts: application of a dielectric (in my

case PMGI) on which to place the bond pad, lithography of photoresist to define the bond pad pattern and placement, and the E-beam metallization of the bond pad itself. As stated above, a dielectric is needed in order to place the bond pads over the laser ridges. I chose to use PMGI over a more conventional choice of polyimide due to its ease of processing. For its use here, PMGI (SF-15) is spun onto the sample at 4000 rpm for 45 seconds. The expected thickness of the PMGI is over 3  $\mu\text{m}$  and easily covers the ridges. To make the PMGI more planar, the PMGI is baked in an oven at 300°C for 3 minutes. After the planarization, the metal ridges need to be exposed. This is done by exposing the PMGI to deep ultraviolet light (DUV) and then developing in a developer solution (in this case SAL 101). For my ridges, the exposure time was about 2 minutes with a 2 minute development.

At this point, the lithography for the bond pads is done. The procedure is nearly identical to the one outlined in Section 1. However, a thicker resist (AZ 4330) is used along with a longer (45 seconds) exposure time. The E-Beam metallization is done as outlined in Section 1. In this case, the metal used is Ti/Au with thickness of 15 and 700 nm respectively. The resist is then removed in acetone. To help in the cleaving of laser facets, the PMGI in the field is removed by exposing the samples for 5 minutes and then developing them for 2 minutes in SAL 101.

#### B.4 Sample thinning and n-metallization

The next step in the process of laser fabrication is the thinning of the sample to facilitate cleaving laser facets. The laser structure is first mounted p-metal side down onto a piece of Si with a wax that can dissolve in acetone and melts around 115°C. After cooling, the sample is then mounted on a brass fixture for thinning. At UCSB, the thinning process involves manually rubbing the laser structure on a paper of 12  $\mu\text{m}$  aluminum oxide grit. The thickness between the



Si and the top of the laser structure is repeatedly measured until its value is between 3 to 5 mils (75 to 125  $\mu\text{m}$ ). The samples is then removed from the brass thinning fixture and cleaned in preparation for the n-metallization.

The n-metallization, like the Ti/Pt/Au metallization discussed in Section 1, is done in a E-Beam evaporator at a base pressure of  $2 \times 10^{-6}$  torr or less. For the n-type contact, a Ni/AuGe/Ni/Au metallization is used with thickness of 5, 100, 20, and 150 nm for each of the layers. After metallization, the sample is removed from the Si, cleaned to remove the mounting wax. Since this contact is a very broad-area contact on the backside of the wafer, the contact resistance should be low and – therefore – this contact is not annealed.

## B.5 Summary

In this chapter, I have covered the creation of a 1.55  $\mu\text{m}$  wafer-fused laser. The process starts with three samples: one with InP-based quantum wells grown by MOCVD and two AlGaAs structures, one p-type and one n-type, grown by MBE. This samples are then joined via wafer fusion and processed into either *50  $\mu\text{m}$  broad-area lasers* or *narrow ridge waveguide lasers with a PMGI bond pad configuration* for testing. In the next chapter, the experimental results of the lasers fabricated by the processes in this chapter are detailed.

## B.6 References

- [1] S. J. Pearton, "Reactive ion etching of III-V semiconductors" *International Journal of Modern Physics B* **8**, 1781 (1994).
- [2] S. J. Pearton and F. Ren, "Science of dry etching of III-V materials" *Journal of Materials Science: Materials in Electronics* **5**, 1 (1994).
- [3] E. L. Hu, "Current trends and issues for low damage dry etching of optoelectronic devices" *Physical Concepts of Materials for Novel Optoelectronic Device Applications I: Materials Growth and Characterization*, Aachen, Germany, 1990, 512.
- [4] E. L. Hu, D. G. Yu, C. H. Chen, B. P. Keller, A. L. Holmes, Jr., and S. P. DenBaars, "Ion damage propagation in dry-etched InP-based structures" *Eighth International Conference on Indium Phosphide and Related Materials (Cat. No.96CH35930) Proceedings of 8th International Conference on Indium Phosphide and Related Materials*, Schwabisch-Gmund, Germany, 1996, 107.
- [5] R. Nagarajan, "Carrier Transport Effects in High Speed Quantum Well Lasers," Dissertation, University of California - Santa Barbara, 1992.